On the Evolution of Large-Scale Structure in a Cosmic Void

Sean Philip February

Thesis Presented for the Degree of
Doctor of Philosophy
in the Department of Mathematics and Applied Mathematics
University of Cape Town
February 2014

Supervised by

Assoc. Prof. Chris A. Clarkson & Prof. George F. R. Ellis

Contents

Declaration

The work presented in this thesis is partly based on collaborations with my supervisor Assoc. Prof. Chris Clarkson (University of Cape Town), together with Prof. Roy Maartens (University of the Western Cape), Dr. Julien Larena (Rhodes University) and Dr. Denis Pollney (Rhodes University). The bulk of this work was performed in the Department of Mathematics and Applied Mathematics at the University of Cape Town between January 2010 and February 2014. This dissertation is the result of my own work, except as stated below or where explicit reference is made to the results of others.

The main results of this thesis is based on the following research papers

- *'Evolution of linear perturbations in spherically symmetric dust models'*

  Sean February, Julien Larena, Chris Clarkson and Denis Pollney

  Submitted to CQG [arXiv: 1311.5241].

- *'Galaxy correlations and the BAO in a void universe: structure formation as a test of the Copernican Principle'*

  Sean February, Chris Clarkson and Roy Marteens

  JCAP 03 (2013) 023 [arXiv: 1206.1602].

The theoretical framework presented in Section 2.3 unpacks much of the work carried out in: '*Linear perturbation theory in Lemaître-Tolman-Bondi spacetime*', Chris Clarkson, Timothy Clifton and Sean February, JCAP (2009) (arXiv:0903.5040 [astro-ph.CO]), the equations of which I had originally cross-checked.

The bulk of the numerical work was carried out in Fortran, and, where possible, double-checked in Maple.

I hereby declare that this dissertation is not substantially the same as any that I have submitted, or am submitting, for a degree, diploma or other qualification at this or any other university.

Signed: ..... Dated: .....

Sean Philip February

Abstract

Future large-scale structure surveys are expected to pin-down the properties of dark energy significantly more by mapping the cosmic web to unprecedented precision. To take advantage of such state-of-the-art technologies, the evermore accurate modelling of structure formation is absolutely necessary. While relativistic linear and non-relativistic (Newtonian) non-linear effects have been well established (although improvements are still being made), a fairly unexplored area is the impact of relativistic, non-linear effects on structure formation. As an attempt in this direction, we consider linear perturbations of a Lemaître-Tolman-Bondi (LTB) spacetime. LTB models are spherically symmetric but inhomogeneous exact dust solutions to the Einstein field equations. They are known to accommodate most observations of the background universe without dark energy. In this work we present a new numerical code to solve the set of coupled partial differential equations that describe the evolution of the (polar) perturbations, test it in the case of a Hubble-scale LTB void, and demonstrate its excellent stability and convergence. We then explore the solutions for a variety of generic initial conditions. The variable that closely resembles the Newtonian potential is shown to excite propagating (tensor) as well as rotational (vector) modes at the percent-level. Comparing our results to that which ignores the full coupling, we estimate percent-level corrections to the amplitude of the galaxy correlation function when only the scalar degrees of freedom are included. In addition, we showed that the anisotropic correlation function can nevertheless be used as a test of the Copernican Principle. Note that our code has applications to other scenarios as well in which spherical symmetry is a good approximation, such as the lensing of gravitational waves by intervening halos/voids.

Acknowledgements

I am extremely grateful to Prof. Roy Maartens for hosting me at the Institute of Cosmology and Gravitation (ICG) at the University of Portsmouth, UK, a few months before my PhD officially began at the University of Cape Town. Roy played not only a huge role in shaping my PhD topic during those initial stages, but also much later on via the first paper we published together, not to mention the various discussions we shared on other interesting projects.

During my visits to the ICG, I also had the opportunity to meet a number of interesting researchers: Guido Pettinari, Dominic Galliano, Heather Campbell, Hana Schumacher, it was a privilege to meet you all! It's amazing how I survived all of those pints. And of course, Nikolai Meures, it was great hanging out with you too. I won't forget you either Ben Hoyle, whom I was to meet as a way to settle in to Portsmouth, mistook me for someone else. I hope to be as great a dancer and comedian as you when I grow up!

I also have to thank the following people for various research-related discussions, hiking as well as partying, whom I've met through my travels abroad : Philip Bull, Celia Rivera, Alicia Belloso, Diego Gomez, Miguel Zumalacárregui, David Alonso, Daniel Figueroa, Danielle Wills and Tomi Koivisto.

A big thanks to the ACGC group at UCT for all their support, and to the Maths secretaries for all their assistance. Special thanks to my classmates Anne Marie Nzioki, Amare Abebe, Obinna Umeh, Maye Elmardi and Bishop Mongwane, to the wonderful postdocs Alvaro Dombriz, Xavier Roy, Marina Seikel, Prina Patel and Vinicius Busti, and to the amazing secretary for NASSP, Nicky Walker.

To my friends and family outside of academia, without you I wouldn't have made it. Special thanks to Anthony, Taswell, and Rudi-lee for lending an ear and offering valuable advice and encouragement when the going got tough.

I would like to thank my co-supervisor, Emeritus Prof. George Ellis, for always showing great interest in the work I am doing, and for, on many occasions, providing an invaluable angle on things I otherwise would never have likely considered.

Last, but not least, I would like to thank my supervisor, Assoc. Prof. Chris Clarkson, for his eloquent guidance, precious ideas, and above-all, patience, especially while I was fighting to achieve results that made sense.

Conventions and Acronyms

Throughout this manuscript, when dealing with the full spacetime components of a rank-n tensor, we will use Greek indices (α, β,..), and reserved the Latin indices from i, j, etc. to label the spatial components. In the spherical coordinate system used, a 2+2 decomposition will also be introduced, whereby the time and radial coordinates will be labelled with capital Latin indices (A, B,..), while the coordinates on the two-sphere will be labelled with lower-case Latin indices (a, b,..). Where necessary, a hat will be used to denote quantities on the background spacetime, a tilde for quantities on the perturbed spacetime after a coordinate transformation or for dimensionless quantities, and an overbar for the axial (odd) parity modes in the case of LTB perturbations.

In the context of the standard perturbation framework, covariant derivatives of quantities on the three-dimensional spatial hypersurface are denoted by a vertical bar. In the LTB case, a vertical bar is reserved for covariant derivatives on the temporal-radial subspace, while a semi-colon indicates covariant derivatives on the 2-sphere.

The signature of the metric is taken to be $(-,+,+,+)$ and we choose units in which $c = 1$.

The acronyms used in this thesis are summarised in Table 1 below.

Name	Description
2PCF	Two-Point Correlation Function
BAO	Baryon Acoustic Oscillation(s)
BV	Big Void (model name)
CMB	Cosmic Microwave Background
CP	Copernican Principle
DE	Dark Energy
Δ	Gauge-invariant density contrast
(C)DM	(Cold) Dark Matter
D_V	Dilation scale
d_z	Averaged BAO scale
EdS	Einstein-de Sitter
EFE	Einstein field equations
FLRW	Friedmann-Lemaître-Robertson-Walker
GI	Gauge-Invariant
GR	General Relativity
GW	Gravitational Wave
Gyr	Gigayear [10^9 years]
H_0	Hubble's constant (km/s/Mpc)
ℓ	Angular momentum quantum number
Λ	Cosmological constant
ΛCDM	Concordance model
LTB	Lemaître-Tolman-Bondi
Mpc/Gpc	Megaparsec/Gigaparsec [$3.09\times10^{22}/10^{25}$ m]
MV	Medium Void (model name)
PDE	Partial Differential Equation
$\mathcal{P}_{\Phi_{\rm init}}$	Primordial power spectrum
RSD	Redshift Space Distortions
RW	Regge-Wheeler
SDSS	Sloan Digital Sky Survey
σ	Scalar shear
SNIa	Type-Ia Supernovae
SV	Small Void (model name)
SVT	Scalar-Vector-Tensor
(I)SW	(Integrated) Sachs-Wolfe
(k)SZ	(kinematic) Sunyaev-Zel'dovich
t_0	Age of the universe
WMAP	Wilkinson Microwave Anisotropy Probe
$Y_{\ell m}$	Scalar spherical harmonic basis function
z	Redshift

Table 1: List of acronyms used in this work.

I like the scientific spirit — the holding off,
the being sure but not too sure, the willingness to
surrender ideas when the evidence is against them: this
is ultimately fine — it always keeps the way beyond open.

WALT WHITMAN

CHAPTER 1

The Standard Model of Cosmology

1.1 Introduction

In this chapter we review the historical, theoretical and observational developments that led to the current concordance model of Cosmology.

1.1.1 Historical Overview

Since its inception in 1916, Einstein's theory of General Relativity (GR) [1] has now been at the heart of cosmology for the better part of the last century. Up until the discovery of the expansion of the universe from Hubble's observations in 1929 [2], a popular belief was that the universe was static. In addition to this assumption, Einstein's original cosmological model [3] further adopted the Cosmological Principle − that the universe is homogeneous and isotropic on large enough scales − and included only ordinary matter. Such a configuration had two requirements to remain static: (1) the universe had to be positively curved (closed), (2) but furthermore to prevent any non-vanishing acceleration had to contain a repulsive "cosmological term" − now known as the cosmological constant Λ − to essentially counteract the attractive gravitational force. Following Hubble's discovery, Einstein subsequently abandoned Λ, calling it his "biggest blunder".

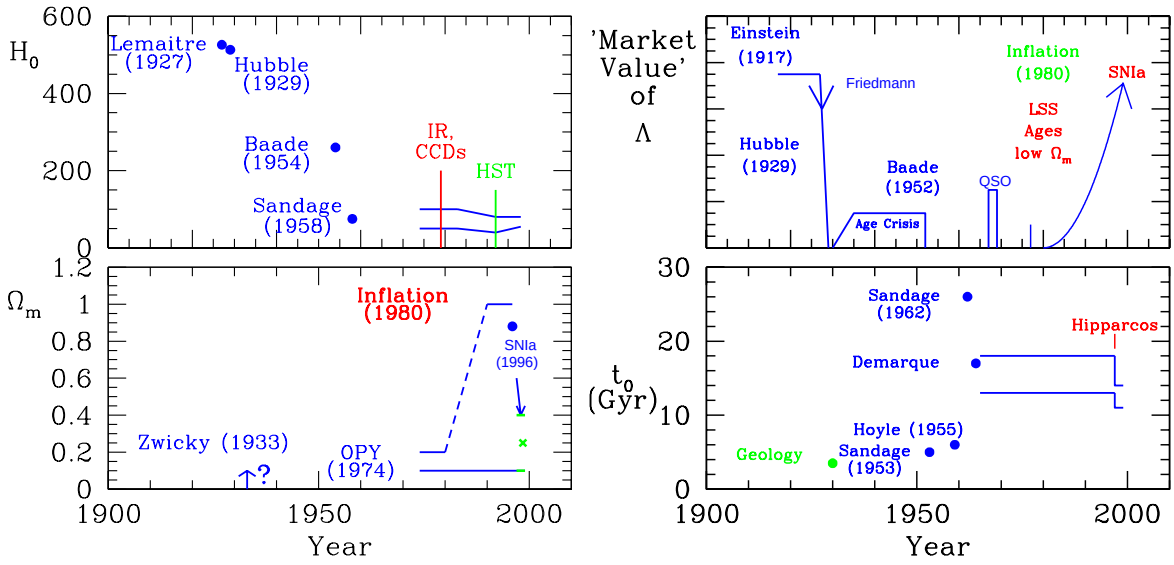

Figure 1.1: Timeline of the values of key cosmological parameters over the last century. From [4].

The discovery of the Cosmic Microwave Background (CMB) radiation in 1965 [5] supported the (hot) big bang hypothesis [6]. The view back then of the standard big bang model was that the universe began from a minuscule state (the so called "primeval atom") of extremely high density and temperature. Within the first three minutes of adiabatic expansion, protons and neutrons condensed out of the quark-gluon plasma. The production of a few light nuclei (deuterium, helium, lithium), through a process called Big Bang Nucleosynthesis (BBN) (see e.g. [7] for a recent review), then followed as a result of the drop in temperature to below ~ 1 MeV due to the expansion. Roughly 380 000 years later, the universe became cool enough ($\sim$ 1eV) to allow electrons to combine with the protons. The formation of these first atoms enabled the photons to escape into rest of the cosmos, leaving behind the relic radiation emitted by the surface of last scattering – this is the CMB light that we measure today. Gravitational collapse then took over, allowing stars and galaxies to form.

This intuitive picture was not without its issues, though. For instance, it could not explain why seemingly causally disconnected regions of the sky had temperatures within 1 part in 10^5 of each other – the so called *horizon problem*. Nor could it explain why the total energy density was so close to the critical density – the *flatness problem*.

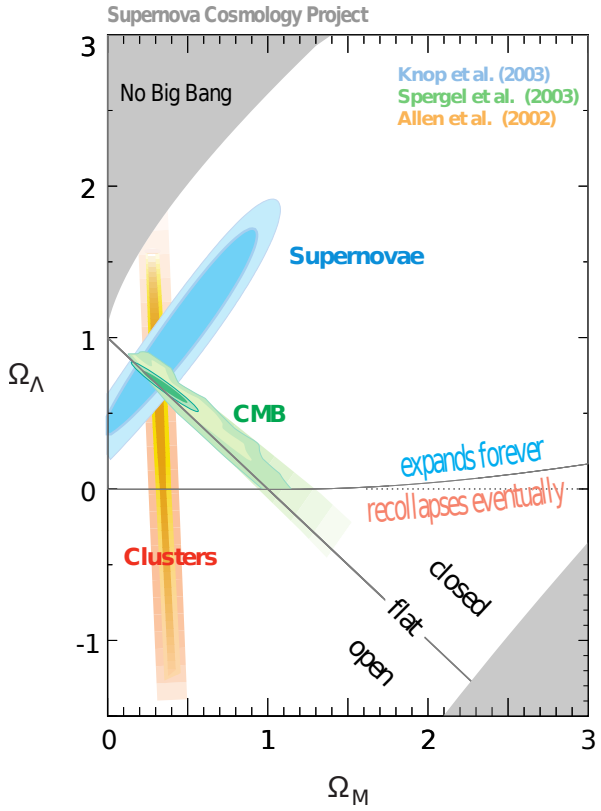

Figure 1.2: The Ω_Λ-Ω_m plane. Courtesy of the Supernova Cosmology Project.

An intriguing solution to these problems arrived in 1981 [8], in the form of a mechanism known as inflation, which involves an exponentially fast expansion of the very early moments of the universe. Remarkably, as a by-product, inflation naturally generates a spectrum of quantum fluctuations, and therefore also provides an origin for the seeds for structure formation.

Around the same time (early 80's), the evidence for a non-luminous matter component within galaxies and clusters thereof – dubbed dark matter (DM) – was mounting [9]. In the context of structure formation, a number of DM candidates were subsequently proposed. In particular, the non-relativistic (or cold) type generally fitted in quite well with the observed distribution of galaxies [10].

The first evidence suggesting the existence of a non-zero (positive) cosmological constant came from the clustering of large-scale structure. [11] showed, via the angular correlation function derived from N-body simulations of low-density universes, that

the observed distribution of galaxies (from the Automatic Plate Measuring machine in Cambridge) may be accounted for if about 80% of the energy budget of the universe was in the form of a cosmological constant.

During the mid 1990's, accurate measurements of the ages of globular clusters ([12] determined a lower limit of $\sim$12 Gyr) presented a problem for flat, matter-dominated cosmologies: unless the (dimensionless) Hubble constant was quite low ($h \lesssim 0.5$), the age of the universe would in fact be younger than some of the objects within it.

By the turn of the century, the cosmological constant made its official return via: independent measurements of distances to type Ia supernovae (SNIa) [13, 14] (for whose efforts were rewarded the 2012 Nobel Prize); the clustering of galaxies in the two-degree field galaxy redshift survey [15]; the X-ray gas mass fraction of galaxy clusters observed by the Chandra Satellite [16]; and through precise all-sky measurements of the CMB temperature anisotropies by the Wilkinson Microwave Anisotropy Probe (WMAP) [17]. These results strongly supported the idea that the expansion of the universe was not slowing down, as expected in a matter dominated universe, but was rather speeding up. Since then, a fiducial cosmology with flat spatial sections, $h \approx 0.7$, and dimensionless density parameters in Λ, cold dark matter (CDM) and baryonic matter of $\Omega_\Lambda = 0.7$, $\Omega_c = 0.25$ and $\Omega_b = 0.05$, respectively, provides a remarkably good fit to the variety of observational probes established to date − see Section 1.3.1 for an overview. This concordant picture, referred to as ΛCDM, is captured in Fig. 1.2.

Unfortunately, though, this is all at the cost of being 95% in the dark about the total mass/energy contained within the cosmos. In particular, it is not clear how to reconcile the discrepancy − around 120 orders of magnitude − between the smallness of the observed value of Λ, and its expected theoretical counterpart i.e. the vacuum energy. This is the *fine-tuning problem*. Furthermore, the fact that the energy density associated with Λ and that of matter is of a similar magnitude today − right when we are here to observe its effects (in terms of an accelerated expansion) − seems quite unnatural. This is known as the *cosmic coincidence problem*. See [18] and references therein for an early discussion on these problems.

Leaving some of the more philosophical issues aside for now, there has been much effort in pursuing alternatives to Λ. Besides the conservative approach that allows for a more general dark energy (DE) component (see e.g. [19]) in which the equation of state $w < -\frac{1}{3}$, or perhaps a scenario in which DE and DM are interacting in some way [20] (note that in both cases, the coincidence problem is somewhat relaxed), other popular alternatives are that of modified gravity [21], backreaction [22] and some classes of inhomogeneous cosmologies [23] − see Section 1.4 for a brief overview of some of these alternatives. Note that in this thesis we will be focusing on a specific class of inhomogeneous models. In particular, one that violates the Copernican Principle (CP) − further details on this topic is provided in the next sub-section (although see also [24] for an in-depth discussion).

Cosmological modeling has always been very much phenomenological by nature, and as such numerous observational and theoretical efforts towards determining the cosmological parameters to more and more precision are continuously being undertaken. What sets the ΛCDM model apart in this endeavour, though, is the fact that it is far simpler to deal with, both theoretically as well as numerically. And, by virtue of Occam's razor, it continues to withstand the test of time.

1.1.2 The Copernican Principle

An underlying assumption still embedded in much of modern-day cosmological modeling is that the Copernican Principle (CP) holds, which states that we do not reside in a special location in the universe. While this seems like a reasonable, albeit philosophically motivated, assumption, it still requires observational confirmation. The assumption of isotropy, on the other hand, is strongly supported − at least on the largest scales by the tiny ($\sim 10^{-5}$) temperature fluctuations of the CMB.

Combining this high degree of observed isotropy with the CP implies a high degree of homogeneity, which is precisely the almost-Ehlers-Geren-Sachs theorem [25]. The latter is a fundamental property of the concordance ΛCDM model, in which the deviation from an otherwise exactly homogeneous and isotropic background Friedmann-Lemaître-

Robertson-Walker (FLRW) geometry is modelled via linear perturbation theory – see Section 1.2 for a review of the theoretical framework. Indeed, if it is found that there does exist a privileged location in space – e.g. our galaxy or local group is situated in a preferred position – we may need to take into account a greater level of inhomogeneity than previously assumed. In fact, a recent study [26] claims the possibility of such a preferred position in the local universe: their observations of the stellar mass density is consistent with the presence of a local underdensity of roughly 300 Mpc across (see Fig. 1.3). Interestingly, an underdensity of similar size, although not locally centered, can account for the observed CMB Cold Spot [27, 28], among other CMB anomalies. Additionally, such structures can also account for the so-called "cosmic

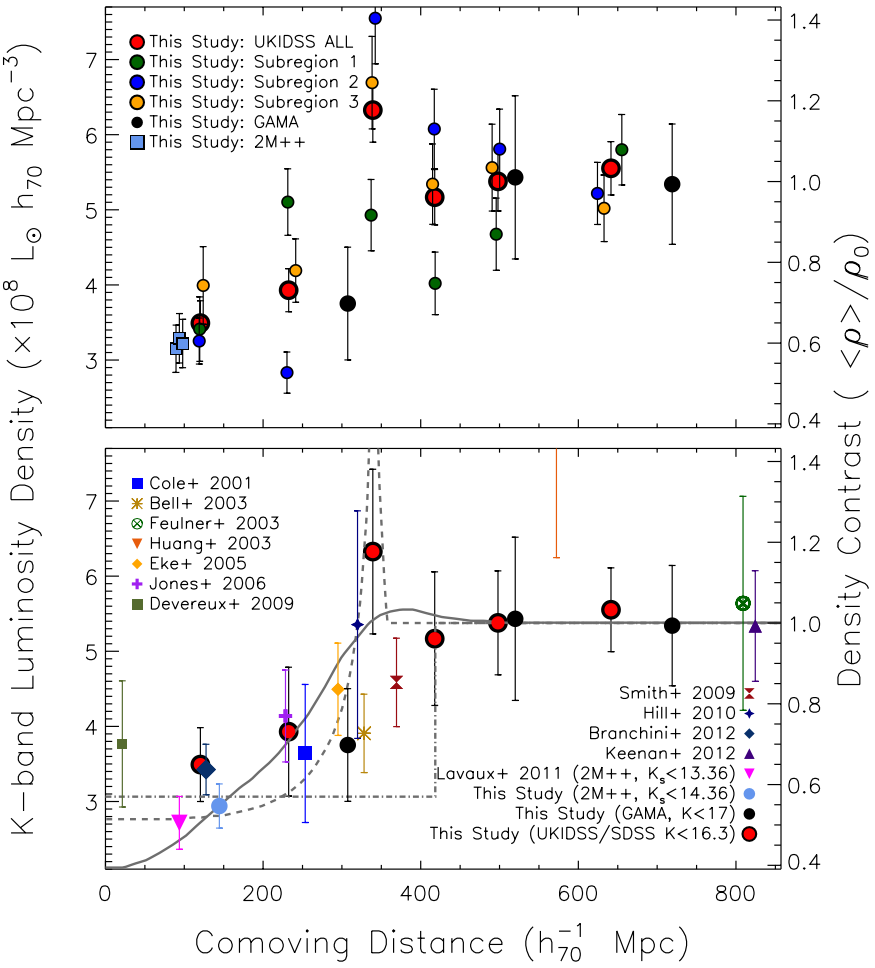

Figure 1.3: Evidence for a large ($\approx$ 300 Mpc) local underdensity (void) in the stellar mass distribution. From [26].

radio dipole" seen in galaxy distribution [29]. The presence of such structures in the universe, including known overdense ones (see e.g. [30]), may have a non-negligible impact on cosmological parameter constraints [31, 32, 33]. Note that, in the case of observers (ourselves) far from the centre of an otherwise acceptedly-large under-/overdensity within the standard model, this is not of particular relevance for the CP since such observers would not be regarded as occupying a privileged location.

The challenging task of testing the CP has already begun within the context of spherically symmetric but inhomogeneous cosmologies based on the Lemaître-Tolman-Bondi (LTB) family of exact solutions (see Section 2.2 for theoretical details). LTB models are necessarily non-Copernican by nature due to the existence of a privileged location as the centre of the cosmos. Furthermore, to satisfy bounds on the observed CMB dipole moment, our location is typically constrained to occupy a region very close to the centre of the universe: within a few tens of Mpc or so [34, 35, 36] of a Hubble-scale underdensity. As such, the task within the context of such models (including approximations thereof, e.g. the so called "Hubble Bubble" model [37]) has been to find the extent to which observations can accommodate *radial* inhomogeneity without DE. In particular, the following popular tests of the CP have been proposed:

CMB scattering. The presence of a local inhomogeneity will contribute two main effects on the observed CMB signal [38]: a kinematic Sunyaev-Zel'dovich (kSZ) effect due to the systematic peculiar motion induced by the inhomogeneity [39, 40, 41, 42], largely contributing to a dipole moment for observers away from the centre of symmetry, as well as a non-zero $\mu-$distortion causing departures from an otherwise blackbody CMB spectrum [43, 44, 45].

Consistency tests. A number of consistency relations have been developed within the context of FLRW models through the reconstruction of certain quantities by purely observational means [46, 47]. For instance, the dimensionless curvature density parameter Ω_k may be expressed in terms of distance and Hubble rate measurements, as a function of redshift. Any significant departure of Ω_k from a constant value will imply a breakdown of FLRW geometry, regardless of the

actual nature of DE. See Fig. 1.4 from [48].

Anisotropy in BAO scales. In a FLRW model, the radial and transverse components of the BAO length scales (after accounting for redshift-space distortions) are known to be equal. Precise measurements of these in future galaxy surveys will serve as a direct probe of the geometry of the underlying spacetime [46, 49, 50], and thereby allow for a robust test of the homogeneity assumption.

Redshift-drift. The time rate of change of the observed redshift, $\dot{z}$, of cosmological sources offers another key test of the CP [51]. In the concordance ΛCDM model, $\dot{z}$ is positive at all redshifts, while typical inhomogeneous (void) models produce a negative $\dot{z}$ [52, 53], although see [54] for the case of an overdense "hump". [51] also introduces a consistency relation using $\dot{z}$, which essentially constrains the level of shear present in the spacetime.

Other tests have also been proposed. For example, via: the local smoothness of the (void) matter density profile [55]; the integrated Sachs-Wolfe (ISW) effect [56]; galaxy-pairs [57]; the galaxy fossil record [58]; cosmic chronometers [59, 60, 61]. Note that, in principle, direct measurements of the line-of-sight and transverse Hubble parameters also serve as a test of the CP, since these will in general differ from each other in non-homogeneous spacetimes. Given the known difficulty that the simplest LTB models have experienced in fitting the combined data [62], though, it is worth mentioning the study carried out by [63], in which Λ is actually included in their LTB models to provide constraints on the amount of inhomogeneity allowed within the concordance model itself.

Finally, note that tests of the CP via probes of structure formation such as the CMB, BAO, kSZ and ISW effects, are in principle incomplete, since these have not yet taken the details of structure growth in non-homogeneous backgrounds into account – although see Section 2.3 and thereafter for progress in this direction.

In the next section, we introduce the theoretical foundations of the standard model, highlighting the key observables contained therein, both coming from the underlying

background geometry as well as from the perturbed level in terms of the growth of cosmic structure.

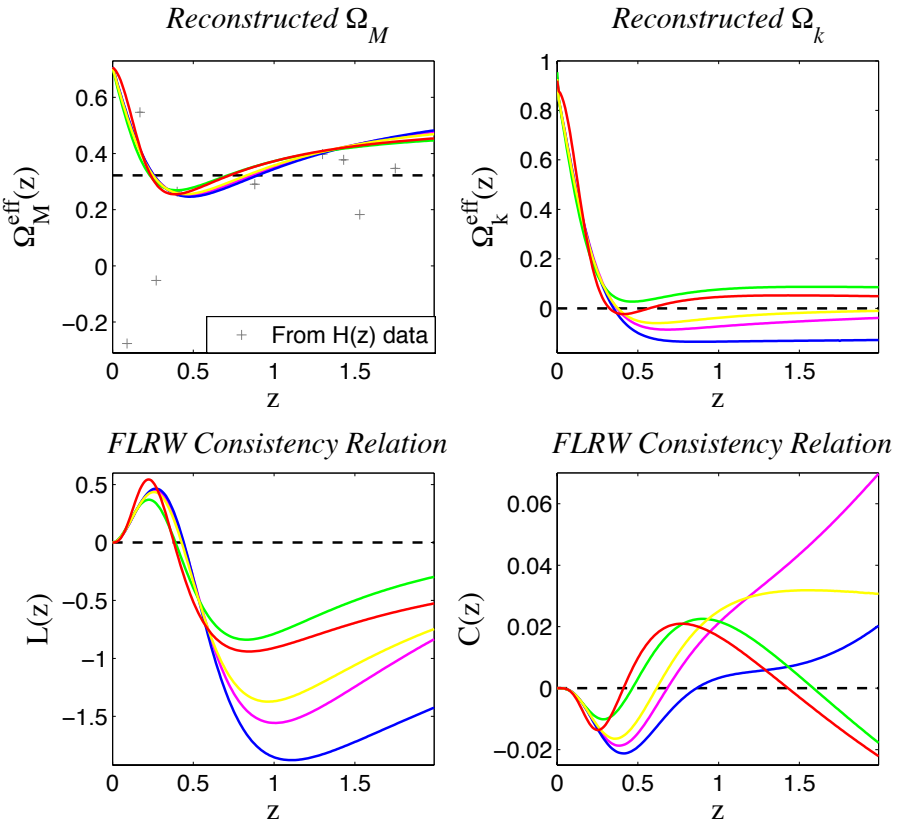

Figure 1.4: Consistency tests of the standard model. *Top*: Reconstructed dimensionless matter (left) and curvature (right) energy densities for a variety of LTB void models (solid colour curves), as a function of redshift. $\Omega_{\rm M}^{\rm eff}$ should be constant in the concordance model, while $\Omega_{\rm M}^{\rm eff}$ should be constant in any FLRW model. The expected value from a fiducial flat ΛCDM model is also shown (black dashed lines). *Bottom*: Corresponding differentials of the quantities in the top panel. These should be zero in all FLRW models. From [48].

1.2 Theoretical Foundations

1.2.1 General Relativity

Einstein's theory of gravity [1] is governed by the following field equations

$$G_{\alpha\beta} \equiv R_{\alpha\beta} - \frac{1}{2}Rg_{\alpha\beta} = 8\pi G T_{\alpha\beta} - \Lambda g_{\alpha\beta}\,. \tag{1.1}$$

The left hand side encodes the underlying spacetime geometry, where $G_{\alpha\beta}$ is the Einstein tensor, $R_{\alpha\beta}$ the Riemann tensor, R the Ricci scalar, $g_{\alpha\beta}$ the metric tensor and Λ the cosmological constant. The right hand side describes the material/energy content contained within the spacetime, where $T_{\alpha\beta}$ is the energy-momentum tensor, defined assuming a perfect fluid description via

$$T_{\alpha\beta} = (\rho + p)u_\alpha u_\beta + p g_{\alpha\beta}\,, \tag{1.2}$$

with ρ the total physical energy density of all the fluid species present, $p \equiv \sum_i w_i \rho_i$ the total pressure, where w_i represents the equation of state of a specific component, and u^α is the fluid's four-velocity. Without any loss of generality, from Eq. (1.1) above, we may absorb Λ into $T_{\alpha\beta}$ and simply treat it as a fluid component with $w = -1$, in which $\rho_\Lambda \equiv \Lambda/8\pi G$. Note that the contracted Bianchi identities lead to the condition of matter-energy conservation,

$$\nabla^\alpha T_{\alpha\beta} = 0\,, \tag{1.3}$$

where ∇_α (equivalently a ;) represents the covariant derivative associated with $g_{\alpha\beta}$.

1.2.2 Background Dynamics

The line element describing an expanding homogeneous and isotropic spacetime is provided by the FLRW metric:

$$ds^2 = g_{\mu\nu}dx^\mu dx^\nu = -dt^2 + a^2(t)\left[\frac{dr^2}{1-Kr^2} + r^2\left(d\theta^2 + \sin^2\theta d\phi^2\right)\right]\,, \tag{1.4}$$

where t is cosmic time, r comoving radial distance, θ and ϕ the polar and azimuthal angles on the sky, respectively, $a(t)$ is the scale factor, ranging from 0 (at the big bang)

to 1 (today), and K is a parameter describing the curvature of the spatial sections, taking on values < 0 (open), 0 (flat) and > 0 (closed).

Including fluid sources of matter/energy typically considered, as summarised in Table 1.1, but replacing Λ with a general DE component, with $p_{DE} = w_{DE}\rho_{DE}$ ($w_{DE} < -\frac{1}{3}$), (1.2) becomes:

$$T_{\mu\nu} = [\rho_m + (4/3)\rho_r + (1 + w_{DE})\rho_{DE}]\, u_\mu u_\nu + [\rho_r/3 - w_{DE}\rho_{DE}]\, g_{\mu\nu}\,, \tag{1.5}$$

where the (comoving) observer four-velocity is given by

$$u^\alpha \equiv [1, 0, 0, 0] \quad , \quad u^\alpha u_\alpha = -1\,. \tag{1.6}$$

The Einstein field equations (EFE) (1.1) in this setup obey the following Friedmann equation, describing the evolution of the Hubble parameter

$$H^2 \equiv \left(\frac{\dot{a}}{a}\right)^2 = \frac{8\pi G}{3}\rho - \frac{K}{a^2}\,, \tag{1.7}$$

where $\rho \equiv \sum_i \rho_i = \rho_m + \rho_r + \rho_{DE}$, as well as the Raychaudhuri equation, describing the rate of change in the expansion

$$\frac{\ddot{a}}{a} = -\frac{4\pi G}{3}\sum_i (1 + 3w_i)\rho_i\,. \tag{1.8}$$

The condition of energy conservation (1.3) leads to the following equation for each fluid component

$$\frac{d\rho_i}{\rho_i} = -3(1 + w_i)\frac{da}{a}\,, \tag{1.9}$$

$$\Rightarrow \quad \rho_i = \rho_{i,0}\exp\left\{-3\int_1^a d\ln a\Big[1 + w_i(a)\Big]\right\}, \tag{1.10}$$

where we have allowed for possible time-dependence in the equation of state − though this will only occur in the case of a general DE component.

Using the subscript '0' for the value of a quantity today, t_0, in which the scale factor $a_0 = 1$, we may also conveniently define present-day dimensionless fluid and curvature

Type	w_i	$\rho_i(a)$ $\propto$	$a(t)$ $\propto$	$\Omega_{i,0}$ $\approx$
radiation	$1/3$	a^{-4}	$t^{1/2}$	10^{-5}
matter	0	a^{-3}	$t^{2/3}$	0.3
Λ	-1	constant	$e^{\sqrt{\frac{\Lambda}{3}}t}$	0.7

Table 1.1: Selected properties of individual fluid components typically considered. The present-day densities shown in the last column corresponds to a typical set of fiducial cosmological parameters, in which Λ accounts for about 70% of the energy budget, pressure-free matter (dark + baryons) 30%, leaving no room for curvature. See Table 1.2 for a more up-to-date list of important concordance model parameters.

density parameters respectively as follows:

$$\Omega_{i,0} \equiv \rho_{i,0}/\rho_{\rm crit}\ , \quad \Omega_k \equiv -\frac{K}{H_0^2}\,, \tag{1.11}$$

where $\rho_{\rm crit} \equiv 3H_0^2/8\pi G$, and H_0 is the Hubble constant. The Friedmann equation (1.7) then becomes

$$H^2 = H_0^2\left[\Omega_{m,0}a^{-3} + \Omega_{r,0}a^{-4} + \Omega_{k,0}a^{-2} + \Omega_{_{DE},0}F(a)\right]\,, \tag{1.12}$$

where

$$\Omega_{m,0} + \Omega_{r,0} + \Omega_{_{DE},0} \equiv \Omega_{\rm tot,0} = 1 - \Omega_{k,0}, \tag{1.13}$$

and $F(a) \equiv \exp\left\{-3\int_1^a d\ln a\left[1 + w_{_{DE}}(a)\right]\right\}$. Using the Raychaudhuri equation (1.8) we may obtain an expression for the deceleration parameter

$$q \equiv -\frac{\ddot{a}}{aH^2} \tag{1.14}$$

$$= \frac{1}{2}\left(\frac{H_0}{H}\right)^2\left\{\Omega_{m,0}a^{-3} + 2\Omega_r a^{-4} + \left[1 + 3w_{_{DE}}(a)\right]\Omega_{_{DE}}F(a)\right\}. \tag{1.15}$$

Note that, while the notion of accelerated expansion makes intuitive sense in a homogeneous spacetime such as FLRW, in non-homogeneous cosmologies it is less trivial to separate temporal from radial variations down the past light cone[1].

We now define a number of quantities that are important for connecting theoretical predictions with observations.

[1]Nevertheless, in Section 2.2 we define an analogous acceleration (Raychaudhuri) equation in a non-homogeneous cosmology. For a more general discussion of this, see e.g. [64, 65] and references therein.

1.2.3 Redshift, Cosmic Age and distances

Cosmological observations rely on the fact that we can detect the light emitted from the various sources of interest. Light rays follow null geodesics, described by a wavevector of the form (see [66])

$$k^\alpha = dx^\alpha/d\lambda \tag{1.16}$$

$$= E(u^\alpha + n^\alpha)\,, \tag{1.17}$$

where λ is a parameter along the light path, $E \equiv -k^\alpha u_\alpha$ its energy, n^α a spacelike 4-vector ($n^\alpha n_\alpha = 1$). k^α satisfies

$$k^\alpha k_\alpha = 0 \;\;,\;\; k^\alpha{}_{;\beta} k^\beta = 0\,, \tag{1.18}$$

the so-called null condition, and null geodesic equations, respectively. The redshift z of a particular source is defined through

$$\frac{\nu_s}{\nu_o} = \frac{(k_\mu u^\mu)_s}{(k_\mu u^\mu)_o} \equiv 1 + z\,, \tag{1.19}$$

where ν represents the frequency of light, 's' indicating evaluation at the source location, 'o' at the observer. Note that since the energy of a photon is proportional to its frequency, we may identify the following ansatz

$$E = E_0(1+z)\,, \tag{1.20}$$

where E_0 is a constant. Moreover, from the time-component of the geodesic equations, we find the relation

$$E = E_0/a\,, \tag{1.21}$$

which then implies the following relation between scale factor and redshift in FLRW spacetimes:

$$1 + z = \frac{1}{a}\,. \tag{1.22}$$

The set of conditions (1.18), together with (1.20), yield the following relations between the coordinates and the redshift

$$\frac{dt}{dz} = -\frac{1}{(1+z)H(z)}\,, \tag{1.23}$$

$$\frac{dr}{dz} = \frac{\sqrt{1-Kr(z)^2}}{H(z)}\,, \tag{1.24}$$

where $H(z)$ is given by

$$H^2(z) = H_0^2\left[\Omega_{m,0}(1+z)^3 + \Omega_{r,0}(1+z)^4 + \Omega_{k,0}(1+z)^2 + \Omega_{_{DE},0}F(z)\right]\,, \tag{1.25}$$

with $F(z) = \exp\left\{3\int_0^z d\ln(1+z)\left[1+w_{_{DE}}(z)\right]\right\}$.

Integrating (1.23) from the time of the big bang ($t = 0, z = \infty$) to today ($t = t_0, z = 0$), we find an expression for the age of the universe:

$$t_{AGE}(\Omega_{m,0}, \Omega_{_{DE},0}, \Omega_{k,0}, \Omega_{r,0}) \equiv t_0 = \int_0^\infty \frac{dz}{(1+z)H(z)}\,. \tag{1.26}$$

Note that this quantity, while obtained independently of the age of astrophysical objects such as globular clusters, must not yield a value below that measured for any object observed in the universe.

Lastly, we introduce some common distance measures in cosmology. The comoving radial distance to a source at redshift z is

$$\chi \equiv \int_0^r \frac{dr}{\sqrt{1-Kr^2}} = \int_0^z \frac{dz}{H(z)}\,, \tag{1.27}$$

which is related to the original radial coordinate via

$$r(\chi) = \begin{cases} \sin\chi & \text{for} \quad K > 0 \\ \chi & \text{for} \quad K = 0 \\ \sinh\chi & \text{for} \quad K < 0\,. \end{cases} \tag{1.28}$$

The angular diameter distance (d_A), i.e. the relation between an objects' transverse size (D) and the observed angle on the sky under which it is subtended ($\Delta\theta$), is defined

as

$$d_A(z) \equiv \frac{D}{\Delta\theta} = a(t(z))r(\chi(z)) = \frac{r(z)}{1+z}\,. \tag{1.29}$$

The final distance measure we will introduce is the luminosity distance (d_L), i.e. the relation between an objects' intrinsic luminosity (L_s) and flux received ($\mathcal{F}_o$), where

$$\mathcal{F}_o \equiv \frac{L_s}{4\pi d_L^2}\,. \tag{1.30}$$

which is defined in the well-known form applied to a static, Euclidian background. Using the fact that the intrinsic luminosity of the source depends on the amount of energy released per unit time, i.e. $L_s = \frac{\Delta E}{\Delta t}$, in an expanding (curved) spacetime the observed luminosity redshifts as $L_o = L_s(1+z)^{-2}$. Furthermore, the cross-sectional area of light emanating from the source at redshift z, which is received by the observer (at $z = 0$), is given by $A = 4\pi r(z)^2$. The observed flux is thus

$$\mathcal{F}_o = \frac{L_o}{A} = \frac{L_s}{4\pi r(z)^2(1+z)^2}\,. \tag{1.31}$$

Equating (1.30) and (1.31) gives us

$$d_L \equiv (1+z)r(z)\,. \tag{1.32}$$

Note the connection between angular diameter and luminosity distance, known as the distance duality relation:

$$d_L = (1+z)^2 d_A\,, \tag{1.33}$$

which is in fact a trait of all metric theories of gravity [**?**].

Since, in this work, we are concerned with the accurate modeling of the *real* universe which is inhomogeneous, we now review the standard theoretical framework for describing the evolution of cosmic structure in a FLRW spacetime.

1.2.4 Growth of Large-Scale Structure

The smooth background geometry provided by the FLRW line element (1.4) cannot account for the observed structure present in the universe on its own. As outlined in the introduction, the inflationary mechanism naturally provides the seeds necessary for an inhomogeneous description of the hot and dense plasma in the very early universe, which, after decoupling, grows for the most part under gravity to become stars, galaxies, and eventually the largest super clusters and voids that we see.

In what follows, we summarise the 3+1 metric approach, presenting the system of equations describing the evolution of linear, first order perturbations on top of the smooth FLRW background. Note that linearity of the perturbations is generally satisfied for scales above 8 h^{-1} Mpc today (i.e. the scale at which the power spectrum is normalised), and so in this work we will generally steer clear of scales smaller than that.

The idea here is to begin by perturbing both sides of (1.1) in the most general way possible. Let us start with the geometrical side of the latter (i.e. the l.h.s.). To simplify the procedure, we work in conformal time, $\eta \equiv \int dt/a$, in which (1.4) takes the following form

$$ds^2 = \hat{g}_{\mu\nu} d\hat{x}^\mu d\hat{x}^\nu = a(\eta)^2 \Big[-d\eta^2 + \frac{dr^2}{1 - Kr^2} + r^2 d\Omega^2 \Big] , \tag{1.34}$$

where we introduced a hat wherever necessary to avoid confusion with perturbed quantities. Decomposing the metric tensor into background and perturbed parts as follows

$$g_{\mu\nu} = \hat{g}_{\mu\nu} + \delta g_{\mu\nu} , \tag{1.35}$$

where $|\delta g_{\mu\nu}| \ll 1$, we may write

$$\delta g_{\mu\nu} = \left(\begin{array}{c|c} A & B_i \\ \hline B_i & C_{ij} \end{array} \right) , \tag{1.36}$$

where $A \equiv 2\phi$ is a scalar, B_i a 3-vector and C_{ij} a symmetric rank-2 3-tensor. We now further decompose B_i and C_{ij} into all possible ways that they may enter into $\delta g_{\mu\nu}$ to expose all the degrees of freedom present, and follow for the most part the variables and notation used by [67]. It is well known that we can decompose any 3-vector into curl- and divergence-free parts

$$B_i = B_{|i} + S_i \,, \tag{1.37}$$

where $B_{|i} = \partial_i B$ is curl-free[2] (a vertical bar denotes covariant differentiation on the spatial hypersurface) and S_i is divergence-free. In a similar manner, we may decompose a symmetric rank-2 tensor as

$$C_{ij} = -2\psi\gamma_{ij} + 2E_{|ij} + 2F_{(i|j)} + h_{ij} \,, \tag{1.38}$$

where ψ is a scalar, γ is the static background 3-metric, E is a scalar, F_i a divergence-free 3-vector, and h_{ij} a transverse (divergence-free), traceless symmetric rank-2 tensor. We can now clearly identify 'scalar', 'vector' and 'tensor' components of the perturbed metric, which in fact turn out to evolve independently (i.e. are decoupled) at first order:

- Scalars: ϕ, ψ, B and E.
- Vectors: S_i and F_i, where $S_i{}^{|i} = 0 = F_i{}^{|i}$.
- Tensors: h_{ij}, where $h_{ij}{}^{|j} = 0 = h_i{}^i$.

Recall that in GR, we are free to choose any coordinate system we like. Furthermore, defining perturbations on top of the background spacetime as follows

$$\delta g_{\mu\nu} = g_{\mu\nu} - \hat{g}_{\mu\nu} \,, \tag{1.39}$$

there is no unique way in which to identify points in the two spacetimes that will allow one to perform the above subtraction and extract the remaining physical degrees of freedom. This is known as the *gauge problem* (see [68] for a review). The way

[2]It can therefore be written as a gradient of a scalar (B in this case).

around this problem is to perform a general coordinate (or gauge) transformation and then construct gauge-invariant (GI) combinations i.e. quantities which have the same meaning in any coordinate system. Dropping the hats on background quantities for now, and using a tilde to denote quantities in the new coordinates, we perform a small gauge transformation away from the background coordinates as follows:

$$\widetilde{x}^{\mu} = \hat{x}^{\mu} + \xi^{\mu}\,, \tag{1.40}$$

$$\xi^{\mu} \equiv \left[\xi^{0}, \xi^{|i} + \overline{\xi}^{i}\right],\ \overline{\xi}^{i}{}_{|i} = 0\,. \tag{1.41}$$

The above transformation yields the following changes to the metric perturbations:

Scalars

$$\widetilde{\phi} = \phi - \widetilde{\mathcal{H}}\xi^{0} - \xi^{0\prime}\,, \tag{1.42}$$

$$\widetilde{\psi} = \psi + \widetilde{\mathcal{H}}\xi^{0}\,, \tag{1.43}$$

$$\widetilde{B} = B + \xi^{0} - \xi^{\prime}\,, \tag{1.44}$$

$$\widetilde{E} = E - \xi\,, \tag{1.45}$$

Vectors

$$\widetilde{S}_{i} = S_{i} + \overline{\xi}^{\prime}_{i}\,, \tag{1.46}$$

$$\widetilde{F}_{i} = F_{i} - \overline{\xi}_{i}\,, \tag{1.47}$$

Tensors

$$\widetilde{h}_{ij} = h_{ij}\,, \tag{1.48}$$

where $\mathcal{H} \equiv \frac{1}{a}\frac{da}{d\eta}$. Note that the tensor h_{ij} is unaffected by the transformation, and thus already gauge-invariant. Given the four scalars, it turns out there are many GI combinations that can be constructed. For now, let us consider two well-known

variables as done by [69]

$$\Phi = \phi + \mathcal{H}(B - E') + (B - E')' , \tag{1.49}$$

$$\Psi = \psi - \mathcal{H}(B - E') , \tag{1.50}$$

For the two vectors, we can construct just one such quantity, namely

$$\overline{\Phi}_i = S_i + F_i' . \tag{1.51}$$

Turning now to the matter side of (1.1), perturbing the fluid 4-velocity as follows

$$u^\mu = \hat{u}^\mu + \delta u^\mu , \tag{1.52}$$

applying the timelike condition on the latter we find

$$u^\mu = a^{-1}\left[(1-\phi), v^{|i} + v^i\right] , \tag{1.53}$$

$$\Rightarrow u_\nu = a\left[-(1+\phi), v_{|j} + v_j + B_{|j} - S_j\right] . \tag{1.54}$$

where $v^{|i} + v^i$ is a general 3-velocity contribution. With $\rho_m = \hat{\rho}_m + \delta\rho_m$, neglecting all contributions from the radiation fluid[3] and perturbations in the DE fluid, ignoring anisotropic stresses, as well as working with a cosmological constant form of the DE, the components of the full energy-momentum tensor

$$T^\mu{}_\nu = \rho_m u^\mu u_\nu - \hat{\rho}_\Lambda \delta^\mu{}_\nu , \tag{1.55}$$

are given below:

$$T^0{}_0 = -(\hat{\rho}_m + \delta\rho_m) , \tag{1.56}$$

$$T^0{}_i = (\hat{\rho}_m - \hat{\rho}_\Lambda)\left[v_{|i} + v_i + B_{|i} - S_i\right] , \tag{1.57}$$

$$T^j{}_0 = (\hat{\rho}_m - \hat{\rho}_\Lambda)\left[v^{|j} + v^j\right] , \tag{1.58}$$

$$T^i{}_j = -\hat{\rho}_\Lambda \delta^i_j . \tag{1.59}$$

[3]We neglect radiation here as we are mainly concerned with the modeling of structure growth in the post-recombination epoch.

Once more, we are required to perform a gauge transformation in order to obtain physically relevant quantities. Let us now work out how the scalar matter density perturbation and velocity perturbation (spatial part) transform under the change of coordinates (2.58). Using the fact that the physical energy density must be invariant under coordinate transformations, we find that

$$\widetilde{\delta\rho_m} = \delta\rho_m - \xi^0\hat{\rho}'_m\,. \tag{1.60}$$

As for the spatial velocity perturbation, these transform according to the shift on spatial hypersurfaces only, which gives us

$$\widetilde{v}^{|i} = \Big(v + \xi'\Big)^{|i}\,, \tag{1.61}$$

or equivalently

$$\widetilde{v} \;=\; v + \xi'\,, \tag{1.62}$$

$$\widetilde{v}^i \;=\; v^i + \overline{\xi}^{i\prime}\,. \tag{1.63}$$

Again, given the many different scalar quantities, we can derive a number of gauge-invariant definitions for $\delta\rho_m$, or equivalently the corresponding density contrast $\delta_m \equiv \delta\rho_m/\hat{\rho}_m$. Two common examples are

$$\delta_m^N \;=\; \delta_m + \frac{\hat{\rho}'_m}{\hat{\rho}_m}\Big(B - E'\Big)\,, \tag{1.64}$$

$$\delta_m^C \;=\; \delta_m + \frac{\hat{\rho}'_m}{\hat{\rho}_m}\Big(v + B\Big)\,, \tag{1.65}$$

where 'N' denotes Newtonian and 'C' denotes comoving gauge, and are related by

$$\delta_m^N \;=\; \delta_m^C - \frac{\hat{\rho}'_m}{\hat{\rho}_m}\Big(v + E'\Big)\,. \tag{1.66}$$

Gauge-invariant definitions for the velocity perturbations are given by

$$V \;=\; v + E'\,, \tag{1.67}$$

and

$$\overline{V}_i = v_i - S_i\,, \tag{1.68}$$

$$\overline{W}_i = v_i + F_i'\,. \tag{1.69}$$

In the Newtonian (or longitudinal) gauge, the metric perturbations B, E and F_i are eliminated, and the line element takes the following form:

$$ds^2 = a(\eta)^2\Big\{-(1+2\Phi)d\eta^2 + 2\overline{\Phi}_i d\eta dx^i + \Big[(1-2\Psi)\gamma_{ij} + h_{ij}\Big]dx^i dx^j\Big\}\,, \tag{1.70}$$

where we have used the GI variables. Furthermore, the components of the energy-momentum tensor are now:

$$T^0{}_0 = -\left(\hat{\rho}_m + \delta\rho_m\right)\,, \tag{1.71}$$

$$T^0{}_i = \left(\hat{\rho}_m - \hat{\rho}_\Lambda\right)\left[V_{|i} + \overline{V}_i\right]\,, \tag{1.72}$$

$$T^j{}_0 = \left(\hat{\rho}_m - \hat{\rho}_\Lambda\right)\left[V^{|j} + \overline{V}^j + \overline{\Phi}^j\right]\,, \tag{1.73}$$

$$T^i{}_j = -\hat{\rho}_\Lambda \delta^i_j\,. \tag{1.74}$$

Below we list the perturbed EFE for the scalar, vector and tensor modes.

Scalar perturbation equations:

$$\eta-\eta: \quad 4\pi G\hat{\rho}_m\Delta = a^{-2}\left[\left(\vec{\nabla}^2 + 3K\right)\Psi - 3\mathcal{H}\Psi_{,\eta} - 3\mathcal{H}^2\Phi\right]\,, \tag{1.75}$$

$$\eta-i: \quad 4\pi G\hat{\rho}_m V = -a^{-2}\left[\Psi_{,\eta} + \mathcal{H}\Phi\right]\,, \tag{1.76}$$

$$i-i: \quad \Psi_{,\eta\eta} = -\mathcal{H}\left(2\Psi_{,\eta} + \Phi_{,\eta}\right) + K\left(\Psi+\Phi\right) - a^2\Lambda\Phi\,, \tag{1.77}$$

$$i-j: \quad \Psi - \Phi = 0\,. \tag{1.78}$$

Here we find a relativistic version of the usual Poisson equation (1.75), which relates the GI matter density contrast $\Delta \equiv \delta^N_m$ to the Newtonian/Bardeen potential Ψ. Furthermore (1.76) relates the peculiar velocity potential V to Ψ, and (1.77) is the standard Bardeen equation giving us the dynamics of Ψ. Note that Ψ will remain constant in an Einstein-de Sitter (EdS) (i.e. $K = 0 = \Lambda$) scenario, while it will decay in the case

of positive Λ or open ($K < 0$) spatial sections.

The requirement of conservation of energy-momentum ($\nabla_\mu T^\mu{}_\nu = 0$) implies that

$$\eta: \quad \Delta_{,\eta} = 3\Psi_{,\eta} - \vec{\nabla}^2 V\,, \tag{1.79}$$

$$i: \quad V_{,\eta} = -\mathcal{H}V - \Phi\,. \tag{1.80}$$

In Section 2.3 we point out analogues to many of the above equations in the case of an inhomogeneous background.

Vector perturbation equations:

$$\eta - i: \quad 16\pi G a^2 \rho \overline{V}_i = (\vec{\nabla}^2 + 2K)\overline{\Phi}_i\,, \tag{1.81}$$

$$i - j: \quad \tau_{ij,\eta} = -\mathcal{H}\tau_{ij}\,. \tag{1.82}$$

where

$$\tau_{ij} \equiv a\overline{\Phi}_{(i|j)}\,. \tag{1.83}$$

Equation (1.82) tells us that a non-zero initial vector mode decays as a^{-2} with time. In Section 2.3 we point out some similarities of this mode to one of the master variables appearing in the inhomogeneous system of perturbations.

Momentum conservation yields

$$\overline{V}_{i,\eta} = -4\mathcal{H}\overline{V}_i\,. \tag{1.84}$$

Tensor perturbation equations:

$$i - j: \quad h_{ij,\eta\eta} = -2\mathcal{H}h_{ij,\eta} - (2K - \vec{\nabla}^2)h_{ij}\,. \tag{1.85}$$

Equation (1.85) describes gravitational waves (GWs). In Section 2.3 we again remark on a variable obeying a similar equation in the inhomogeneous case.

We now take a look at some key observational windows that are now well established probes of DE.

1.3 Observational Constraints

In this section we review some important observational probes of DE, as well as unpack some of the physics and statistics behind the baryon acoustic oscillations.

1.3.1 Overview

There are a number of observational avenues now firmly established in the field of cosmology. Focussing on some of the key probes of DE, these include:

***Type Ia supernovae* (SNIa).** Initially observed by two independent groups in the late 90's [13, 14], these objects are well-known today for their role as 'standard(-isable) candles', due to their near-uniform light curve patterns. Their discovery became the latest game-changer in the field − chiefly responsible for the most recent return of the cosmological constant − and as such leading to a Nobel Prize in 2012 for the teams' efforts. Recent datasets include that from the Supernova Legacy Survey three-year (SNLS3) sample [70], as well as the Sloan Digital Sky Survey II (SDSS-II) [71]. Much anticipated future surveys include that of the Dark Energy Survey (DES) [72], the Large Synoptic Survey Telescope (LSST) [73], and the Euclid mission [74]. While the number of SNIa discovered to date is well within the thousands[4], in order to achieve percent-level (or better) accuracy in SNIa light curves, much work remains in beating down systematic errors such as various host-galaxy properties (see e.g. [75]), dust extinction (e.g. [76, 77]), and more recently weak gravitational lensing [78].

***Hubble constant* (H_0).** The discovery by Edwin Hubble [2] of the linear relationship between distances to extra-galactic "nebulae" and their radial velocities revealed that our universe is expanding. Using Cepheid variables for distance calibtration, initial estimates of the Hubble constant (i.e. the slope of the $v = H_0 d$ curve) typically put H_0 around 500 km/s/Mpc. Nowadays, in a addition to more precise distance estimates of Cepheids, the inclusion of the Large and Small Magellanic

[4]This is nearly two orders of magnitude more than that found in the late 90's. These numbers are expected to rise drastically over the next few years.

Clouds as well as nearby SN1a in the calibration process, H_0 seems to be converging to around 70 km/s/Mpc within a few percent [79, 80]. A brief report from a recent workshop [81] drawn up by various teams highlights key prospects for controlling systematics, thereby improving constraints on H_0 and ultimately DE. Note, however, that the most recent estimate from the Planck satellite [82] puts H_0 at a slightly lower value than that measured locally. Not surprisingly, this has caused some debate within the community − see e.g. [83]. Nevertheless, efforts to shrink the error bars within each team will continue, and any real discrepancy will be revealed in due course.

***Age dating* ($H(z)$).** Pioneering work by Jimenez and Loeb [84] has led to a program that extends the measurements of the local expansion rate (H_0) to that at deeper redshifts. Using passively-evolving luminous red galaxies, they do this by essentially tracking the differential age of these objects with redshift, and then relating the latter to $H(z)$ via the one of the geodesic equations. This effort allows for a more direct handle on the equation of state of DE, and thus makes for an important complementary probe of its nature. In fact, recent studies that measure $H(z)$ to a depth of $z = 1.75$ [85] show constraints on cosmological parameters that are are comparable to that obtained via e.g. SN1a and CMB, and even sets competitive limits on the effective number of neutrino species.

***Cosmic Microwave Background* (CMB).** The CMB is undoubtedly a key driving-force in much of modern cosmology. From experiments such as the Cosmic Background Explorer [86] to that of the WMAP satellite [17], and now most recently the Planck satellite [87], the state of the very early universe has to date been captured to remarkable precision on a wide range of angular scales. Apart from the temperature anisotropies, this also includes the so-called E− and B−mode polarisation patterns. While we await confirmation from Planck's polarisation data, in the mean time the polarisation instrument of another CMB experiment, the South Pole Telescope [88], has for the first time detected a significant (7.7σ) B−mode signal [89], perhaps finally placing the elusive GWs generated during in-

	Parameter	Description	Best-fit
Base	$\Omega_b h^2$	Baryon density today	0.022068
	$\Omega_c h^2$	CDM density today	0.12029
	$100\theta_*$	100 $\times$ angular size of sound horizon at z_*	1.04122
	τ	Optical depth due to reionisation	0.0925
	n_s	Scalar spectrum power-law index	0.9624
	$\ln(10^{10}A_s)$	Log power of the primordial curvature perturbations	3.098
Derived	h	Normalised Hubble constant	0.6711
	Ω_X	Density of component X divided by critical density today	0.3175
	σ_8	RMS matter fluctuations today in linear theory	0.8344
	z_*	Redshift for which optical depth equals unity	1090.43
	t_0	Age of the universe today (in Gyr)	13.819

Table 1.2: Planck-only constraints of the base 6-parameter flat ΛCDM model, along with selected derived parameters. Here the power spectrum is parameterised as $\mathcal{P}_\mathcal{R}(k) = A_s\left(\frac{k}{k_0}\right)^{n_s-1+(1/2)(dn_s/d\ln k)\ln(k/k_0)}$, where $k_0 = 0.05$ Mpc^{-1} is the pivot scale. From [82].

flation within arms reach. Many of the anomalies initially pointed out by WMAP, such as mode alignments, the Cold Spot, and Hemispherical Asymmetry to name but a few [90], still remain with Planck's findings.

***Baryon Acoustic Oscillations* (BAO).** Initially pioneered by [91], observations of BAO in the galaxy distribution serves as a complimentary probe of the physics of the CMB, with the added benefit of being more sensitive to the nature of DE itself. To date, and within the context of the concordance model, the BAO feature has proved quite powerful, providing a standard ruler with which to constrain cosmological parameters to high precision using the ever widening and deepening surveys of the underlying large-scale structure, such as that from SDSS [92, 93], the 6-degree field [94], WiggleZ [95] and the SDSS-III Baryon Oscillation Spectroscopic Survey [96]. While the majority of papers thus far focussed on a spherically averaged feature, more and more studies are now considering the individual ra-

dial and transverse components [97, 98, 99, 100, 101]. Doing so causes the usual degeneracy between angular diameter distance and the Hubble rate to be broken, thus tightening the parameter constraints. An exciting avenue for future BAO studies will lie in photometric surveys since they allow for much wider and deeper volume coverage, but at the cost of redshift accuracy (though see e.g. [102, 103, 104], which highlights possible ways to improve the accuracy of such photo-z measurements). An interesting experiment to look out for is the Physics of the Accelerating Universe [105] survey, which has dual (i.e. photometric and spectroscopic) capabilities.

Galaxy Clusters. Not surprisingly, like the BAO, the mass distribution of clusters of galaxies (at low redshifts) serves as a complimentary probe of DE (with respect to SN1a and CMB). For example, [16] carried out precise measurements of the X-ray gas mass fraction of luminous, relaxed lensing clusters using the Chandra X-ray observatory. By modeling the total cluster mass (i.e. baryonic plus dark matter) with a Navarrow, Frenk and White density profile [106], and making use of independent baryonic density constraints as well as the Hubble Key Project's measurement of the Hubble parameter, the authors obtained a mean matter density of $\Omega_m = 0.3$ (to about 10%), and found evidence for a positive cosmological constant ($\Omega_\Lambda > 0$). A recent review of this topic (i.e. cosmological constraints from galaxy clusters) can be found here [107], which highlights the various other avenues to look out for in the future, such as space-based infrared surveys, and ongoing mm surveys that are able to detect clusters via the up-scattering of CMB photons by the hot intracluster gas (i.e. the thermal SZ effect).

Other interesting observational probes of DE include that of the late ISW effect (see [108] for a recent review), as well as weak gravitational lensing [109]. The late ISW effect is sensitive to both dark energy as well as background curvature − for a discussion of this see also Section 2.3.7. Weak lensing, on the other hand, is sensitive to both dark matter and dark energy on cosmological scales determined by the level of distortion in the imaged sky field. These are expected to serve as important contributions to the

field over the coming decade. A selection of cosmological parameters constrained by the recent Planck data is shown in Table 1.2.

1.3.2 A Closer Look at the BAO

In this section we delve a little deeper into the physics surrounding the BAO, touch on some key techniques used to measure its properties observationally, as well as summarise how it has been used to constrain cosmological parameters. For a more detailed review of this topic, see e.g. [110] and references therein.

1.3.2.1 Physical picture

The BAO are generated during the pre-decoupling phase of the universe's history through the tug-of-war between gravity trying to clump baryonic overdensities together, and pressure from the photons trying to escape. Each overdense pulse in this baryon-photon plasma (as well as in the underlying dark matter) is thought to arise from the conversion of quantum fluctuations, generated during inflation, into classical density perturbations. To a good approximation, the spectrum of these fluctuations are statistically homogeneous and isotropic, are of a Gaussian nature, independent of each other (i.e. uncorrelated) and nearly scale-invariant. All relevant information is then captured the two-point correlation function (2PCF) – see [111] for a review of the basic hypotheses and framework, and Section 1.3.2.3 for more on the 2PCF.

As the universe expands and cools, each pulse travels outwards at the speed of sound in this plasma, leaving behind the dark matter clump where it was initially generated to grow under its own gravity – these are the seeds for structure formation later on. Once the universe cools to ~ 3000 K, the free electrons are able to combine with the protons to form neutral atoms, allowing the photons to escape freely into the cosmos – the resulting radiation pattern is what we measure today (at ~ 2.7 K) as the CMB. At this point, the dark matter notices the shell of baryons (now frozen-in) surrounding it, and begins to clump at this scale of ~ 150 Mpc. As a result, the large-scale structure of the universe has a tendency to be separated by this distance – the BAO scale – more often than any other, which shows up as the peak in the galaxy 2PCF (or equivalently

as a series of peaks and troughs in the power spectrum).

1.3.2.2 Geometrical picture: observed and physical length scales

Built into the above picture, it is common to assume that the physical BAO scale imprinted into the underlying DM distribution at recombination, L_{rec}, is isotropic. Note, however, that depending on the nature of the cosmological expansion − barring the effects from redshift-space distortions (RSD) − the BAO scale in different directions may not be the same at later times. As an example, and one that will be entertained later (in the context of LTB models), is one in which the line-of-sight expansion rate ($H_{\parallel}$) and that transverse to it ($H_{\perp}$) are different. In such a (special) case, the physical scales along and transverse to the line of sight are determined geometrically by

$$L_{\parallel}^{geo}(z) = L_{rec}\frac{a_{\parallel}(z)}{a_{\parallel}(t_{rec}, r(z))}\,, \text{ and } L_{\perp}^{geo}(z) = L_{rec}\frac{a_{\perp}(z)}{a_{\perp}(t_{rec}, r(z))}\,, \tag{1.86}$$

respectively.

Observationally speaking, what we measure from galaxy redshift surveys is the redshift extent, $\delta z(z)$, and angular size, $\delta\theta(z)$, of the BAO feature. These may be transformed into physical length scales via

$$L_{\parallel}(z) = \frac{\delta z(z)}{(1+z)H_{\parallel}(z)}\,, \quad L_{\perp} = d_{\rm A}(z)\delta\theta(z)\,, \tag{1.87}$$

for small δz and $\delta\theta$. These two observable scales may be combined into a single averaged quantity [112]

$$d_z = \left[\frac{(\delta\theta)^2\delta z}{z}\right]^{1/3}, \tag{1.88}$$

which in a FLRW model reduces to

$$d_z = \frac{L_{rec}(1+z_{rec})}{D_V}\,, \tag{1.89}$$

where $L_{rec}(1+z_{rec})$ is the comoving sound horizon, and

$$D_V(z) = \left[(1+z)^2 d_{\rm A}^2(z)\frac{z}{H(z)}\right]^{1/3} \tag{1.90}$$

is the standard volume averaged dilation scale [91]. In Section 2.2 we present the form

of Eq. (1.89) and (1.90) for LTB models (which are in fact generalisations of FLRW).

1.3.2.3 Statistical picture: 2-point correlation function

To make any sense of the large volumes of data that come out of galaxy redshift surveys, it is useful to perform statistical analyses. A popular quantity to use is the 2PCF. The latter may be determined observationally via e.g. the so-called Landy-Szalay estimator [113]

$$\xi^{obs}(s) \equiv \frac{\langle DD(s)\rangle - \langle DR(s)\rangle + \langle RR(s)\rangle}{\langle RR(s)\rangle}\,, \tag{1.91}$$

where s is the galaxy separation distance, D represents the data and R a randomly generated sample. Of course, the latter may be applied to particular directions on the sky (i.e. radial and transverse) if the survey allows for this. An important point to keep in mind here, though, is that a cosmological model is required to convert the redshifts into distances. Indeed, using an incorrect cosmology to interpret distances from redshifts may lead us to incorrect conclusions. Nevertheless, while this model-dependency is yet to be fully characterised − beyond the FLRW model that is − a typical approach around this is to assume a fiducial cosmology but introduce deviations from the latter using the dilation scale (Eq. (1.90)) of the non-fiducial model (see e.g. [91] for an example of this).

From the theoretical side, the anisotropic 2PCF of the galaxy distribution as measured by a central observer looking down their past light cone is

$$\xi_{\Delta}(z_1, z_2, \delta\theta) \equiv \Big\langle \Delta\Big(t(z_1), \boldsymbol{r}(z_1)\Big)\Delta\Big(t(z_2), \boldsymbol{r}(z_2)\Big)\Big\rangle\,, \tag{1.92}$$

where Δ is the gauge-invariant matter density contrast, and $\hat{\boldsymbol{r}}_1\cdot\hat{\boldsymbol{r}}_2 = \cos\delta\theta$. Indeed, the measured Δ is always biased relative to the underlying one for the DM, and moreover, RSD plays an important role. Note, however, for the purposes of this work we may safely neglect both bias and RSD, and leave their inclusion for future work (more on this in the next chapter). Unpacking (1.92) in a flat FLRW context (see Appendix C for a detailed derivation), and splitting into components parallel and perpendicular to the line-of-sight, we get

$$\text{radial 2PCF: } \xi^{\parallel}_{\Delta}(z_1,z_2) \equiv \xi_{\Delta}(z_1, z_1+\delta z, 0) = \sum_{\ell}(2\ell+1)\mathcal{C}^{\parallel}_{\ell}(z_1,z_2), \quad (1.93)$$

$$\text{transverse 2PCF: } \xi^{\perp}_{\Delta}(z_1,\delta\theta) \equiv \xi_{\Delta}(z_1, z_1, \delta\theta) = \sum_{\ell}(2\ell+1)P_{\ell}(\cos\delta\theta)\mathcal{C}^{\perp}_{\ell}(z_1), \quad (1.94)$$

where $P_\ell(\cos\delta\theta)$ the associated Legendre polynomials,

$$\mathcal{C}^{\parallel}_{\ell}(z_1,z_2) = \Big[(4\pi G a_1 a_2)^2 \rho_{m1}\rho_{m2}\Big]^{-1} \int \frac{dk}{k}\ \mathcal{J}_{\ell}(z_1,k)\mathcal{J}_{\ell}(z_1+\delta z,k)\mathcal{P}_{\Phi_{\rm init}}(k), \quad (1.95)$$

$$\mathcal{C}^{\perp}_{\ell}(z_1) = \Big(4\pi G a_1^2 \rho_{m1}\Big)^{-2} \int \frac{dk}{k}\ {\mathcal{J}_{\ell}}^2(z_1,k)\mathcal{P}_{\Phi_{\rm init}}(k), \quad (1.96)$$

and

$$\mathcal{J}_{\ell}(z,k) \ = \ -\Big[3a^2H\dot{\phi} + \Big(3a^2H^2 + k^2\Big)\phi\Big] j_{\ell}(kr)\,, \quad (1.97)$$

with $\phi(z)$ the time-dependent solution to (1.77), $j_\ell(kr)$ the spherical Bessel function, and $\mathcal{P}_{\Phi_{\rm init}}(k)$ the primordial power spectrum. The latter is related to the primordial curvature perturbation via

$$\mathcal{P}_{\Phi_i}(k) = \frac{9}{25}\mathcal{P}_{\mathcal{R}}(k_0)T^2(k)\,, \quad (1.98)$$

where $\mathcal{P}_{\mathcal{R}}(k_0) = 2.41\times10^{-9}$ is the amplitude of the primordial curvature perturbation on the (pivot) scale $k_0 = 0.002$ Mpc^{-1}, and $T(k)$ is the matter transfer function, with $T(k_0)\approx 1$. The usual flat FLRW correlation function may then be obtained using the following identity:

$$\sum_{\ell=0}(2\ell+1)P_{\ell}(\cos\delta\theta)j_{\ell}(kr_1)j_{\ell}(kr_2) = \frac{\sin ks}{ks}\,, \quad (1.99)$$

where $s \equiv s(z_1,z_2,\delta\theta) = \sqrt{r_1^2 + r_2^2 - 2r_1r_2\cos\delta\theta}$. Note of course that in the absence of RSD (and some parameterisations of bias), $\xi^{\parallel}_{\Delta}$ and $\xi^{\perp}_{\Delta}$ will necessarily have equivalent shapes in FLRW. In Section 5.3 we point out the form that the correlation functions in a LTB model take; as we will show, the main differences come about through a modified form of the $\mathcal{J}_\ell(z,k)$ functions, i.e. Eq. (1.97).

1.4 Challenges, and Steps Beyond

Although alluded to already, the cosmological constant problem is currently the main drawback for the concordance model. Interesting proposals to get around the problem includes the multiverse idea (see e.g. [114]), in which our universe is but one of an uncountable number, each with a different set of the physical constants − ours just happens to be what it is by pure chance. This may be regarded as somewhat philosophical (perhaps even anthropic at some level) at present given the difficulty in testing this hypothesis.

Another, perhaps more conservative (but seemingly related) explanation/possibility is that Λ may very well be just another constant of nature. Just like many of the other constants of nature that we have incorporated into our physical theories thus far, there is no underlying theory that predicts its value − rather, we have to determine its value phenomenologically.

Besides the aforementioned issues, though, there are a handful of other issues facing the concordance model, such as: unexpectedly large *bulk flows* [115] (although see [116, 117]); the *core-cusp problem* (see [118] and references therein), and various CMB *anomalies* [119, 90]. While some of these may still be of some concern for the integrity of the ΛCDM model, improvements of both theoretical modeling as well as observational techniques will ultimately decide upon these issues.

Extensions to the constant equation of state and flat spatial curvature paradigm are known to be consistent with the data (see e.g. [120] and references therein), as well as models in which DE and DM interact [20]. However, these models still fall short of explaining the physical nature of the DE that is purported to dominate the energy budget of the universe. Given all of these challenges, a number of authors have re-evaluated the assumptions that under-pin the concordance model. We end this chapter off by highlighting three main streams that go beyond the standard model in this regard, namely: Modified Gravity, Backreaction, and exact inhomogeneous solutions to the field equations.

Modified Gravity. Without giving up the underlying FLRW geometry, the key motivation here is that, instead of a gravitationally-repulsive fluid being responsible for the observed accelerated expansion, it may just be that the gravitational force itself is weaker on larger scales. Popular classes of such theories include that of $f(R)$ (R being the Ricci scalar, where GR is defined by $f(R) = R$), and higher-dimensional theories such as Dvali-Gabadadze-Porrati (DGP) braneworld models and Kaluza-Klein gravity (see [21] for a recent review). Note that in order for these theories to satisfy solar system constraints, one often has to employ a kind of screening mechanism e.g. Chameleon [121] or Vainshtein [122]. Just focusing on the $f(R)$ class, there are indeed certain viable parameterisations that are capable of producing an accelerated expansion at both early (i.e. to mimic inflation) and late (i.e. to mimic DE) times [123], thereby offering a very tantalising alternative to the concordance model. As such, much work is under way in order to narrow-down the space of possibilities even further by confronting these models with observations of large-scale structure, both via linear perturbation theory [124, 125] as well as an investigation into the non-linear sector via N-body simulations [126], but also through local universe tests [127].

Backreaction. A key issue arose in cosmology several decades ago [128, 129] as to whether the perturbed FLRW geometry adopted in the standard model adequately captures the average properties of the universe. If not, then the question is how and where do we expect such a breakdown to occur. As such, much debate has ensued more recently as to whether the small-scale non-linear terms arising from a suitable averaging procedure may be large enough to sufficiently affect the dynamics of the universe on the larger scales, possibly mimicking the effects of DE (see [130, 131, 22] and references therein). Nevertheless, as it currently stands, the contributions to the accelerated expansion from backreaction appears to be insufficiently convincing.

Exact inhomogeneous cosmologies. The EFE permit several exact solutions that fall under the umbrella of inhomogeneous models. Some examples used mainly in

the astrophysics and cosmology arenas include LTB [132, 133, 134] (as alluded to already in Section 1.1.2), Szekeres [135, 136] and Stephani models [137] − for a more extensive list see [138, 23]. Since we will focus on the LTB class of solutions in this work, in the next chapter we provide a brief summary of the literature, and also introduce the theoretical framework required for the applications we carry out in later chapters. In short, we explore the full evolution of linear (polar) perturbations in a background LTB void model (that accommodates distances to SNIa). This extends previous works which approximated the full details of the evolution of such perturbations. We then ultimately quantify typical corrections to the amplitude of the galaxy correlation function in the context of the BAO.

CHAPTER 2

Lemaître-Tolman-Bondi Cosmology

2.1 Motivation and Review

The LTB model provides us with one of the simplest frameworks with which to study the influence of non-linear inhomogeneities on the dynamics of the universe − with the advantage of being an exact solution to the field equations. Its simplicity stems from the fact that it features spherical symmetry about a single world line only, allowing central observers to capture a variety of non-homogeneous characteristics in just one or two radial functions, e.g. the mass density profile and bang-time function. This is all, however, at the cost of violating the CP.

Nevertheless, in light of the DE problem, a number of simple toy models have demonstrated the capacity to explain key observations of the background dynamics [139, 140, 141, 142, 55, 48], such as distances to SNIa and measurements of the Hubble parameter, without an exotic energy component. Such toy models typically feature a local suppression in the matter density (i.e. void) spanning several Gpc in diameter at the present time. Furthermore, in order to be consistent with a high degree of homogeneity in the early universe as predicted by inflation, it is common to avoid spatial gradients in the bang-time function. As a consequence, such a void develops from a tiny initial perturbation away from an otherwise EdS spacetime. These simplistic void

models have the benefit of providing an intuitive explanation as an alternative to DE: the region inside the void expands faster than the surrounding region, thus effectively mimicking the effects of DE.

Note, however, that LTB models are essentially guaranteed to fit a given pair of background observations (e.g. angular diameter distances and number counts), regardless of the details of source evolution [143]. More recently, though, using a best-fit void model from [62], [144] showed that source evolution is necessary for such models to accommodate observed number counts of far-infrared selected galactic sources.

With regards to constraints from the CMB and BAO, several authors [145, 146, 147, 148, 149, 112, 62] have taken the liberty of confronting such toy models with the latter observables, without actually taking the effects of structure formation on inhomogeneous backgrounds into account. This is not surprising though, since structure formation in LTB is still a new venture − we review this in more detail in the Section (2.3).

A few studies to date have considered minor extensions to the simplest class of void models, such as: allowing for off-centre observers [34, 35], including a non-uniform bang-time [41, 150], allowing for asymptotic curvature [112, 62], and even modifying the primordial baryon-to-photon ratio [151]. Interestingly, the latter ([151]) indicated how the lithium problem[1] could be resolved using such an additional degree of freedom as a radial dependence in the primordial baryon-to-photon ratio. In general, these extensions alleviate, to some extent, some problems that typically arise in the simplest case, e.g. a low H_0 [112], or large kSZ signal [41]. Note that, while the void class of LTB models is generally more popular, giant hump models [152] can also be accommodated when the bang-time function is allowed to vary.

As more abundant and more precise observations are being made available, several recent studies (see e.g. [149, 150, 62]) have indicated that the simplest void models are strongly disfavoured compared to ΛCDM. In particular, [62] pointed out the existence of an inherent tension between the SNIa+H_0 and the BAO+CMB constraints within

[1]This is the discrepancy between the observed abundance of lithium today and that predicted by BBN, the latter being a factor of three or so greater than the former.

these models, even when allowing for background curvature. Furthermore, the CP is increasingly being supported from stringent tests based on scattered CMB photons [44, 42], which alone causes major issues for LTB models in general.

As such, it appears that somewhat more fine-tuning will be required for the LTB framework to remain a possible contender for describing a universe without DE. While such additional degrees of freedom may ultimately not survive a full Bayesian onslaught with all of the available data, the mammoth task still lies ahead in constructing a complete picture that includes radiation at early times, as well as a spectrum of linear perturbations performed on top of such an inhomogeneous background.

In the next section we introduce the background features of the LTB spacetime, highlighting our approach for modeling specific inhomogeneous configurations as well as our method for solving for the dynamics.

2.2 Background Dynamics

2.2.1 Metric and field equations

The general unperturbed LTB line element may be written as [140]

$$ds^2 = g_{\mu\nu}dx^\mu dx^\nu = -dt^2 + X^2(t,r)dr^2 + A^2(t,r)d\Omega^2\,, \tag{2.1}$$

where $X(t,r)$ and $A(t,r)$ are functions to be solved for, and we are again working in spherical coordinates. Eq. (2.1) permits a spacetime in which the matter/energy content is pressure-free matter (dust) only, although a cosmological constant is allowed. Note also that in general, the spatial hypersurface describing the big bang singularity $t_B(r)$, in which $X(t_B(r),r) = 0 = A(t_B(r),r)$, may vary radially about the centre of symmetry.

The general form of the dust energy-momentum tensor including a cosmological constant is given by

$$T^\mu{}_\nu = \rho_m u^\mu u_\nu - \rho_\Lambda \delta^\mu{}_\nu\,, \tag{2.2}$$

where the (comoving) observer four-velocity is

$$u^\mu = [1,0,0,0] \quad , \quad u_\mu = [-1,0,0,0] \; . \tag{2.3}$$

The resulting EFE are

$$t-t: \quad 8\pi G(\rho_m+\rho_\Lambda) = -2\frac{A''}{AX^2} + 2\frac{\dot{A}\dot{X}}{AX} - \left(\frac{A'}{AX}\right)^2 + 2\frac{A'X'}{AX^3} + \left(\frac{\dot{A}}{A}\right)^2 + \frac{1}{A^2}\,, \tag{2.4}$$

$$t-r: \quad 0 = \frac{\dot{A}'}{A'} - \frac{\dot{X}}{X}\,, \tag{2.5}$$

$$r-r: \quad 8\pi G\rho_\Lambda = -\left(\frac{A'}{AX}\right)^2 + \left(\frac{\dot{A}}{A}\right)^2 + \frac{1}{A^2} + 2\frac{\ddot{A}}{A}\,, \tag{2.6}$$

$$\theta-\theta\,,\phi-\phi: \quad 8\pi G\rho_\Lambda = \frac{\dot{A}\dot{X}}{AX} + \frac{\ddot{X}}{X} + \frac{A'X'}{AX^3} + \frac{\ddot{A}}{A} - \frac{A''}{AX^2}\,. \tag{2.7}$$

Conservation of energy-momentum, i.e. $T_{\mu\nu}{}^{;\mu} = 0$, gives us

$$\dot{\rho_m} = \rho_m\left(2\frac{\dot{A}}{A} + \frac{\dot{X}}{X}\right)\,. \tag{2.8}$$

Integrating (2.5) we find

$$X = CA'\,, \tag{2.9}$$

where $C = C(r)$ is a function of integration. Motivated by the form of the FLRW metric, we apply the following redefinition: $C(r) \equiv 1/\sqrt{1-\kappa(r)r^2}$. Furthermore, we recognise $A(t,r) \equiv r a_\perp(t,r)$ as the angular diameter distance d_A (also referred to as the areal radius), which defines a transverse scale factor. The radial (or line-of-sight) scale factor is defined through $a_\parallel \equiv A'$. Our metric above then becomes

$$ds^2 = -dt^2 + \frac{a_\parallel^2(t,r)}{1-\kappa(r)r^2}dr^2 + a_\perp^2(t,r)r^2 d\Omega^2\,. \tag{2.10}$$

The FLRW spacetime is then recovered in the limit $\kappa(r) \to K$, $a_\perp(t,r) \to a(t)$, which implies that $a_\parallel(t,r) \to a(t)$.

Returning to the EFE, plugging (2.9) into (2.4) and (2.6) we are left with the following two independent equations

$$\frac{\dot{A}^2 + \kappa r^2}{A^2} + \frac{2\dot{A}\dot{A}' + 2\kappa r + \kappa' r^2}{AA'} = 8\pi G(\rho_m + \rho_\Lambda)\,, \tag{2.11}$$

$$\frac{\dot{A}^2 + \kappa r^2}{A^2} + 2\frac{\ddot{A}}{A} = 8\pi G\rho_\Lambda\,. \tag{2.12}$$

Integrating (2.12) we obtain

$$\left(\frac{\dot{A}}{A}\right)^2 = \frac{M(r)r^3}{A^3} - \frac{\kappa r^2}{A^2} + \frac{8\pi G}{3}\rho_\Lambda\,, \tag{2.13}$$

where $M = M(r)$ is another function of integration. Substituting (2.13) into (2.11) we find the following relation between M and the physical matter energy density:

$$8\pi G\rho_m = \frac{(Mr^3)'}{A^2A'}\,. \tag{2.14}$$

Futhermore, merging Eq.'s (2.11) and (2.12) allows us to write down a generalised acceleration equation

$$\frac{2}{3}\frac{\ddot{A}}{A} + \frac{1}{3}\frac{\ddot{X}}{X} = -\frac{4\pi G}{3}\left(\rho_m - 2\rho_\Lambda\right)\,. \tag{2.15}$$

Note also that we may rewrite Eq.'s (2.13), (2.15), (2.11) and (2.8) respectively in terms of the radial and transverse quantities explicitly as follows:

$$H_\perp^2 = \frac{M}{a_\perp^3} - \frac{\kappa}{a_\perp^2} + \frac{\Lambda}{3}\,, \tag{2.16}$$

$$\frac{2}{3}\frac{\ddot{a_\perp}}{a_\perp} + \frac{1}{3}\frac{\ddot{a_\parallel}}{a_\parallel} = -\frac{4\pi G}{3}(\rho_m - 2\rho_\Lambda)\,, \tag{2.17}$$

$$8\pi G(\rho_m + \rho_\Lambda) = H_\perp^2 + 2H_\perp H_\parallel + \left(1 + 2\frac{a_\perp}{a_\parallel}\right)\frac{\kappa}{a_\perp^2} + \frac{r\kappa'}{a_\perp a_\parallel}\,, \tag{2.18}$$

$$\dot{\rho_m} = -\rho_m\Big(2H_\perp + H_\parallel\Big)\,. \tag{2.19}$$

we identified

$$\frac{\dot{A}}{A} = \frac{\dot{a_\perp}}{a_\perp} \equiv H_\perp\,, \quad \frac{\dot{X}}{X} = \frac{\dot{a_\parallel}}{a_\parallel} \equiv H_\parallel\,. \tag{2.20}$$

2.2.2 Determining the solution

We may alternatively express (2.16) and (2.18) in terms of present-day quantities:

$$H_\perp^2(t,r) = H_{\perp 0}^2\Big[\Omega_m a_\perp^{-3} + \Omega_k a_\perp^{-2} + \Omega_\Lambda\Big]\,, \tag{2.21}$$

$$8\pi G(\rho_m+\rho_\Lambda) = \frac{\Omega_m H_{\perp 0}^2}{a_\parallel a_\perp^2}\left\{3 + r\left[2\frac{H_{\perp 0}{}'}{H_{\perp 0}} + \frac{\Omega_m{}'}{\Omega_m}\right]\right\} + 3\Omega_\Lambda H_{\perp 0}^2\,, \tag{2.22}$$

where

$$\Omega_m(r) \equiv \frac{M(r)}{H_{\perp 0}^2(r)}\,,\ \Omega_k(r) \equiv -\frac{\kappa(r)}{H_{\perp 0}^2(r)}\,,\ \Omega_\Lambda(r) \equiv \frac{\Lambda}{3H_{\perp 0}^2(r)}\,, \tag{2.23}$$

$$\Omega_m(r) + \Omega_k(r) + \Omega_\Lambda(r) = 1\,. \tag{2.24}$$

Here $H_{\perp 0}(r)$ is the radial profile of the transverse expansion rate today, and, motivated by the FLRW case, we used the gauge choice $a_{\perp 0}(r) = 1$.

Now, to make any progress, we need the solution to (2.21), i.e. $a_\perp$, from which everything else follows. Integrating (2.21) we find

$$t - t_B(r) = \frac{1}{H_{\perp 0}(r)}\int_0^{a_\perp}\frac{dx}{\sqrt{\Omega_m(r)x^{-1} + \Omega_k(r) + \Omega_\Lambda(r)x^2}}\,, \tag{2.25}$$

where $t_B(r)$ is the bang time function.

In the special case of pure dust (i.e. $\Omega_\Lambda = 0$), we may solve (2.25) parametrically, depending on the sign of the curvature:

$$\Omega_k > 0: \quad a_\perp(t,r) = \frac{\Omega_m(r)}{2\Omega_k(r)}\Big[\cosh 2u(t,r) - 1\Big]\,, \tag{2.26}$$

$$t = \frac{\Omega_m(r)}{2H_{\perp 0}(r)}\frac{\Big[\sinh 2u(t,r) - 2u(t,r)\Big]}{\Big[\Omega_k(r)\Big]^{3/2}} + t_B(r)\,, \tag{2.27}$$

$$\Omega_k < 0: \quad a_\perp(t,r) = \frac{\Omega_m(r)}{2\Omega_k(r)}\Big[\cos 2u(t,r) - 1\Big]\,, \tag{2.28}$$

$$t = \frac{\Omega_m(r)}{2H_{\perp 0}(r)}\frac{\Big[2u(t,r) - \sin 2u(t,r)\Big]}{\Big[-\Omega_k(r)\Big]^{3/2}} + t_B(r)\,, \tag{2.29}$$

$$\Omega_k = 0: \quad a_\perp(t,r) = \Big\{\frac{3}{2}\,H_{\perp 0}(r)\Big[t - t_B(r)\Big]\Big\}^{2/3}\,. \tag{2.30}$$

In this case, we may proceed by parameterising two of the three free radial functions. Leaving $\Omega_m(r)$ and $t_B(r)$ free, $H_{\perp 0}(r)$ is then, depending on the sign of the curvature, given by

$$\Omega_k > 0 : H_{\perp 0}(r) = \frac{\Omega_m(r)}{2\Big[\Omega_k(r)\Big]^{3/2}} \frac{\Big[\sinh 2u_0(r) - 2u_0(r)\Big]}{\Big[t_0 - t_B(r)\Big]}\,, \tag{2.31}$$

$$u_0(r) = \frac{1}{2}\cosh^{-1}\left[\frac{2}{\Omega_m(r)} - 1\right], \tag{2.32}$$

$$t_0 \equiv \frac{\Omega_m^{\rm in}}{2H_0} \frac{\Big[\sinh 2u_0^{\rm in} - 2u_0^{\rm in}\Big]}{\Big[\Omega_k^{\rm in}\Big]^{3/2}} + t_B^{\rm in}\,, \tag{2.33}$$

$$\Omega_k < 0 : H_{\perp 0}(r) = \frac{\Omega_m(r)}{2\Big[-\Omega_k(r)\Big]^{3/2}} \frac{\Big[2u_0(r) - \sin 2u_0(r)\Big]}{\Big[t_0 - t_B(r)\Big]}\,, \tag{2.34}$$

$$u_0(r) = \frac{1}{2}\cos^{-1}\left[\frac{2}{\Omega_m(r)} - 1\right], \tag{2.35}$$

$$t_0 \equiv \frac{\Omega_m^{\rm in}}{2H_0} \frac{\Big[2u_0^{\rm in} - \sin 2u_0^{\rm in}\Big]}{\Big[-\Omega_k^{\rm in}\Big]^{3/2}} + t_B^{\rm in}\,, \tag{2.36}$$

$$\Omega_k = 0 : H_{\perp 0}(r) = \frac{2}{3\Big[t_0 - t_B(r)\Big]}\,, \tag{2.37}$$

$$t_0 \equiv \frac{2}{3H_0} + t_B^{\rm in}\,, \tag{2.38}$$

where quantities with "in" superscripts imply evaluation at the origin, and we have defined the Hubble constant as $H_0 \equiv H_{\perp 0}^{\rm in} = H_{\parallel 0}^{\rm in}$.

2.2.3 Connecting to observables

To constrain the free parameters of the LTB model from the observations, we need to know the time and radial coordinates in terms of the redshift z. Using the same procedure as we did to obtain (1.23) and (1.24), the past lightcone of a central observer

in this spacetime has null geodesics that are given by

$$\frac{dt}{dz} = -\frac{1}{(1+z)H_{\parallel}(t(z),r(z))}\,, \tag{2.39}$$

$$\frac{dr}{dz} = \frac{[1-\kappa(r(z))r^2(z)]^{1/2}}{(1+z)a_{\parallel}(t(z),r(z))H_{\parallel}(t(z),r(z))}\,. \tag{2.40}$$

With the latter, we are now in a position to compute a number of observable quantities as a function of redshift, such as: the expansion rates, $H_{\perp}$ and $H_{\parallel}$; the angular diameter distance, d_A; and thus the average BAO scale, d_z, which in a LTB model is given by

$$d_z^{LTB} = \frac{L_{rec}}{D_V^{LTB}}\left(a_{\perp}{}^2_{rec}a_{\parallel_{rec}}\right)^{-1/3}\,, \tag{2.41}$$

where

$$D_V^{LTB} = \left[\frac{z\,d_{\rm A}^2}{(1+z)a_{\perp}^2 a_{\parallel}H_{\parallel}}\right]^{1/3} \tag{2.42}$$

is the dilation scale. Note that we obtained (2.41) by equating (5.1) and (1.87), solving each respective equality for $\delta z(z)$ and $\delta\theta(z)$, and finally plugging the latter results into (1.88). It is straightforward to show that, in the homogeneous limit, (2.41) and (2.42) reduce to their FLRW counterparts, i.e. (1.88) and (1.90), respectively.

For the purposes of this work, we assume that the epoch from the big bang until a redshift of $z \approx 100$ is well described by a FLRW model. This restricts us to employing a constant bang-time function (setting $t_B = 0$ will suffice) since, otherwise, a decaying mode will be present which will cause the early universe to be highly inhomogeneous, contradicting predictions from inflation. Consequently, the dynamics of the LTB model is completely described by the form of $\Omega_m(r)$. In addition, throughout this thesis we only focus on open LTB models that describe a local underdensity, i.e. those that have $\Omega_{k,0} > 0$ and $\Omega_m^{\rm in} < \Omega_m^{\rm out}$, where the transition from $\Omega_m^{\rm in}$ to $\Omega_m^{\rm out}$ is parameterised with a Gaussian:

$$\Omega_m(r) = \Omega_m^{\rm out} - (\Omega_m^{\rm out} - \Omega_m^{\rm in})\exp\left(-\frac{2.773\,r^2}{\rm FWHM^2}\right)\,. \tag{2.43}$$

Here "out" refers to the asymptotic region outside the void, which we fix to an EdS one (i.e. $\Omega_m^{\rm out}$=1), and FWHM is the void's Full Width at Half Maximum.

We now present some selected background quantities for the three different void

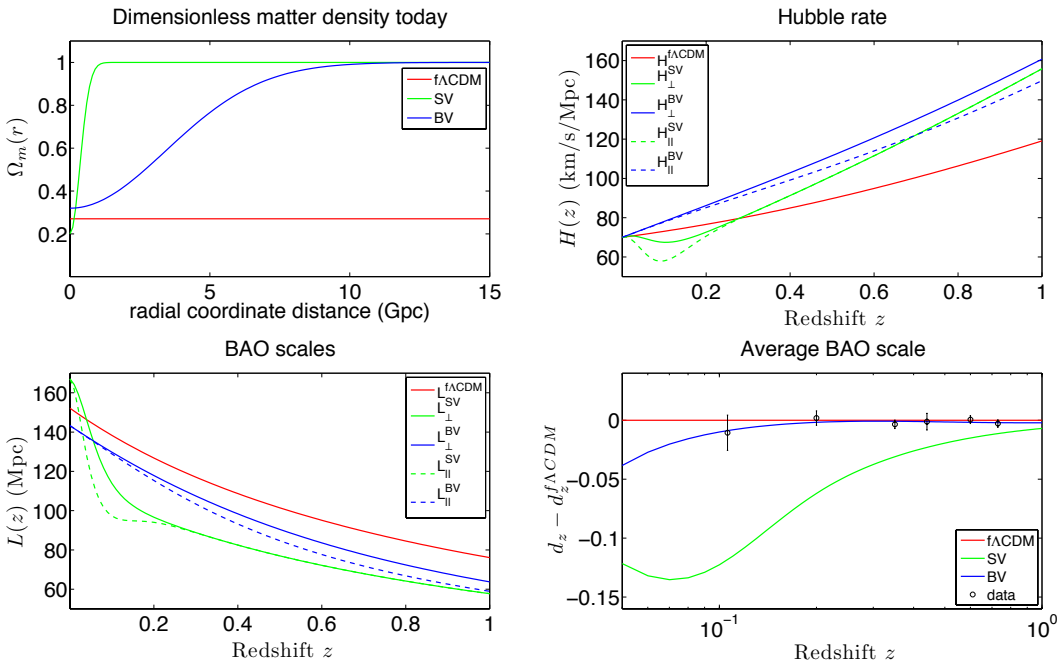

Figure 2.1: *Upper panel:* Background density (left) and expansion rates (right) for the models (2.44), (2.46) and (2.47). *Lower panel:* Using the geometric approximation (5.1), the evolution of the BAO length scales (left), and the average BAO scale (right) normalised to fΛCDM. Black circles indicate measurements from [95].

models that we consider in this work, using the parameterisation (2.43), as well as that for a fiducial ΛCDM model. The models we consider are:

- SV: a small void (compared to those that fit SNIa luminosity distances [48]), with

$$\text{SV:} \quad \Omega_m^{\text{in}} = 0.2, \quad \text{FWHM} = 500\sqrt{2.773}\,\text{Mpc}. \tag{2.44}$$

  This model we consider in the context of the galaxy correlation function (Chapter 5).

- MV: a medium void, chosen as such to represent typical void models that comfortably accommodate distances to SNIa:

$$\text{MV:} \quad \Omega_m^{\text{in}} = 0.2, \quad \text{FWHM} = 2.0\sqrt{2.773}\,\text{Gpc}. \tag{2.45}$$

  This model we consider in the context of the evolution of structure in a cosmic void (Chapters 3 and 4).

- BV: a big void, chosen so that its anisotropic expansion rates provide a good fit to observations of the average BAO scale (1.88). We performed a χ^2 fit to measurements of d_z (see Table 3 of [95]), and found the following best-fit parameters:

$$\text{BV:} \quad \Omega_m^{\text{in}} = 0.32, \quad \text{FWHM} = 4.84\sqrt{2.773}\,\text{Gpc}. \tag{2.46}$$

  This model we also consider in the context of the galaxy correlation function (Chapter 5).

- fΛCDM: a flat concordance model, with $\Omega_b h^2 = 0.02273$ and $\Omega_c h^2 = 0.1099$, as given by WMAP 5-year CMB-only best-fit results (see Table 6 of [153]). Setting $h = 0.7$ implies

$$\text{fΛCDM:} \quad \Omega_m \equiv \Omega_b + \Omega_c = 0.2707, \ \Omega_\Lambda = 1 - \Omega_m = 0.7293\,. \tag{2.47}$$

  This is our benchmark model which we use to compare with the SV and BV LTB models in Chapter 5.

In Fig. 2.1 we show plots of $\Omega_m(r)$, $H_\perp(z)$ and $H_\parallel(z)$, $L_\perp(z)$ and $L_\parallel(z)$, and $d_z(z)$ for the SV, BV and fΛCDM models. Notice how different the expansion rates of the BV and fΛCDM are, even though both models accommodate the average BAO data.

In Fig. 2.2 we plot the spacetime evolution of the contrasts in ρ_m, $H_\perp$ and $H_\parallel$ for our MV model. The growth of the background void over time, both in terms of size and amplitude, is clear.

While our choice of assumptions and parameterisation for the underlying LTB model used in this work is perhaps the simplest conceivable one − let alone one that has trouble fitting the data [62] − it makes for reasonable background toy model to consider in the case of the additions of linear perturbations, as we now introduce.

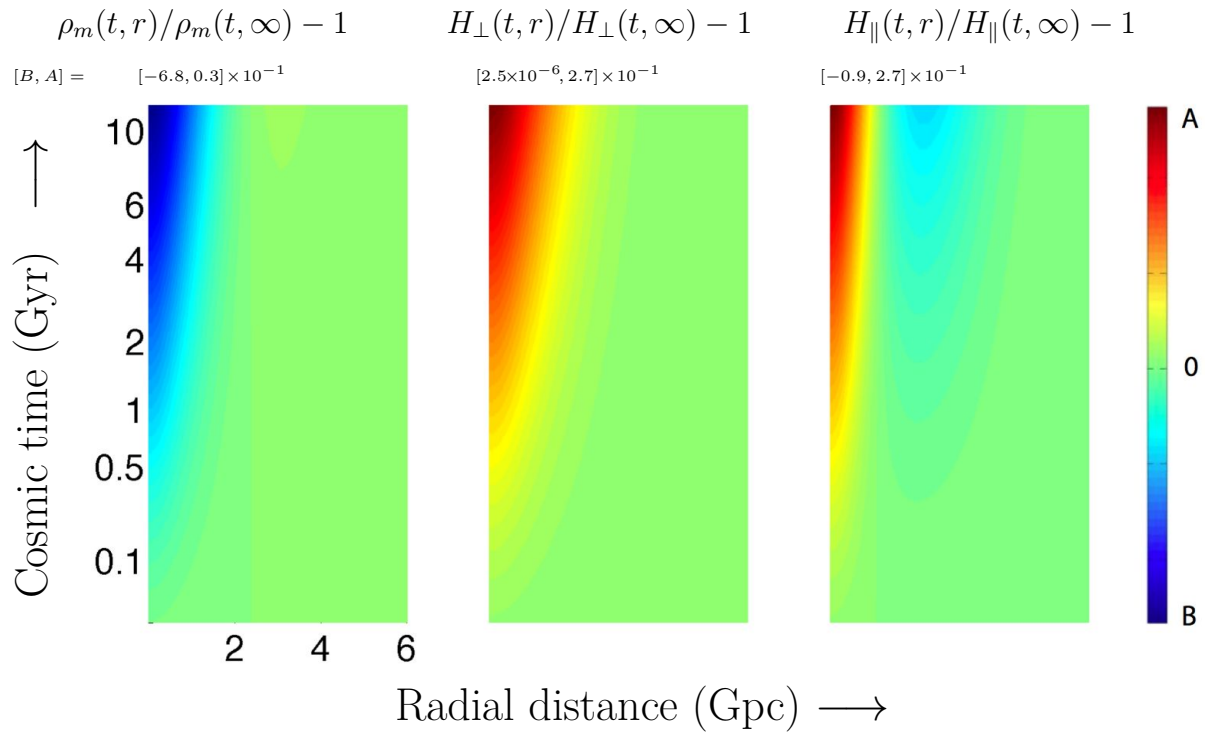

Figure 2.2: The spacetime evolution of selected contrasts in the background dynamics, illustrating the growth of the background void over time. *Left:* Contrast in the energy density ρ_m. *Centre:* Contrast in $H_\perp$. *Right:* Contrast in $H_\parallel$. Note that scales of the vertical and horizontal axes apply to all such 2D plots in Chapter 4. The values of A and B (respectively the maximum and minimum of the color scale) can be read at the top of each 2D plot.

2.3 Linear Perturbation Theory in LTB

2.3.1 Introduction

Structure formation in LTB is still poorly understood. This is not surprising, though, since the presence of background shear induces an inherent coupling between the dynamical variables already at first order in linear perturbation theory [154]. Initial attempts towards such an endeavor included a "2+2" covariant approach in the self-similar case [155], as well as a "1+1+2" covariant split of the spacetime [156, 157].

But why study perturbations in LTB if the background model itself already has trouble fitting much of the data? Two key reasons are: (i) the effects of perturbations may either strengthen or weaken current constraints coming from the BAO and CMB data; (ii) perturbations in LTB will provide insight into relativistic corrections on top of a strongly non-linear background − currently a fairly unexplored area in cosmological structure formation.

For the purposes of this work, we follow [154], unpacking much of the details presented there. The approach here is based on a 2+2 decomposition of the spacetime (see [158]), which is ideal for relativistic setups that obey spherical symmetry − see [159] for the case of stellar perturbations. This decomposition naturally defines two independent modes, namely axial and polar − an analogue to the scalar, vector and tensor modes in the more familiar "3+1" split used in perturbation theory within FLRW models.

As we shall demonstrate below, the dynamical variables that describe the perturbations turn out to couple at first order. From the homogeneous limit of these equations, we point out that the variables inevitably contain mixtures of all three types of the standard scalar-vector-tensor (SVT) perturbations, thus making it difficult to interpret in the usual way. Nevertheless, we proceed to present an example set of variables that do reduce, in the homogeneous limit, to perturbations of the scalar, vector, and tensor type.

The smooth background LTB spacetime we perturb in the next section may be

written compactly as

$$g_{\mu\nu} = \Big[g_{AB}, \mathcal{R}^2 \gamma_{ab} \Big] , \tag{2.48}$$

where A, B belongs to the submanifold M^2 and runs over (t, r), a, b belongs to the submanifold S^2 and runs over (θ, ϕ), $\mathcal{R} \equiv a_\perp r$ is the areal radius (or angular diameter distance) and γ_{ab} is the metric of the unit 2-sphere. The unperturbed energy-momentum tensor takes the form

$$T_{\mu\nu} = \Big[T_{AB}, -\rho_\Lambda \gamma_{ab} \Big] , \tag{2.49}$$

where

$$T_{AB} = \rho_m u_A u_B - \rho_\Lambda g_{AB} , \tag{2.50}$$

$$u^A = [1, 0] . \tag{2.51}$$

2.3.2 Defining the perturbations

The most sensible basis functions to use for this 2+2 split are the scalar spherical harmonics, $Y_{\ell m}(x^a)$, which obey (from now dropping the ℓ-m dependence, unless otherwise necessary to include it)

$$\vec{\nabla}^2 Y \equiv \gamma^{ab} Y_{:ab} = -\ell(\ell + 1) Y , \tag{2.52}$$

where $\vec{\nabla}^2$ is the Laplacian on the two-sphere (S^2) (a colon denotes covariant differentiation on S^2), and the integer ℓ indicates the angular scale of the perturbation. Scalar perturbations on S^2 may then be expanded as follows

$$\phi(x^A, x^a) = \sum_{\ell=0}^{\infty} \sum_{m=-\ell}^{m=\ell} \phi^{\ell m}(x^A) Y_{\ell m}(x^a) . \tag{2.53}$$

We may now construct bases for all higher rank tensors from Y, specifically via covariant derivatives thereof, as well as from contractions of those derivatives with the antisymmetric tensor ϵ_{ab}. Note that we will have two independent modes here, in some sense analogous to the usual three (i.e. scalar, vector and tensor) present in the FLRW framework. Modes that do not depend on ϵ_{ab} are called polar (or even), while modes that do are called axial (or odd).

In the polar case, we may define vector (rank-1) and traceless tensor (rank-2) quantities as follows:

$$S_a \equiv Y_{:a} \quad (\ell \geq 1)\,, \tag{2.54}$$

$$Z_{ab} \equiv Y_{:ab} + \frac{\ell(\ell+1)}{2}\gamma_{ab}Y \quad (\ell \geq 2)\,, \tag{2.55}$$

and for the axial mode, we define a divergence-free vector and traceless tensor as follows:

$$\overline{S}_a \equiv \epsilon_a{}^b Y_{:b} \quad (\ell \geq 1)\,, \tag{2.56}$$

$$\overline{Z}_{ab} \equiv 2\overline{S}_{(a:b)} = -2\epsilon^d{}_{(a}Y_{:b)d} \quad (\ell \geq 2)\,, \tag{2.57}$$

where round brackets around indices denote symmetrisation. There are no scalar (rank-0) quantities in the axial case. The components of these are listed in Appendix B.

In order to ultimately construct GI perturbations, we proceed with the passive approach again (as we have in the FLRW case), and begin by applying a coordinate transformation.

2.3.2.1 Gauge transformations

Following the approach in the FLRW case, and again using a tilde to denote quantities in the new coordinates, we apply a gauge transformation of the form

$$\tilde{x}^\mu = x^\mu + \xi^\mu\,, \tag{2.58}$$

where

$$\xi^\mu \equiv \left[\xi^A Y,\, \xi Y^{:a} + \overline{M}\,\overline{S}^a\right]\,. \tag{2.59}$$

We now consider separately how the coordinates change when applying the gauge transformation for each mode.

- ***Polar:*** Under the gauge transformation, the original coordinates become

$$x^A = \tilde{x}^A - \xi^A Y\,, \tag{2.60}$$

$$x^a = \tilde{x}^a - \xi Y^{:a}\,. \tag{2.61}$$

The corresponding infinitesimal displacements of the latter become

$$dx^A = d\tilde{x}^A - Y d\xi^A - \xi^A dY\,, \tag{2.62}$$

$$dx^a = d\tilde{x}^a - Y^{:a} d\xi - \xi dY^{:a}\,. \tag{2.63}$$

With

$$d\xi^A = \xi^A{}_{|B} d\tilde{x}^B\,, \tag{2.64}$$

$$dY = Y_{:b} d\tilde{x}^b\,, \tag{2.65}$$

$$d\xi = \xi_{|B} d\tilde{x}^B\,, \tag{2.66}$$

$$dY^a_{:} = (Y^{:a})_{:b} d\tilde{x}^b\,, \tag{2.67}$$

we find that

$$dx^A = d\tilde{x}^A - Y\xi^A_{|B} d\tilde{x}^B - \xi^A Y_{:b} d\tilde{x}^b\,, \tag{2.68}$$

$$dx^a = d\tilde{x}^a - \xi (Y^{:a})_{:b} d\tilde{x}^b - Y^{:a}\xi_{|B} d\tilde{x}^B\,. \tag{2.69}$$

From (2.68) and (2.69) we find

$$\begin{aligned} dx^A dx^B &= d\tilde{x}^A d\tilde{x}^B - Y(\xi^A_{|E} d\tilde{x}^B + \xi^B_{|E} d\tilde{x}^A) d\tilde{x}^E \\ &\quad - Y_{:e}(\xi^A d\tilde{x}^B + \xi^B d\tilde{x}^A) d\tilde{x}^e, \end{aligned} \tag{2.70}$$

$$\begin{aligned} dx^A dx^a &= d\tilde{x}^A d\tilde{x}^a - \xi Y^a_{:}{}_b d\tilde{x}^A d\tilde{x}^b - Y^a_{:}\xi_{|B} d\tilde{x}^A d\tilde{x}^B \\ &\quad - Y\xi^A_{|C} d\tilde{x}^C d\tilde{x}^a - \xi^A Y_{:c} d\tilde{x}^a d\tilde{x}^c\,, \end{aligned} \tag{2.71}$$

$$\begin{aligned} dx^a dx^b &= d\tilde{x}^a d\tilde{x}^b - \xi\Big[(Y^{:a})_{:e} d\tilde{x}^b + (Y^{:b})_{:e} d\tilde{x}^a\Big] d\tilde{x}^e \\ &\quad - \xi_{|E}(Y^{:a} d\tilde{x}^b + Y^{:b} d\tilde{x}^a) d\tilde{x}^E\,. \end{aligned} \tag{2.72}$$

- ***Axial:*** The original coordinates become

$$x^A = \tilde{x}^A\,, \tag{2.73}$$

$$x^a = \tilde{x}^a - \overline{M}\,\overline{S}^a\,. \tag{2.74}$$

The corresponding infinitesimal displacements of the latter become

$$dx^A = d\tilde{x}^A\,, \tag{2.75}$$

$$dx^a = d\tilde{x}^a - \overline{S}^a d\overline{M} - \overline{M} d\overline{S}^a\,. \tag{2.76}$$

With

$$d\overline{M} = \overline{M}_{|A} d\tilde{x}^A\,, \tag{2.77}$$

$$d\overline{S}^a = \overline{S}^a{}_{:b} d\tilde{x}^b\,, \tag{2.78}$$

we find that

$$dx^a = d\tilde{x}^a - \overline{M}\,\overline{S}^a{}_{:b} d\tilde{x}^b - \overline{S}^a \overline{M}_{|A} d\tilde{x}^A\,. \tag{2.79}$$

From (2.75) and (2.79) we find

$$dx^A dx^B = d\tilde{x}^A d\tilde{x}^B\,, \tag{2.80}$$

$$dx^A dx^a = d\tilde{x}^A d\tilde{x}^a - \overline{M}\,\overline{S}^a{}_{:b} d\tilde{x}^A d\tilde{x}^b - \overline{S}^a \overline{M}_{|B} d\tilde{x}^A d\tilde{x}^B\,, \tag{2.81}$$

$$\begin{aligned} dx^a dx^b = {} & d\tilde{x}^a d\tilde{x}^b - \overline{M}_{|E}\Big(\overline{S}^b d\tilde{x}^a + \overline{S}^a d\tilde{x}^b\Big) d\tilde{x}^E \\ & - \overline{M}\Big(\overline{S}^b{}_{:e} d\tilde{x}^a + \overline{S}^a{}_{:e} d\tilde{x}^b\Big) d\tilde{x}^e\,. \end{aligned} \tag{2.82}$$

We now compare the original line element with that that was gauge-transformed, in order to identify how the perturbation variables transform under a change of coordinates.

2.3.2.2 The perturbed line element

It is convenient to start from (2.48) and add on general terms corresponding to the all the possible metric perturbations we may have. Decomposing the metric tensor

corresponding to the observed universe into the background and perturbed parts as follows

$$g_{\mu\nu} = \hat{g}_{\mu\nu} + \delta g^{polar}_{\mu\nu} + \delta g^{axial}_{\mu\nu}\,, \tag{2.83}$$

we may write

$$\delta g^{polar}_{\mu\nu} = \begin{pmatrix} h_{AB}Y & 2h_A Y_{:a} \\ * & \mathcal{R}^2(KY\gamma_{ab} + GY_{:ab}) \end{pmatrix}, \tag{2.84}$$

where h_{AB} is a symmetric 2-tensor, h_A a 2-vector, K and G are scalars, and

$$\delta g^{axial}_{\mu\nu} = \begin{pmatrix} 0 & \overline{h}_A \overline{S}_a \\ * & 2\mathcal{R}^2 \overline{hS}_{(a:b)} \end{pmatrix}, \tag{2.85}$$

where $\overline{h}_A$ is a 2-vector and $\overline{h}$ a scalar. Again, let us look at each mode separately.

- ***Polar:*** The full line element in this case is given by

$$\begin{aligned} ds^2 &= \Big(\hat{g}_{AB} + h_{AB}Y\Big)dx^A dx^B + 2h_A Y_{:a} dx^A dx^a \\ &\quad + \mathcal{R}^2\Big[(1+KY)\gamma_{ab} + GY_{:ab}\Big]dx^a dx^b\,. \end{aligned} \tag{2.86}$$

  Plugging (2.70), (2.71) and (2.72) into (2.86) we get

$$\begin{aligned} ds^2 &= \Big[\hat{g}_{AB} + \Big(h_{AB} - \xi_{A|B} - \xi_{B|A}\Big)Y\Big]d\tilde{x}^A d\tilde{x}^B \\ &\quad + 2\Big(h_A - \xi_A - \mathcal{R}^2\xi_{|A}\Big)Y_{:a}dx^A dx^a \\ &\quad + \mathcal{R}^2\Big[(1+KY)\gamma_{ab} + \Big(G - 2\xi\Big)Y_{:ab}\Big]dx^a dx^b\,. \end{aligned} \tag{2.87}$$

  Finally, applying the transformation of the areal radius to the new coordinate system,

$$\mathcal{R} = \tilde{\mathcal{R}} - Y\tilde{\mathcal{R}}\xi^A V_A\,, \tag{2.88}$$

$$\mathcal{R}^2 = \tilde{\mathcal{R}}^2 - 2Y\tilde{\mathcal{R}}^2\xi^A V_A\,, \tag{2.89}$$

where $V_A \equiv \mathcal{R}_{|A}/\mathcal{R}$, we end up with

$$\begin{aligned} ds^2 &= \Big[\hat{g}_{AB} + \Big(h_{AB} - \xi_{A|B} - \xi_{B|A}\Big)Y\Big]d\tilde{x}^A d\tilde{x}^B + 2\Big(h_A - \tilde{\mathcal{R}}^2\xi_{|A}\Big)Y_{:a}dx^A dx^a \\ &\quad + \tilde{\mathcal{R}}^2\Big\{\Big[1 + \Big(K - 2\xi^A V_A\Big)Y\Big]\gamma_{ab} + \Big(G - 2\xi\Big)Y_{:ab}\Big\}dx^a dx^b\,. \end{aligned} \tag{2.90}$$

The perturbed variables in the new coordinate system are then identified through the following relations,

$$\tilde{h}_{AB} = h_{AB} - \xi_{A|B} - \xi_{B|A}\,, \tag{2.91}$$

$$\tilde{h}_A = h_A - \xi_A - \tilde{\mathcal{R}}^2\xi_{|A}\,, \tag{2.92}$$

$$\tilde{K} = K - 2\xi^A V_A\,, \tag{2.93}$$

$$\tilde{G} = G - 2\xi\,. \tag{2.94}$$

- ***Axial:*** The full line element in this case is given by

$$\begin{aligned} ds^2 &= \hat{g}_{AB}dx^A dx^B + 2\overline{h}_A\overline{S}_a dx^A dx^a \\ &\quad + \mathcal{R}^2\Big[\gamma_{ab} + 2\overline{h}\,\overline{S}_{(a:b)}\Big]dx^a dx^b\,. \end{aligned} \tag{2.95}$$

Plugging (2.80), (2.81) and (2.82) into (2.95) we get

$$\begin{aligned} ds^2 &= g^{(0)}_{AB}d\tilde{x}^A d\tilde{x}^B + 2\Big(\overline{h}_A - \tilde{\mathcal{R}}^2\overline{M}_{|A}\Big)\overline{S}_a dx^A dx^a \\ &\quad + \tilde{\mathcal{R}}^2\Big[\gamma_{ab} + 2\Big(\overline{h} - \overline{M}\Big)\overline{S}_{(a:b)}\Big]dx^a dx^b\,. \end{aligned} \tag{2.96}$$

where we used the fact that $\mathcal{R} = \tilde{\mathcal{R}}$. The perturbed variables in the new coordinate system are then identified through the following relations,

$$\tilde{\overline{h}}_A = \overline{h}_A - \tilde{\mathcal{R}}^2\overline{M}_{|A}\,, \tag{2.97}$$

$$\tilde{\overline{h}} = \overline{h} - \overline{M}\,. \tag{2.98}$$

2.3.2.2.1 Gauge-invariant variables Recall that a quantity is GI if it has no dependence on the coordinate transformation (as specified by ξ^μ). To achieve this, we simply take linear combinations of the variables in the new coordinate system (denoted

by a tilde). Again, let's consider the two modes separately.

- ***Polar:*** One particular set of GI combinations is given by

$$k_{AB} = h_{AB} - (p_{A|B} + p_{B|A}), \tag{2.99}$$

$$\varphi = K - 2V^A p_A, \tag{2.100}$$

  where $p_A \equiv h_A - \frac{\mathcal{R}^2}{2} G_{|A}$. One can easily verify that $k_{AB} = \tilde{k}_{AB}$ and $\varphi = \tilde{\varphi}$.

- ***Axial:*** One particular set of GI combinations is given by

$$\overline{k}_A = \overline{h}_A - \mathcal{R}^2 \overline{h}_{|A}. \tag{2.101}$$

  One can easily verify that $\overline{k}_A = \tilde{\overline{k}}_A$.

Now that we have constructed GI variables for the metric perturbations, we proceed to doing the same for the matter perturbations.

2.3.2.3 The perturbed matter

Following the same logic as perturbing the metric above, the perturbed energy momentum tensor takes the form

$$T_{\mu\nu} = \hat{T}_{\mu\nu} + \delta T^{polar}_{\mu\nu} + \delta T^{axial}_{\mu\nu}, \tag{2.102}$$

$$= \hat{\rho}_m \left\{ \hat{u}_\mu \hat{u}_\nu + \left[(1+\Delta Y) \hat{u}_\mu \hat{u}_\nu + 2\hat{u}_\mu \delta u^{polar}_\nu \right] + \left[2\hat{u}_\mu \delta u^{axial}_\nu \right] \right\}, \tag{2.103}$$

where

$$\delta T^{polar}_{\mu\nu} \equiv \begin{pmatrix} \delta T_{AB} Y & 2\delta T_A Y_{:a} \\ * & \delta T^1 Y \gamma_{ab} + \delta T^2 Y_{:ab} \end{pmatrix}, \tag{2.104}$$

with δT_{AB} a symmetric 2-tensor, δT_A a 2-vector, δT^1 and δT^2 scalars,

$$\delta T^{axial}_{\mu\nu} \equiv \begin{pmatrix} 0 & 2\overline{\delta T}_A \overline{S}_a \\ * & 2\overline{\delta T}\, \overline{S}_{(a:b)} \end{pmatrix}, \tag{2.105}$$

with $\overline{\delta T}_A$ a 2-vector and $\overline{\delta T}$ a scalar,

$$\delta u_\mu^{polar} = \left[\left(w\hat{n}_A + \frac{1}{2}h_{AB}\hat{u}^B\right)Y, vY_{:a}\right], \tag{2.106}$$

and

$$\delta u_\mu^{axial} = \left[0, \overline{v}\overline{S}_a\right]. \tag{2.107}$$

Let us now look at each mode separately.

- ***Polar:*** The components of the energy-momentum tensor may be written in the following form

$$\begin{aligned} T_{\mu\nu}dx^\mu dx^\nu &= \left(\hat{T}_{AB} + \delta T_{AB}Y\right)dx^A dx^B + 2\delta T_A Y_{:a}dx^A dx^a \\ &\quad + \left[\left(\hat{\rho}_m + \delta T^1 Y\right)\gamma_{ab} + \delta T^2 Y_{:ab}\right]dx^a dx^b\,. \end{aligned} \tag{2.108}$$

  Substituting (2.70), (2.71), (2.72) and (2.89) into the latter we find

$$\begin{aligned} T_{\mu\nu}dx^\mu dx^\nu &= \left[\hat{T}_{AB} + \left(\delta T_{AB} - \widetilde{T}_{AB|C}\xi^C - \widetilde{T}_{AC}\xi^C{}_{|B} - \widetilde{T}_{BC}\xi^C{}_{|A}\right)Y\right]d\tilde{x}^A d\tilde{x}^B \\ &\quad + 2\left(\delta T_A - \widetilde{T}_{AC}\xi^C - \hat{\widetilde{\rho}}_m\xi_{|A}\right)Y_{:a}d\tilde{x}^A d\tilde{x}^a \\ &\quad + \left\{\left[\hat{\widetilde{\rho}}_m + \left(\delta T^1 - 2\hat{\widetilde{\rho}}_m\xi^A V_A - \hat{\widetilde{\rho}}_{m|A}\xi^A\right)Y\right]\gamma_{ab} \right. \\ &\quad \left. + \left(\delta T^2 - 2\hat{\widetilde{\rho}}_m\xi\right)Y_{:ab}\right\}d\tilde{x}^a d\tilde{x}^b\,, \end{aligned} \tag{2.109}$$

  where we used the fact that

$$\hat{T}_{AB} = \widetilde{T}_{AB} - \widetilde{T}_{AB|C}\xi^C\,, \text{ and} \tag{2.110}$$

$$\hat{\rho}_m = \hat{\widetilde{\rho}}_m - \hat{\widetilde{\rho}}_{m|A}\xi^A\,. \tag{2.111}$$

  We may now identify the following relations between the new and old coordinate systems

$$\widetilde{\delta\widetilde{T}}_{AB} = \delta T_{AB} - \widetilde{T}_{AB|C}\xi^C - \widetilde{T}_{AC}\xi^C{}_{|B} - \widetilde{T}_{BC}\xi^C{}_{|A}\,, \tag{2.112}$$

$$\widetilde{\delta\widetilde{T}}_A = \delta T_A - \widetilde{T}_{AC}\xi^C - \hat{\widetilde{\rho}}_m\xi_{|A}\,, \tag{2.113}$$

$$\widetilde{\delta\widetilde{T}}^1 = \delta T^1 - 2\hat{\widetilde{\rho}}_m\xi^A V_A - \hat{\widetilde{\rho}}_{m|A}\xi^A\,, \tag{2.114}$$

$$\widetilde{\delta T}^2 \;=\; \delta T^2 - 2\hat{\tilde{\rho}}_m \xi\,. \tag{2.115}$$

As for the 4-velocity perturbation, we have

$$\begin{aligned}\delta T^{polar}_{\mu\nu} dx^\mu dx^\nu &= \Big[(1+\Delta Y)\hat{u}_\mu \hat{u}_\nu + 2\hat{u}_\mu \delta u^{polar}_\nu\Big] dx^\mu dx^\nu \\ &= \Big[(1+\Delta Y)\hat{u}_A \hat{u}_B + 2\hat{u}_A \delta u^{polar}_B\Big] dx^A dx^B \\ &\quad + 2\hat{\rho}_m \hat{u}_A \delta u^{polar}_a dx^A dx^a\,. \end{aligned}\tag{2.116}$$

Substituting (2.70), (2.71) and (2.111) into the latter, we find

$$\begin{aligned}\delta T^{polar}_{\mu\nu} dx^\mu dx^\nu = \hat{\tilde{\rho}}_m \Bigg\{ &\Big[1 + \Big(\Delta - \hat{\tilde{\rho}}_{m|A}/\hat{\tilde{\rho}}_m \xi^A\Big) Y\Big] \hat{u}_A \hat{u}_B \\ &+ 2\hat{u}_A \Big(\delta u^{polar}_B - \hat{u}_C \xi^C{}_{|B} Y - \hat{u}_{B|C}\xi^C\Big)\Bigg\} dx^A dx^B \\ &+ 2\hat{\tilde{\rho}}_m \hat{u}_A \Big(\delta u^{polar}_a - \hat{u}_C \xi^C Y_{:a}\Big) dx^A dx^a\,, \end{aligned}\tag{2.117}$$

where we used

$$\hat{u}_A = \hat{\tilde{u}}_A - \hat{\tilde{u}}_{A|B}\xi^B Y\,, \tag{2.118}$$

and may thus identify

$$\widetilde{\Delta} \;=\; \Delta - \hat{\tilde{\rho}}_{m|A}/\hat{\tilde{\rho}}_m \xi^A\,, \tag{2.119}$$

$$\widetilde{\delta u^{polar}_A} \;=\; \delta u^{polar}_A - \hat{\tilde{u}}_B \xi^B{}_{|A} Y\,, \tag{2.120}$$

$$\widetilde{\delta u^{polar}_a} \;=\; \delta u^{polar}_a - \hat{\tilde{u}}_C \xi^C Y_{:a}\,. \tag{2.121}$$

Unpacking (2.120) and (2.121) using (2.106) and (2.91), we find

$$\tilde{w} \;=\; w - \hat{\tilde{u}}_{A|B}\hat{\tilde{n}}^A \xi^B + \frac{1}{2}\hat{\tilde{u}}^B \hat{\tilde{n}}^A (\xi_{A|B} - \xi_{B|A})\,, \tag{2.122}$$

$$\tilde{v} \;=\; v - \hat{\tilde{u}}_A \xi^A\,. \tag{2.123}$$

- ***Axial:*** The components of the energy-momentum tensor in this case is given by

$$\begin{aligned} T_{\mu\nu} dx^\mu dx^\nu \;&=\; \hat{T}_{AB} dx^A dx^B + 2\overline{\delta T}_A S_{:a} dx^A dx^a \\ &\quad + \Big[\hat{\rho}_m \gamma_{ab} + 2\overline{\delta T} S_{(a:b)}\Big] dx^a dx^b\,. \end{aligned}\tag{2.124}$$

Substituting (2.80), (2.81) and (2.82) into the latter we find

$$\begin{aligned} T_{\mu\nu}dx^\mu dx^\nu &= \widetilde{T}_{AB}d\tilde{x}^A d\tilde{x}^B + 2\Big(\overline{\delta T}_A - \hat{\bar{\rho}}_m \overline{M}_{|A}\Big) S_{:a} d\tilde{x}^A d\tilde{x}^a \\ &\quad + \Big[\hat{\bar{\rho}}_m \gamma_{ab} + 2\Big(\overline{\delta T} - \hat{\bar{\rho}}_m \overline{M}\Big) S_{(a:b)}\Big] d\tilde{x}^a d\tilde{x}^b \,. \end{aligned} \tag{2.125}$$

where we used the fact that

$$\hat{T}_{AB} = \widetilde{T}_{AB} \,, \tag{2.126}$$

and

$$\hat{\rho}_m = \hat{\bar{\rho}}_m \,. \tag{2.127}$$

We may now identify the following relations between the new and old coordinate systems

$$\widetilde{\overline{\delta T}}_A = \overline{\delta T}_A - \hat{\bar{\rho}}_m \overline{M}_{|A} \,, \tag{2.128}$$

$$\widetilde{\overline{\delta T}} = \overline{\delta T} - \overline{M} \,. \tag{2.129}$$

The 4-velocity perturbation is

$$\begin{aligned} \delta T^{axial}_{\mu\nu} dx^\mu dx^\nu &= 2\hat{\rho}_m \hat{u}_\mu \delta u^{axial}_\nu dx^\mu dx^\nu \\ &= 2\hat{\rho}_m \hat{u}_A \delta u^{axial}_a dx^A dx^a \,. \end{aligned} \tag{2.130}$$

Substituting (2.82) into the latter gives

$$\delta T^{axial}_{\mu\nu} dx^\mu dx^\nu = 2\hat{\bar{\rho}}_m \hat{\bar{u}}_A \delta u^{axial}_a d\tilde{x}^A d\tilde{x}^a \,, \tag{2.131}$$

which implies

$$\widetilde{\delta u^{axial}_a} = \delta u^{axial}_a \,. \tag{2.132}$$

Unpacking the latter using (2.107) we get

$$\widetilde{\bar{v}} = \bar{v} \,. \tag{2.133}$$

2.3.2.3.1 Gauge-invariant variables The set of GI quantities we find for each mode are:

- ***Polar:***

$$F_{AB} \equiv \delta T_{AB} - \hat{T}_{AB|C}p^C - \hat{T}_{AC}p^C_{|B} - \hat{T}_{BC}p^C_{|A}\,, \tag{2.134}$$

$$F_A \equiv \delta T_A - \hat{T}_{AC}p^C - \frac{1}{2}\hat{\rho}_m G_{|A}\,, \tag{2.135}$$

$$F^1 \equiv \delta T^1 - (2\hat{\rho}_m V_C + \hat{\rho}_{m|C})p^C\,, \tag{2.136}$$

$$F^2 \equiv \delta T^2 - \hat{\rho}_m G \tag{2.137}$$

$$\Delta^{G.I.} \equiv \Delta - \ln\left(\hat{\rho}_m\right)_{|A}p^A\,, \tag{2.138}$$

$$w^{G.I.} \equiv w - \hat{u}_{A|B}\hat{n}^A p^B + \frac{1}{2}\hat{u}^B\hat{n}^A\Big(p_{A|B} - p_{B|A}\Big)\,, \tag{2.139}$$

$$v^{G.I.} \equiv v - \hat{u}_A p^A\,. \tag{2.140}$$

- ***Axial:***

$$J_A \equiv \overline{\delta T}_A - \hat{\rho}_m\overline{h}_A\,, \tag{2.141}$$

$$J \equiv \overline{\delta T} - \hat{\rho}_m\overline{h}\,, \tag{2.142}$$

$$\overline{v}^{G.I.} \equiv \overline{v}\,. \tag{2.143}$$

2.3.3 Einstein equations

In what follows, we will make use of the Regge-Wheeler (RW) gauge, in which $\overline{h} = 0 = h_A = G$. This gauge is useful since all the bare perturbations (i.e. metric + matter) are then automatically GI, although only for $\ell > 1$. For the very large-scale modes, $\ell = 0$ (polar only) or 1, it turns out that additional gauge fixing is required to construct GI variables in those cases [159]. While these modes are certainly necessary to consider for computing a quantity like the 2PCF in which one is required to sum up all modes from $\ell = 0$, we do not include them explicitly in this work − however, see Chapter 5 in which we compute the 2PCF anyway in a specific approximation of the EFE.

2.3.3.1 Polar case

Decomposing h_{AB} into three scalars as follows,

$$h_{AB} \equiv \eta(-u_A u_B + n_A n_B) + \psi(u_A u_B + n_A n_B) + \varsigma(u_A n_B + n_A u_B)\,, \tag{2.144}$$

and furthermore introducing $\chi \equiv \psi - \varphi + \eta$ to replace ψ, we may write the line element representing the polar perturbations in the RW gauge as

$$\begin{aligned} ds^2 &= -\Big[1 + \Big(2\eta - \chi - \varphi\Big)Y\Big]dt^2 - 2\varsigma Y X(t,r)dtdr \\ &\quad + \Big[1 + \Big(\chi + \varphi\Big)Y\Big]X^2(t,r)dr^2 + \Big[1 + \varphi Y\Big]A^2(t,r)d\Omega^2\,, \end{aligned} \tag{2.145}$$

where η, χ, φ and ς are functions of (ℓ, t, r).

For $\ell > 1$, η conveniently vanishes, and the 1st-order perturbed EFE are

$$\begin{aligned} t-t: \quad 8\pi G\rho_m\Delta &= -X^{-2}\varphi'' + X^{-2}\left[\frac{a_\parallel{}'}{a_\parallel} + \frac{\kappa r + \frac{1}{2}r^2\kappa'}{1-\kappa r^2} - 2\frac{a_\parallel}{r a_\perp}\right]\varphi' \\ &\quad + 2X^{-1}H_\perp\varsigma' + X^{-2}\frac{a_\parallel}{r a_\perp}\chi' + \Theta\dot{\varphi} + H_\perp\dot{\chi} \\ &\quad + \left[3H_\perp\Big(\sigma^2 + H_\perp\Big) - \Big(1 + 2\frac{a_\perp}{a_\parallel}\Big)\frac{\kappa}{a_\perp^2} - \frac{r\kappa'}{a_\perp a_\parallel}\right. \\ &\quad \left. + \frac{\ell(\ell+1)}{a_\perp^2 r^2}\right]\Big(\varphi + \chi\Big) - \left[\frac{\ell(\ell+1)-2}{2a_\perp^2 r^2}\right]\chi \\ &\quad + X^{-1}\frac{a_\parallel}{r a_\perp}\Big(3\sigma^2 + 4H_\parallel\Big)\varsigma\,, \end{aligned} \tag{2.146}$$

$$\begin{aligned} t-r: \quad 8\pi G\rho_m w &= X^{-1}\left\{\dot{\varphi}' - \Big(3\sigma^2 - H_\parallel\Big)\varphi' - \frac{a_\parallel}{r a_\perp}\dot{\chi} + H_\perp\chi'\right\} \\ &\quad + \left[\frac{3}{2}H_\perp\Big(\sigma^2 + H_\perp\Big) - \Big(\frac{a_\perp}{a_\parallel} - \frac{1}{2}\Big)\frac{\kappa}{a_\perp^2}\right. \\ &\quad \left. - \frac{r\kappa'}{2a_\perp a_\parallel} + \frac{\ell(\ell+1)}{2a_\perp^2 r^2} - \frac{\Lambda}{2}\right]\varsigma\,, \end{aligned} \tag{2.147}$$

$$t-\theta, t-\phi: \quad 8\pi G\rho_m v = \dot{\varphi} + \frac{1}{2}\dot{\chi} + \frac{1}{2X}\varsigma' + H_\parallel\Big(\varphi + \chi\Big)\,, \tag{2.148}$$

$$
\begin{aligned}
r-r: \qquad \ddot{\varphi} &= -H_\perp\Big(4\dot{\varphi}+\dot{\chi}\Big)+X^{-2}\frac{a_\parallel}{ra_\perp}\chi'+\left[\left(\frac{2\kappa}{a_\perp^2}\right)-\Lambda\right]\varphi \\
&\quad+\left[\frac{2\kappa}{a_\perp^2}-\Lambda+\frac{\ell(\ell+1)-2}{2a_\perp^2r^2}\right]\chi+\frac{3}{X}\frac{a_\parallel}{ra_\perp}\sigma^2\varsigma\,, \qquad (2.149)\\
r-\theta, r-\phi: \qquad \dot{\varsigma} &= -2H_\parallel\varsigma-X^{-1}\chi'\,, \qquad (2.150)\\
\theta-\theta, \phi-\phi: \qquad \ddot{\chi} &= X^{-2}\chi''-X^{-2}\left[\frac{a_\parallel{}'}{a_\parallel}+\frac{\kappa r+\frac{1}{2}r^2\kappa'}{1-\kappa r^2}+2\frac{a_\parallel}{ra_\perp}\right]\chi' \\
&\quad+3X^{-1}\sigma^2\varsigma'-6\sigma^2\dot{\varphi}-3H_\parallel\dot{\chi} \\
&\quad+\left[4\left(\frac{a_\perp}{a_\parallel}-1\right)\frac{\kappa}{a_\perp^2}+\frac{2r\kappa'}{a_\perp a_\parallel}\right](\chi+\varphi) \\
&\quad+2X^{-1}\Big[H_\parallel-2H_\perp\Big]'\varsigma-\left[\frac{\ell(\ell+1)-2}{a_\perp^2r^2}\right]\chi\,. \qquad (2.151)
\end{aligned}
$$

Note how Eq. (2.146) resembles the Poisson equation (1.75), in which φ here acts as some effective Newtonian potential. Indeed, φ satisfies an equation (2.149) quite similar to the standard Bardeen equation (1.77). Eq. (2.148) looks strikingly similar to that relating the peculiar velocity to the Bardeen variable as given by (1.76). Lastly, note how the evolution equations for ς (2.150) and χ (2.151) resemble those of the vector (1.82) and tensor (1.85) modes in the FLRW case.

Conservation of the perturbed energy-momentum, i.e. $\nabla_\mu T^\mu{}_\nu=0$, implies that our solutions must satisfy

$$
\begin{aligned}
\dot{\Delta} &= -\frac{3}{2}\dot{\varphi}-\frac{1}{2}\dot{\chi}-X^{-1}\Big(w+\varsigma/2\Big)' \\
&\quad-X^{-1}\left[\frac{\rho_m{}'}{\rho_m}+2\frac{a_\parallel}{ra_\perp}\right]\Big(w+\varsigma/2\Big)+\frac{\ell(\ell+1)}{a_\perp^2r^2}v\,, \qquad (2.152)\\
\dot{w} &= \frac{1}{2X}\varphi'-H_\parallel\Big(w+\varsigma/2\Big)\,, \qquad (2.153)\\
\dot{v} &= \frac{1}{2}\Big(\varphi+\chi\Big)\,. \qquad (2.154)
\end{aligned}
$$

2.3.3.2 Axial case

The line element representing the axial perturbations in the RW gauge is

$$\begin{aligned} ds^2 &= -dt^2 + 2\overline{k}_A \overline{S}_a dx^A dx^a \\ &\quad + X^2(t,r)dr^2 + A^2(t,r)d\Omega^2\,, \end{aligned} \tag{2.155}$$

The resulting EFE for $\ell > 1$ are then

$$t-t: \qquad 0 = \overline{k}_r' + \left(\frac{A'}{A} - \frac{X'}{X}\right)\overline{k}_r - X^2(H_\perp + H_\parallel)\overline{k}_t\,, \tag{2.156}$$

$$t-r: \qquad 0 = \overline{k}_t' + \frac{1}{2}\dot{\overline{k}}_r - H_\parallel \overline{k}_r\,, \tag{2.157}$$

$$r-r: \qquad 0 = \dot{\overline{k}}_t - \frac{A'}{AX^2}\overline{k}_r + H_\perp \overline{k}_t\,, \tag{2.158}$$

$$\begin{aligned} t-a: \quad 8\pi G\hat{\rho}_m X^2 \overline{v} &= -\frac{1}{2}\dot{\overline{k}}_r' + \frac{1}{2}\left(\frac{X'}{X} - 2\frac{A'}{A}\right)\dot{\overline{k}}_r + H_\perp \overline{k}_r' \\ &\quad + \left(\frac{A^2 H_\perp}{X}\right)'\frac{\overline{k}_r}{A^2} + \frac{1}{2}\overline{k}_t'' - \frac{1}{2}\frac{X'}{X}\overline{k}_t'\,, \end{aligned} \tag{2.159}$$

$$\begin{aligned} r-a: \qquad 0 &= \frac{1}{2}\ddot{\overline{k}}_r - \frac{H_\parallel}{2}\dot{\overline{k}}_r - \frac{1}{2}\Bigg[H_\perp(H_\perp - 2H_\parallel) - \Lambda \\ &\quad + \frac{2-\kappa r^2}{a_\perp r^2}\Bigg]\overline{k}_r - \frac{1}{2}\dot{\overline{k}}_t' + \frac{A'}{A}\dot{\overline{k}}_t \\ &\quad + \frac{1}{2}\left(H_\parallel - 2H_\perp\right)\overline{k}_t' + \left(\frac{A^2 H_\perp}{X}\right)'\frac{\overline{k}_t}{A^2} \end{aligned} \tag{2.160}$$

$$a-b: \qquad 0 = \dot{\overline{k}}_t - X^{-2}\overline{k}_r' + H_\parallel \overline{k}_t + \frac{X'}{X^3}\overline{k}_r\,. \tag{2.161}$$

We may simplify the above considerably by defining

$$\Pi \equiv \epsilon^{AB}\left(\frac{k_A}{a_\perp^2 r^2}\right)_{|B}\,, \tag{2.162}$$

which yields

$$(\ell-1)(\ell+2)k_A = 16\pi\hat{\rho}_m (a_\perp r)^2 \overline{v}\hat{u} - \epsilon_{AB}(a_\perp^4 r^4 \Pi)^{|B}\,. \tag{2.163}$$

In fact, by contracting the above once with u^A, and then once more with ∇_B, we obtain

$$-\ddot{\Pi} + X^{-2}\Pi'' - (6H_\perp + H_\parallel)\dot{\Pi} + \frac{6a_\parallel}{a_\perp r}\Pi' - \left[16\pi\rho + \frac{(\ell-2)(\ell+3)}{a_\perp^2 r^2}\right]\Pi = -16\pi\frac{(\hat{\rho}_m\overline{v})'}{Xa_\perp^2 r^2}\,. \tag{2.164}$$

The variable Π clearly satisfies a wave equation.

Finally, conservation of the perturbed energy-momentum gives

$$\dot{\overline{v}} = 0. \tag{2.165}$$

2.3.4 The homogeneous (FLRW) limit

In this section we consider the homogeneous limit, i.e. $\kappa(r) \to K$, $a_\perp(t,r) \to a_\parallel(t,r) \to a(t(\eta))$, of both the master equations and the fluid constraints presented in the previous section. This will assist us in trying to connect the LTB GI's with that of FLRW.

Polar case. The polar master equations (2.149)−(2.151) reduce to

$$\left[\partial_\eta^2 + 3\mathcal{H}\partial_\eta - 2K + a^2\Lambda\right]\varphi = \Big\{ -\mathcal{H}\partial_\eta + \frac{(1-Kr^2)}{r}\partial_r + \frac{\left[\ell(\ell+1) - 2 + 4Kr^2 - 2(ra)^2\Lambda\right]}{2r^2}\Big\}\chi\,, \tag{2.166}$$

$$\left[\partial_\eta + 2\mathcal{H}\right]\varsigma = \sqrt{1-Kr^2}\partial_r\chi\,, \tag{2.167}$$

and

$$\left[\partial_\eta^2 + 2\mathcal{H}\partial_\eta - \vec{\nabla}^2 + \frac{4(1-Kr^2)}{r}\partial_r - \frac{2}{r^2}\right]\chi = 0\,, \tag{2.168}$$

where

$$\vec{\nabla}^2 = (1-Kr^2)\partial_r^2 + \frac{(2-3Kr^2)}{r}\partial_r - \frac{\ell(\ell+1)}{r^2}\,.$$

Note that χ is the only variable that evolves independently from the other two in this limit. While ς is only coupled to χ, φ is coupled to both ς and χ. The corresponding

polar fluid constraints are

$$8\pi G\rho_m a^2\Delta = -\Big[\vec{\nabla}^2 - 3\mathcal{H}\partial_\eta - 3\mathcal{H}^2 + 3K\Big]\varphi + 2\sqrt{1-Kr^2}\mathcal{H}\left[\partial_r + \frac{2}{r}\right]\varsigma + \left[\mathcal{H}\partial_\eta + \frac{(1-Kr^2)}{r}\partial_r + 3\mathcal{H}^2 - 3K + \frac{\ell(\ell+1)+2}{2r^2}\right]\chi\,, \quad (2.169)$$

$$8\pi G\rho_m a^2 w = \left\{\sqrt{1-Kr^2}\Big[\partial_\eta + 3\mathcal{H}\Big]\partial_r\varphi - \sqrt{1-Kr^2}\left[\frac{1}{r}\partial_\eta - \mathcal{H}\partial_r\right]\chi + \left[\frac{3}{2}\mathcal{H}^2 - K + \frac{\ell(\ell+1)}{2r^2} - \frac{\Lambda}{2}\right]\varsigma\right\}, \quad (2.170)$$

$$8\pi G\rho_m a v \;=\; \Big[\partial_\eta + \mathcal{H}\Big]\varphi + \frac{1-Kr^2}{2}\partial_r\varsigma + \left[\frac{1}{2}\partial_\eta + \mathcal{H}\right]\chi\,. \quad (2.171)$$

Axial case. In the axial sector, (2.164) and (2.165) reduces to

$$\left[\partial_\eta^2 + 6\mathcal{H}\partial_\eta - \vec{\nabla}^2 - \frac{4(1-\kappa r^2)}{r}\left(\partial_r + \frac{3}{2r}\right) + 6\mathcal{H}^2\right]\Pi = 16\hat{\rho}_m\frac{\sqrt{1-Kr^2}}{ar^2}\partial_r\overline{v}\,, \quad (2.172)$$

and

$$\partial_\eta\overline{v} = 0\,, \quad (2.173)$$

respectively.

Due to the coupling between the three (polar) master variables in the FLRW limit, their interpretation in terms of standard FLRW GI's is expected to be non-trivial. As pointed out in [154], this is indeed so. Nevertheless, it is possible to write down a set of quantities that reduce to the pure scalars, vectors and tensors in the FLRW limit – we list these in the next section.

2.3.5 Scalar-Vector-Tensor variables

The previous section highlights the fact that the GI metric perturbations in LTB contains, at first order, mixtures of an otherwise independent set of SVT variables as seen in the case of a FLRW model. Here we present linear combinations of LTB variables that reduce to scalars, vectors and tensors in the homogeneous limit, allowing us to compare, more sensibly, the evolution of perturbations in LTB and FLRW models.

Scalars

$$\text{polar:}\quad \zeta \equiv X^{-2}\lambda'' + X^{-2}\left(2\frac{a_\parallel}{a_\perp r} - \frac{X'}{X}\right)\lambda' - \frac{\ell(\ell+1)}{(a_\perp r)^2}\lambda + X^{-2}\frac{a_\parallel}{a_\perp}\xi' + r(2-3\kappa r^2)\xi\,, \tag{2.174}$$

$$\text{axial:}\quad none\,, \tag{2.175}$$

Vectors

$$\text{polar:}\quad \xi \equiv \frac{3}{2}\frac{a_\perp^2}{a_\parallel X}\left\{\varsigma'' + X\dot{\chi}' + \left[\frac{2}{r}\left(\frac{a_\parallel}{a_\perp} - 1\right) - \frac{X'}{X}\right]\varsigma' + \frac{2X}{r}\dot{\chi} - \left(\frac{X}{ra_\perp}\right)^2\ell(\ell+1)\varsigma\right\}, \tag{2.176}$$

$$\text{axial:}\quad \overline{v}\,, \tag{2.177}$$

Tensors

$$\text{polar:}\quad \chi \tag{2.178}$$

$$\text{axial:}\quad \Upsilon \equiv X^{-2}\Pi'' + X^{-2}\left[6\frac{a_\parallel}{ra_\perp} - \frac{X'}{X}\right]\Pi' + \left(ra_\perp\right)^{-2}\left[6 - 8\kappa r^2 - \ell(\ell+1)\right]\Pi + \frac{16\pi G}{X(ra_\perp)^2}\left(\hat{\rho}_m\overline{v}\right)', \tag{2.179}$$

where

$$\lambda \equiv 8\pi G\hat{\rho}_m\left[H_\perp^{-1}\Delta - 3v\right], \tag{2.180}$$

$$\Rightarrow\quad \lambda' = \lambda\left\{\frac{\hat{\rho}_m'}{\hat{\rho}_m} + \left(H_\perp^{-1}\Delta - 3v\right)^{-1}\left[H_\perp^{-1}\Delta' - H_\perp^{-2}H_\perp'\Delta - 3v'\right]\right\}, \tag{2.181}$$

$$\Rightarrow\quad \lambda'' = \frac{\lambda'^2}{\lambda} + \lambda\left\{\frac{\hat{\rho}_m''}{\hat{\rho}_m} - \left(\frac{\hat{\rho}_m'}{\hat{\rho}_m}\right)^2 + \left(H_\perp^{-1}\Delta - 3v\right)^{-1}\left[H_\perp^{-1}\Delta'' - 2H_\perp^{-2}H_\perp'\Delta' + 2H_\perp^{-3}H_\perp'^2\Delta - 3v''\right]\right\}, \tag{2.182}$$

and

$$\begin{aligned}\xi' &= \left[2\frac{a'_\perp}{a_\perp} - \frac{a'_\parallel}{a_\parallel} - \frac{X'}{X}\right]\xi + \frac{3}{2}\frac{a_\perp^2}{a_\parallel X}\Bigg\{\varsigma''' + X\dot{\chi}'' + X'\dot{\chi}' \\ &+ \left[\frac{2}{r}\left(\frac{a_\parallel}{a_\perp} - 1\right) - \frac{X'}{X}\right]\varsigma'' + \left[\frac{2}{r}\frac{a_\parallel}{a_\perp}\left(\frac{a'_\parallel}{a_\parallel} - \frac{a'_\perp}{a_\perp}\right)\right. \\ &\left. - \frac{2}{r^2}\left(\frac{a_\parallel}{a_\perp} - 1\right) + \left(\frac{X'}{X}\right)^2 - \frac{X''}{X} - \left(\frac{X}{ra_\perp}\right)^2\ell(\ell+1)\right]\varsigma' \\ &-2\left(\frac{X}{ra_\perp}\right)^2\left(\frac{X'}{X} - \frac{a'_\perp}{a_\perp} - \frac{1}{r}\right)\ell(\ell+1)\varsigma\Bigg\}. \end{aligned} \tag{2.183}$$

These variables will prove useful when comparisons of the evolution of these perturbations are made with the standard model.

2.3.6 Weyl information

The Weyl tensor, $C_{\alpha\beta\gamma\delta}$, encodes the tidal forces acting on body in free-fall, and is given by the trace-free part of the Riemann tensor

$$\begin{aligned}C_{\alpha\beta\gamma\delta} &\equiv R_{\alpha\beta\gamma\delta} - \frac{1}{2}\Big(g_{\alpha\gamma}R_{\beta\gamma} - g_{\alpha\delta}R_{\beta\gamma} + g_{\beta\delta}R_{\alpha\gamma} - g_{\beta\gamma}R_{\alpha\delta}\Big) \\ &\quad + \frac{1}{6}\Big(g_{\alpha\gamma}g_{\beta\delta} - g_{\alpha\delta}g_{\beta\gamma}\Big)R\,. \end{aligned} \tag{2.184}$$

The latter can be split into electric and magnetic parts as follows:

$$E_{\alpha\beta} = C_{\alpha\gamma\beta\delta}\hat{u}^\gamma\hat{u}^\delta \quad , \quad H_{\alpha\beta} = \frac{1}{2}\hat{\epsilon}_{\alpha\gamma\delta}C^{\gamma\delta}{}_{\beta\lambda}\hat{u}^\lambda\,, \tag{2.185}$$

where u^a is the chosen 4-velocity field of comoving observers,

$$\epsilon_{\alpha\beta\gamma} = \eta_{\alpha\beta\gamma\delta}\hat{u}^\delta \tag{2.186}$$

is the projection of the spacetime alternating tensor $\eta_{abcd} = -\sqrt{\hat{g}}\delta^0{}_{[a}\delta^1{}_b\delta^2{}_c\delta^3{}_{d]}$, and $\delta^a{}_b$ is the Kronecka delta symbol.

Note that $E_{\mu\nu}$ and $H_{\mu\nu}$ are purely spatial. Furthermore, we may write each one in the following form:

$$Q_{ij} = \hat{Q}_{ij} + \delta Q_{ij}\,, \tag{2.187}$$

where $\hat{Q}_{ij}$ and δQ_{ij} represents the background and perturbed parts, respectively. For the perturbed part, it is useful to perform the following split into radial and angular parts,

$$\delta Q_{ij} = \left(\begin{array}{c|c} \delta Q_{rr} & \delta Q_{ra} \\ \hline \delta Q_{ra} & \delta Q_{ab} \end{array} \right), \tag{2.188}$$

and then decompose each part in a spherical harmonic fashion, so that

$$\delta Q_{rr} = \sum_{\ell m} \delta Q_{rr}^{(\ell m)} Y^{(\ell m)}, \tag{2.189}$$

$$\delta Q_{ra} = \sum_{\ell m} \left[\delta Q_{r}^{(\ell m)} Y_{a}^{(\ell m)} + \overline{\delta Q}_{r}^{(\ell m)} \overline{Y}_{a}^{(\ell m)} \right], \tag{2.190}$$

$$\delta Q_{ab} = \sum_{\ell m} \left[\delta Q_{(T)}^{(\ell m)} \gamma_{ab} Y^{(\ell m)} + \delta Q_{(TF)}^{(\ell m)} Y_{ab}^{(\ell m)} + \overline{\delta Q}_{(TF)}^{(\ell m)} \overline{Y}_{ab}^{(\ell m)} \right], \tag{2.191}$$

where

$$Y_a \equiv Y_{:a} = \left[Y_{,\theta}\,,\, Y_{,\phi} \right], \tag{2.192}$$

$$\overline{Y}_a \equiv \hat{\epsilon}_a{}^b Y_{:b} = \frac{1}{2} \left[(\sin\theta)^{-1} Y_{,\phi}\,,\, -\sin\theta Y_{,\theta} \right], \; \hat{\epsilon}_a{}^b = \frac{1}{2} \begin{pmatrix} 0 & \sin\theta^{-1} \\ -\sin\theta & 0 \end{pmatrix}, \tag{2.193}$$

$$\begin{aligned} Y_{ab} &\equiv Y_{:ab} + \frac{\ell(\ell+1)}{2} \gamma_{ab} Y \\ &= \begin{pmatrix} Y_{,\theta\theta} + \ell(\ell+1) Y & Y_{,\theta\phi} - \cot\theta Y_{,\phi} \\ * & \sin^2\theta \left[Y_{,\phi\phi} / \sin^2\theta + \cot\theta Y_{,\theta} + \ell(\ell+1) Y \right] \end{pmatrix}, \end{aligned} \tag{2.194}$$

$$\begin{aligned} \overline{Y}_{ab} &\equiv 2 \overline{Y}_{(a:b)} \\ &= (\sin\theta)^{-1} \begin{pmatrix} Y_{,\theta\phi} - \cot\theta Y_{,\phi} & \frac{1}{2} \left[Y_{,\phi\phi} + \sin\theta\cos\theta Y_{,\theta} - \sin^2\theta Y_{,\theta\theta} \right] \\ * & -\sin^2\theta Y_{,\theta\phi} + \sin\theta\cos\theta Y_{,\phi} \end{pmatrix}. \end{aligned} \tag{2.195}$$

The background H_{ij} is zero, and the only non-zero background parts for E_{ij} are:

$$\hat{E}_{rr} = X^2 \left[H_\perp \sigma^2 + \frac{2}{3} \left(\frac{a_\perp}{a_\parallel} - 1 \right) \frac{\kappa}{a_\perp^2} + \frac{1}{3} \frac{r\kappa'}{a_\perp a_\parallel} \right], \tag{2.196}$$

$$\hat{E}_{ab} = -\frac{1}{2} \left(\frac{A}{X} \right)^2 \hat{E}_{rr} \gamma_{ab}\,. \tag{2.197}$$

The non-zero perturbed parts for the electric and magnetic Weyl tensors are:

$$\delta E_{rr} = -\frac{1}{3}\Bigg\{\varphi'' - \left[\frac{a_\parallel{}'}{a_\parallel} + \frac{\kappa r + \frac{1}{2}r^2\kappa'}{1-\kappa r^2} + \frac{a_\parallel}{r a_\perp}\right]\varphi' - 2XH_\perp\varsigma' \\ - \frac{a_\parallel}{r a_\perp}\chi' - \frac{3}{2}\sigma^2\dot{\varphi} - X^2H_\perp\dot{\chi} + X^2\Bigg[\left(\frac{a_\perp}{a_\parallel}-1\right)\frac{\kappa}{a_\perp^2} - 3H_\perp\sigma^2 \\ + \frac{r\kappa'}{a_\perp a_\parallel} + \frac{\ell(\ell+1)}{2a_\perp^2 r^2}\Bigg](\varphi+\chi) - 2X\frac{a_\parallel}{r a_\perp}(3\sigma^2 - H_\parallel)\varsigma \\ - X^2\left[\frac{\ell(\ell+1)-2}{a_\perp^2 r^2}\right]\chi\Bigg\}, \tag{2.198}$$

$$\delta E_r = -\frac{1}{2}\Bigg[\varphi' - \frac{a_\parallel}{r a_\perp}\Big(\varphi+\chi\Big) - XH_\perp\varsigma\Bigg], \tag{2.199}$$

$$\delta E_{(T)} = -\frac{1}{2}\left(\frac{A}{X}\right)^2\delta E_{rr} + \frac{A^2}{3}\left[\frac{3}{2}H_\perp\sigma^2 + \left(\frac{a_\perp}{a_\parallel}-1\right)\frac{\kappa}{a_\perp^2} + \frac{1}{2}\frac{r\kappa'}{a_\parallel a_\perp}\right]\chi, \tag{2.200}$$

$$\delta E_{(TF)} = -\frac{1}{2}\Big(\varphi+\chi\Big), \tag{2.201}$$

and

$$\overline{\delta H}_r = -\frac{1}{4}\varsigma' - \frac{1}{4}X\dot{\chi} - \frac{3}{4}X\sigma^2\Big(\varphi+\chi\Big) + \frac{1}{2}\frac{a_\parallel}{r a_\perp}\varsigma, \tag{2.202}$$

$$\overline{\delta H}_{(TF)} = -\frac{1}{2}\varsigma, \tag{2.203}$$

respectively.

2.3.7 The integrated Sachs-Wolfe effect

CMB photons propagating away from the surface of last scattering are distorted in a number of ways on their journey to an observer at some later time [160, 161]. Firstly, these photons are subjected to the inhomogeneities already present in the relativistic potentials at the surface of last scattering at the time of emission: this is the ordinary SW effect. As the universe expands, the photons inevitably interact with intervening clumps of matter and voids. For example, if the universe contains DE (of positive amplitude), or is curved (negatively), then photons gain (lose) energy as they pass through overdense (underdense) regions due to the flattening of the potentials over

time: this is the ISW effect, and is important on large scales. In addition, photons traversing regions that contain hot gas will receive a boost in energy, known as the thermal SZ effect. While the kinematic component of the SZ effect is expected to be negligible in FLRW models on average, it may nevertheless be relevant to the final photon temperature measured by an observer in the case of very large bulk velocity flows. Another well-known contribution related to peculiar motion is the Doppler effect. Finally, the gravitational lensing of photons by the intervening structure also modifies the photon temperature in some way. All these effects, including other possible ones not mentioned here, play a role in deciding the best underlying model with which to describe the universe.

In this sub-section, we derive the ISW effect in a LTB model. We have chosen to focus on the ISW effect mainly due to its is extreme sensitivity to the DE content of the universe, which will be an important probe in future large-scale structure surveys, as well as the fact that it can be used to test the CP (see [56]). Note that in [56], the authors constructed their inhomogeneous model by joining three FLRW models of different curvature, so that the standard ISW formulas may be applied. In [162], a first attempt at a derivation of the ISW formula within general spherically symmetric spacetimes was carried out. Here we derive the ISW formula explicitly for a LTB model, and include the terms coming from the perturbation theory presented in Section 2.3.

In what follows, we make use of the following form of the linearly perturbed LTB metric in the polar case ($\ell > 1$):

$$\begin{aligned} ds^2 = g_{\mu\nu}dx^\mu dx^\nu &= \Big(\hat{g}_{\mu\nu} + \sum_{\ell m} h_{\mu\nu}Y\Big)dx^\mu dx^\nu\,, \\ &= \bigg[-1 + \sum_{\ell m}\Big(\varphi + \chi\Big)Y\bigg]dt^2 - 2X(t,r)\sum_{\ell m}\varsigma Y\,dtdr \\ &\quad + X(t,r)^2\bigg[1 + \sum_{\ell m}\Big(\varphi+\chi\Big)Y\bigg]dr^2 + A(t,r)^2\bigg[1+\sum_{\ell m}\varphi Y\bigg]d\Omega^2\,, \end{aligned} \tag{2.204}$$

where φ, ς and χ are GI perturbations, being functions of (t, r, ℓ), $Y = Y^{\ell m}(\theta, \phi)$ are the spherical harmonics, $X(t,r) \equiv a_\parallel(t,r)/\sqrt{1-\kappa(r)r^2}$, and $A(t,r) \equiv a_\perp(t,r)r$. From

here on we will drop the $\sum_{lm}$, but it is implicitly implied whenever a factor Y is present.

Following [66], the ratio between the observed temperature today (in a direction $\hat{\boldsymbol{x}}_{\boldsymbol{o}}$) and that at the time of emission (originating from position $\boldsymbol{x_e}$) is defined as

$$\frac{T_o(\hat{\boldsymbol{x}}_{\boldsymbol{o}})}{T_e(\boldsymbol{t_e},\boldsymbol{x_e})} \equiv (1+z)^{-1} = \frac{(k^\mu u_\mu)_o}{(k^\nu u_\nu)_e}\,, \tag{2.205}$$

where k^μ is the null wavevector, and u^μ the observer four-velocity, given by

$$k^\mu = \hat{k}^\mu + \delta k^\mu\,,\ \hat{k}^\mu \equiv \left[\frac{dx^A}{d\lambda}, 0\right],\ \delta k^\mu = \left[\delta k^A(t,r,\ell)Y, \delta k(t,r,\ell)Y^{,a}_{,}\right], \tag{2.206}$$

$$u^\mu = \hat{u}^\mu + \delta u^\mu\,,\ \hat{u}^\mu \equiv \delta^\mu_t\,,\ \delta u^\mu = \left[\left(w(t,r,\ell)\hat{n}^A + \frac{1}{2}h^A_B\hat{u}^B\right)Y, v(t,r,\ell)Y^{,a}_{,}\right] \tag{2.207}$$

respectively[2].

Now, expanding $k^\mu u_\mu$ to first order we find

$$\begin{aligned} k^\mu u_\mu &= \left(\hat{k}^\mu + \delta k^\mu\right)\left(\hat{u}^\nu + \delta u^\nu\right)\left(\hat{g}_{\mu\nu} + h_{\mu\nu}Y\right) && (2.208)\\ &= \hat{g}_{\mu\nu}\hat{k}^\mu\hat{u}^\nu + \hat{g}_{\mu\nu}\left(\hat{k}^\mu\delta u^\nu + \hat{u}^\nu\delta k^\mu\right) + \hat{k}^\mu\hat{u}^\nu h_{\mu\nu}Y \\ &= \hat{g}_{tt}\hat{k}^t + \left[\hat{g}_{tt}\delta k^t + \hat{g}_{tt}\hat{k}^t\delta u^t + \hat{g}_{rr}\hat{k}^r\delta u^r + \hat{k}^t h_{tt} + \hat{k}^r h_{rt}\right]Y\,. && (2.209)\end{aligned}$$

From the null condition at the background level

$$\begin{aligned} \hat{g}_{\mu\nu}\hat{k}^\mu\hat{k}^\nu = \hat{g}_{tt}\left(\hat{k}^t\right)^2 + \hat{g}_{rr}\left(\hat{k}^r\right)^2 &= 0 \\ \therefore\ -\left(\hat{k}^t\right)^2 + X^2\left(\hat{k}^r\right)^2 &= 0 \\ \Rightarrow\ \hat{k}^r &= \pm X^{-1}\hat{k}^t\,, \end{aligned} \tag{2.210}$$

and, since from (2.207) we can define

$$\delta u^A(t,r,\ell) \equiv \left[w\hat{n}^A + \frac{1}{2}h^A_B\hat{u}^B\right] = -\frac{1}{2}\left[\varphi + \chi\,,\ X^{-1}\left(\varsigma - 2w\right)\right], \tag{2.211}$$

we then find

$$\begin{aligned} k^\mu u_\mu &= -\hat{k}^t + \left[-\delta k^t + \frac{1}{2}\hat{k}^t\left(\varphi+\chi\right) \pm \frac{1}{2}\hat{k}^t\left(2w - \varsigma\right) + \hat{k}^t\left(\varphi+\chi\right) \mp \hat{k}^t\varsigma\right]Y \\ \Rightarrow\ k^\mu u_\mu &= -\hat{k}^t\left\{1 + \left[\frac{\delta k^t}{\hat{k}^t} - \frac{3}{2}\left(\varphi+\chi\right) \pm \frac{1}{2}\left(3\varsigma - 2w\right)\right]Y\right\}\,. \end{aligned} \tag{2.212}$$

[2]Recall that upper case indices span $\{t,r\}$, that for lower case $\{\theta,\phi\}$, and $\hat{n}^\mu \equiv X^{-1}\delta^\mu_r$.

Plugging the latter into (2.205) we find

$$\frac{T_o(\hat{\boldsymbol{x}}_{\boldsymbol{o}})}{T_e(\boldsymbol{t_e},\boldsymbol{x_e})} = (1+\hat{z})^{-1}\left\{1+\left[\frac{\delta k^t}{\hat{k}^t}-\frac{3}{2}\big(\varphi+\chi\big)\pm\frac{1}{2}\big(3\varsigma-2w\big)\right]\Big|_e^o Y\right\}, \tag{2.213}$$

where we identified $1+\hat{z}=\hat{k}^t_e/\hat{k}^t_o$. Defining the observed and emitted temperatures in terms of their averages and perturbed contribution, we have

$$\begin{aligned}
\frac{\overline{T}_o\!\!\!\!/}{\overline{T}_e\!\!\!\!/}\frac{\Big[1+\Theta_o(\hat{\boldsymbol{x}}_{\boldsymbol{o}})Y\Big]}{\Big[1+\Theta_e(\boldsymbol{t_e},\boldsymbol{x_e})Y\Big]} &= \cancel{(1+\hat{z})^{-1}}\left\{1+\left[\frac{\delta k^t}{\hat{k}^t}-\frac{3}{2}\big(\varphi+\chi\big)\pm\frac{1}{2}\big(3\varsigma-2w\big)\right]\Big|_e^o Y\right\}\\
\Rightarrow\quad \Theta_o(\hat{\boldsymbol{x}}_{\boldsymbol{o}}) &= \Theta_e(\boldsymbol{t_e},\boldsymbol{x_e})+\left[\frac{\delta k^t}{\hat{k}^t}-\frac{3}{2}\big(\varphi+\chi\big)\pm\frac{1}{2}\big(3\varsigma-2w\big)\right]\Big|_e^o .
\end{aligned} \tag{2.214}$$

Let us now turn to the time component of the perturbed part of the geodesic equation to obtain δk^t. But first, we will need some specific components of the background and perturbed connection coefficients, the form of the zeroth order time component of the geodesic equation, as well as the null condition at first order. These are given by:

$$\hat{\Gamma}^t_{tr} = 0 \tag{2.215}$$

$$\hat{\Gamma}^t_{rr} = X^2 H_\parallel , \tag{2.216}$$

$$\delta\Gamma^t_{tt} = -\frac{1}{2}\big(\dot{\varphi}+\dot{\chi}\big) \tag{2.217}$$

$$\delta\Gamma^t_{rt} = -\frac{1}{2}\big(\varphi'+\chi'+2XH_\parallel\varsigma\big) \tag{2.218}$$

$$\delta\Gamma^t_{rr} = \frac{X^2}{2}\big(\dot{\varphi}+\dot{\chi}\big)+2X^2H_\parallel\big(\varphi+\chi\big)+X\varsigma' , \tag{2.219}$$

$$\begin{aligned}
\hat{k}^\mu\nabla_\mu\hat{k}^\nu &= \hat{k}^\mu\hat{k}^\nu_{,\alpha}+\hat{k}^\mu\hat{k}^\gamma\hat{\Gamma}^\nu_{\alpha\gamma}=0\\
\therefore\quad \hat{k}^t\hat{k}^t_{,t} &= -\hat{k}^r\hat{k}^t_{,r}-(\hat{k}^r)^2\hat{\Gamma}^t_{rr}\\
\Rightarrow\quad \hat{k}^t_{,t} &= \mp X^{-1}\hat{k}^t_{,r}-H_\parallel\hat{k}^t , \text{ and}
\end{aligned} \tag{2.220}$$

$$\begin{aligned}
k^\mu k_\mu &= \Big(\hat{k}^\mu+\delta k^\mu\Big)\Big(\hat{k}^\nu+\delta k^\nu\Big)\Big(\hat{g}_{\mu\nu}+h_{\mu\nu}\Big)=0\\
&= 2\hat{g}_{\mu\nu}\hat{k}^\mu\delta k^\nu+\hat{k}^\mu\hat{k}^\nu h_{\mu\nu}Y\\
&= \Big[2\hat{g}_{tt}\hat{k}^t\delta k^t+2\hat{g}_{rr}\hat{k}^r\delta k^r+(\hat{k}^t)^2h_{tt}+2\hat{k}^t\hat{k}^r h_{tr}+(\hat{k}^r)^2h_{rr}\Big]Y
\end{aligned}$$

$$\begin{aligned}
\therefore\ 0 &= -2\hat{k}^t\delta k^t \pm 2X\hat{k}^t\delta k^r + (\hat{k}^t)^2(\varphi+\chi) \mp 2(\hat{k}^t)^2\varsigma + (\hat{k}^t)^2(\varphi+\chi) \\
\Rightarrow\ \delta k^r &= X^{-1}\Big\{ \pm\delta k^t - \hat{k}^t\big[\pm\big(\varphi+\chi\big) - \varsigma\big]\Big\}\,, \qquad (2.221)
\end{aligned}$$

respectively. Continuing with the perturbed part of the geodesic equation, we find

$$\begin{aligned}
k^\mu\nabla_\mu k^\nu &= k^\mu k^\nu_{,\alpha} + k^\mu k^\gamma\Gamma^\nu_{\alpha\gamma} = 0 \\
&= \hat{k}^\mu\delta k^\nu_{,\alpha} + \hat{k}^\nu_{,\alpha}\delta k^\mu + 2\hat{k}^\mu\hat{\Gamma}^\nu_{\alpha\gamma}\delta k^\gamma + \hat{k}^\mu\hat{k}^\gamma\delta\Gamma^\nu_{\alpha\gamma}\,,
\end{aligned}$$

$$\begin{aligned}
\therefore\ \frac{d}{d\lambda}\delta k^t &= -\hat{k}^t_{,t}\delta k^t - \hat{k}^t_{,r}\delta k^r - 2\hat{k}^r\hat{\Gamma}^t_{rr}\delta k^r - (\hat{k}^t)^2\delta\Gamma^t_{tt} - 2\hat{k}^t\hat{k}^r\delta\Gamma^t_{tr} - (\hat{k}^r)^2\delta\Gamma^t_{rr}\,, \\
&= \Big(\pm X^{-1}\hat{k}^t_{,r} + H_\parallel\hat{k}^t\Big)\delta k^t - \Big(\hat{k}^t_{,r} \pm 2XH_\parallel\hat{k}^t\Big)X^{-1}\Big\{ \pm\delta k^t \\
&\quad -\hat{k}^t\big[\pm\big(\varphi+\chi\big) - \varsigma\big]\Big\} + \cancel{\frac{1}{2}(\hat{k}^t)^2\Big(\dot{\varphi}+\dot{\chi}\Big)} \\
&\quad \pm X^{-1}(\hat{k}^t)^2\Big(\varphi'+\chi'+2XH_\parallel\varsigma\Big) \\
&\quad -(\hat{k}^t)^2\left[\cancel{\frac{1}{2}\Big(\dot{\varphi}+\dot{\chi}\Big)} + 2H_\parallel\Big(\varphi+\chi\Big) + X^{-1}\varsigma'\right], \\
\Rightarrow\ \frac{1}{\hat{k}^t}\frac{d}{d\lambda}\delta k^t &= -H_\parallel\delta k^t + X^{-1}\hat{k}^t_{,r}\big[\pm\big(\varphi+\chi\big) - \varsigma\big] \\
&\quad +X^{-1}\hat{k}^t\big[\pm\big(\varphi'+\chi'\big) - \varsigma'\big]\,, \qquad (2.222)
\end{aligned}$$

where

$$\frac{d}{d\lambda} \equiv \hat{k}^t\big[\partial_t \pm X^{-1}\partial_r\big]\,. \qquad (2.223)$$

Now, using

$$\frac{d\mathrm{X}}{d\lambda} = (1+z)^2H_\parallel\frac{d\mathrm{X}}{dz}\,, \qquad (2.224)$$

from [163], as well as the ansatz

$$\hat{k}^\mu = (1+z)[-\hat{u}^\mu + \hat{n}^\mu] = (1+z)[-1, X^{-1}, 0, 0]\,, \qquad (2.225)$$

we can write

$$\frac{d\hat{k}^t}{d\lambda} = -H_\parallel(\hat{k}^t)^2\,, \qquad (2.226)$$

Therefore, writing

$$\frac{d}{d\lambda}\left(\frac{\delta k^t}{\hat{k}^t}\right) = \frac{1}{\hat{k}^t}\frac{d}{d\lambda}\delta k^t - \frac{\delta k^t}{(\hat{k}^t)^2}\frac{d\hat{k}^t}{d\lambda}\,, \qquad (2.227)$$

implies that

$$\begin{aligned}\frac{d}{d\lambda}\left(\frac{\delta k^t}{\hat{k}^t}\right) &= \cancel{-H_{\parallel}\delta k^t} + X^{-1}\hat{k}^t_{,r}\big[\pm\big(\varphi+\chi\big)-\varsigma\big] + X^{-1}\hat{k}^t\big[\pm\big(\varphi'+\chi'\big)-\varsigma'\big] \\ &\quad \cancel{+H_{\parallel}\delta k^t} \\ \Rightarrow\ \frac{\delta k^t}{\hat{k}^t}\Big|_e^o &= \int_e^o d\lambda\,\frac{d}{d\lambda}\left(\frac{\delta k^t}{\hat{k}^t}\right) = \int_e^o d\lambda\left\{X^{-1}\hat{k}^t_{,r}\big[\pm\big(\varphi+\chi\big)-\varsigma\big]\right. \\ &\quad \left. +X^{-1}\hat{k}^t\big[\pm\big(\varphi'+\chi'\big)-\varsigma'\big]\right\}. \end{aligned} \tag{2.228}$$

From (2.223) we have

$$\partial_r = \pm X^{-1}\left[\frac{1}{\hat{k}^t}\frac{d}{d\lambda}-\partial_t\right], \tag{2.229}$$

and so (2.228) becomes

$$\begin{aligned}\frac{\delta k^t}{\hat{k}^t}\Big|_e^o &= \pm\int_e^o d\lambda\left\{\big[\pm\big(\varphi+\chi\big)-\varsigma\big]\left(\frac{1}{\hat{k}^t}\frac{d\hat{k}^t}{d\lambda}-\partial_t\hat{k}^t\right)+\frac{d}{d\lambda}\big[\pm\big(\varphi+\chi\big)-\varsigma\big]\right. \\ &\quad \left. -\hat{k}^t\big[\pm\big(\dot{\varphi}+\dot{\chi}\big)-\dot{\varsigma}\big]\right\}. \end{aligned} \tag{2.230}$$

Since $\hat{k}^t \equiv dt/d\lambda \Rightarrow d\lambda = dt/\hat{k}^t$, we may rewrite

$$\frac{d\hat{k}^t}{d\lambda} = \hat{k}^t\frac{d\hat{k}^t}{dt}, \tag{2.231}$$

and converting the partial derivative of $\hat{k}^t$ with respect to time to a total via

$$\frac{\partial\hat{k}^t}{\partial t} = \frac{d\hat{k}^t}{dt} - \frac{dr}{dt}\frac{\partial\hat{k}^t}{\partial r} = \frac{d\hat{k}^t}{dt} \mp X^{-1}\frac{\partial\hat{k}^t}{\partial r}, \tag{2.232}$$

we find

$$\begin{aligned}\frac{\delta k^t}{\hat{k}^t}\Big|_e^o &= \big[\big(\varphi+\chi\big)\mp\varsigma\big]\Big|_e^o \pm\int_e^o d\lambda\left\{\pm X^{-1}\big[\pm\big(\varphi+\chi\big)-\varsigma\big]\partial_r\hat{k}^t\right. \\ &\quad \left. -\hat{k}^t\big[\pm\big(\dot{\varphi}+\dot{\chi}\big)-\dot{\varsigma}\big]\right\}, \end{aligned}$$

$$\begin{aligned}\therefore\ \frac{\delta k^t}{\hat{k}^t}\Big|_e^o &= \big[\big(\varphi+\chi\big)\mp\varsigma\big]\Big|_e^o + \int_e^o d\lambda\, X^{-1}\big[\pm\big(\varphi+\chi\big)-\varsigma\big]\partial_r\hat{k}^t \\ &\quad -\int_e^o dt\;\partial_t\big[\big(\varphi+\chi\big)\pm\varsigma\big]. \end{aligned} \tag{2.233}$$

Plugging the latter into (2.214) we end up with

$$\begin{aligned}\Theta_o(\hat{\boldsymbol{x}}_{\boldsymbol{o}}) &= \Theta_e(\boldsymbol{t_e},\boldsymbol{x_e}) - \left[\frac{1}{2}\big(\varphi+\chi\big) \pm \frac{1}{2}\big(2w-\varsigma\big)\right]\Bigg|_e^o - \int_e^o dt\,\partial_t\Big[\big(\varphi+\chi\big)\pm\varsigma\Big] \\ &\quad + \int_e^o d\lambda\, X^{-1}\Big[\pm\big(\varphi+\chi\big)-\varsigma\Big]\partial_r\hat{k}^t\,. \end{aligned} \tag{2.234}$$

Note that in the LTB spacetime we find an additional term, proportional to $\partial_r\hat{k}^t$, that vanishes in a FLRW spacetime (see below). We may attempt to estimate $\partial_r\hat{k}^t$ by Taylor expanding the wavevector in the radial direction around the origin, as follows

$$\hat{k}^t(t,r+\delta r) = \hat{k}^t(t,r) + \delta r\,\partial_r\hat{k}^t(t,r)\,. \tag{2.235}$$

Plugging the latter into (2.226) we get

$$\begin{aligned}\frac{d}{d\lambda}\left(\partial_r\hat{k}^t\right) &= \frac{\partial}{\partial r}\left(\frac{d\hat{k}^t}{d\lambda}\right) \\ &= -2H_\parallel\hat{k}^t\partial_r\hat{k}^t - (\hat{k}^t)^2\partial_r H_\parallel\,. \end{aligned} \tag{2.236}$$

Setting $S = \partial_r\hat{k}^t$, $\hat{k}^t = -(1+z)$, $\alpha(z) = -2(1+z)^{-1}$, $\beta(z) = -H_\parallel^{-1}\partial_r H_\parallel$, and $d/d\lambda = (1+z)^2 H_\parallel d/dz$, we have

$$\frac{d}{dz}S(z) + \alpha(z)S(z) = \beta(z)\,, \tag{2.237}$$

which has the solution

$$\begin{aligned} S(z) &= \exp\left[-\int_0^z dz\,\alpha(z)\right]\left\{S(0) + \int_0^z dz\,\beta(z)\exp\left[\int_0^z dz\,\alpha(z)\right]\right\} \\ \Rightarrow\quad \partial_r\hat{k}^t(z) &= -(1+z)^2\sqrt{\frac{3}{2}}\int_0^z dz\,(1+z)^{-2}\frac{a_\parallel(t(z),r(z))}{r(z)a_\perp(t(z),r(z))}\frac{\sigma^2(z)}{H_\parallel(t(z),r(z))}\,, \end{aligned} \tag{2.238}$$

where we used the fact that $S(0) = \partial_r(1+0) = 0$, and $\sigma^2 \equiv \sigma_{\mu\nu}\sigma^{\mu\nu} = \sqrt{\frac{2}{3}}\frac{a_\perp r}{a_\parallel}\partial_r H_\parallel$ is the shear scalar.

In the FLRW limit, neglecting the vectors and tensors (i.e. $\varsigma = 0 = \chi$) in (2.234)

implies $\varphi \to -2\Psi$, $w \to \boldsymbol{n}\cdot\boldsymbol{v}$, $\sigma \to 0$, and we find

$$\Theta_o^{FL}(\hat{\boldsymbol{x}}_{\boldsymbol{o}}) \;=\; \Theta_e^{FL}(\boldsymbol{t_e},\boldsymbol{x_e}) + \Psi\Big|_e^o \mp \boldsymbol{n}\cdot\boldsymbol{v}\Big|_e^o + 2\int_e^o dt\;\partial_t\Psi\,, \tag{2.239}$$

where the first two terms on the rhs are those of the ordinary SW effect, the third term the Doppler contribution (where $\boldsymbol{n}\cdot\boldsymbol{v} = n^r\partial_r \mathrm{v} = \sqrt{1-Kr^2}\partial_r \mathrm{v}$, with v the velocity potential perturbation), and finally the last term is the standard ISW contribution.

2.4 Conclusion

In this chapter, after providing a motivation and literature review of the LTB model, we summarised the equations which describe its background evolution, and presented example plots of how the background evolves in the case of different void models that will be used in the next chapters.

We then moved on to a summary of the efforts to perform perturbation theory in such a spacetime, and then recapped a derivation of the perturbation equations that arise in our approach to the problem. We pointed out that there is a natural mixing between scalar, vector and tensor degrees of freedom − identified by taking the homogeneous limit. We then presented a set of variables which reduce to pure scalar, vector and tensor modes in the homogeneous limit. We also derived the forms of the electric and magnetic parts of the Weyl tensor in this model, since these will expose any relativistic degrees of freedom present.

Finally, we derived the ISW effect in LTB, and pointed out an additional contribution to the perturbed redshift compared to the FLRW case.

Note that while we have specialised to the case of open void models containing a uniform bang-time, exploring more sophisticated models (even ones that include Λ) is certainly possible given that we have kept our equations as general as possible.

As we point out in the next chapters, the perturbation equations developed here may be used to study a variety of cosmological and astrophysical effects, which will be left for future work.

CHAPTER 3

Numerical code for perturbations of spherically symmetric dust spacetimes

3.1 Introduction

In this chapter we present a numerical code that solves the first order linear perturbation equations in a LTB background, as derived in Section 2.3. We focus on the polar sector here, since this is where the density contrast is defined. We also restrict ourselves to all but the lowest frequencies ($\ell > 1$). Note, however, that our general approach may also be applied to the axial case, as well as to the polar $\ell = 0, 1$ modes.

Recall that LTB models are spherically symmetric but inhomogeneous dust solutions of the EFE. A natural result of the inherent background shear is to mix the (usual) scalar, vector and tensor modes (which are decoupled in FLRW at first order) − even when the homogeneous limit is taken. Note that while this makes an immediate comparison between the perturbed LTB and FLRW variables tricky, it is possible to construct perturbed LTB quantities which reduce to pure SVT variables in the homogeneous limit − an example set is shown in Section 2.3.5.

With our code, a number of interesting physical scenarios can be modelled. For example:

Relativistic corrections for structure formation. At present, cosmological struc-

ture formation is modelled either via Newtonian (non-relativistic) methods that capture non-linear aspects (see e.g. [164]), or via linear perturbation theory in a general relativistic setting (e.g. [165]). A fairly unexplored area here is that which captures the non-linear relativistic aspects – see, e.g., [166] for a review. Some steps in this direction have begun in the context of N-body codes which incorporate relativistic corrections to the gravitational potentials [167, 168]. Using our model, structure growth *on top of* a strongly non-linear background may be studied — either an over-density such as a cluster, or a large void, both which produces large curvature and shear. The effects of vector and tensor degrees of freedom on density perturbations can also be explored, and the errors in neglecting this coupling estimated.

Evolution of perturbations in void models. If, instead of dark energy, we resided at the center of a deep spherically symmetric void of a few Gpc across, GR may still be a suitable theory to use on the largest scales to describe the apparent accelerated expansion (see, e.g., [140, 148, 48, 112] and [50] for a comprehensive review). Furthermore, cosmic structure will develop differently in such models compared to the concordance one, and therefore opens up another test of the CP [169] − see Chapter 5. Structure formation in LTB models has only been quantified for the special case which neglects the coupling of the scalar gravitational potential to vector and tensor degrees of freedom [155, 169, 156, 157, 170, 171]. While this seems reasonable, the accuracy in this assumption has not been quantified. A recent alternative approach to this problem, based on second-order perturbation theory in FLRW, can be found here: [172].

Weak lensing of gravitational waves The merging of supermassive black holes produces a powerful and well-understood GW signal, potentially allowing such sources to be used as "standard sirens", and possibly improving upon standard(-isable) candles such as SN1a (see e.g., [173]). Unfortunately, the expected GW signal will suffer weak lensing by the intervening dark matter distribution, thus degrading their use as cosmological distance estimators [174]. An interesting scenario to

consider is when the GW wavelength is comparable to the size of the dark matter halos, since this is where the geometric optics approximation for the lensing is expected to break down. By modelling a dark matter halo using an LTB model, and scattering gravitational waves off it using our code, we can hope to quantify the lensing of gravitational waves more accurately.

To illustrate the performance of the code and the physics of the evolution of perturbations, we consider a Gpc cosmological void that is asymptotically EdS and that accommodates the distance-redshift relations given by SN1a observations as well as age data − this is the MV model introduced in Section 2.2 (see Eq. 2.45 for details).

We measure our code's performance by computing error and convergence statistics for several different spherical harmonic frequencies, considering a specific set of initial conditions at different locations throughout the void.

Before showing the details of our particular numerical algorithm, we first present our equations in non-dimensional form in order to make it more code-ready.

3.2 Non-dimensionalising the equations

The set of perturbation equations we deal with here, (2.146)−(2.154), can be recast in terms of dimensionless variables through the following transformations:

$$\widetilde{r} \equiv H_0 r\,, \tag{3.1}$$

$$\widetilde{\eta} \equiv H_0 \int \frac{dt}{a_\perp^{\rm in}(t)}\,, \tag{3.2}$$

where the particular form of $\widetilde{\eta}$ is motivated by the standard definition of conformal time. Then, using

$$\partial_t = \frac{H_0}{a_\perp^{\rm in}}\partial_{\widetilde{\eta}}\,, \tag{3.3}$$

$$\partial_r = H_0\partial_{\widetilde{r}}\,, \tag{3.4}$$

we have

$$H_{\perp/\parallel} = \frac{H_0}{a_\perp^{\rm in}}\widetilde{\mathcal{H}}_{\perp/\parallel}\,, \tag{3.5}$$

$$\kappa = H_0^2\widetilde{\kappa}\,, \tag{3.6}$$

$$\rho_m = \left(\frac{H_0}{a_\perp^{\rm in}}\right)^2\widetilde{\rho}_m\,, \tag{3.7}$$

$$X = a_\perp^{\rm in}\widetilde{X}\,, \tag{3.8}$$

where we defined

$$8\pi G\widetilde{\rho}_m \equiv \widetilde{\mathcal{H}}_\perp^2 + 2\widetilde{\mathcal{H}}_\perp\widetilde{\mathcal{H}}_\parallel + \left(1+2\frac{a_\perp}{a_\parallel}\right)\left(\frac{a_\perp^{\rm in}}{a_\perp}\right)^2\widetilde{\kappa} + \frac{\widetilde{r}a_\perp^{\rm in\,2}}{a_\perp a_\parallel}\widetilde{\kappa}_{,\widetilde{r}}\,. \tag{3.9}$$

We introduce the following dimensionless angular peculiar velocity,

$$\tilde{v} \equiv \frac{a_\perp^{\rm in}}{H_0}v\,, \tag{3.10}$$

and relate the cosmic time t to the dimensionless conformal time by

$$t = \frac{\Omega_m^{\rm in}}{2\left[\Omega_k^{\rm in}\right]^{3/2}}\left[\sinh\left(\widetilde{\eta}\sqrt{\Omega_k^{\rm in}}\right) - \widetilde{\eta}\sqrt{\Omega_k^{\rm in}}\right] + t_B^{\rm in}\,. \tag{3.11}$$

Thus, to evolve the system from some initial time, $t_{\rm init}$, until today, t_0, we compute the corresponding initial and final values for $\widetilde{\eta}$ using:

$$\widetilde{\eta}(t) = \frac{2}{\sqrt{\Omega_k^{\rm in}}}u^{\rm in}(t)\,. \tag{3.12}$$

Incorporating all of the above changes into our original perturbation equations, our system of PDE's is now given by

$$\begin{aligned}\ddot{\varphi} = {} & \left(\widetilde{\mathcal{H}}_\perp^{\rm in} - 4\widetilde{\mathcal{H}}_\perp\right)\dot{\varphi} + a_\perp^{\rm in\,2}\left[\frac{2\widetilde{\kappa}}{a_\perp^2} - \frac{\Lambda}{H_0^2}\right]\varphi - \widetilde{\mathcal{H}}_\perp\dot{\chi} + \widetilde{X}^{-2}\frac{a_\parallel}{\widetilde{r}a_\perp}\chi' \\ & + a_\perp^{\rm in\,2}\left[\frac{2\widetilde{\kappa}}{a_\perp^2} - \frac{\Lambda}{H_0^2} + \frac{\ell(\ell+1)-2}{2a_\perp^2\widetilde{r}^2}\right]\chi + 3\widetilde{X}^{-1}\frac{a_\parallel}{\widetilde{r}a_\perp}\widetilde{\sigma}\varsigma\,, \end{aligned} \tag{3.13}$$

$$\dot{\varsigma} = -2\widetilde{\mathcal{H}}_\parallel\varsigma - \widetilde{X}^{-1}\chi'\,, \tag{3.14}$$

$$\ddot{\chi} = \widetilde{X}^{-2}\chi'' - \widetilde{X}^{-2}\left[\frac{a_\parallel{}'}{a_\parallel} + \frac{(\widetilde{r}\widetilde{\kappa} + \frac{1}{2}\widetilde{r}^2\widetilde{\kappa}')}{1-\widetilde{\kappa}\widetilde{r}^2} + 2\frac{a_\parallel}{\widetilde{r}a_\perp}\right]\chi' + (\widetilde{\mathcal{H}}^{\rm in}_\perp - 3\widetilde{\mathcal{H}}_\parallel)\dot{\chi}$$
$$+ 3\widetilde{X}^{-1}\widetilde{\sigma}\varsigma' - 6\widetilde{\sigma}\dot{\varphi} - \left(\frac{a^{\rm in}_\perp}{a_\perp}\right)^2\left[\frac{\ell(\ell+1)-2}{\widetilde{r}^2}\right]\chi + 2\widetilde{X}^{-1}\left[\widetilde{\mathcal{H}}_\parallel - 2\widetilde{\mathcal{H}}_\perp\right]'\varsigma$$
$$+ \left(\frac{a^{\rm in}_\perp}{a_\perp}\right)^2\left[4\left(\frac{a_\perp}{a_\parallel}-1\right)\widetilde{\kappa} + 2\widetilde{r}\widetilde{\kappa}'\left(\frac{a_\perp}{a_\parallel}\right)\right](\chi+\varphi)\,, \tag{3.15}$$

where the matter perturbations are obtained from

$$8\pi G\widetilde{\rho}_m\Delta = -\widetilde{X}^{-2}\varphi'' + \widetilde{X}^{-2}\left[\frac{a_\parallel{}'}{a_\parallel} + \frac{\left(\widetilde{\kappa}\widetilde{r} + \frac{1}{2}\widetilde{r}^2\widetilde{\kappa}'\right)}{1-\widetilde{\kappa}\widetilde{r}^2} - 2\frac{a_\parallel}{\widetilde{r}a_\perp}\right]\varphi' + 2\widetilde{X}^{-1}\widetilde{\mathcal{H}}_\perp\varsigma'$$
$$+ \widetilde{X}^{-2}\frac{a_\parallel}{\widetilde{r}a_\perp}\chi' + \widetilde{\Theta}\dot{\varphi} + \widetilde{\mathcal{H}}_\perp\dot{\chi} + \left[3\widetilde{\mathcal{H}}_\perp\left(\widetilde{\sigma}+\widetilde{\mathcal{H}}_\perp\right) - \widetilde{r}\widetilde{\kappa}'\left(\frac{a^{\rm in}_\perp{}^2}{a_\perp a_\parallel}\right)\right.$$
$$\left. - \left(1+2\frac{a_\perp}{a_\parallel}\right)\left(\frac{a^{\rm in}_\perp}{a_\perp}\right)^2\widetilde{\kappa} + \frac{\ell(\ell+1)}{\widetilde{r}^2}\left(\frac{a^{\rm in}_\perp}{a_\perp}\right)^2\right]\left(\varphi+\chi\right)$$
$$- \left[\frac{\ell(\ell+1)-2}{2\widetilde{r}^2}\right]\left(\frac{a^{\rm in}_\perp}{a_\perp}\right)^2\chi + \widetilde{X}^{-1}\frac{a_\parallel}{\widetilde{r}a_\perp}\left(3\widetilde{\sigma}+4\widetilde{\mathcal{H}}_\parallel\right)\varsigma\,, \tag{3.16}$$

$$8\pi G\widetilde{\rho}_m w = \widetilde{X}^{-1}\dot{\varphi}' - \widetilde{X}^{-1}\left(3\widetilde{\sigma}-\widetilde{\mathcal{H}}_\parallel\right)\varphi' - \frac{a_\parallel}{\widetilde{X}\widetilde{r}a_\perp}\dot{\chi} + \widetilde{X}^{-1}\widetilde{\mathcal{H}}_\perp\chi'$$
$$+ \left[\frac{3}{2}\widetilde{\mathcal{H}}_\perp\left(\widetilde{\sigma}+\widetilde{\mathcal{H}}_\perp\right) - \left(\frac{a_\perp}{a_\parallel}-\frac{1}{2}\right)\left(\frac{a^{\rm in}_\perp}{a_\perp}\right)^2\widetilde{\kappa}\right.$$
$$\left. - \widetilde{r}\widetilde{\kappa}'\left(\frac{a^{\rm in}_\perp{}^2}{2a_\perp a_\parallel}\right) + \frac{\ell(\ell+1)}{2\widetilde{r}^2}\left(\frac{a^{\rm in}_\perp}{a_\perp}\right)^2 - \frac{\Lambda}{2}\right]\varsigma\,, \tag{3.17}$$

$$8\pi G\widetilde{\rho}_m\widetilde{v} = \dot{\varphi} + \frac{1}{2}\dot{\chi} + \frac{1}{2}\widetilde{X}^{-1}\varsigma' + \widetilde{\mathcal{H}}_\parallel\left(\varphi+\chi\right). \tag{3.18}$$

The conservation equations are now

$$C_\Delta \equiv \dot{\Delta} + \frac{3}{2}\dot{\varphi} + \frac{1}{2}\dot{\chi} + \widetilde{X}^{-1}\left(w+\varsigma/2\right)'$$
$$+ \widetilde{X}^{-1}\left[\frac{\rho_m{}'}{\rho_m} + 2\frac{a_\parallel}{\widetilde{r}a_\perp}\right]\left(w+\varsigma/2\right) - \frac{\ell(\ell+1)}{\widetilde{r}^2}\left(\frac{a^{\rm in}_\perp}{a_\perp}\right)^2\widetilde{v} = 0\,, \tag{3.19}$$

$$C_w \equiv \dot{w} - \frac{1}{2}\widetilde{X}^{-1}\varphi' + \widetilde{\mathcal{H}}_\parallel\left(w+\varsigma/2\right) = 0\,, \tag{3.20}$$

$$C_{\tilde{v}} \equiv \dot{\tilde{v}} + \widetilde{\mathcal{H}}^{\rm in}_\perp\widetilde{v} - \frac{1}{2}\left(\varphi+\chi\right) = 0\,. \tag{3.21}$$

The resulting dimensionless electric and magnetic Weyl tensor coefficients at the

background-level are

$$\hat{\tilde{E}}_{rr} \equiv \frac{\hat{E}_{rr}}{H_\perp^2} = \left(\frac{\widetilde{X}}{a_\perp^{\rm in}\widetilde{\mathcal{H}}_\perp}\right)^2\left[\widetilde{\mathcal{H}}_\perp\tilde{\sigma} + \frac{2}{3}\left(\frac{a_\perp}{a_\parallel}-1\right)\left(\frac{a_\perp^{\rm in}}{a_\perp}\right)^2\tilde{\kappa} + \frac{\tilde{r}\tilde{\kappa}'}{3}\frac{a_\perp^{\rm in\,2}}{a_\perp a_\parallel}\right], \tag{3.22}$$

$$\hat{\tilde{E}}_{ab} \equiv \hat{E}_{ab} = -\frac{1}{2}\left(\frac{1}{a_\perp^{\rm in}}\right)^4\left(\frac{a_\perp\tilde{r}\widetilde{\mathcal{H}}_\perp}{\widetilde{X}}\right)^2\hat{\tilde{E}}_{rr}\gamma_{ab}\,. \tag{3.23}$$

The corresponding non-zero dimensionless perturbed parts for the electric and magnetic Weyl tensors are:

$$\begin{aligned}\widetilde{\delta E}_{rr} \equiv \frac{\delta E_{rr}}{H_\perp^2} = -\frac{1}{3}\left(\frac{a_\perp^{\rm in}}{\widetilde{\mathcal{H}}_\perp}\right)^2\Bigg\{&\varphi'' - \left[\frac{a_\parallel{}'}{a_\parallel} + \frac{(\tilde{\kappa}\tilde{r}+\frac{1}{2}\tilde{r}^2\tilde{\kappa}')}{1-\tilde{\kappa}\tilde{r}^2} + \frac{a_\parallel}{\tilde{r}a_\perp}\right]\varphi' - \frac{a_\parallel}{\tilde{r}a_\perp}\chi' \\ &- 2\widetilde{X}\widetilde{\mathcal{H}}_\perp\varsigma' - \frac{3}{2}\left(\frac{1}{a_\perp^{\rm in}}\right)^2\sigma\dot{\varphi} - \widetilde{X}^2\widetilde{\mathcal{H}}_\perp\dot{\chi} + \left[\left(\frac{a_\perp}{a_\parallel}-1\right)\left(\frac{a_\perp^{\rm in}}{a_\perp}\right)^2\tilde{\kappa} - 3\widetilde{\mathcal{H}}_\perp\tilde{\sigma}\right. \\ &\left. + \left(\frac{a_\perp^{\rm in\,2}}{a_\perp a_\parallel}\right)\tilde{r}\tilde{\kappa}' + \frac{\ell(\ell+1)}{2(\tilde{r})^2}\left(\frac{a_\perp^{\rm in}}{a_\perp}\right)^2\right](\varphi+\chi) - 2\widetilde{X}\frac{a_\parallel}{\tilde{r}a_\perp}(3\tilde{\sigma}-\widetilde{\mathcal{H}}_\parallel)\varsigma \\ &- \left[\frac{\ell(\ell+1)-2}{(\tilde{r})^2}\right]\left(\frac{a_\perp^{\rm in}}{a_\perp}\right)^2\chi\Bigg\},\end{aligned} \tag{3.24}$$

$$\widetilde{\delta E}_r \equiv \frac{\delta E_r}{H_\perp} = -\left(\frac{a_\perp^{\rm in}}{2\widetilde{\mathcal{H}}_\perp}\right)\left[\varphi' - \frac{a_\parallel}{\tilde{r}a_\perp}\big(\varphi+\chi\big) - \widetilde{X}\widetilde{\mathcal{H}}_\perp\varsigma\right], \tag{3.25}$$

$$\begin{aligned}\widetilde{\delta E}_{(T)} \equiv \delta E_{(T)} = -\frac{1}{2}\left(\frac{1}{a_\perp^{\rm in}}\right)^4&\left(\frac{a_\perp\tilde{r}\widetilde{\mathcal{H}}_\perp}{\widetilde{X}}\right)^2\widetilde{\delta E}_{rr} + \frac{1}{3}\left(\frac{a_\perp\tilde{r}}{a_\perp^{\rm in}}\right)^2\left[\frac{3}{2}H_\perp\sigma\right. \\ &\left. + \left(\frac{a_\perp}{a_\parallel}-1\right)\left(\frac{a_\perp^{\rm in}}{a_\perp}\right)^2\tilde{\kappa} + \frac{\tilde{r}\tilde{\kappa}'}{2}\left(\frac{a_\perp^{\rm in\,2}}{a_\parallel a_\perp}\right)\right]\chi\,,\end{aligned} \tag{3.26}$$

$$\widetilde{\delta E}_{(TF)} \equiv \delta E_{(TF)} = -\frac{1}{2}\Big(\varphi+\chi\Big)\,, \tag{3.27}$$

and

$$\widetilde{\overline{\delta H}}_r \equiv \frac{\overline{\delta H}_r}{H_\perp} = -\frac{1}{4}\left(\frac{a_\perp^{\rm in}}{\widetilde{\mathcal{H}}_\perp}\right)\left[\varsigma' + \widetilde{X}\dot{\chi} + \widetilde{X}\tilde{\sigma}\Big(\varphi+\chi\Big) - 2\frac{a_\parallel}{\tilde{r}a_\perp}\varsigma\right], \tag{3.28}$$

$$\widetilde{\overline{\delta H}}_{(TF)} \equiv \overline{\delta H}_{(TF)} = -\frac{1}{2}\varsigma\,, \tag{3.29}$$

respectively.

Our next step is to define a numerical grid onto which we shall discretise the above setup.

3.2.1 Discretising the grid

We introduce discretized time and space coordinates $\tilde{\eta}_i$ and $\tilde{r}_j$ given by

$$\widetilde{\eta}_i = \widetilde{\eta}_{\rm init} + i\Delta\widetilde{\eta}/\alpha\,, \tag{3.30}$$

$$\widetilde{r}_j = \widetilde{r}_{\rm min} + j\Delta\widetilde{r}/\alpha\,, \tag{3.31}$$

where $\Delta\widetilde{\eta}$ and $\Delta\widetilde{r}$ are grid spacings in η and r, respectively, and $i = 0...N_{\tilde{\eta}}$ and $j = 0...N_{\tilde{r}}$. The factor α determines the grid resolution relative to an $\alpha = 1$ baseline (with the number of grid points $N_{\tilde{\eta}}$ and $j = 0...N_{\tilde{r}}$ increased proportionally to cover the same domain). For our PDE system, the Courant-Friedrics-Lewy (CFL) condition requires that

$$\frac{\Delta\widetilde{\eta}}{\Delta\widetilde{r}} \lesssim \widetilde{X}\,, \tag{3.32}$$

for numerical stability, where $\widetilde{X}\epsilon\{1, 1.47\}$. For our simulations we use

$$\frac{\Delta\widetilde{\eta}}{\Delta\widetilde{r}} = 0.98\alpha^{-1}\,. \tag{3.33}$$

Spatial derivatives are calculated using 2nd-order finite difference operators. For some quantity $Q_{i,j}$ evaluated at time $\tilde{\eta}_i$ and position $\tilde{r}_j$ at the baseline resolution,

$$H_0^{-1}Q'_{i,j} = \frac{Q_{i,j+1} - Q_{i,j-1}}{2\Delta\tilde{r}} + \mathcal{O}(\Delta\tilde{r}^2)\,, \tag{3.34}$$

$$H_0^{-2}Q''_{i,j} = \frac{Q_{i,j+1} - 2Q_{i,j} + Q_{i,j-1}}{\Delta\tilde{r}^2} + \mathcal{O}(\Delta\tilde{r}^2)\,. \tag{3.35}$$

The RHS of Eqs. (2.149)−(2.151) are evaluated on a $\widetilde{\eta}$ = constant slice, via the method of lines [175], and evolved forward in time using a standard 4th-order Runge-Kutta time integrator. The overall scheme is 2nd-order accurate due to the our choice of spatial finite differencing.

3.2.2 The Runge-Kutta Scheme

Our final task is to split any of our master equations that are 2nd-order in time, into two 1st-order ones. Doing this we get

$$\varphi_{,\widetilde{\eta}} = \bar{\varphi}\,, \tag{3.36}$$

$$\bar{\varphi}_{,\widetilde{\eta}} = \mathcal{F}^{\varphi} + \mathcal{S}^{\varphi}\,, \tag{3.37}$$

$$\varsigma_{,\widetilde{\eta}} = \mathcal{F}^{\varsigma} + \mathcal{S}^{\varsigma}\,, \tag{3.38}$$

$$\chi_{,\widetilde{\eta}} = \bar{\chi}\,, \tag{3.39}$$

$$\bar{\chi}_{,\widetilde{\eta}} = \mathcal{F}^{\chi} + \mathcal{S}^{\chi}\,, \tag{3.40}$$

where, for compactness, we isolated each force ($\mathcal{F}$) and source ($\mathcal{S}$) term as follows:

$$\mathcal{F}^{\varphi} \equiv \left(\widetilde{\mathcal{H}}_{\perp}^{\rm in} - 4\widetilde{\mathcal{H}}_{\perp}\right)\overline{\varphi} + \left[2\widetilde{\kappa}\left(\frac{a_{\perp}^{\rm in}}{a_{\perp}}\right)^2 - \Lambda\right]\varphi\,, \tag{3.41}$$

$$\mathcal{S}^{\varphi} \equiv \frac{a_{\parallel}}{\widetilde{r}a_{\perp}\widetilde{X}^2}\chi' - \widetilde{\mathcal{H}}_{\perp}\dot{\chi} + \frac{3a_{\parallel}}{\widetilde{r}a_{\perp}\widetilde{X}}\widetilde{\sigma}\varsigma + \left[2\widetilde{\kappa} - \Lambda + \frac{\ell(\ell+1)-2}{2\widetilde{r}^2}\right]\left(\frac{a_{\perp}^{\rm in}}{a_{\perp}}\right)^2\chi\,, \tag{3.42}$$

$$\mathcal{F}^{\varsigma} \equiv -2\widetilde{\mathcal{H}}_{\parallel}\varsigma\,, \tag{3.43}$$

$$\mathcal{S}^{\varsigma} \equiv -\widetilde{X}^{-1}\chi'\,, \tag{3.44}$$

$$\begin{aligned}\mathcal{F}^{\chi} \equiv\ & \widetilde{X}^{-2}\chi'' - \widetilde{X}^{-2}\left[\frac{a_{\parallel}{}'}{a_{\parallel}} + \frac{(\widetilde{r}\widetilde{\kappa} + \frac{1}{2}\widetilde{r}^2\widetilde{\kappa}')}{1-\widetilde{\kappa}\widetilde{r}^2} + 2\frac{a_{\parallel}}{\widetilde{r}a_{\perp}}\right]\chi' + (\widetilde{\mathcal{H}}_{\perp}^{\rm in} - 3\widetilde{\mathcal{H}}_{\parallel})\dot{\chi} \\ & + \left[4\left(\frac{a_{\perp}}{a_{\parallel}} - 1\right)\widetilde{\kappa} + 2\widetilde{r}\widetilde{\kappa}'\left(\frac{a_{\perp}}{a_{\parallel}}\right) - \frac{\ell(\ell+1)-2}{(LH_0\widetilde{r})^2}\right]\left(\frac{a_{\perp}^{\rm in}}{a_{\perp}}\right)^2\chi\end{aligned} \tag{3.45}$$

$$\begin{aligned}\mathcal{S}^{\chi} \equiv\ & 3\widetilde{X}^{-1}\widetilde{\sigma}\varsigma' - 6\widetilde{\sigma}\dot{\varphi} + 2\widetilde{X}^{-1}\left[\widetilde{\mathcal{H}}_{\parallel} - 2\widetilde{\mathcal{H}}_{\perp}\right]'\varsigma \\ & + \left[4\left(\frac{a_{\perp}}{a_{\parallel}} - 1\right)\widetilde{\kappa} + 2\widetilde{r}\widetilde{\kappa}'\left(\frac{a_{\perp}}{a_{\parallel}}\right)\right]\left(\frac{a_{\perp}^{\rm in}}{a_{\perp}}\right)^2\varphi\,.\end{aligned} \tag{3.46}$$

Our equations are now ready to be discretised in a Runge-Kutta fashion for the time dependence. Doing this we get

$$\varphi_{i+1,j} = \varphi_{i,j} + \frac{\Delta\widetilde{\eta}}{6}\Big(a_{1i,j} + 2a_{2i,j} + 2a_{3i,j} + a_{4i,j}\Big)\,, \tag{3.47}$$

$$\overline{\varphi}_{i+1,j} = \overline{\varphi}_{i,j} + \frac{\Delta\widetilde{\eta}}{6}\Big(b_{1i,j} + 2b_{2i,j} + 2b_{3i,j} + b_{4i,j}\Big)\,, \tag{3.48}$$

$$\varsigma_{i+1,j} = \varsigma_{i,j} + \frac{\Delta\widetilde{\eta}}{6}\Big(c_{1i,j} + 2c_{2i,j} + 2c_{3i,j} + c_{4i,j}\Big)\,, \tag{3.49}$$

$$\chi_{i+1,j} = \chi_{i,j} + \frac{\Delta\widetilde{\eta}}{6}\Big(d_{1i,j} + 2d_{2i,j} + 2d_{3i,j} + d_{4i,j}\Big)\,, \tag{3.50}$$

$$\overline{\chi}_{i+1,j} = \overline{\chi}_{i,j} + \frac{\Delta\widetilde{\eta}}{6}\Big(e_{1i,j} + 2e_{2i,j} + 2e_{3i,j} + e_{4i,j}\Big)\,, \tag{3.51}$$

where

$$a_{1i,j} = \overline{\varphi}_{i,j}\,, \tag{3.52}$$

$$b_{1i,j} = \mathcal{F}^{\varphi}\Big(\widetilde{\eta}_i, \overline{\varphi}_{i,j}, \varphi_{i,j}\Big) + \mathcal{S}^{\varphi}\Big(\widetilde{\eta}_i, \partial_{\tilde{r}}\chi_{i,j}, \overline{\chi}_{i,j}, \chi_{i,j}, \varsigma_{i,j}\Big)\,, \tag{3.53}$$

$$c_{1i,j} = \mathcal{F}^{\varsigma}\Big(\widetilde{\eta}_i, \varsigma_{i,j}\Big) + \mathcal{S}^{\varsigma}\Big(\widetilde{\eta}_i, \partial_{\tilde{r}}\chi_{i,j}\Big)\,, \tag{3.54}$$

$$d_{1i,j} = \overline{\chi}_{i,j}\,, \tag{3.55}$$

$$e_{1i,j} = \mathcal{F}^{\chi}\Big(\widetilde{\eta}_i, \partial^2_{\tilde{r}}\chi_{i,j}, \partial_{\tilde{r}}\chi_{i,j}, \overline{\chi}_{i,j}, \chi_{i,j}\Big) + \mathcal{S}^{\chi}\Big(\widetilde{\eta}_i, \overline{\varphi}_{i,j}, \varphi_{i,j}, \partial_{\tilde{r}}\varsigma_{i,j}, \varsigma_{i,j}\Big)\,, \tag{3.56}$$

$$a_{2i,j} = a_{1i,j} + b_{1i,j}\Delta\widetilde{\eta}/2\,, \tag{3.57}$$

$$d_{2i,j} = d_{1i,j} + e_{1i,j}\Delta\widetilde{\eta}/2\,, \tag{3.58}$$

$$\begin{aligned} b_{2i,j} = {} & \mathcal{F}^{\varphi}\Big(\widetilde{\eta}_i + \Delta\widetilde{\eta}/2, a_{2i,j}, \varphi_{i,j} + a_{1i,j}\Delta\widetilde{\eta}/2\Big) + \mathcal{S}^{\varphi}\Big(\widetilde{\eta}_i + \Delta\widetilde{\eta}/2, \\ & \partial_{\tilde{r}}\chi_{i,j} + \partial_{\tilde{r}}d_{1i,j}\Delta\widetilde{\eta}/2, d_{2i,j}, \chi_{i,j} + d_{1i,j}\Delta\widetilde{\eta}/2, \varsigma_{i,j} + c_{1i,j}\Delta\widetilde{\eta}/2\Big)\,, \end{aligned} \tag{3.59}$$

$$\begin{aligned} c_{2i,j} = {} & \mathcal{F}^{\varsigma}\Big(\widetilde{\eta}_i + \Delta\widetilde{\eta}/2, \varsigma_{i,j} + c_{1i,j}\Delta\widetilde{\eta}/2\Big) + \mathcal{S}^{\varsigma}\Big(\widetilde{\eta}_i + \Delta\widetilde{\eta}/2, \\ & \partial_{\tilde{r}}\chi_{i,j} + \partial_{\tilde{r}}d_{1i,j}\Delta\widetilde{\eta}/2\Big)\,, \end{aligned} \tag{3.60}$$

$$e_{2i,j} = \mathcal{F}^{\chi}\Big(\widetilde{\eta}_i + \Delta\widetilde{\eta}/2, \partial_{\tilde{r}}^2\chi_{i,j} + \partial_{\tilde{r}}^2 d_{1i,j}\Delta\widetilde{\eta}/2, \partial_{\tilde{r}}\chi_{i,j} + \partial_{\tilde{r}} d_{1i,j}\Delta\widetilde{\eta}/2, d_{2i,j},$$
$$\chi_{i,j} + d_{1i,j}\Delta\widetilde{\eta}/2\Big) + \mathcal{S}^{\chi}\Big(\widetilde{\eta}_i + \Delta\widetilde{\eta}/2, a_{2i,j}, \varphi_{i,j} + a_{1i,j}\Delta\widetilde{\eta}/2,$$
$$\partial_{\tilde{r}}\varsigma_{i,j} + \partial_{\tilde{r}} c_{1i,j}\Delta\widetilde{\eta}/2, \varsigma_{i,j} + c_{1i,j}\Delta\widetilde{\eta}/2\Big), \tag{3.61}$$

$$a_{3i,j} = a_{1i,j} + b_{2i,j}\Delta\widetilde{\eta}/2\,, \tag{3.62}$$
$$d_{3i,j} = d_{1i,j} + e_{2i,j}\Delta\widetilde{\eta}/2\,, \tag{3.63}$$
$$b_{3i,j} = \mathcal{F}^{\varphi}\Big(\widetilde{\eta}_i + \Delta\widetilde{\eta}/2, a_{3i,j}, \varphi_{i,j} + a_{2i,j}\Delta\widetilde{\eta}/2\Big) + \mathcal{S}^{\varphi}\Big(\widetilde{\eta}_i + \Delta\widetilde{\eta}/2,$$
$$\partial_{\tilde{r}}\chi_{i,j} + \partial_{\tilde{r}} d_{2i,j}\Delta\widetilde{\eta}/2, d_{3i,j}, \chi_{i,j} + d_{2i,j}\Delta\widetilde{\eta}/2, \varsigma_{i,j} + c_{2i,j}\Delta\widetilde{\eta}/2\Big), \tag{3.64}$$
$$c_{3i,j} = \mathcal{F}^{\varsigma}\Big(\widetilde{\eta}_i + \Delta\widetilde{\eta}/2, \varsigma_{i,j} + c_{2i,j}\Delta\widetilde{\eta}/2\Big) + \mathcal{S}^{\varsigma}\Big(\widetilde{\eta}_i + \Delta\widetilde{\eta}/2,$$
$$\partial_{\tilde{r}}\chi_{i,j} + \partial_{\tilde{r}} d_{2i,j}\Delta\widetilde{\eta}/2\Big), \tag{3.65}$$

$$e_{3i,j} = \mathcal{F}^{\chi}\Big(\widetilde{\eta}_i + \Delta\widetilde{\eta}/2, \partial_{\tilde{r}}^2\chi_{i,j} + \partial_{\tilde{r}} d_{2i,j}\Delta\widetilde{\eta}/2, \partial_{\tilde{r}}\chi_{i,j} + \partial_{\tilde{r}} d_{2i,j}\Delta\widetilde{\eta}/2, d_{3i,j},$$
$$\chi_{i,j} + d_{2i,j}\Delta\widetilde{\eta}/2\Big) + \mathcal{S}^{\chi}\Big(\widetilde{\eta}_i + \Delta\widetilde{\eta}/2, a_{3i,j}, \varphi_{i,j} + a_{2i,j}\Delta\widetilde{\eta}/2,$$
$$\partial_{\tilde{r}}\varsigma_{i,j} + \partial_{\tilde{r}} c_{2i,j}\Delta\widetilde{\eta}/2, \varsigma_{i,j} + c_{2i,j}\Delta\widetilde{\eta}/2\Big), \tag{3.66}$$

$$a_{4i,j} = a_{1i,j} + b_{3i,j}\Delta\widetilde{\eta}\,, \tag{3.67}$$
$$d_{4i,j} = d_{1i,j} + e_{3i,j}\Delta\widetilde{\eta}\,, \tag{3.68}$$
$$b_{4i,j} = \mathcal{F}^{\varphi}\Big(\widetilde{\eta}_i + \Delta\widetilde{\eta}, a_{4i,j}, \varphi_{i,j} + a_{3i,j}\Delta\widetilde{\eta}\Big) + \mathcal{S}^{\varphi}\Big(\widetilde{\eta}_i + \Delta\widetilde{\eta},$$
$$\partial_{\tilde{r}}\chi_{i,j} + \partial_{\tilde{r}} d_{3i,j}\Delta\widetilde{\eta}/2, d_{4i,j}, \chi_{i,j} + d_{3i,j}\Delta\widetilde{\eta}, \varsigma_{i,j} + c_{3i,j}\Delta\widetilde{\eta}\Big), \tag{3.69}$$
$$c_{4i,j} = \mathcal{F}^{\varsigma}\Big(\widetilde{\eta}_i + \Delta\widetilde{\eta}, \varsigma_{i,j} + c_{3i,j}\Delta\widetilde{\eta}\Big) + \mathcal{S}^{\varsigma}\Big(\widetilde{\eta}_i + \Delta\widetilde{\eta}, \partial_{\tilde{r}}\chi_{i,j} + \partial_{\tilde{r}} d_{3i,j}\Delta\widetilde{\eta}\Big), \tag{3.70}$$
$$e_{4i,j} = \mathcal{F}^{\chi}\Big(\widetilde{\eta}_i + \Delta\widetilde{\eta}, \partial_{\tilde{r}}^2\chi_{i,j} + \partial_{\tilde{r}}^2 d_{3i,j}\Delta\widetilde{\eta}, \partial_{\tilde{r}}\chi_{i,j} + \partial_{\tilde{r}} d_{3i,j}\Delta\widetilde{\eta}, d_{4i,j},$$
$$\chi_{i,j} + d_{3i,j}\Delta\widetilde{\eta}\Big) + \mathcal{S}^{\chi}\Big(\widetilde{\eta}_i + \Delta\widetilde{\eta}, a_{4i,j}, \varphi_{i,j} + a_{3i,j}\Delta\widetilde{\eta},$$
$$\partial_{\tilde{r}}\varsigma_{i,j} + \partial_{\tilde{r}} c_{3i,j}\Delta\widetilde{\eta}, \varsigma_{i,j} + c_{3i,j}\Delta\widetilde{\eta}\Big). \tag{3.71}$$

All we require now are the initial and boundary conditions.

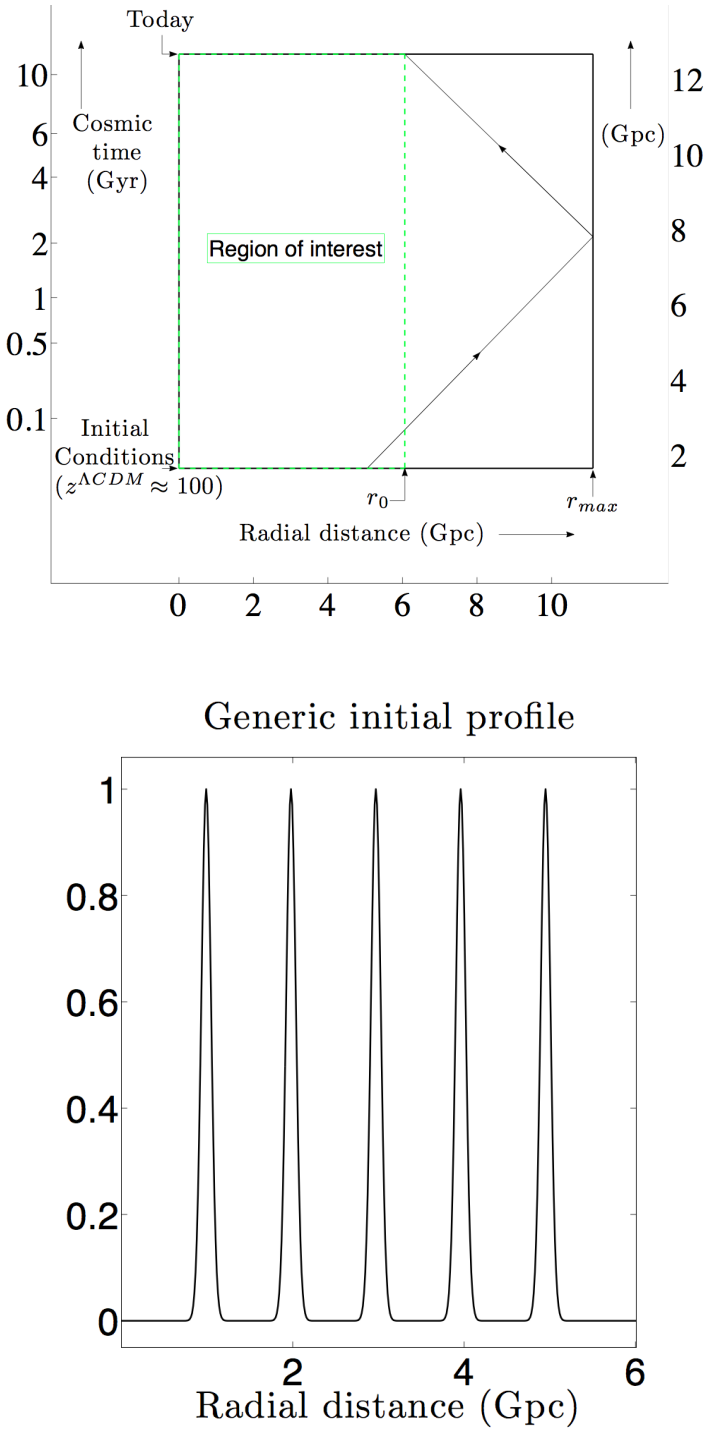

Figure 3.1: An illustration of the setup of our problem from a spacetime perspective (top), along with the generic form of the initial conditions used (bottom).

3.2.3 Initial and boundary conditions

In this work, we have used a generic set of initial conditions for each of the three master variables:

$$Q_{0,j} = \sum_{k=1}^{5} \exp\left(-\frac{(r_j - p_k)^2}{s^2}\right), \tag{3.72}$$

$$\dot{Q}_{0,j} = 0, \tag{3.73}$$

where $p_k \equiv 0.99 \times \{1, 2, 3, 4, 5\}$ Gpc is an array of five equally spaced points between $r_{\rm min}$ and our desired region of interest r_0, and $s \equiv 0.08$ Gpc sets the width of each pulse – see the right panel of Fig. 3.1. These conditions are set at $\widetilde{\eta}_{\rm min} = 0.42$ (corresponding to a time $t_{\rm min} = 0.018$ Gyr, or a redshift $z \approx 100$ in a fiducial ΛCDM cosmology).

Regularity conditions determine the variables in the neighbourhood of the origin according to the prescription of [159]. Near $r = 0$, we require (for all $\ell \geq 2$):

$$\chi \equiv r^{\ell+2}\hat{\chi}, \quad \varphi \equiv r^{\ell}\hat{\varphi}, \quad \varsigma \equiv r^{\ell+1}\hat{\varsigma}, \tag{3.74}$$

where the hatted variables are all polynomials of even power in r. Using

$$\hat{\chi} = \sum_{n=0}^{\infty} a_n r^{2n}, \quad \hat{\varphi} = \sum_{n=0}^{\infty} b_n r^{2n}, \quad \hat{\varsigma} = \sum_{n=0}^{\infty} c_n r^{2n}, \tag{3.75}$$

we find that

$$\chi_{,r} = \sum_{n=0}^{\infty} (\ell + 2n + 2) a_n r^{\ell+n+1}, \tag{3.76}$$

$$\chi_{,rr} = \sum_{n=0}^{\infty} (\ell + 2n + 2)(\ell + 2n + 1) a_n r^{\ell+n}, \tag{3.77}$$

$$\varphi_{,r} = \sum_{n=0}^{\infty} (\ell + 2n) b_n r^{\ell+2n-1}, \tag{3.78}$$

$$\varsigma_{,r} = \sum_{n=0}^{\infty} (\ell + 2n + 1) c_n r^{\ell+2n}, \tag{3.79}$$

which vanish at $r = 0 = r_{\rm min}$. Fixing the value of all variables to zero at the origin takes care of this requirement.

We require an additional boundary condition at the outer edge of the computational domain, $r_{\rm max}$. This boundary condition is necessarily artificial since we do not

compactify the spatial coordinate. To reduce its effect on the computational domain, we place it at a sufficient distance that it is causally disconnected from the physical measurements (at least for the continuum equations) − our region of interest. We can determine an appropriate distance by tracing null geodesics inward from the outer boundary. Using the background LTB line element, radial null geodesics are given by

$$\frac{d\widetilde{\eta}}{d\widetilde{r}} = \widetilde{X}\,, \tag{3.80}$$

where our characteristics approach 45° at late times; at earlier times our characteristics propagate at $\approx 55°$ on average. An appropriate value for $\widetilde{r}_{\max}$ which is sufficiently removed from the measurement domain is

$$\tilde{r}_{\max} = \tilde{r}_0 + \frac{1}{2}\int_{\widetilde{\eta}i}^{\widetilde{\eta}_0} d\widetilde{\eta}\,\widetilde{X}^{-1}\,, \tag{3.81}$$

where r_0 is the outer boundary of the domain in which we would like to make physical measurements between times $\widetilde{\eta}_0$ and $\widetilde{\eta}_i$. Since we are working in a single spatial dimension, this grid extension to remove outer boundary effects is not overly costly in terms of memory or computation time. Given that the spacetime in our MV model is effectively homogeneous above $r = 5$ Gpc, we choose a conservative region of interest of 6 Gpc.

3.2.4 Summary of code setup

A generic code applying to all the cases above is setup to read in the following inputs (specified in a parameter file):

- Parameters of the background model, if any (e.g. $H_0, \Omega_m^{\text{in}}$, etc.).
- Spatial extent of the grid, i.e. $r_{\min}$ and $r_{\max}$.
- Starting time of the simulation, i.e. $\widetilde{\eta}_{\text{init}} = \widetilde{\eta}(t_{\text{init}})$.
- Position of first peak of the five Gaussian I.C.'s.
- Width of each Gaussian, s, and it's amplitude.

- Angular momentum quantum number ℓ of the simulation.
- Value for the spatial resolution improvement factor (i.e. n).
- Value for the temporal resolution improvement factor (i.e. α).

In order to deal with outputs that are of manageable size (such as to avoid excessive memory usage), we may choose the reference grid to be the one with the lowest spatial resolution, i.e. $n_{ref} = 1$. In addition, we also skip the writing to file of a specified number of time steps. Note that changing n and or α would not affect the dimensions of the resulting spacetime data that is outputted.

3.3 Convergence tests

To establish the correctness of the discretization, we carry out a standard convergence test. We verify the 2nd-order convergence empirically by carrying out a series of runs of the same initial data at successively doubled resolution, corresponding to $\alpha = n$, $\alpha = 2n$, and $\alpha = 4n$ in Eqs. (3.30) and (3.31). The rate of convergence for a variable Q is given by

$$\beta_Q^{(n)} = \log_2 \left| \frac{\|Q^{(n)}\| - \|Q^{(2n)}\|}{\|Q^{(2n)}\| - \|Q^{(4n)}\|} \right| , \tag{3.82}$$

where $\|Q^{(n)}\|$ is the L_2-norm on the fixed-resolution grid,

$$\|Q^{(n)}\| \equiv \frac{1}{N} \left(\sum_{j=1}^{N} (Q_{i,j}^{(n)})^2 \right)^{1/2} , \tag{3.83}$$

with N ($< N_{\tilde{r}}$) the number of spatial grid-points stored for analysis within the range $0 \leq \tilde{r} \leq \tilde{r}_0$. We used the following dimensionless measure for quantifying how well our constraints are being satisfied:

$$\mathcal{C}_Q^{(n)}(\tilde{\eta}) \equiv \frac{||C_Q^n(\tilde{\eta})||_2}{||\dot{Q}^n(\tilde{\eta})||_2} , \tag{3.84}$$

where $Q \, \epsilon \, \{\Delta, w, \tilde{v}\}$, C_Q is one of (3.19)$-$(3.21), and we estimate $\dot{Q}$ via a centered difference, i.e.

$$\frac{a_\perp^{\rm in}(\tilde{\eta})}{H_0} \dot{Q}^n(\tilde{\eta}) = \left[\frac{Q^n(\tilde{\eta} + \Delta\tilde{\eta}) - Q^n(\tilde{\eta} - \Delta\tilde{\eta})}{2\Delta\tilde{\eta}} \right] . \tag{3.85}$$

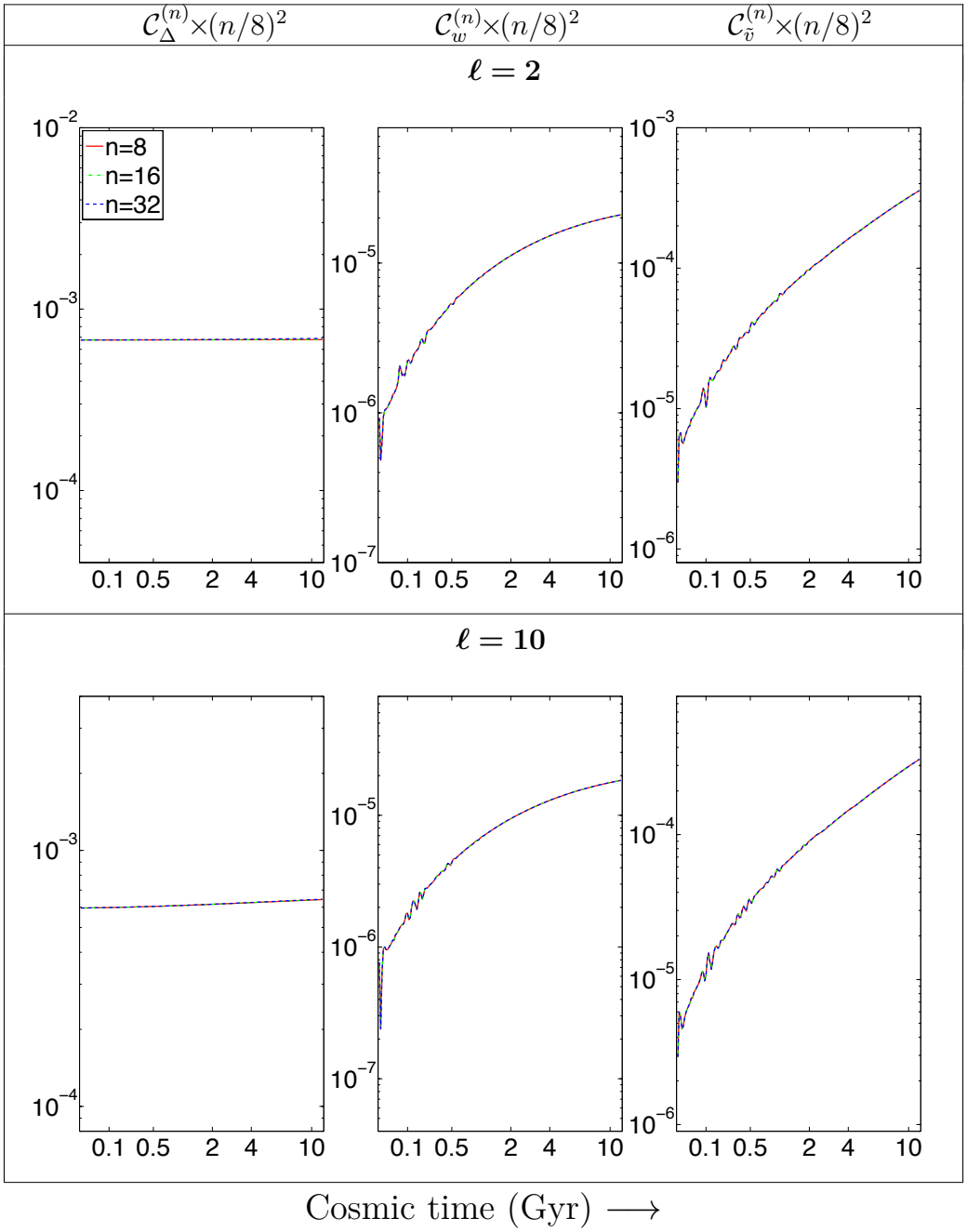

Figure 3.2: Performance of our measure of error $\mathcal{C}^{(n)}$ over time for each constraint equation, in the case of an initialised φ, for $\ell = 2$ and $\ell = 10$. Starting from a reference resolution of $n = 8$, we include curves of double ($n = 16$) and four times ($n = 32$) the resolution, multiplying each by a factor of 4 and 16, respectively. Where the curves line up indicates exact 2nd-order convergence.

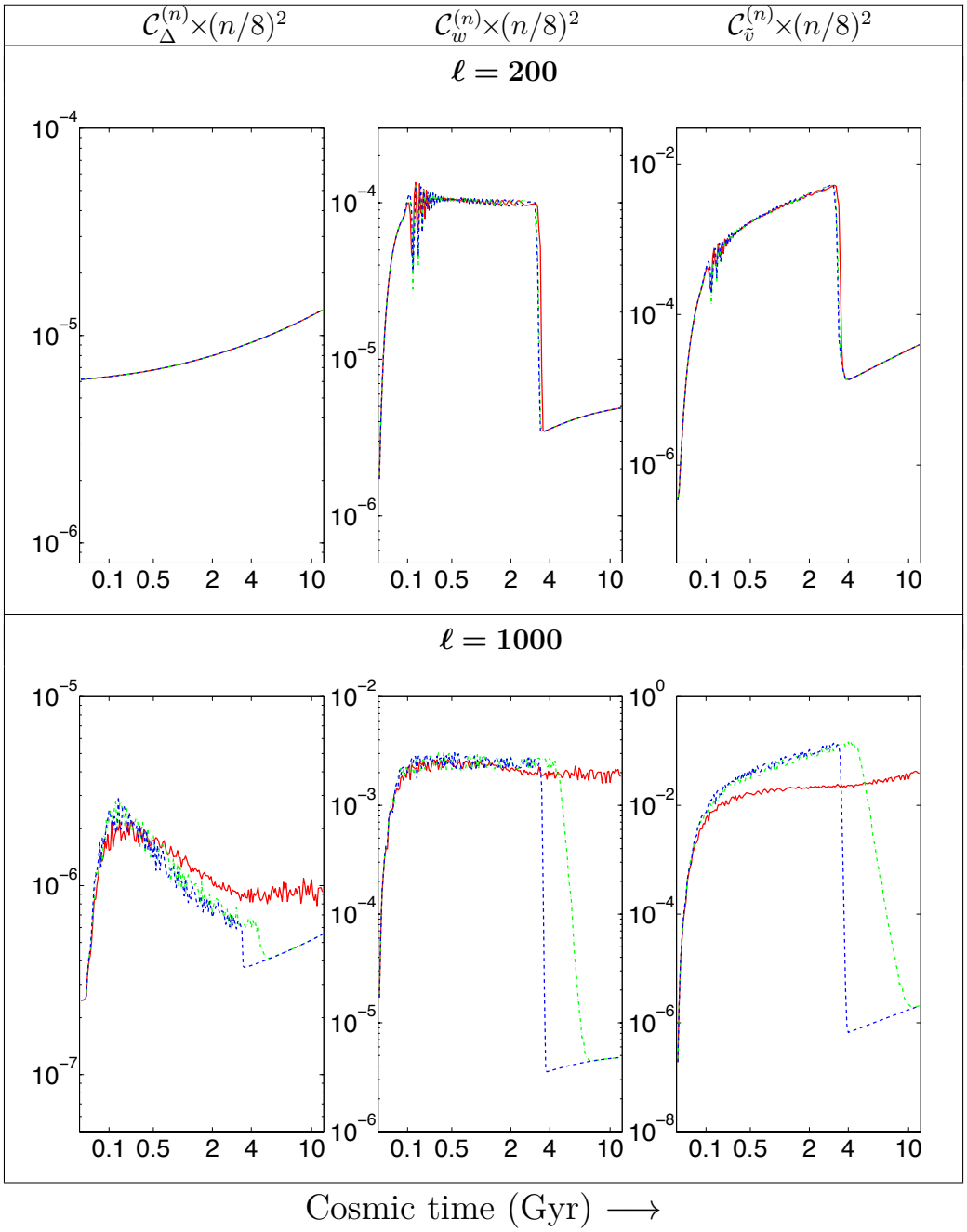

Figure 3.3: Same as Fig. 3.2, but for $\ell = 200$ and $\ell = 1000$.

For all of our evolution variables and constraints, we observe the expected 2nd-order convergence rate ($\beta = 2$). We illustrate this in Fig.'s 3.2 and 3.2, which show how well the constraint equations perform for various multipole moments in the case of an initial φ. Using a reference resolution of $n = 8$, we include curves of double ($n = 16$) and four times ($n = 32$) the resolution, multiplying each by a factor of 4 and 16, respectively. Where the curves line up implies $\beta = 2$. We have used a base resolution of $H_0^{-1}\Delta\tilde{r} = 1.375$ Gpc throughout, typically with $4 \leq \alpha \leq 32$.

3.4 Conclusion

We have developed a numerical code that solves the set of coupled partial differential equations (PDE's) describing the evolution of polar ($\ell > 1$) perturbations in a large void modelled by the LTB metric. The code, written in Fortran, makes use of a standard 4th-order Runge-Kutta time integrator applied to each spatial grid-point via the method of lines. The code is shown to be stable, and converges at the expected (2nd-order) rate. This gives us confidence in using it for modelling a variety of other interesting cosmological/astrophysical situations, such as relativistic corrections to structure formation and the weak lensing of gravitational waves by dark matter halos, to name a few.

Substantial speed-up in the run-time of the code may be achieved in an updated version which incorporates a non-uniform grid, as well as parallel (MPI/OpenMP) capability. This and other enhancements to the code will be carried out in future versions.

In the next chapter, we explore the full set of solutions our code yields for the same void model used to for convergence testing.

CHAPTER 4

Evolution of structure in a large void

4.1 Introduction

In Chapter 3 we tested our numerical code that solves a system of coupled PDE's that describe the evolution of first-order linear perturbations in a spherically symmetric dust spacetime containing a local Hubble-scale suppression in the matter density. Here we explore solutions to the latter for a variety of initial conditions and scales of interest.

Let us emphasize though that we are not trying to develop a full analysis of realistic structure formation in a LTB Universe. Rather, we would like to demonstrate that the code we developed can integrate the perturbation equations, and therefore allows us to study a few remarkable features of the evolution of perturbations in a large cosmic void.

For the sake of illustration, we concentrate on the evolution of the perturbation variables for the spherical modes $\ell = 2$ and $\ell = 10$, in three distinct cases: we initialise the profile of any one of φ, ς and χ according to (3.72) while setting the others to zero, and apply (3.73) to all variables (except ς since it satisfies a 1st-order PDE). In other

words, we consider

- Case 1 : $\varphi(t_i, r) = \sum_{k=1}^{5} \exp\Big[-\Big(\frac{r-p_k}{s}\Big)^2\Big]$, $\varsigma(t_i, r) = 0 = \chi(t_i, r)$, (4.1)
- Case 2 : $\varsigma(t_i, r) = \sum_{k=1}^{5} \exp\Big[-\Big(\frac{r-p_k)}{s}\Big)^2\Big]$, $\varphi(t_i, r) = 0 = \chi(t_i, r)$, (4.2)
- Case 3 : $\chi(t_i, r) = \sum_{k=1}^{5} \exp\Big[-\Big(\frac{r-p_k}{s}\Big)^2\Big]$, $\varphi(t_i, r) = 0 = \varsigma(t_i, r)$, (4.3)

in which $\dot{\varphi}_i = 0 = \dot{\chi}_i$ throughout, $p_k \equiv 0.99 \times \{1, 2, 3, 4, 5\}$ Gpc and $s = 0.08$ Gpc.

4.2 Results

4.2.1 Evolution of the full system of perturbations

The evolution of each of the variables is presented in Fig.'s 4.1, 4.2 and 4.3 for each of the 3 cases, for both the $\ell = 2$ and $\ell = 10$ runs. The resolutions used in all of the plots are typically in the range $32 \leq n \leq 128$, $4 \leq \alpha \leq 32$. Note that the colour-scheme for each 2D plot has been chosen such that red indicates positive amplitude, blue negative, and green zero. The actual minimum and maximum values are indicated in square brackets above the top left corner of each plot.

Case 1: In these cases, we initialise φ, and set $\varsigma = \chi = 0$ initially. We clearly see the "bleeding" of the modes due to the coupling.

On the 2D plot, Fig. 4.1, χ behaves like a propagating degree of freedom, evolving along the characteristics of the spacetime, and radiating energy away from each pulse. The behaviour of ς is more difficult to qualitatively describe because it is a mixture of frame dragging and GW degrees of freedom – the combination of non-propagating decay with some radiation can be seen in the figures. It is proportional to the trace-free part of the magnetic Weyl curvature (2.203), and thus represents a true relativistic degree of freedom. Then, φ follows a standard evolution throughout the spacetime: staying constant around the EdS region, while decaying faster deep inside the void.

The top panel of Fig. 4.4 presents the profile of φ initially and today for these cases, as well as its time evolution along selected radii. As expected, φ remains constant in the outer, quasi-FLRW regions of the void, given that it essentially satisfies the Bardeen equation there. Deep inside the void, φ decreases for the most part as the usual Bardeen potential would in an open FLRW dust model, but there is evidence of influence from ς and χ at least at the sub-percent-level, as can be seen by the amplitudes of the latter in the middle and bottom panels of Fig. 4.4; see also Section 4.2.2 for a discussion on the importance of the couplings.

We show the spacetime configuration of Δ in Fig. 4.7: its growth appears to follow the peaks where φ is concentrated, suggesting that the tiny χ and ς generated by the dynamics have little impact on the profile of density perturbations. Also included in Fig. 4.7 is the resulting radial peculiar velocity w and the trace-free part of the electric Weyl curvature.

Case 2: Here, we initialise ς, and set $\varphi = \chi = 0$ initially.

From the middle panels of Fig. 4.2 we see that ς decays very quickly − in fact, roughly proportional to $a_{\parallel}^{-2}$ − along the peaks from where it is initially located, while sourcing φ and χ. As expected, χ is very well described as a propagating degree of freedom, but one also sees that the sourced φ has a propagating component that follows the characteristics of the background spacetime and escapes the void.

The middle panel of Fig. 4.5 presents the profile of ς initially and today for these cases, including the time evolution along selected radii. It's clear that ς decays, for the most part, approximately as $a_{\parallel}^{-2}$. (In the FLRW limit this would be a pure vector mode with this exact decay rate.) The greater decay in ς seen in the central regions of the void can be attributed to the faster expansion rate there. The top and bottom panels of Fig. 4.5 show the profiles for the other variables, φ and χ.

We also show the spacetime configuration of Δ in Fig. 4.8. Remarkably, the

density contrast generated initially by the presence of the perturbation ς also decays very rapidly at the peak locations, except deep inside the void (first few peaks) where it bounces back at later times (much more at small angular scales than at large ones). This is associated with the potential φ deepening in this region at the same time: the decay of ς into φ is associated with a growth of structure deep within the void.

Case 3: Here, we initialise χ, and set $\varphi = \varsigma = 0$ initially.

According to Fig. 4.3, χ and the generated ς propagate to the outskirts of the void along the characteristics of the background, resulting in the localised generation of the potential φ, and the associated growth of density perturbations, as is shown in Fig. 4.9.

The bottom panel of Fig. 4.6 presents the profile of χ initially and today for these cases, as well as the time evolution along selected radii, while the profiles for the other variables, φ and ς, are shown in the top and middle panels.

All of these cases demonstrate that φ, χ and ς are much more difficult to interpret than on an FLRW background. As emphasised in [154], they are mixtures of scalar, vector and tensor modes and therefore their coupling is an essential ingredient of first order perturbation theory around an LTB background: in principle, they cannot be treated as separate, independent modes that describe different physical aspects of perturbations.

In the next subsection, we consider the case in which φ is decoupled from ς and χ *by hand* − as done before in various ways to simplify the analysis [156, 157, 169]. We then compare the subsequent evolution φ and Δ to the case in which the full coupling is included.

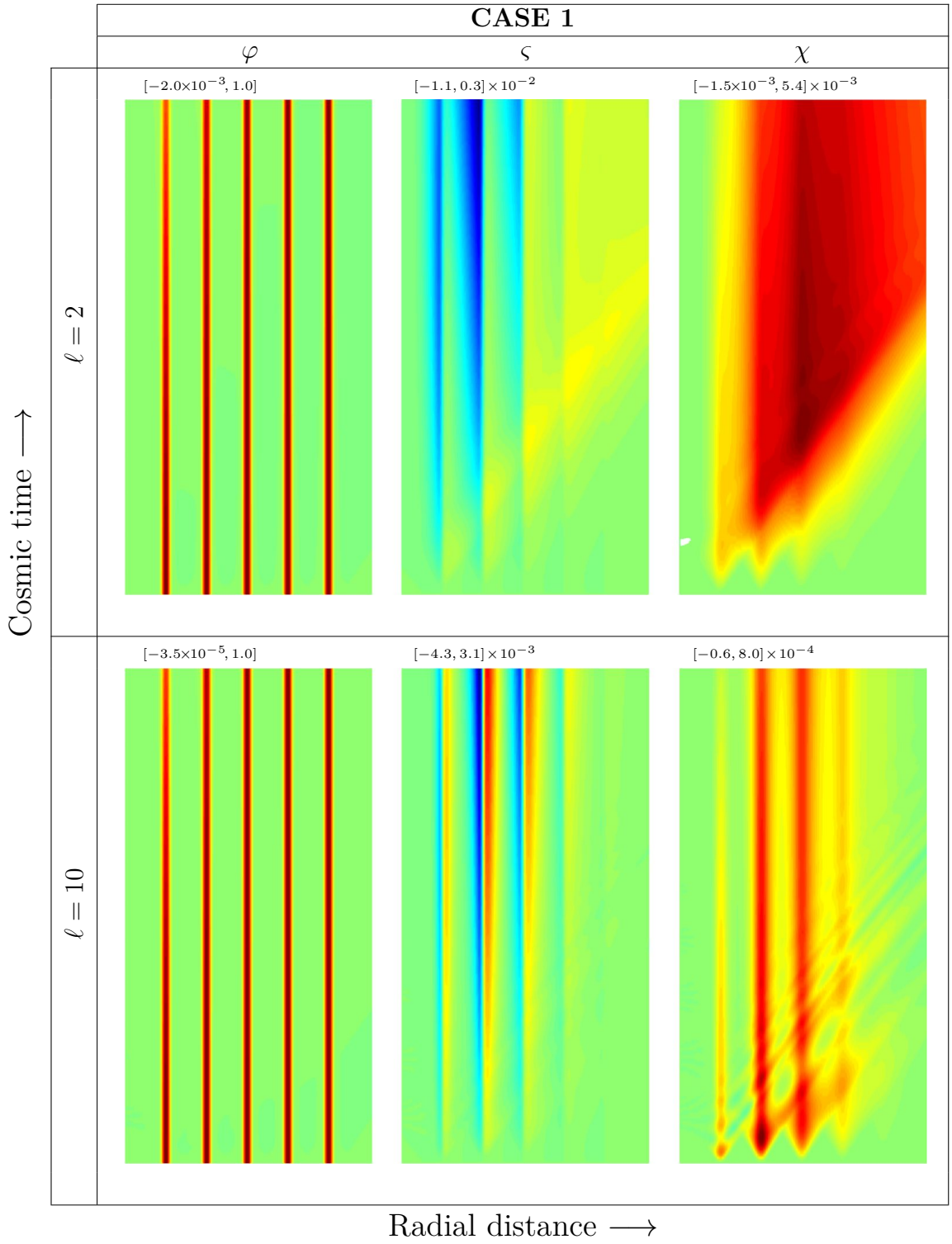

Figure 4.1: Spacetime evolution of each of the master variables for Case 1. Notice how an initial φ excites both ς and χ to about the sub-percent level. The propagating modes resulting from χ is visible in ς, or alternatively the trace-free part of the magnetic Weyl tensor $\delta\overline{H}_{(TF)}$ (2.203), thus clearly showing relativistic degrees of freedom at work.

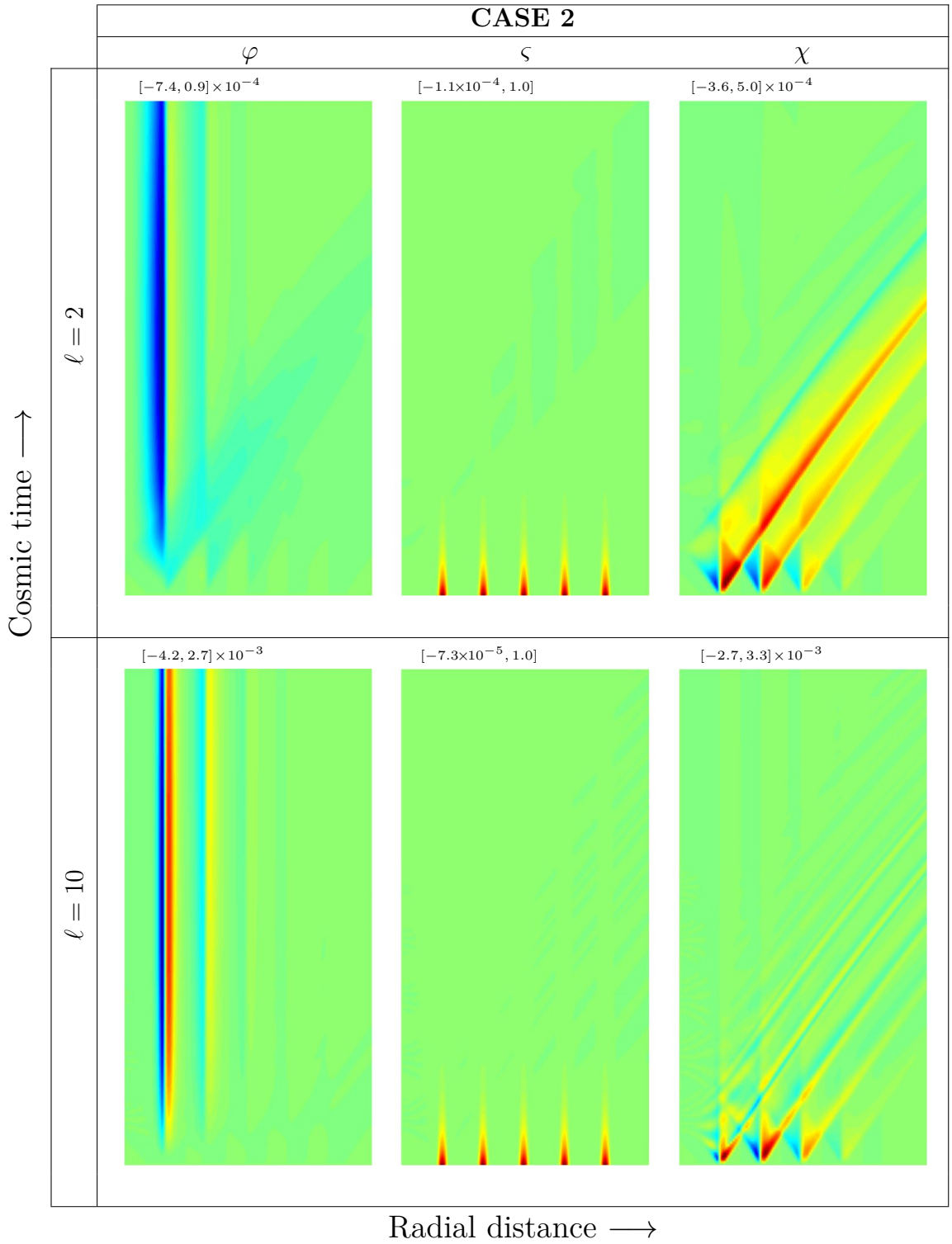

Figure 4.2: Spacetime evolution of each of the master variables for Case 2. While an initial ς decays away quickly due to the Hubble friction, it still manages to excite the other two variables, albeit to a very low level (below sub-percent).

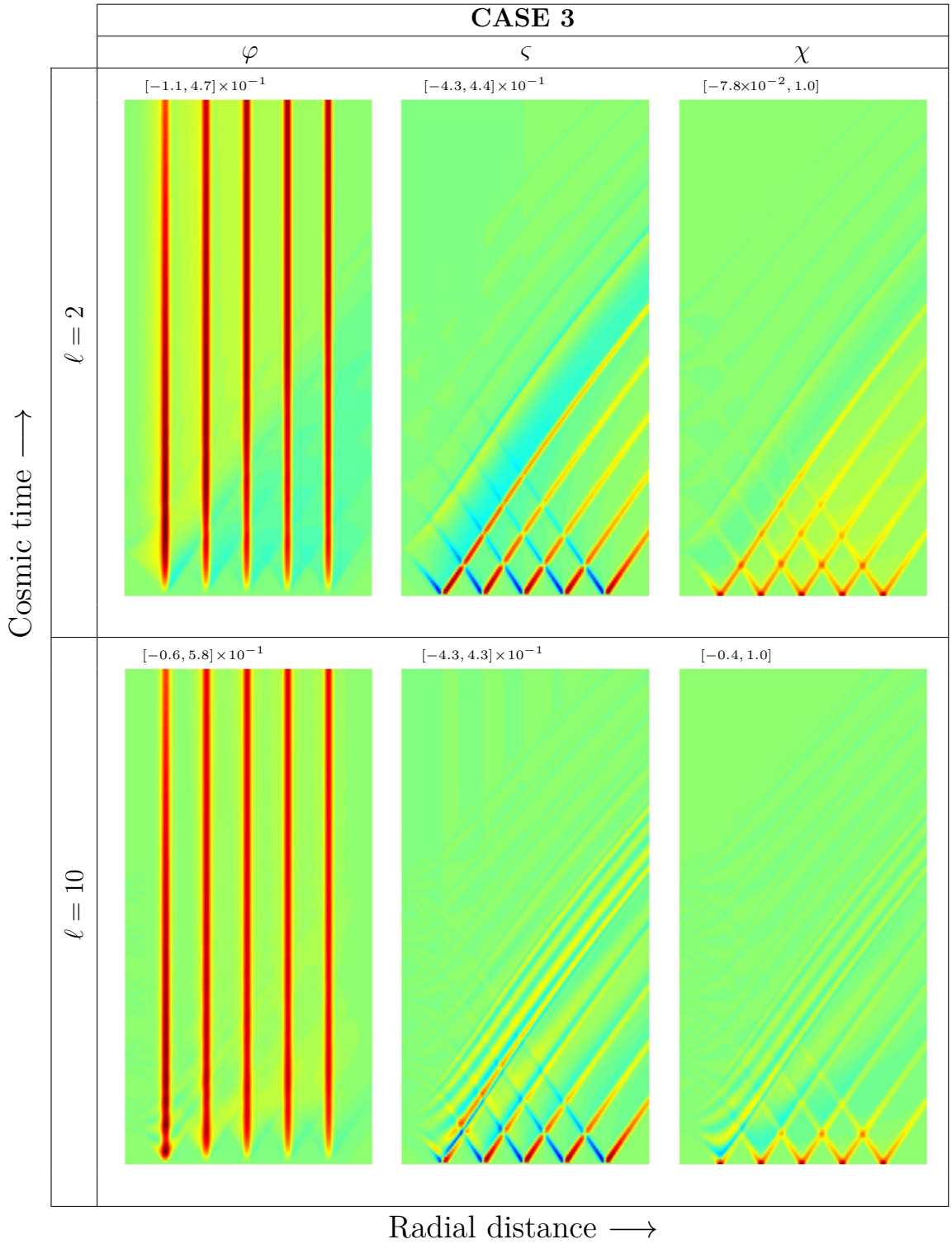

Figure 4.3: Spacetime evolution of each of the master variables for Case 3. an initial χ generated inside a void excites a relatively significant amount of φ and ς. The presence of propagating modes is more apparent in all the variables here.

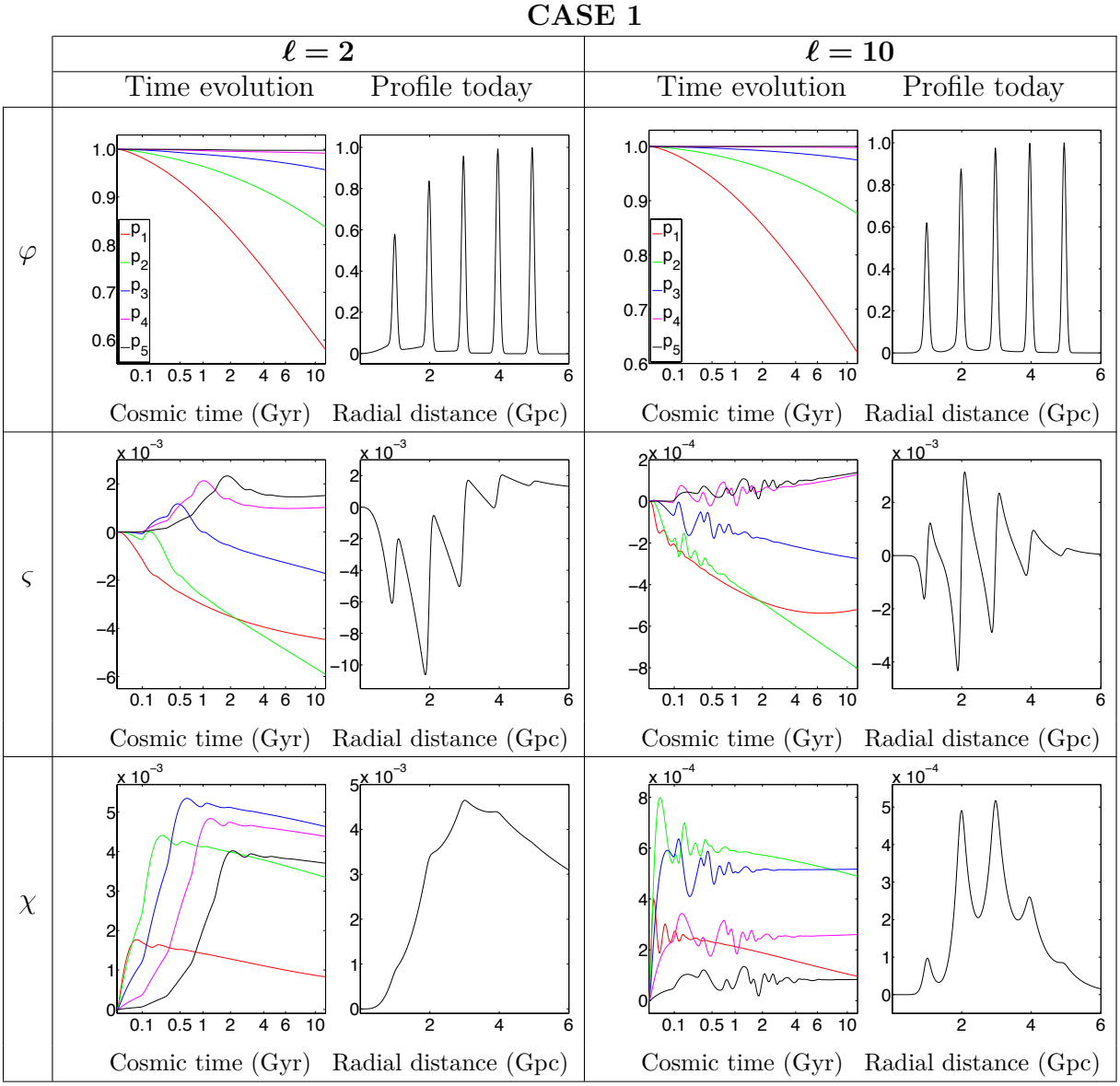

Figure 4.4: Temporal and spatial slices through the spacetime evolution observed in Fig. 4.1. The variable φ is largely unaffected on the outskirts of the void in which the spacetime is almost EdS. Since ς and χ are relatively sub-percent in amplitude, on each radial shell φ more or less behaves as expected in an open, dust-dominated FLRW model, i.e. decays with time. Propagating features are nevertheless evident (via the boxes showing the time dependence) in both ς and χ, especially on smaller scales ($\ell = 10$).

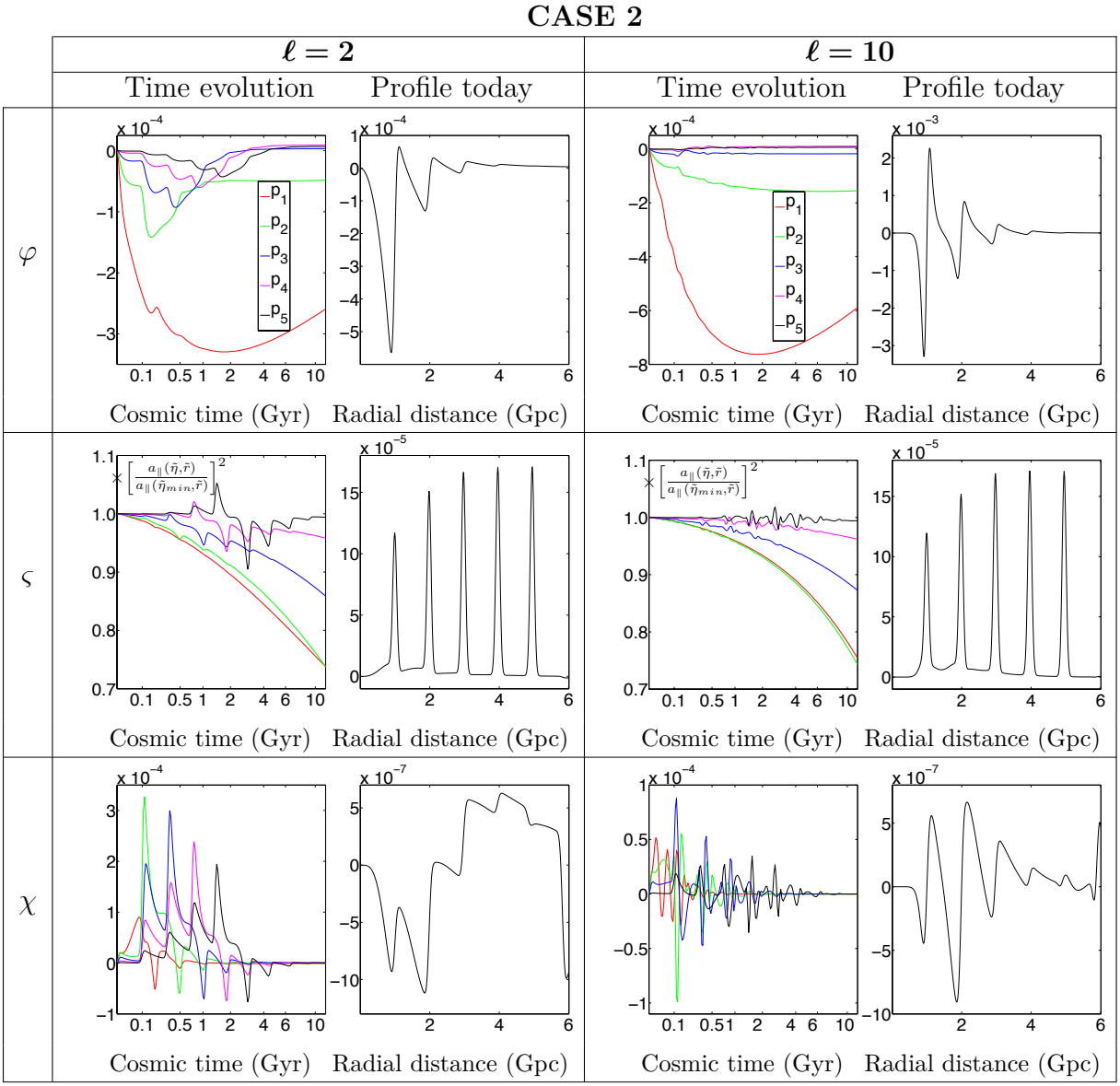

Figure 4.5: Temporal and spatial slices through the spacetime evolution observed in Fig. 4.1. The variable ς decays roughly $\propto a_{\parallel}^{-2}$ in the quasi-FLRW regions, but decreases more quickly deep inside the void due to the faster expansion rate there. Compared to the initial amplitude of ς, φ and χ remains sub-percent in magnitude and both shows propagating features.

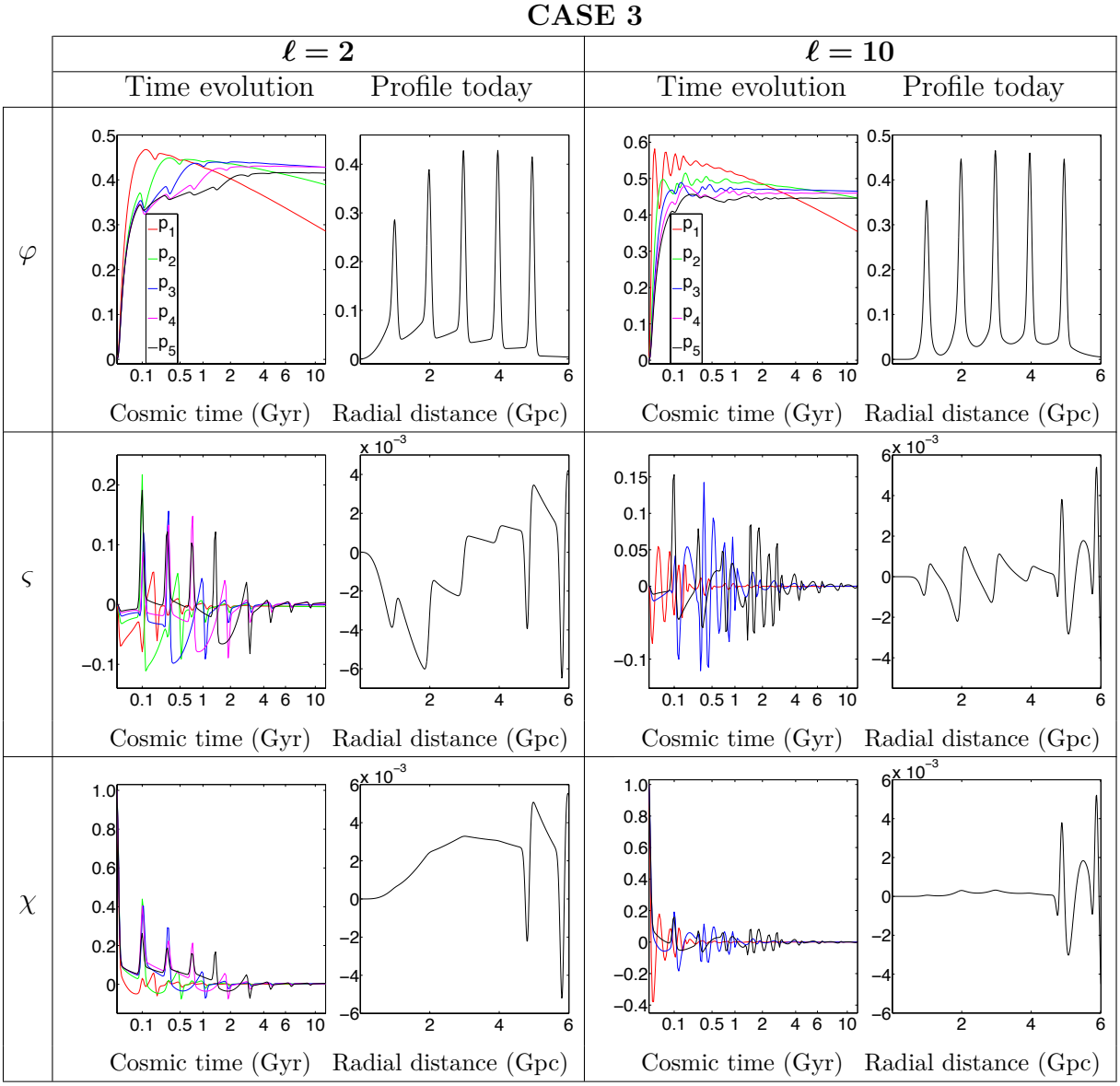

Figure 4.6: Temporal and spatial slices through the spacetime evolution observed in Fig. 4.3. Here it is clear that the evolution of χ is dominated by a propagating mode. It is interesting to note that the level of φ generated is of a similar order of magnitude than the initial χ, and again showing a slower ($\sim 25\%$) growth rate inside the void compared to the outskirts. The variable ς is also produced to a significant proportion early on, but nevertheless decays quickly with time. Both φ and ς show strong propagating features in this case.

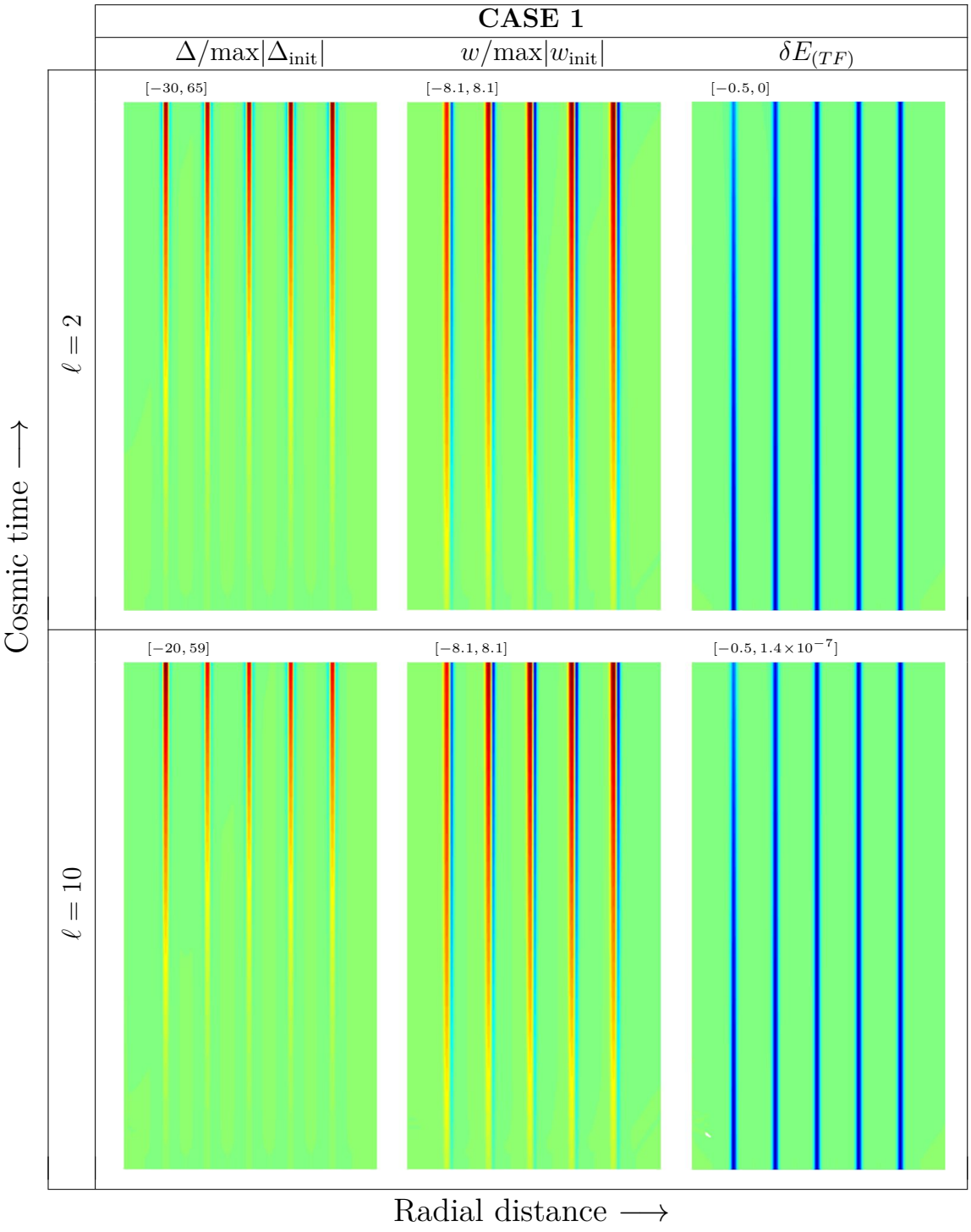

Figure 4.7: Spacetime evolution of selected quantities derived from those presented in Fig. 4.1 for Case 1. We show: Δ and w normalised to their maximum values (along the radial dimension) at $t_{\rm init}$, as well as $\delta E_{(TF)}$, which describes the sum of φ and χ. Note that, due to our choice of $\max|\varphi_{\rm init}(r)| = 1$, Δ here eventually becomes less than -1; while Δ does not reduce to the usual density contrast in the FLRW limit – it is sourced by propagating degrees of freedom – an appropriate rescaling of the initial amplitudes (fluctuations in the standard Newtonian potential Φ are $\sim 10^{-4}$ at $z = 100$) is sufficient to avoid any issues regarding the physical interpretation of Δ as a density contrast.

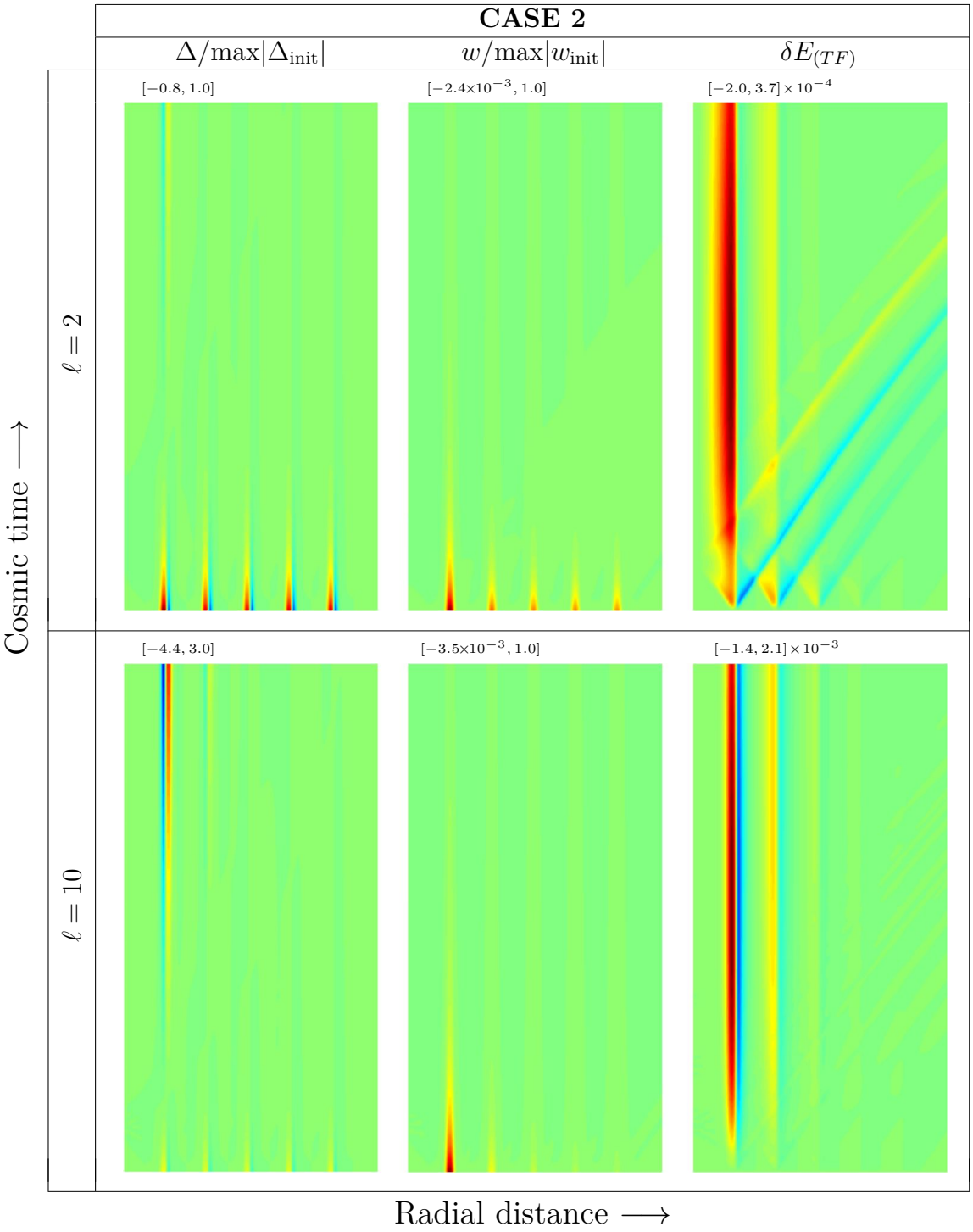

Figure 4.8: Spacetime evolution of selected quantities derived from those presented in Fig. 4.2 for Case 2. We show: Δ and w normalised to their maximum values (along the radial dimension) at $t_{\rm init}$, as well as $\delta E_{(TF)}$, which describes the sum of φ and χ. Note the decaying behaviour in Δ and w, due to the latter tracing the evolution of ς. The propagating degrees of freedom seen in $\delta E_{(TF)}$ is largely due to χ.

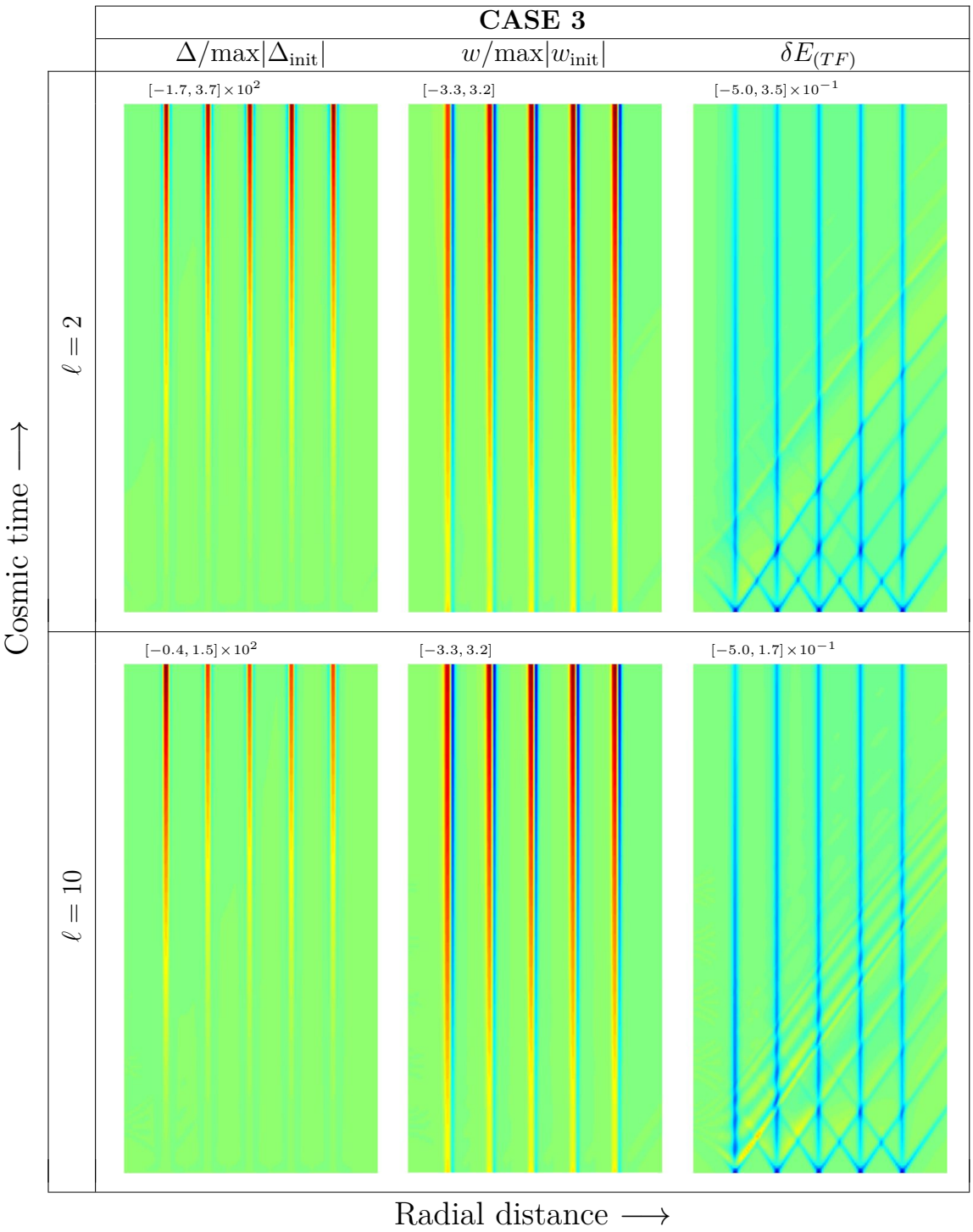

Figure 4.9: Spacetime evolution of selected quantities derived from those presented in Fig. 4.3 for Case 3. We show: Δ and w normalised to their maximum values (along the radial dimension) at $t_{\rm init}$, as well as $\delta E_{(TF)}$, which describes the sum of φ and χ. Δ and w behave more or less like that seen in Case 1, since χ generates a φ of similar order of magnitude. The propagating degrees of freedom seen in $\delta E_{(TF)}$, caused by χ, is clear, as well as the contribution from φ.

4.2.2 How important is the coupling?

In this section, we quantify the errors induced when assuming that the coupling of φ to χ and ς is negligible by considering models which initialise φ only. We compare these to cases where Eqs. (2.149), (2.150) and (2.151) are solved retaining terms with no coupling between φ and $\{\chi, \varsigma\}$, that is, by solving the reduced system:

$$\ddot{\varphi} = -4H_\perp\dot{\varphi} + \left[\frac{2\kappa}{a_\perp^2} - \Lambda\right]\varphi \tag{4.4}$$

$$\begin{aligned} 8\pi G\rho_m\Delta = & -X^{-2}\varphi'' + X^{-2}\left[\frac{a_\parallel{}'}{a_\parallel} + \frac{\kappa r + \frac{1}{2}r^2\kappa'}{1-\kappa r^2} - \ -2\frac{a_\parallel}{a_\perp r}\right]\varphi' + \Theta\dot{\varphi} \\ & + \left[3H_\perp\Big(\sigma + H_\perp\Big) - \Big(1 + 2\frac{a_\perp}{a_\parallel}\Big)\frac{\kappa}{a_\perp^2} - \ \frac{r\kappa'}{a_\perp a_\parallel} + \frac{\ell(\ell+1)}{a_\perp^2 r^2}\right]\varphi. \end{aligned} \tag{4.5}$$

As it turns out, the full coupling is seen to be important for the dynamics of φ, and also for the behaviour of Δ on small angular scales (large l) − see Figs. 4.10 and 4.11.

From Fig.'s 4.10 and 4.11 we see that deep inside the void (first peak) the differences in φ are already of order 8% for $\ell = 2$ and 15% for $\ell = 10$, respectively. This could have a major impact down the central observer's past light-cone and therefore such couplings could be very important in determining observables accurately. On the other hand, Δ is well approximated by the uncoupled dynamics for large scales, with errors below 1% for $\ell = 2$; but, already for $\ell = 10$, we see errors of order 7 to 8%.

Including a few more angular scales, all the way up to $\ell = 1000$, as well as intermediate snapshots in time, an overall picture of the error in neglecting the couplings is captured in Fig.'s 4.12 and 4.13. Regardless of where (in radial distance) we choose to observe φ and Δ, as we go to smaller scales their expected errors approach some equivalent maximum value − equivalent due to their relation via the analogue of the Poisson equation (2.146) which has $\Delta \propto \ell^2\varphi$ on small scales (large ℓ).

As for observable quantities such as the two-point correlation function of the galaxy distribution, we should expect corrections of a few percent in the amplitude of the BAO bump when including the full coupling (because this quantity is of order the square of Δ) − see [169] for the particular case in which the coupling is neglected.

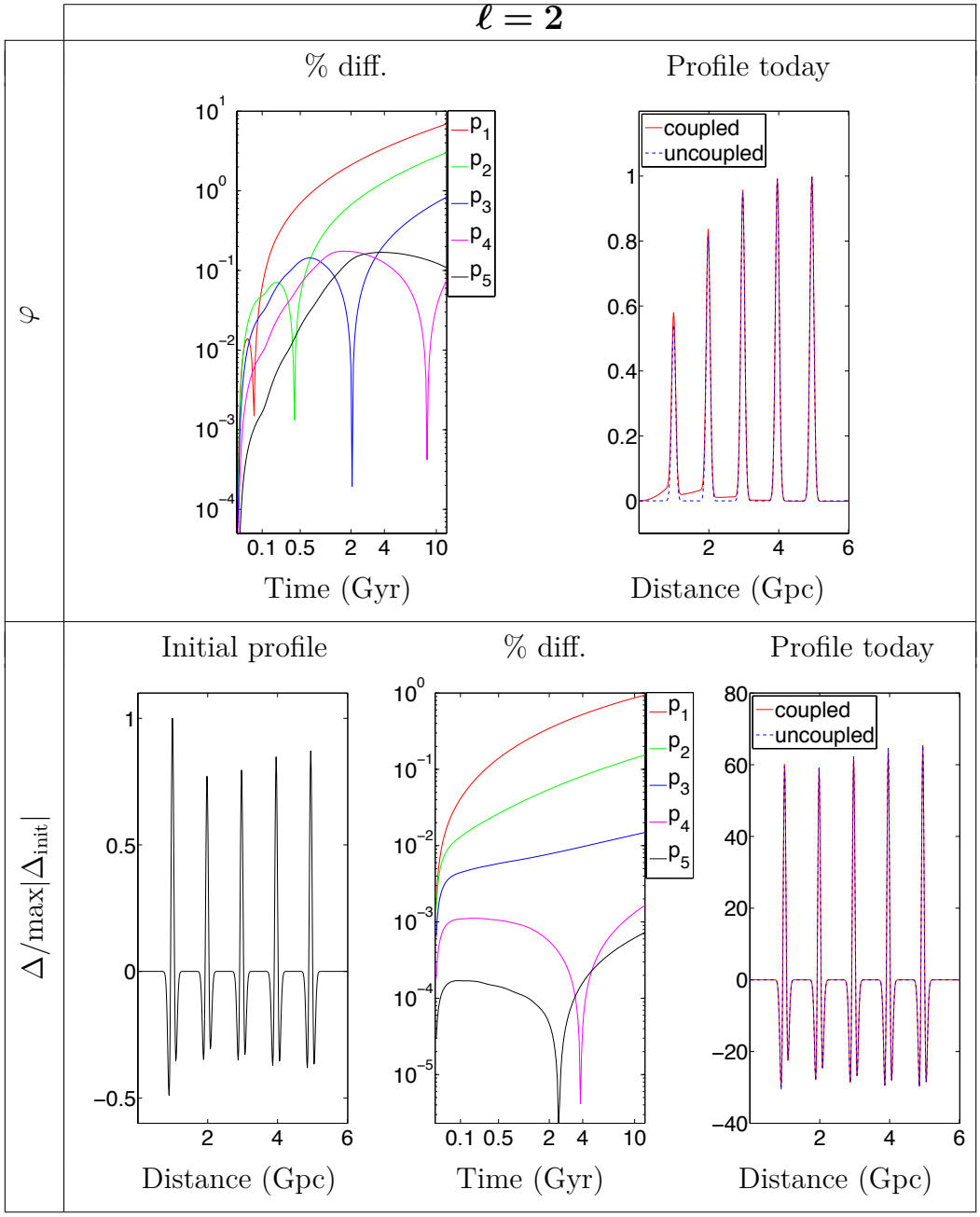

Figure 4.10: Comparison of coupled to uncoupled runs for Case 1. On the largest scales ($\ell = 2$), and deep within the void (p_1), φ is enhanced by $\sim 10\%$ when the coupling is present, while Δ is enhanced by $\sim 1\%$. As we approach the outskirts of the void, the differences are sub-percent, as expected.

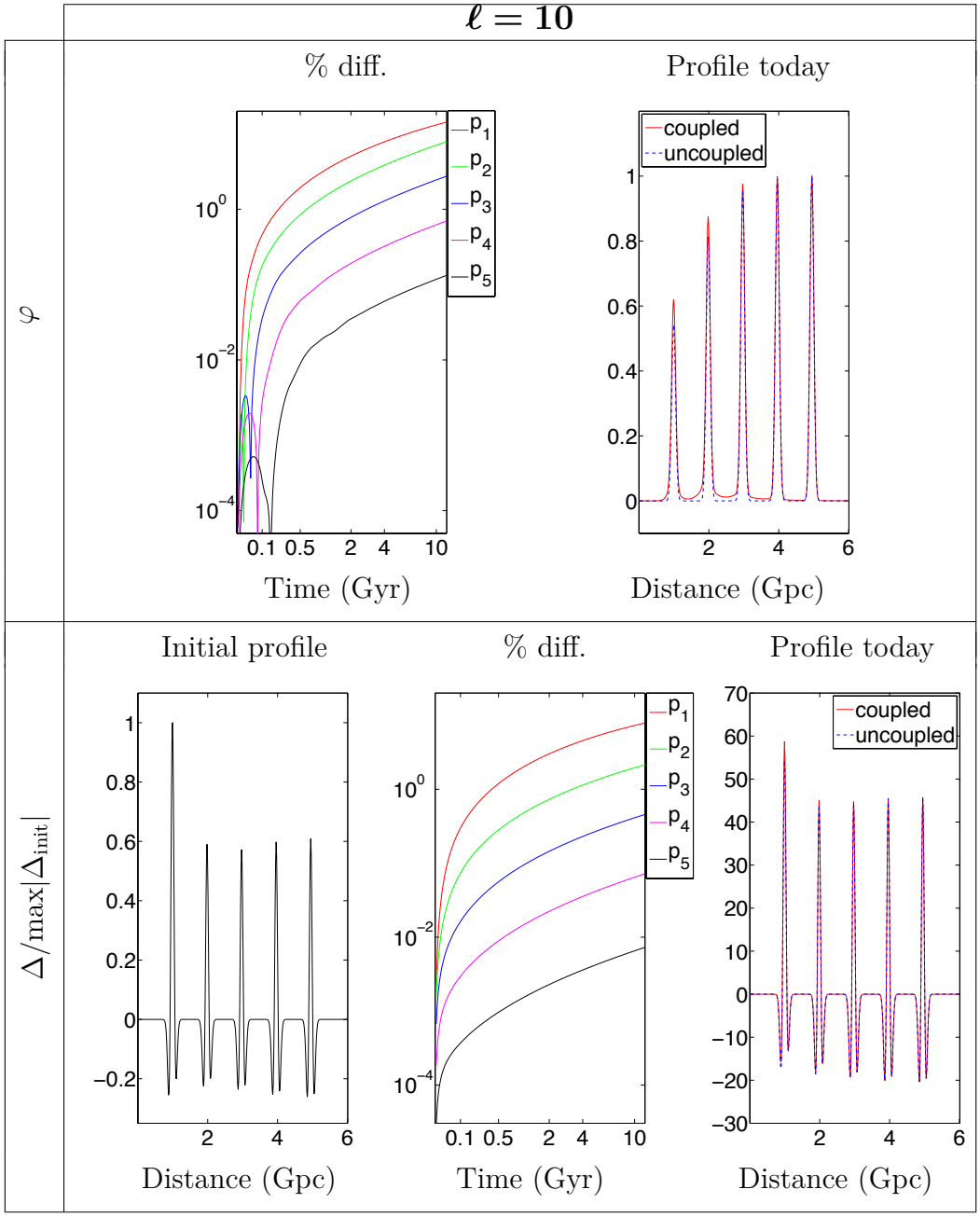

Figure 4.11: Comparison of coupled to uncoupled runs for Case 1. On smaller scales ($\ell = 2$), and deep within the void (p_1), φ is enhanced by a few tens of percent when the coupling is present, while Δ is enhanced by a few percent. As we approach the outskirts of the void, the differences remain sub-percent, as expected.

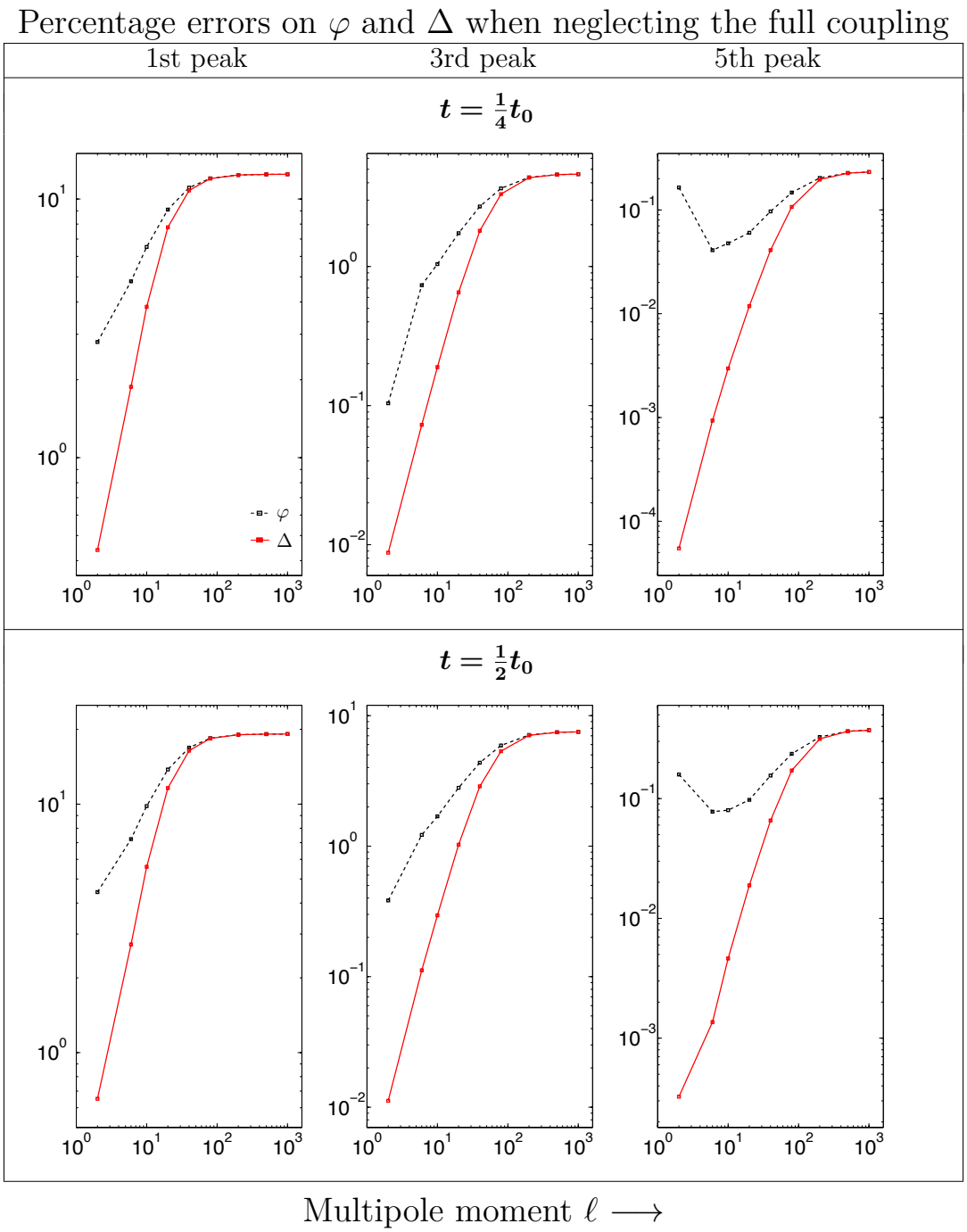

Figure 4.12: Percentage errors acquired on φ (black, dashed) and Δ (red, solid) from neglecting the coupling of φ to ς and χ, as a function of ℓ at selected times and radii. We see in general that the errors increase with time, as well as with increasing ℓ, and are larger deep within the void than towards the outskirts, as expected. The errors on φ and Δ converge on smaller scales since the term in Eq. (2.146) proportional to $\ell(\ell+1)\varphi$ dominates.

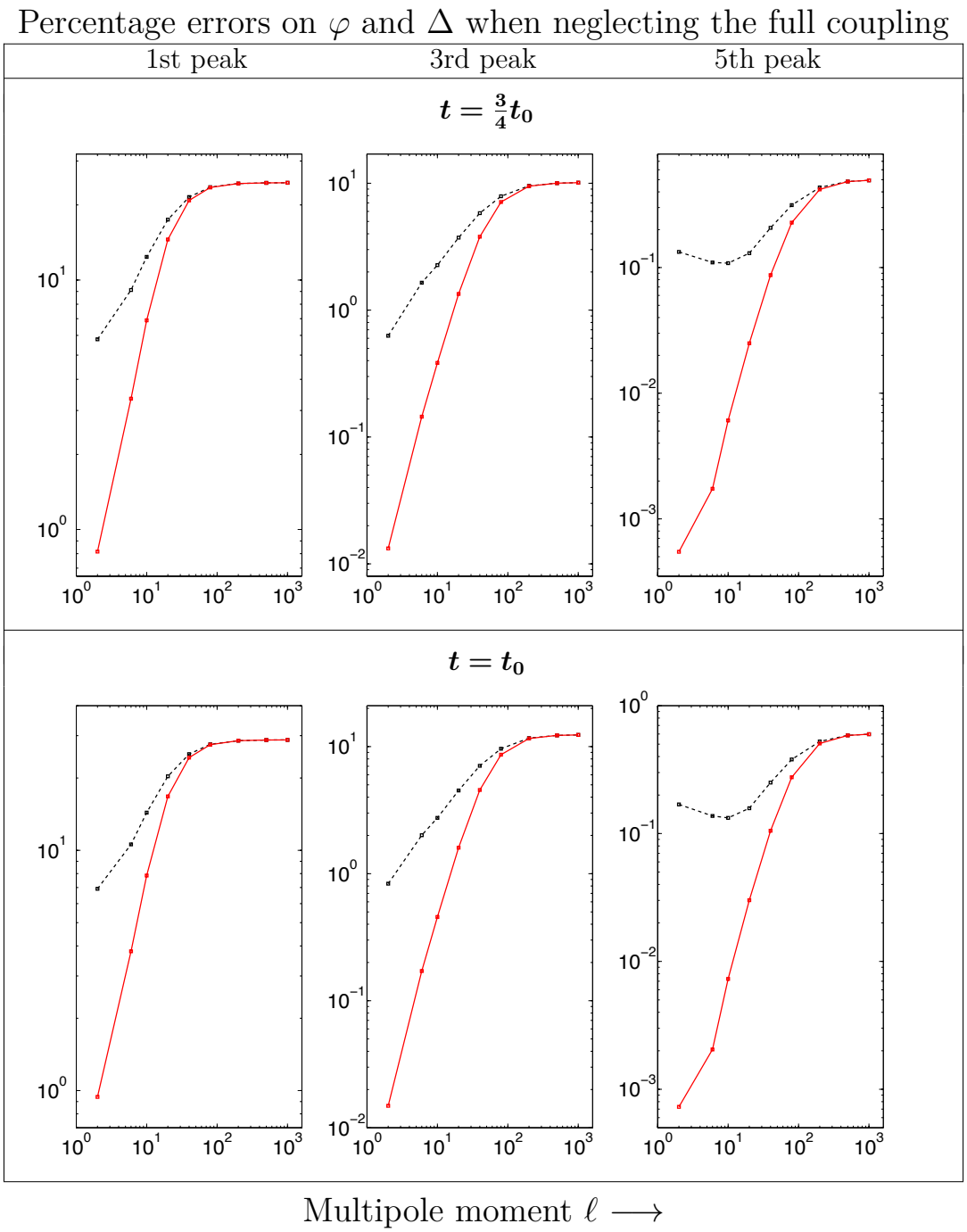

Figure 4.13: Same as Fig. 4.12, but at later time slices. Note that by $t = t_0$ we reach errors of around 30% well within the void, on scales relevant for the BAO. We can therefore expect percent-level corrections to the amplitude of the BAO bump in the two-point correlation function of the galaxy distribution at low redshift.

4.3 Conclusion

We have developed a numerical scheme to solve the system of coupled, linear PDE's describing the evolution of (polar) perturbations on a background LTB spacetime. The implementation is numerically consistent, attaining the expected 2nd-order convergence with resolution over a wide range of scales. To illustrate the nature of the coupling between the three master variables in the problem, in separate runs we initialised the data by several Gaussian peaks in each variable, spanning regions both inside and outside the void while setting the remaining two variables to zero initial amplitude. Initial pulses in φ result in growth of ς and χ at the sub-percent level, implying that the variable φ – commonly ascribed to the analogue of the Bardeen/Newtonian potential – nevertheless contains relativistic degrees of freedom. Initialising non-zero ς induces a sub-percent signal in φ and χ, all while decaying roughly as $a_{\parallel}^{-2}$ – analogous, but not equivalent, to the vector mode in a FLRW spacetime. Finally, a non-zero χ induces a φ to the level of nearly 50% today, while inducing only a sub-percent level of ς (from a maximum level of $\sim 20\%$ at earlier times). The propagating nature of χ is clearly seen in this case.

We also investigated whether the coupling between the master variables may be safely ignored. In particular, we focused on the case of an initialised φ, and considered how much error we expect to obtain on Δ and φ when neglecting the coupling of φ to ς and χ. Our results indicate that, well inside the void and on the largest scales, the errors picked up on Δ are at the sub-percent level, and so neglecting the coupling in that case is not an unreasonable assumption. However, the corresponding corrections to φ itself will be more important, and contributions from lensing and integrated Sachs-Wolfe effects may be enhanced at around the 10% level when taking the coupling into account. On smaller scales though, corrections to the assumption of negligible coupling can grow to a few tens of percent for both φ and Δ for regions well inside the void. For an observable such as the galaxy-galaxy correlation function, we estimate corrections to the amplitude of the BAO peak at the percent-level. Of course, since we have considered aspects of structure formation only valid in the linear regime, we

expect that any non-linear effects – the details of which is not clear at this point – will modify small-scale corrections in some non-trivial way. In any case, as we approach the outskirts of the void corrections are well below the percent-level on all scales, as expected in regions of spacetime close to FLRW. Having performed such a calculation for the case of a cosmological-sized void, our analysis can be easily adapted to smaller astrophysical-sized voids, and even halos. This will be left for future work.

CHAPTER 5

The galaxy correlation function as a test of the Copernican Principle

5.1 Introduction

The handful of studies that have confronted LTB models with observations of the BAO and CMB have all but included the effects of structure growth on top of such an inhomogeneous background. Here we calculate, for the first time, the galaxy 2PCF arising from a linearly perturbed LTB background, and use it to extract the radial and transverse BAO scales. The perturbation formalism that we make use of was developed in [154] − see also Section 2.3.

LTB models have sufficient freedom in them to always fit the average BAO scale. In fact, typically better than the concordance model does − see e.g. the MV model in Fig. 2.1. Intuitively, at the background level, the presence of shear causes the acoustic sphere of proper radius $L_{\rm init}$ at an initial high redshift $z_{\rm init}$ to deform, by redshift z, into an axisymmetric ellipsoid with semi-axes given by

$$L_{\parallel}^{geo}(z) = L_{\rm init}\frac{a_{\parallel}(z)}{a_{\parallel}(t_{\rm init}, r(z))}\,, \text{ and } L_{\perp}^{geo}(z) = L_{\rm init}\frac{a_{\perp}(z)}{a_{\perp}(t_{\rm init}, r(z))}\,. \tag{5.1}$$

Here we assume the following generic form for the proper radius of the sound horizon

at the drag epoch [176]

$$L_{\rm init} = \frac{121.4 \ln\left(2690 f_b/\eta_{10}\right)}{\sqrt{1+0.149{\eta_{10}}^{3/4}}} \left[\frac{1\,{\rm K}}{T_d(f_b,\eta_{10})}\right] {\rm Mpc}\,. \tag{5.2}$$

where $N_{\rm eff} = 3.04$, $f_b = \Omega_b/\Omega_m$ is the local baryon fraction, $\eta = 10^{-10}\eta_{10}$ is the baryon-photon ratio at that time, T_d is the temperature at the drag epoch and it is assumed that during the process of recombination, the scale of the void inhomogeneity is much larger than the horizon size at that time ($\sim 100\,{\rm Mpc}$). In general, f_b and η_{10} may exhibit radial dependence, implying that $L_{\rm init}$ could vary over the scale of the model. Unless we have access to independent measurements of f_b and η in the same shell at early times – which lie inside our past lightcone – this results in weaker constraints on late-time inhomogeneity. Note that, by adjusting the bang time function suitably, it is possible to fine-tune these models to have the same radial and angular BAO scales.

For the purposes of this study, we consider the SV and BV LTB models introduced in Section 2.2, and compare these to the fΛCDM model. In all models, we choose FLRW initial conditions to ensure that the effects we find arise from the evolution of structure on the inhomogeneous background. We take the early-time parameters f_b and η in (5.2) to be those derived from the same WMAP 5-year values used for the fΛCDM model. This fixes the initial proper BAO scale to be the same in all models. The background density Ω_m and expansion rates $H_\parallel, H_\perp$ are shown for these three models in Fig. 2.1 (upper panels). We also show (lower panels) the geometric approximations to the radial and transverse scales, $L_\parallel^{\rm geo}$ and $L_\perp^{\rm geo}$, and the average BAO scale d_z calculated from them.

In this work, we ignore the coupling that naturally arises between the master variables of the full PDE system describing the evolution of the polar LTB perturbations − this is expected to be a good approximation for the simplest LTB models in which the background shear is typically of the order of a few percent [177]. In fact, in Chapter 4 we provided a more rigorous handle on the expected error on the amplitude of the correlation function when neglecting the coupling: typically a few percent. Note here that we also ignore complications from bias and redshift space distortions − this is

reasonable since we are only interested in comparisons with the standard model, not with the actual observed correlation function.

5.2 Scalar Perturbations on an LTB background

The full perturbation theory on a LTB background was presented in Section 2.3. Recall that the latter involved a 2+2 split of the spacetime, and makes explicit the coupling of vector and tensor modes to scalar modes at linear order. A first approximation is to neglect this mode-mixing, and focus only on 'scalar' modes − which only occur in the polar sector. Then the perturbed metric in the RW gauge is ([154], with notational change, $\varphi \to -2\Phi$)

$$ds^2 = -\left[1 + 2\Phi(t, \boldsymbol{x})\right] dt^2 + \left[1 - 2\Phi(t, \boldsymbol{x})\right] \bar{g}_{ij} dx^i dx^j \,, \tag{5.3}$$

where $\bar{g}_{ij}$ is the spatial part of (2.10). The Newtonian potential here obeys a simple generalization of the standard FLRW evolution equation for the Newtonian potential (1.77):

$$\ddot{\Phi} + 4H_\perp \dot{\Phi} - \frac{2\kappa}{a_\perp^2}\Phi = 0 \,. \tag{5.4}$$

Because there are no spatial gradients, Φ evolves independently in each r =const. shell, as if in a separate dust FLRW model. This does not mean that there is no dependence on spatial gradients: density fluctuations depend on spatial gradients of Φ which couple to the anisotropic expansion of the model. The gauge-invariant matter density perturbation Δ is found via the equivalent of the Poisson equation in LTB [154]:

$$4\pi G a_\parallel^2 \rho \Delta = \mathcal{L}\left[\Phi\right], \tag{5.5}$$

$$\begin{aligned} \text{where} \quad \mathcal{L} &= (1-\kappa r^2)\partial_r^2 + \left[\frac{2a_\parallel}{a_\perp r} - \left(1 + \frac{2a_\parallel}{a_\perp}\right)\kappa r - \frac{r^2\kappa'}{2} - \frac{a_\parallel{}'}{a_\parallel}\left(1-\kappa r^2\right)\right]\partial_r \\ &\quad - a_\parallel^2 \Theta \partial_t - \frac{a_\parallel^2}{a_\perp^2}\frac{\ell(\ell+1)}{r^2} + \frac{a_\parallel}{a_\perp}\left[r\kappa' + \left(2 + \frac{a_\parallel}{a_\perp}\right)\kappa\right] - a_\perp^2 H_\perp(\sigma + H_\perp). \end{aligned} \tag{5.6}$$

In the homogeneous limit, we recover the standard Poisson equation as derived in FLRW (1.75):

$$4\pi G a^2 \rho \Delta = \left[\vec{\nabla}^2 + 3K\right]\Phi - 3a^2 H(\dot{\Phi} + H\Phi), \tag{5.7}$$

$$\text{where} \quad \vec{\nabla}^2 = (1 - Kr^2)\partial_r^2 + \frac{(2 - 3Kr^2)}{r}\partial_r - \frac{\ell(\ell+1)}{r^2}\,. \tag{5.8}$$

Here ℓ is the angular wave number in a spherical harmonic expansion,

$$\Phi(t, \boldsymbol{x}) = \sum_{\ell m} \Phi^{\ell m}(t, r) Y_{\ell m}(\theta, \varphi), \tag{5.9}$$

and similarly for Δ.

We set initial conditions for Φ at a high redshift, $z_{\rm init} = 100$, where we assume the background is effectively FLRW. We write

$$\Phi^{\ell m}(t, r) = \phi(t, r)\Phi^{\ell m}_{\rm init}(r), \quad \phi(t_{\rm init}, r) = 1\,. \tag{5.10}$$

The subsequent time evolution of $\phi(t, r)$ is then determined by (5.4) for each r. Using (2.26) and (2.27), a parametric form of the solution is given by

$$\phi(t, r) = C(r)\frac{\cosh u(t, r)}{\sinh^5 u(t, r)}\Big[\sinh 2u(t, r) - 6u(t, r) + 4\tanh u(t, r)\Big]\,, \tag{5.11}$$

$$C(r) = \frac{\sinh^5 u_{\rm init}(r)}{\cosh u_{\rm init}(r)\Big[\sinh 2u_{\rm init}(r) - 6u_{\rm init}(r) + 4\tanh u_{\rm init}(r)\Big]}. \tag{5.12}$$

Note that $\Phi^{\ell m}_{\rm init}(r)$ can be written as

$$\Phi^{\ell m}_{\rm init}(r) = \sqrt{\frac{2}{\pi}}\, i^\ell \int d^3k\, j_\ell(kr)\Phi_{\rm init}(\boldsymbol{k}) Y_{\ell m}(\hat{\boldsymbol{k}})\,, \tag{5.13}$$

which is related to the power spectrum via

$$\left\langle \Phi_{\rm init}\left(\boldsymbol{k}_1\right)\Phi^*_{\rm init}\left(\boldsymbol{k}_2\right)\right\rangle = \frac{2\pi^2}{k_1^3}\mathcal{P}_{\Phi_{\rm init}}\left(k_1\right)\delta^3\left(\boldsymbol{k}_1 - \boldsymbol{k}_2\right). \tag{5.14}$$

Finally, note that when assigning a flat FLRW initial power spectrum to the LTB models, we need to use the flat FLRW comoving coordinate r_F in (5.13) at $t_{\rm init}$, as opposed to the LTB coordinate r. Since proper radial distance is independent of

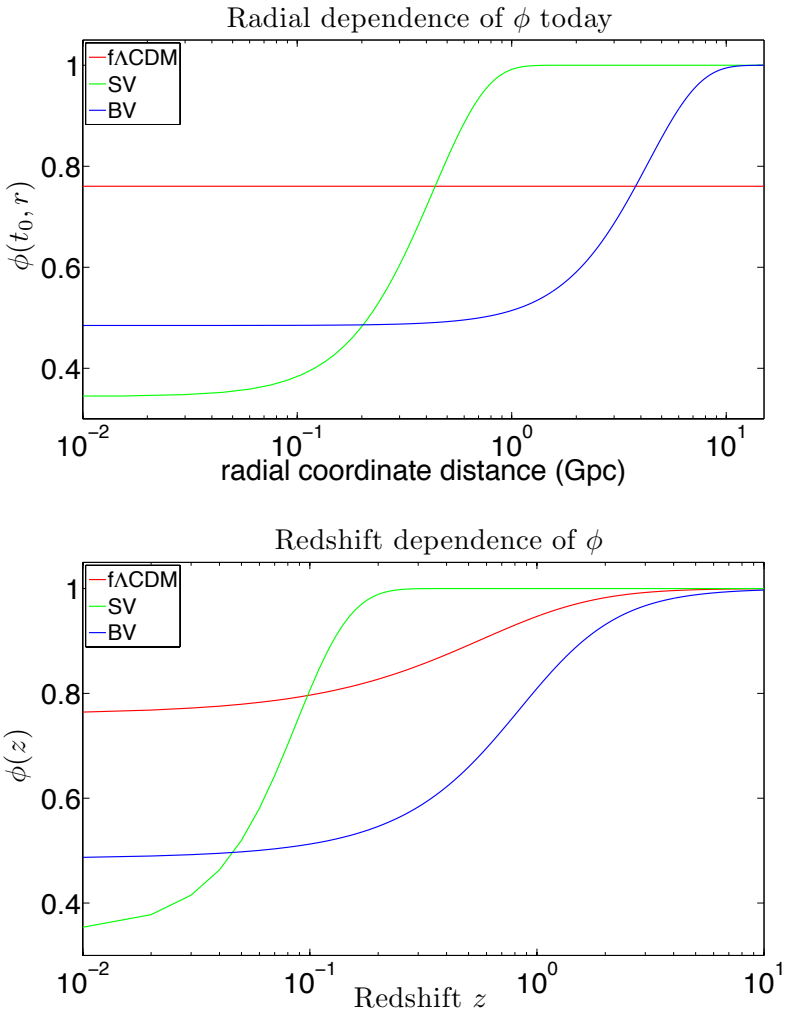

Figure 5.1: The gravitational potential ϕ as a function of radius today (top), and of redshift (bottom).

coordinates, we have $d_p(t_{\rm init}, r_F) = d_p(t_{\rm init}, r)$. With $d_p(t_{\rm init}, r_F) = a(t_{\rm init}) r_F$, we find that

$$r_F = (1 + z_{\rm init}) \int_0^r dr \, \frac{a_\parallel(t_{\rm init}, r)}{\sqrt{1 - \kappa(r) r^2}} \equiv f(r) \,, \tag{5.15}$$

where $f(r) \approx (1 + z_{\rm init}) a_\perp(t_{\rm init}, r) r$ since $\sqrt{1 - \kappa(r) r^2} \approx 1$ for all r and $a_\parallel = \partial_r(a_\perp r)$. Then (5.13) becomes

$$\Phi^{\ell m}_{\rm init}(r) = \sqrt{\frac{2}{\pi}} \, i^\ell \int d^3k \, j_\ell(k f(r)) \Phi_{\rm init}(\boldsymbol{k}) Y_{\ell m}(\hat{\boldsymbol{k}}) \,. \tag{5.16}$$

We now proceed to the derivation of the form of the 2PCF that our LTB models obey.

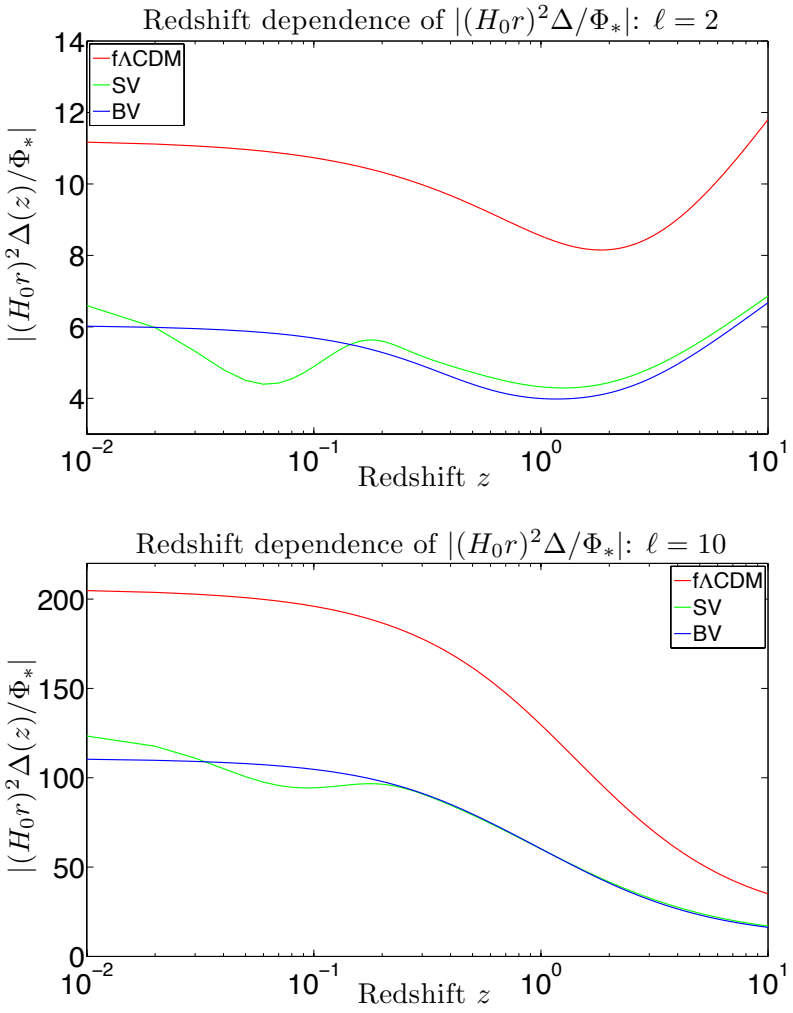

Figure 5.2: The normalized density perturbation $|(H_0 r)^2 \Delta_{\ell m}/\Phi_{*\ell m}|$ against redshift, for small (top) and large (bottom) ℓ. The subscript '$*$' on Φ indicates evaluation at $t_{\rm init}$.

5.3 The anisotropic galaxy-galaxy correlation function

Recall, from Eq. (1.92), that the 2PCF for the density perturbation Δ, as observed by a central observer down their past lightcone, is

$$\begin{aligned} \xi_\Delta(t_1, t_2, \boldsymbol{x}_1, \boldsymbol{x}_2) &\equiv \Big\langle \Delta(t_1, \boldsymbol{x}_1) \Delta^*(t_2, \boldsymbol{x}_2) \Big\rangle = \xi_\Delta(t(z_1), t(z_2), r(z_1)\hat{\boldsymbol{r}}_1, r(z_2)\hat{\boldsymbol{r}}_2) \\ &= \xi_\Delta(t(z_1), t(z_2), r(z_1), r(z_2), \delta\theta)\,, \end{aligned} \tag{5.17}$$

where $\hat{\boldsymbol{r}}_1 \cdot \hat{\boldsymbol{r}}_2 = \cos\delta\theta$. The second line follows from statistical isotropy, which applies for central observers. Using (5.5), (5.9), (5.14) and (5.16) the correlation function above becomes

$$\begin{aligned}
\xi_\Delta(z_1, z_2, \delta\theta) &= \Big[(4\pi G a_{\parallel_1} a_{\parallel_2})^2 \rho_1 \rho_2\Big]^{-1} \sum_{\ell\ell' mm'} \mathcal{L}_1\phi_1\, \mathcal{L}_2\phi_2 \Big\langle \Phi^{\ell m}_{\text{init}\,1} \Phi^{*\ell' m'}_{\text{init}\,2} \Big\rangle \\
&\quad \times Y_{\ell m}(\hat{\boldsymbol{r}}_1) Y_{\ell' m'}(\hat{\boldsymbol{r}}_2) \\
&= \Big[8\pi^3 (G a_{\parallel_1} a_{\parallel_2})^2 \rho_1 \rho_2\Big]^{-1} \sum_{\ell\ell' mm'} i^{\ell-\ell'} \int d^3k_2 \int d^3k_1\, \mathcal{L}_1\Big[\phi_1 j_\ell(k_1 f_1)\Big] \\
&\quad \times \mathcal{L}_2\Big[\phi_2 j_{\ell'}(k_2 f_2)\Big] Y_{\ell m}(\hat{\boldsymbol{r}}_1) Y_{\ell' m'}(\hat{\boldsymbol{r}}_2) \Big\langle \Phi_{\text{init}}(\boldsymbol{k}_1) \Phi^*_{\text{init}}(\boldsymbol{k}_2) \Big\rangle Y_{\ell m}(\hat{\boldsymbol{k}}_1) Y_{\ell' m'}(\hat{\boldsymbol{k}}_2) \\
\Rightarrow\ \xi_\Delta(z_1, z_2, \delta\theta) &= \sum_\ell \frac{(2\ell+1)\mathrm{P}_\ell(\cos\delta\theta)}{[(4\pi G a_{\parallel_1} a_{\parallel_2})^2 \rho_1 \rho_2]} \int \frac{dk}{k} \mathcal{J}_\ell(z_1, k) \mathcal{J}_\ell(z_2, k) \mathcal{P}_{\Phi_{\text{init}}}(k)\,, \qquad (5.18)
\end{aligned}$$

where a subscript $n = 1, 2$ on a function of (t, r) means the quantity is evaluated at $(t(z_n), r(z_n))$,

$$\mathcal{J}_\ell(z, k) = \mathcal{L}\Big[\phi(t(z), r(z)) j_\ell(k f(z))\Big]\,, \qquad (5.19)$$

and our simplifications came about via of the following properties

$$\begin{aligned}
\int d^3k' \delta^3(\boldsymbol{k} - \boldsymbol{k}') g(k') &= g(k)\,, & (5.20)\\
k^3 &= k^2\, dk\, d\Omega_k\,, & (5.21)\\
\int d\Omega_k Y_{\ell m}(\hat{\boldsymbol{k}}) Y_{\ell' m'}(\hat{\boldsymbol{k}}) &= \delta_{\ell\ell'}\delta_{mm'}\,, & (5.22)\\
\sum_m Y_{\ell m}(\hat{\boldsymbol{r}}_1) Y_{\ell m}(\hat{\boldsymbol{r}}_2) &= \frac{(2\ell+1)}{4\pi} \mathrm{P}_\ell(\hat{\boldsymbol{r}}_1 \cdot \hat{\boldsymbol{r}}_2)\,, & (5.23)
\end{aligned}$$

where P_ℓ are the associated Legendre polynomials.

To evaluate (5.19), we use (5.6) and the following identities for the spherical Bessel function

$$\begin{aligned}
\partial_r j_\ell(kf) &= \ell \frac{f'}{f} j_\ell - k f' j_{\ell+1}\,, & (5.24)\\
\partial_r^2 j_\ell(kf) &= \left[\ell \frac{f''}{f} + \ell(\ell-1)\frac{f'^2}{f^2} - k^2 f'^2\right] j_\ell - \left(f'' - 2\frac{f'^2}{f}\right) k j_{\ell+1}\,. & (5.25)
\end{aligned}$$

The result is

$$\mathcal{J}_\ell = \Big[\alpha + \beta\ell + \gamma\ell^2 - (1 - \kappa r^2) f'^2 k^2 \phi\Big] j_\ell - \nu k j_{\ell+1}\,, \qquad (5.26)$$

where

$$\alpha = (1-\kappa r^2)\phi'' + A\phi' - a_\parallel^2(H_\parallel + 2H_\perp)\dot{\phi} + B\phi, \tag{5.27}$$

$$\beta = \left[(1-\kappa r^2)\left(\frac{f''}{f} - \frac{f'^2}{f^2}\right) + A\frac{f'}{f} - \frac{a_\parallel^2}{r^2 a_\perp^2}\right]\phi + 2(1-\kappa r^2)\frac{f'}{f}\phi', \tag{5.28}$$

$$\gamma = \left[(1-\kappa r^2)\frac{f'^2}{f^2} - \frac{a_\parallel^2}{r^2 a_\perp^2}\right]\phi\,, \tag{5.29}$$

$$\nu = \left[(1-\kappa r^2)\left(f'' - \frac{2f'^2}{f}\right) + Af'\right]\phi + 2f'(1-\kappa r^2)\phi'\,, \tag{5.30}$$

and

$$A = \frac{2a_\parallel}{a_\perp r} - \left(1 + \frac{2a_\parallel}{a_\perp}\right)\kappa r - \frac{r^2\kappa'}{2} - \frac{a_\parallel{}'}{a_\parallel}\left(1-\kappa r^2\right)\,, \tag{5.31}$$

$$B = -a_\parallel^2 H_\perp(H_\perp + 2H_\parallel) + \frac{a_\parallel}{a_\perp}\left[r\kappa' + \left(2 + \frac{a_\parallel}{a_\perp}\right)\kappa\right]. \tag{5.32}$$

Note that we recover the FLRW correlation function in the homogeneous limit.

In LTB, the real-space radial and transverse BAO scales are different, and are given by the peaks in the radial and transverse correlation functions. In the same way as performed earlier (Section 1.3.2.3), we define these here as:

$$\xi_\Delta^\parallel(z_1, z_2) \equiv \xi_\Delta(z_1, z_1+\delta z, 0) = \sum_\ell (2\ell+1)\mathcal{C}_\ell^\parallel(z_1, z_2), \tag{5.33}$$

$$\xi_\Delta^\perp(z_1, \delta\theta) \equiv \xi_\Delta(z_1, z_1, \delta\theta) = \sum_\ell (2\ell+1)P_\ell(\cos\delta\theta)\mathcal{C}_\ell^\perp(z_1), \tag{5.34}$$

where the radial and transverse coefficients follow from (5.18):

$$\mathcal{C}_\ell^\parallel(z_1, z_2) = \left[(4\pi G a_{\parallel_1} a_{\parallel_2})^2 \rho_{m1}\rho_{m2}\right]^{-1} \int \frac{dk}{k}\ \mathcal{J}_\ell(z_1, k)\mathcal{J}_\ell(z_1+\delta z, k)\mathcal{P}_{\Phi_{\rm init}}(k), \tag{5.35}$$

$$\mathcal{C}_\ell^\perp(z_1) = \left(4\pi G a_{\parallel_1}^2 \rho_{m1}\right)^{-2} \int \frac{dk}{k}\ \mathcal{J}_\ell{}^2(z_1, k)\mathcal{P}_{\Phi_{\rm init}}(k). \tag{5.36}$$

Equations (5.18), (5.26) and (5.33)–(5.36) summarize our new results that derive the anisotropic correlation function of matter density perturbations on a radially inhomogeneous background.

5.4 Computation of the anisotropic information

We can now compute the anisotropic power spectra and correlation functions for the two LTB models we are interested in, and compare with the standard case (see e.g. [97, 178, 98, 160, 179, 180] for various approaches to compute these quantities from galaxy surveys in the standard homogeneous framework.)

Figure 5.1 shows the current profile and the redshift evolution of the gravitational potential for the three models. Note the greater decay in the amplitude of ϕ for the void models, due to the presence of curvature, which explains the decrease in the overall amount of clustering relative to ΛCDM. The normalized density perturbation is illustrated in Fig. 5.2 for the three models. For small-scale modes (large ℓ), Δ scales approximately as $(1+z)^{-1}$. For the large-scale mode $\ell = 2$, the 'decaying' behaviour at high redshift is due to the mode entering the Hubble-scale at low redshift.

We calculate the correlation functions by smoothing away power on scales below $1\,\mathrm{Mpc}$, via $\mathcal{P}_{\Phi_{\rm init}}(k) \to \mathcal{P}_{\Phi_{\rm init}}(k)\exp[-k^2/(1\,\mathrm{Mpc}^{-1})^2]$. This makes the sums over ℓ in the correlation functions (5.33), (5.34) converge relatively quickly (typically we require $\ell_{\rm max}(z) \lesssim 10\,r(z)/\mathrm{Mpc}$), but without altering the resulting correlation function.

5.4.1 Power spectra

Fig.'s 5.3 and 5.4 show the angular and radial power spectra, respectively, multiplied by $\ell(\ell+1)$ for the three models. The drop in power for high ℓ, seen in all models, is a consequence of the small-scale smoothing. Note also in general the larger overall power in the concordance model compared to the void models: this is due to the larger amplitude in Δ as shown in Fig. 5.2.

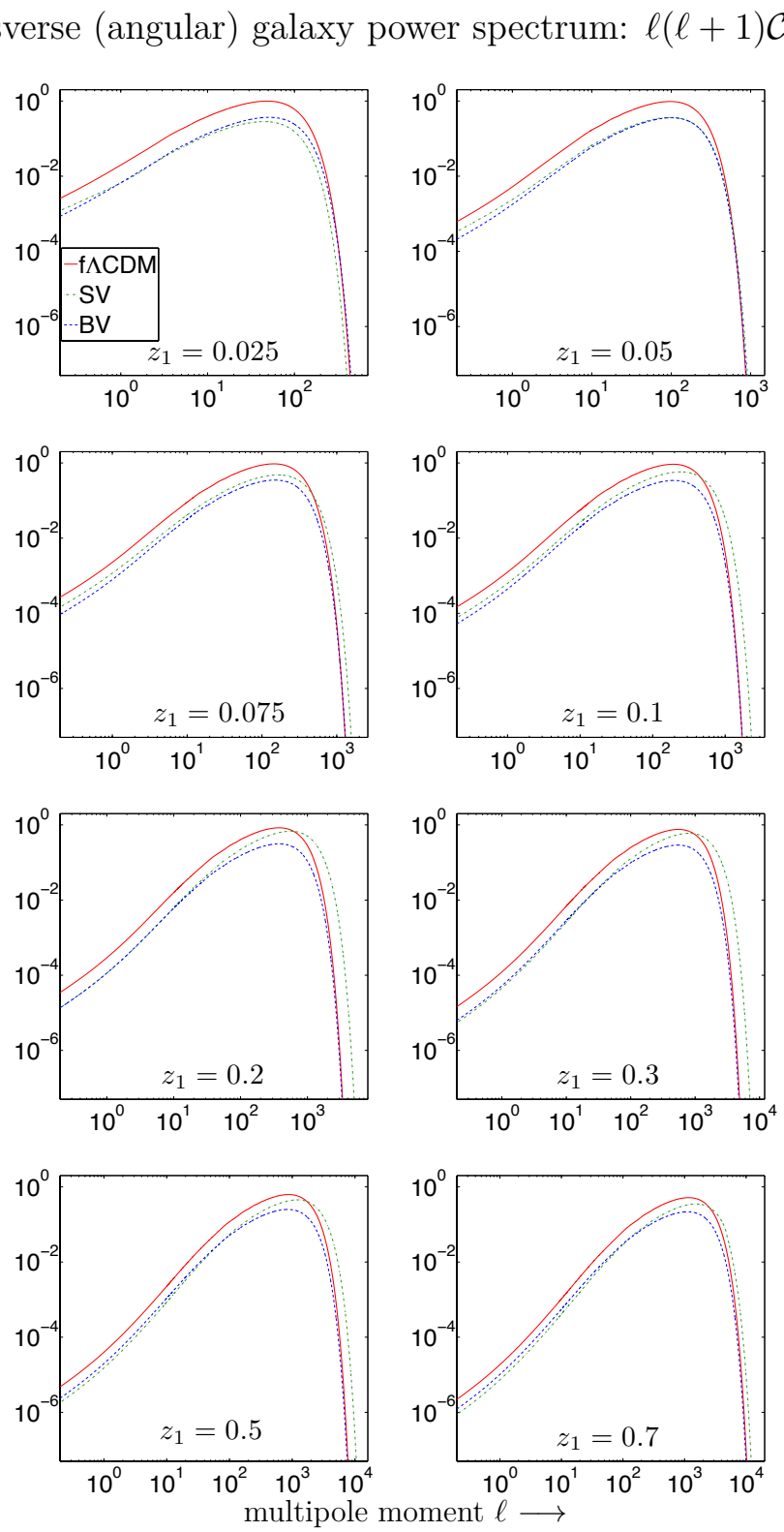

Figure 5.3: Transverse (angular) galaxy power spectra for the fΛCDM (red, solid), SV (black, dot-dashed) and BV (blue, dashed) models at the various redshifts of interest.

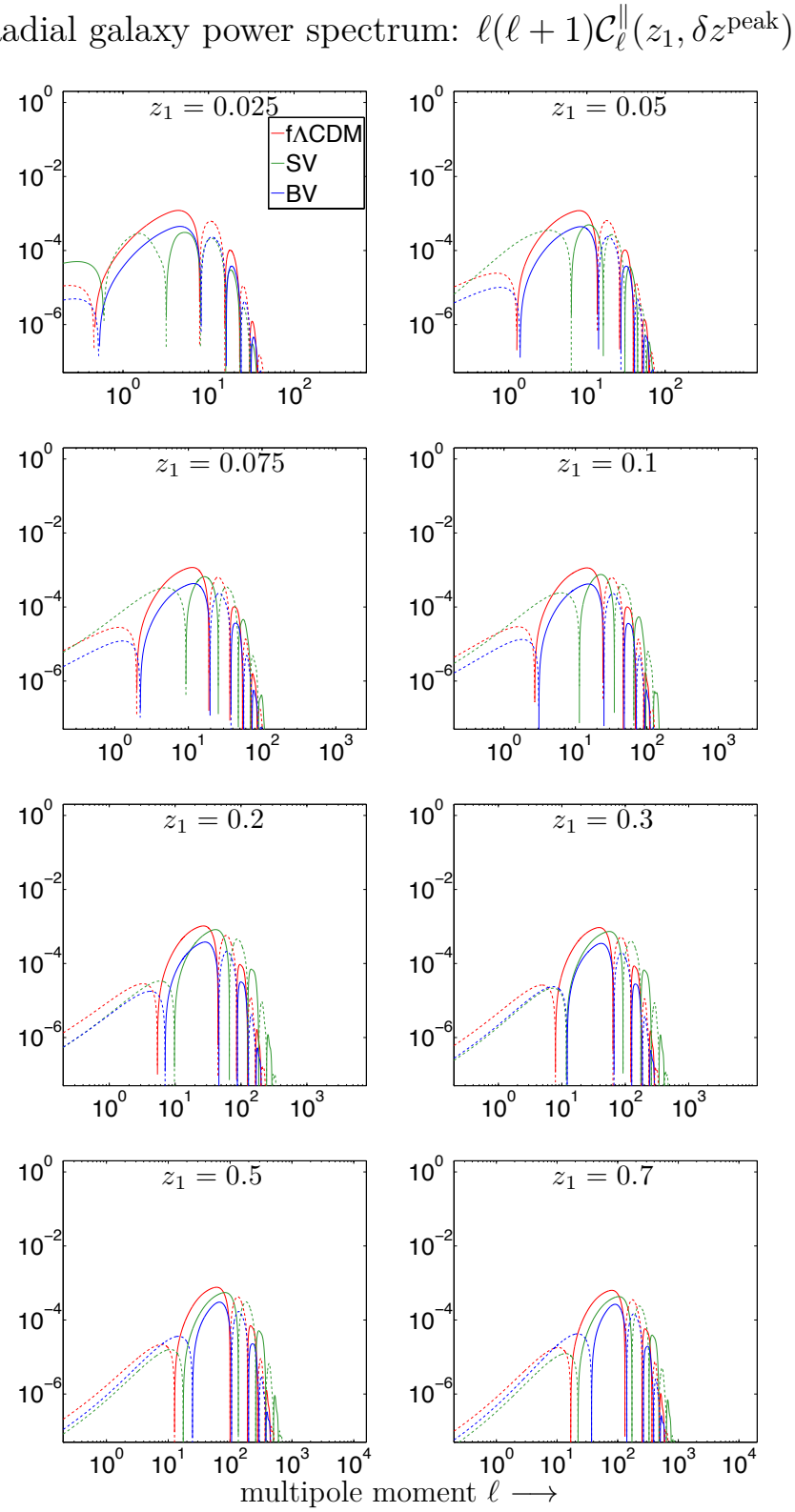

Figure 5.4: Radial galaxy power spectra for the fΛCDM (red, solid), SV (black, dot-dashed) and BV (blue, dashed) models at the various redshifts of interest.

5.4.2 Correlation functions

The transverse and radial galaxy correlation functions each model are shown in Fig.'s 5.6 and 5.5, respectively. $\xi^{\perp}$ describes the correlation across the sky in a sphere at redshift z_1. The angular size of the BAO is $\delta\theta_{\rm peak}$, given by the bump in $\xi^{\perp}$. $\xi^{\parallel}$, which starts at various redshifts z_1 and extends to $z_2 = z_1 + \delta z$, shows the correlation of structure along a line of sight, as the observer looks into higher density regions. The redshift extent of the radial BAO feature is $\delta z_{\rm peak}$, which is given by the location of the bump in $\xi^{\parallel}$.

These plots illustrate, in the context of void models, how different the transverse and radial correlation functions can be from each other, as well as that from the concordance model. For instance, in the case of the SV model, the transverse correlation function can be entirely positive (i.e. no zero-crossing), while the radial correlation function can be entirely negative. This is due to the large curvature gradients at low redshift, compared to typical void models that fit SN1a data. While such drastic behaviour is not as obvious for the void model that fits the average BAO scale, i.e the BV model, the amplitude differences are still noticeable compared to that of the concordance model. Curiously, even though we neglect redshift space distortions, the effect of the void is qualitatively similar to the effect of redshift space distortions in FLRW (see [181]).

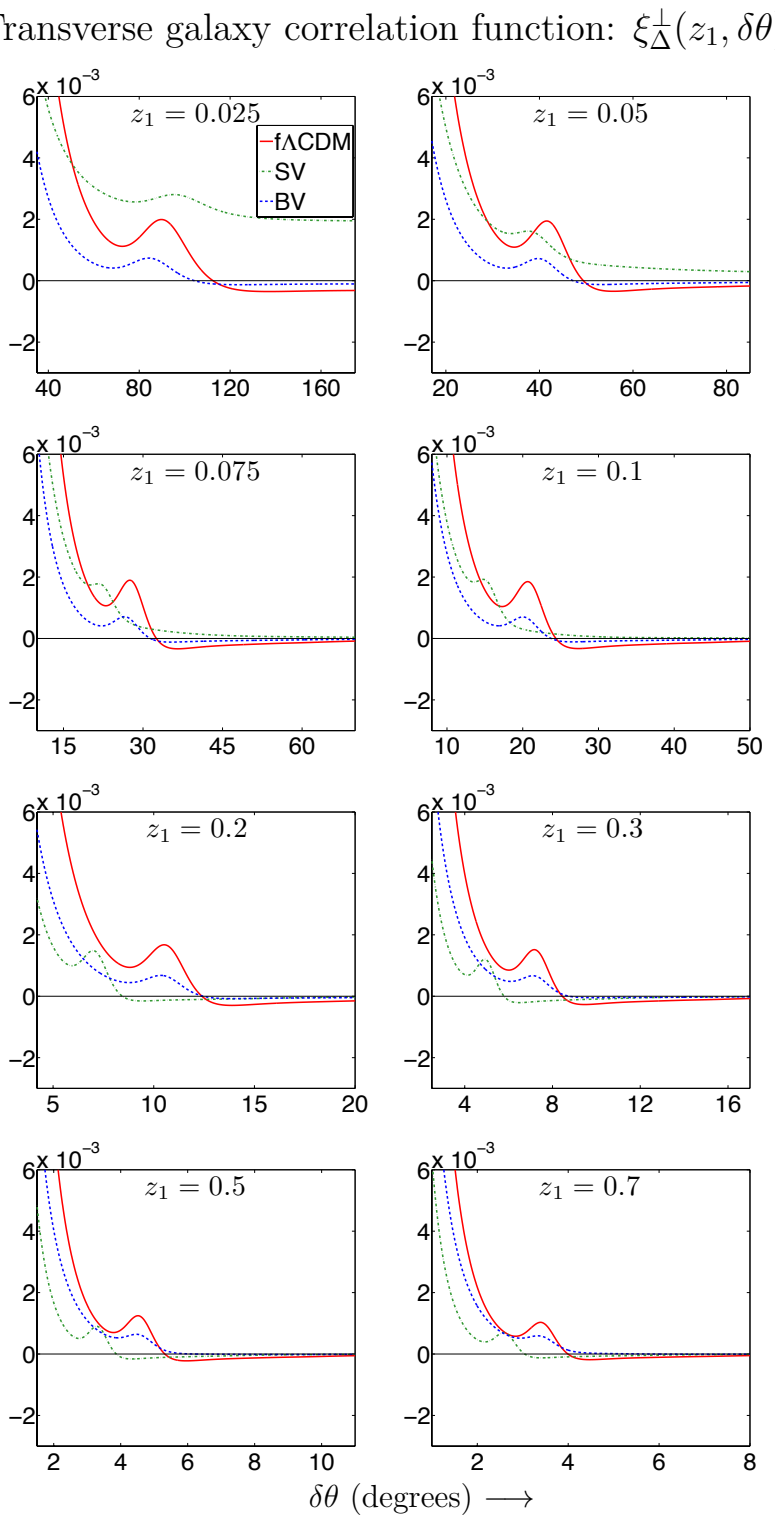

Figure 5.5: Transverse galaxy correlation functions for the fΛCDM (red, solid), SV (black, dot-dashed) and BV (blue, dashed) models at the various redshifts of interest.

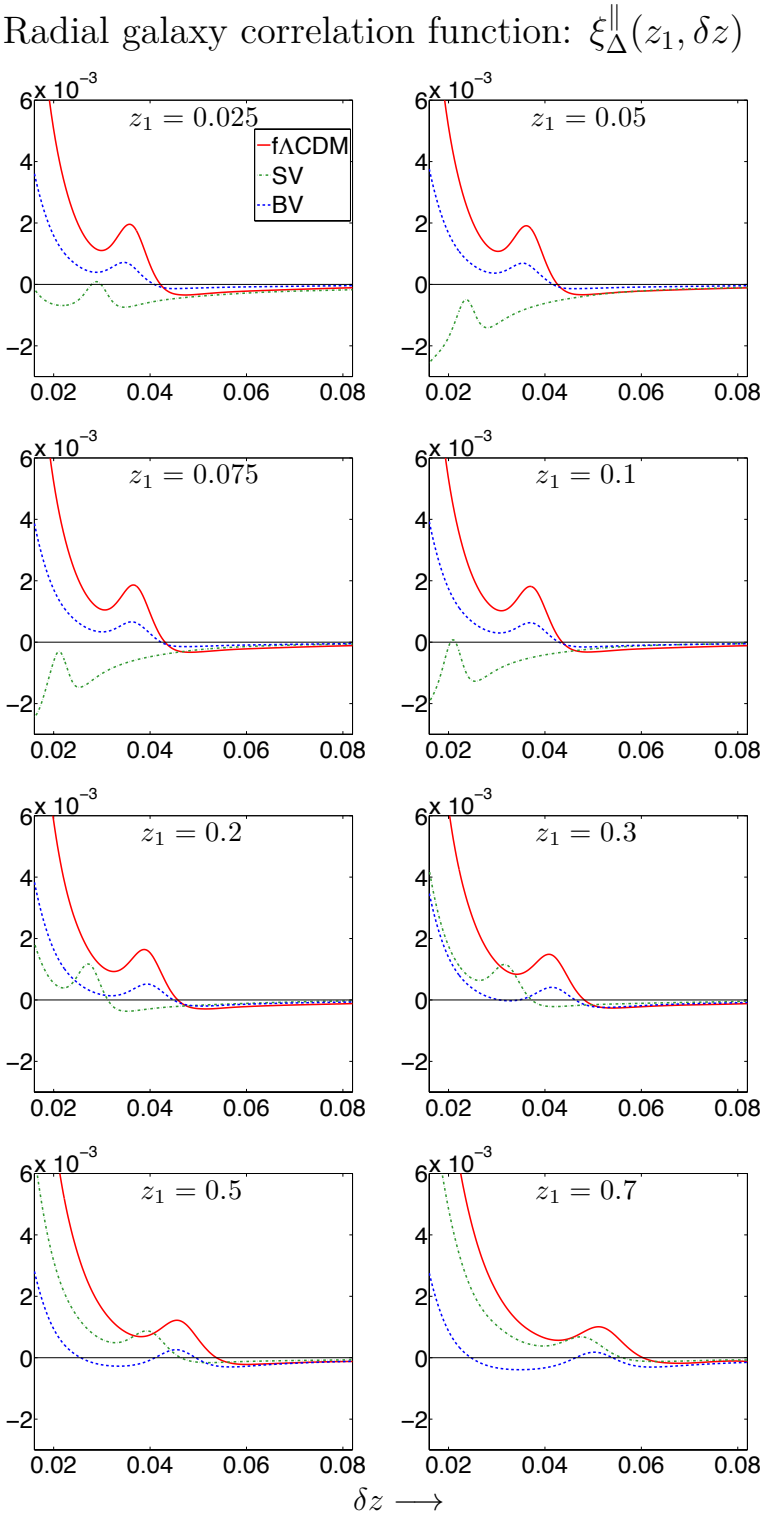

Figure 5.6: Radial galaxy correlation functions for the fΛCDM (red, solid), SV (black, dot-dashed) and BV (blue, dashed) models at the various redshifts of interest.

Redshift (z_1)	fΛCDM		SV		BV	
	$\delta z_{\rm peak}$	$\delta\theta_{\rm peak}$ (degrees)	$\delta z_{\rm peak}$	$\delta\theta_{\rm peak}$ (degrees)	$\delta z_{\rm peak}$	$\delta\theta_{\rm peak}$ (degrees)
0.025	0.03573	89.779	0.02887	95.347	0.03457	84.207
0.05	0.03613	41.552	0.02367	37.554	0.03541	39.704
0.075	0.03653	27.506	0.02113	21.584	0.03619	26.491
0.1	0.03695	20.653	0.02093	14.791	0.03691	20.013
0.2	0.03877	10.517	0.02712	6.985	0.03937	10.351
0.3	0.04082	7.171	0.03160	4.911	0.04141	7.103
0.5	0.04557	4.516	0.03929	3.285	0.04539	4.468
0.7	0.05111	3.392	0.04745	2.585	0.05025	3.334

Table 5.1: BAO scales extracted from the simulated galaxy correlation functions.

5.4.3 Extraction of the BAO scales

We determined $\delta z_{\rm peak}$ and $\delta\theta_{\rm peak}$ numerically, see Table. 5.1, from the local maxima in the correlation functions. These results are also shown in Fig 5.7, along with the geometric approximations (i.e., without incorporating the effect of perturbations),

$$\delta z^{\rm geo} = L_{\parallel}^{\rm geo}(1+z)H_{\parallel}, \quad \delta\theta^{\rm geo} = \frac{L_{\perp}^{\rm geo}}{d_A}, \tag{5.37}$$

where $L_{\parallel}^{\rm geo}, L_{\perp}^{\rm geo}$ are given by (5.1). Our results show that the geometric formulas commonly used for constraining LTB with BAO fail at the percent level. While current data are not able to resolve such differences, this may be possible with future surveys such as SKA and Euclid. Furthermore, note that the size of these corrections are of a similar order to the corrections from redshift space distortions in FLRW [181]. Also, while the geometric formulas in (5.37) give the correct observed scales for fΛCDM, care should be taken for large $\delta\theta$, since Eq. (5.37) is only valid for small angles.

5.5 Conclusion

We have derived for the first time the anisotropic real-space two-point correlation function for the gauge-invariant matter density perturbation, in a LTB universe with radial inhomogeneity in the background – summarized in (5.18), (5.26) and (5.33)–(5.36). For this we neglected the coupling of the scalar mode (i.e. gravitational potential)

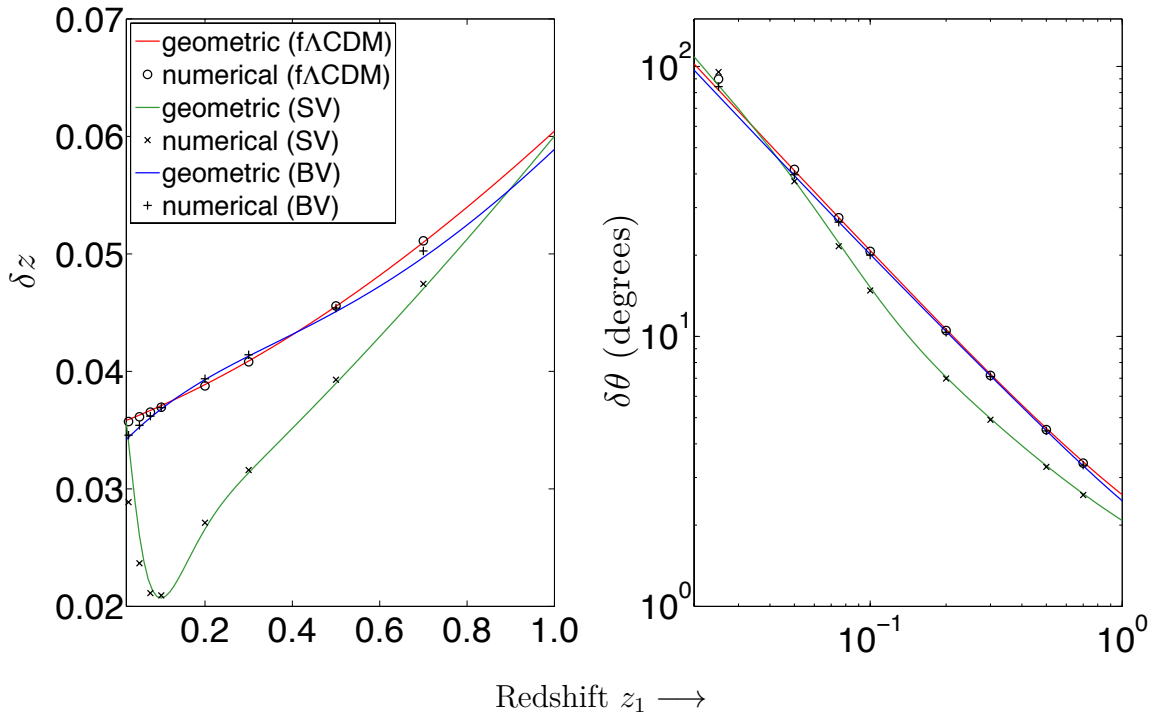

Figure 5.7: Radial galaxy correlation functions for the fΛCDM (red, solid), SV (black, dot-dashed) and BV (blue, dashed) models at the various redshifts of interest.

with vector and tensor modes – which should be a good approximation, at least on the large scales relevant for the BAO. An analysis of the effects of mode-coupling, which would entail the integration of PDE's, is carried out in [182] – see Chapter 4. We also neglected contributions from bias and redshift space distortions, since our primary focus was a comparison with the concordance model, not to test void models against data. Redshift space distortions in LTB void models deserve further investigation, in particular to check whether the FLRW formula provides a useful approximation.

We computed the radial and angular correlation functions for two void models, one relatively small (SV) and one Hubble-sized void that fits the average BAO data (BV) – see Figs. 5.6 and 5.5. We used the peaks of the computed correlation functions to extract the radial and transverse BAO scales. The results were compared with the geometric approximation that has been used in all previous work, showing that the geometric approximation to the BAO scales in LTB fails at the percent level – see Fig. 5.7. Future large-volume surveys, such as SKA and Euclid, may thus be able to rule

out the void models on the basis of their BAO scales.

However, even if void models can be fine-tuned to reproduce the radial and transverse BAO scales, these scales represent only one feature in the galaxy correlation functions. The void correlation functions differ significantly from those of the concordance model (Figs. 5.6 and 5.5). In particular, the void radial correlation can become negative (anti-correlation) before, and even at, the BAO peak, while the concordance correlation is positive. The void transverse correlation may be positive for all scales, unlike the concordance one. These features resemble the effect of redshift space distortions in FLRW (see Figs. 4 and 6 in [181]), since the anisotropic expansion rate in LTB can mimic the effect of radial peculiar velocities in FLRW. However, there are significant further differences between the two models which arise from the effect of LTB perturbations.

This leads to our key final result: even if the radial and transverse BAO scales match observations, the radial and transverse *correlation functions* contain direct signatures of the anisotropic growth of perturbations in a non-FLRW model. These correlation functions can thus be used as direct tests of the Copernican Principle.

CHAPTER 6

Summary and Future Work

Cosmologists of the forthcoming decade will experience an unveiling of incredibly powerful telescopes that will map the cosmic web to unprecedented accuracy. It is expected that we will be able to track the evolution, if any, of the equation of state of DE to percent-level precision. In order to take advantage of this, however, theories of structure formation have to be even more accurate than before. This has sparked numerous studies which address possible corrections to current models of structure formation, be it in the linear regime via relativistic corrections [165], or in the non-linear regime via N-body simulations [164].

In this work, we have developed a new code that will allow us to peer into a fairly unexplored area: relativistic corrections on top of a strongly nonlinear background. We pointed out that this will be important for not just corrections to cosmological structure formation, but also for other applications in which spherical symmetry is a good approximation − see below for a list of planned future work. Our code makes use of a 4th-order Runge-Kutta numerical scheme, which we showed to be stable and convergent at the expected (2nd-order) rate, in the case of a background Gpc LTB void model.

We then explored the solutions to our set of master equations, under a specific set of

boundary conditions, but for three different sets of initial conditions. The background chosen for this was the same Gpc LTB void model we used to check for convergence (i.e. the MV model). We certainly found no shortage of interesting features contained within the solutions: apart from the usual growing part of the density contrast, we see contributions from rotational (vector) and propagating (tensor) degrees of freedom. Initial pulses in φ result in growth of ς and χ at the sub-percent level, implying that the variable φ – commonly ascribed to the analogue of the Bardeen/Newtonian potential – nevertheless contains relativistic degrees of freedom. Initialising non-zero ς induces a sub-percent signal in φ and χ, all while decaying roughly as $a_{\parallel}^{-2}$ – analogous, but not equivalent, to the vector mode in a FLRW spacetime. Finally, a non-zero χ induces a φ to the level of nearly 50% today, while inducing only a sub-percent level of ς (from a maximum level of $\sim 20\%$ at earlier times). The propagating nature of χ is clearly seen in this case.

We then estimated the errors acquired on the gravitational potential φ and density contrast Δ when the full coupling to vector and tensor degrees of freedom is neglected. This approximation is expected to be reasonable for void models which accommodate SNIa distances, in which the background shear is of the order of a few percent [177]. It was found that, well inside the void and on the largest scales, the corrections to Δ are sub-percent, implying that it is reasonable to neglect the full coupling in this regime. However, the corresponding corrections to lensing and ISW contributions from φ may be enhanced at around the 10% level when taking the coupling into account. Still inside the void, but on smaller scales, corrections to the assumption of negligible coupling can be as large as a few tens of percent for both φ and Δ. corrections to φ can be as large as 10% deep within the void, while percent-level corrections to Δ is to be expected. This translates to corrections to the correlation function − including the amplitude of the BAO peak − at the percent level. Of course, since we have considered aspects of structure formation only valid in the linear regime, we expect that any non-linear effects – the details of which is not clear at this point – will modify small-scale corrections in some non-trivial way. In any case, as we approach the outskirts of the

void corrections are well below the percent-level on all scales, as expected in regions of spacetime close to FLRW.

In an attempt to gauge the effect that these new corrections have on cosmological structure formation, we computed the anisotropic galaxy 2PCF for a small (SV) and large (BV) LTB void model in the case of negligible coupling of φ to ς and χ. We found that, even for the simplest void model that fits the averaged BAO scale, the amplitudes of the transverse and radial correlation functions in real space may be very different. Interestingly, the effects of such anisotropic structure growth mimics that of RSD in FLRW: the radial correlation function is lowered in amplitude, while the transverse correlation function is raised. There are even cases in which the BAO peak occurs around a scale of (radial) anti-correlation, as well as a completely positive (transverse) correlation function at all scales. Since we can expect such differences to be detected with future galaxy surveys, the anisotropic correlation function therefore provides us with another tool with which to probe the Copernican assumption. In addition to this, we also showed that such anisotropic growth in structure shifts the BAO peak positions, expected by geometric approximations, by roughly 1%.

The code we developed here has opened up a number of interesting topics that will be considered in future work, such as:

Generalising to other LTB models, and realistic initial conditions. A satisfactory dust-only LTB model that can fit all the available data is yet to be established. Only by taking the effects of linear perturbations into account as we have done here, as well as including realistic initial conditions into the setup, can any final conclusions be made about these models as alternatives to ΛCDM. To do this fairly, however, would require us to explore a more general set of LTB backgrounds. Such as, those that contain asymptotic curvature, describe a local overdensity (as opposed to an underdensity), contain a non-uniform bang-time, and those that have non-central observers. In addition, it would be useful to work with variables that reduce to SVT in the FLRW limit, since we can then make more straightforward comparison with the standard predictions.

Quantifying the full ISW effect. The ISW effect is a sensitive probe of the nature of DE, as well as the underlying spacetime curvature. In this work we derived a formula that captures the full ISW effect in a LTB model. By cross-correlating the ISW signal with that of the CMB, we hope to further constrain the space of viable LTB models. This, however, again requires a careful choice of variable to use that makes sense from a standard model perspective.

Estimating the weak lensing of GW's via halos/voids. In order to use the collisions of supermassive black holes as "standard sirens" . (see e.g., [173]), we need, among other things, to carefully model any distortions the GWs encounter along their journey to our detectors. A particular type of distortion on the expected GW signal comes from their weak lensing by intervening dark matter halos/voids (see [174]). Note, however, that in the case that the GW wavelength is of the same order as the size of the dark matter halos/voids, the geometric optics approximation for the lensing is expected to break down. Our code, for instance, can provide help quantify the lensing of GW's more accurately by modelling a dark matter halo/void using a LTB model, and scattering GW's off of it.

Including the effects of redshift-space distortions and bias. To properly compare predictions of e.g. the 2PCF within a LTB model with the observed 2PCF, we need to take RSD and bias into account. The effect from RSD is expected to come from the radial component of the velocity perturbation in LTB, i.e. the variable w (see Eq. (2.147)). By including this term, as well as some appropriate form(s) for the bias, we hope to constrain the space of LTB models even further.

Observing GW's from structure growth. Finally, if observations by e.g. [26] are confirmed to be the case, i.e. that we do live near the centre of a large spherical void, it seems fair to ask the following: what is the expected GW signal that will be produced by more realistic structure growth within such a non-linear background? Can we use this to further constrain the space of viable LTB models?

These are just some of the avenues we hope to explore in future work.

APPENDIX A

Useful analytic formulas: LTB background and scalar gravitational potential (φ)

In this appendix, we list all of the remaining analytic expressions (not shown in the main text) required to evaluate the LTB background quantities appearing in this thesis. We do the same for the scalar gravitational potential (φ) as required for the computation of the galaxy correlation function in Chapter 5.

The LTB background quantities we require are:

$$\Omega_m{}' = 2\,r(\Omega_m^{\rm out} - \Omega_m^{\rm in})\exp\Big[-(r/L)^2\Big]/L^2, \tag{A.1}$$

$$\Omega_m{}'' = 2(\Omega_m^{\rm out} - \Omega_m^{\rm in})\Big(1-2(r/L)^2\Big)\exp\Big[-(r/L)^2\Big]/L^2, \tag{A.2}$$

$$u_0{}' = -\frac{\Omega_m{}'}{2\Omega_m\sqrt{\Omega_k}}, \tag{A.3}$$

$$u_0{}'' = u_0{}'\left[\frac{\Omega_m{}''}{\Omega_m{}'} + \frac{\Omega_m{}'(3\Omega_m-2)}{2\Omega_m\Omega_k}\right], \tag{A.4}$$

$$H_{\perp 0}{}' = H_{\perp 0}\left[\frac{\Omega_m{}'(\Omega_m+2)}{2\Omega_m\Omega_k} + \frac{2u_0{}'\,[\cosh 2u_0 - 1]}{\sinh 2u_0 - 2u_0}\right], \tag{A.5}$$

$$\begin{aligned} H_{\perp 0}{}'' = H_{\perp 0}\Bigg\{&\frac{1}{2\Omega_m\Omega_k}\left(\Omega_m''(\Omega_m+2) + \Omega_m'^2\left[1 + \frac{(\Omega_m+2)(2\Omega_m-1)}{\Omega_m\Omega_k}\right]\right) \\ &+ \left(\frac{H_{\perp 0}{}'}{H_{\perp 0}}\right)^2 + \frac{2u_0''[\cosh 2u_0 - 1]}{\sinh 2u_0 - 2u_0} + 8u_0'^2\frac{[\cosh 2u_0 - 1 - u_0\sinh 2u_0]}{(\sinh 2u_0 - 2u_0)^2}\Bigg\}, \end{aligned} \tag{A.6}$$

$$\kappa' = \kappa\Big[2\frac{H'_{\perp 0}}{H_{\perp 0}} - \frac{\Omega'_m}{\Omega_k}\Big], \tag{A.7}$$

$$\kappa'' = \kappa\Big[\Big(\frac{\kappa'}{\kappa}\Big)^2 + 2\frac{H''_{\perp 0}}{H_{\perp 0}} - 2\Big(\frac{H'_{\perp 0}}{H_{\perp 0}}\Big)^2 - \frac{\Omega''_m}{\Omega_k} - \Big(\frac{\Omega'_m}{\Omega_k}\Big)^2\Big], \tag{A.8}$$

$$u' = \frac{\sinh 2u - 2u}{2[\cosh 2u - 1]}\left[\frac{{H_{\perp 0}}'}{H_{\perp 0}} - \frac{{\Omega_m}'(\Omega_m + 2)}{2\Omega_m\Omega_k}\right], \tag{A.9}$$

$$u'' = 4u'^2\frac{[\cosh 2u - 1 - u\sinh 2u]}{(\sinh 2u - 2u)(1 - \cosh 2u)} + \frac{\sinh 2u - 2u}{2[\cosh 2u - 1]}\Bigg\{\frac{{H_{\perp 0}}''}{H_{\perp 0}} - \Big(\frac{{H_{\perp 0}}'}{H_{\perp 0}}\Big)^2 - \left[\frac{{\Omega_m}''(\Omega_m + 2)}{2\Omega_m\Omega_k} + \Big(\frac{\Omega'_m}{\Omega_m\Omega_k}\Big)^2\Big(\frac{\Omega_m^2 + 4\Omega_m - 2}{2}\Big)\right]\Bigg\}, \tag{A.10}$$

$$\dot{u} = \frac{H_{\perp 0}\sqrt{\Omega_k}}{2a_\perp}, \tag{A.11}$$

$$\dot{u}' = \dot{u}\left[\frac{{H_{\perp 0}}'}{H_{\perp 0}} - \frac{{\Omega_m}'}{2\Omega_k} - \frac{{a_\perp}'}{a_\perp}\right], \tag{A.12}$$

$$\dot{u}'' = \dot{u}\Big[\Big(\frac{\dot{u}'}{\dot{u}}\Big)^2 + \frac{H''_{\perp 0}}{H_{\perp 0}} - \Big(\frac{H'_{\perp 0}}{H_{\perp 0}}\Big)^2 - \frac{\Omega''_m}{2\Omega_k} - \frac{1}{2}\Big(\frac{\Omega'_m}{\Omega_k}\Big)^2 - \frac{a''_\perp}{a_\perp} + \Big(\frac{a'_\perp}{a_\perp}\Big)^2\Big], \tag{A.13}$$

$${a_\perp}' = a_\perp\left[\frac{{\Omega_m}'}{\Omega_m\Omega_k} + \frac{2u'\sinh 2u}{\cosh 2u - 1}\right], \tag{A.14}$$

$${a_\perp}'' = a_\perp\Big[\Big(\frac{{a_\perp}''}{a_\perp}\Big)^2 + \frac{{\Omega_m}''}{\Omega_m\Omega_k} + (2\Omega_m - 1)\Big(\frac{{\Omega_m}'}{\Omega_m\Omega_k}\Big)^2 + 2\frac{u''\sinh 2u - 2u'^2}{\cosh 2u - 1}\Big], \tag{A.15}$$

$$\dot{a_\perp} = 2\frac{a_\perp\sinh 2u}{\cosh 2u - 1}\dot{u}\,, \tag{A.16}$$

$$\dot{a_\perp}' = \dot{a_\perp}\left[\frac{\dot{u}'}{\dot{u}} + \frac{a'_\perp}{a_\perp} - \frac{2u'}{\sinh 2u}\right], \tag{A.17}$$

$$\dot{a_\perp}'' = \dot{a_\perp}\Big[\Big(\frac{\dot{a_\perp}'}{\dot{a_\perp}}\Big)^2 + \frac{\dot{u}''}{\dot{u}} - \Big(\frac{\dot{u}'}{\dot{u}}\Big)^2 + \frac{a''_\perp}{a_\perp} - \Big(\frac{a'_\perp}{a_\perp}\Big)^2 + \frac{4u'^2\coth 2u - 2u''}{\sinh 2u}\Big], \tag{A.18}$$

$${a_\parallel}' = {a_\perp}''r + 2{a_\perp}'\,, \tag{A.19}$$

$$\dot{a_\parallel}' = \dot{a_\perp}''r + 2\dot{a_\perp}'\,, \tag{A.20}$$

$${H_\perp}' = \frac{a_\parallel}{ra_\perp}\Big[H_\parallel - H_\perp\Big], \tag{A.21}$$

$${H_\parallel}' = H_\parallel\left[\frac{\dot{a_\parallel}'}{\dot{a_\parallel}} - \frac{a'_\parallel}{a_\parallel}\right], \tag{A.22}$$

Appendix A. Useful analytic formulas: LTB background and scalar gravitational potential (φ)

$$8\pi G{\rho_m}' = 2H_\perp {H_\parallel}' + 2(H_\perp + H_\parallel){H_\perp}' - 2\Big[\frac{(a_\perp - a_\parallel){a_\perp}'}{a_\perp a_\parallel} - \frac{a_\perp {a_\parallel}'}{a_\parallel^2}\Big]\frac{\kappa}{a_\perp^2} + \Big[\frac{a_\parallel}{a_\perp} + 3 - \frac{r}{a_\parallel a_\perp}\Big(\frac{a_\perp'}{a_\perp} - \frac{a_\parallel'}{a_\parallel}\Big)\Big]\frac{\kappa'}{a_\perp a_\parallel} + \frac{r\kappa''}{a_\perp a_\parallel}, \tag{A.23}$$

For all expressions pertaining to the scalar gravitational potential, φ, we require:

$$C' = Cu_{\rm init}'\Big[5\coth u_{\rm init} - \tanh u_{\rm init} - \frac{2\cosh 2u_{\rm init} - 6 + 4\,\mathrm{sech}^2 u_{\rm init}}{\sinh 2u_{\rm init} - 6u_{\rm init} + 4\tanh u_{\rm init}}\Big], \tag{A.24}$$

$$\varphi' = \varphi\Big[\frac{C'}{C} + u'\Big(\tanh u - 5\coth u + \frac{2\cosh 2u - 6 + 4\,\mathrm{sech}^2 u}{\sinh 2u - 6u + 4\tanh u}\Big)\Big], \tag{A.25}$$

$$\dot\varphi = \dot u\,\varphi\Big[\tanh u - 5\coth u + \frac{2\cosh 2u - 6 + 4\mathrm{sech}^2 u}{\sinh 2u - 6u + 4\tanh u}\Big], \tag{A.26}$$

$$C' = \frac{(C')^2}{C} + \frac{u_{\rm init}''}{u_{\rm init}'}C' + C(u_{\rm init}')^2\Big[\Big(\frac{2\cosh 2u_{\rm init} - 6 + 4\,\mathrm{sech}^2 u_{\rm init}}{\sinh 2u_{\rm init} - 6u_{\rm init} + 4\tanh u_{\rm init}}\Big)^2 - 5\mathrm{cosech}^2 u_{\rm init} - \mathrm{sech}^2 u_{\rm init} - \frac{4\sinh 2u_{\rm init} - 8\mathrm{sech}^2 u_{\rm init}\tanh u_{\rm init}}{\sinh 2u_{\rm init} - 6u_{\rm init} + 4\tanh u_{\rm init}}\Big], \tag{A.27}$$

$$\varphi'' = \varphi\Big[\frac{C''}{C} - \Big(\frac{C'}{C}\Big)^2 + u''\tanh u + (u'\mathrm{sech}u)^2 - 5u''\coth u + 5(u'\mathrm{cosech}u)^2\Big] + \varphi'\Big[\frac{C''}{C} + u'\tanh u - 5u'\coth u\Big] + \Big(u''\varphi + \varphi' u'\Big)\Big[\frac{2\cosh 2u - 6 + 4\,\mathrm{sech}^2 u}{\sinh 2u - 6u + 4\tanh u}\Big] + \frac{u'\varphi}{\sinh 2u - 6u + 4\tanh u}\Big[4\sinh 2u - 8\mathrm{sech}^2 u\tanh u - \frac{2\cosh 2u - 6 + 4\mathrm{sech}^2 u}{\sinh 2u - 6u + 4\tanh u}\Big]. \tag{A.28}$$

APPENDIX B

Spherical harmonics: components of vector and tensor basis functions

Here we list the components of the vector and tensor basis functions that are derived from the scalar spherical harmonic functions, $Y_{\ell m}(\theta, \phi)$, as made use of in this thesis (see Section 2.3).

- Polar case:

  The vector basis functions here are $Y_a \equiv Y_{,a}$. The components are simply

$$Y_\theta = Y_{,\theta}\,, \tag{B.1}$$

$$Y_\phi = Y_{,\phi}\,. \tag{B.2}$$

  The tensor basis functions are $Y_{ab} \equiv Y_{:ab} + \frac{\ell(\ell+1)}{2}\gamma_{ab}Y$. The components are

$$Y_{\theta\theta} = Y_{,\theta\theta} + \frac{\ell(\ell+1)}{2}Y\,, \tag{B.3}$$

$$Y_{\theta\phi} = Y_{,\theta\phi} - \cot\theta Y_{,\phi}\,, \tag{B.4}$$

$$Y_{\phi\phi} = Y_{,\phi\phi} + \sin\theta\cos\theta Y_{,\theta} + \frac{\ell(\ell+1)}{2}\sin^2\theta Y\,. \tag{B.5}$$

- Axial case:

The vector basis functions here are $\overline{Y}_a \equiv \hat{\epsilon}_a{}^b Y_{,b}$. The components are given by

$$\overline{Y}_\theta = \frac{1}{\sin\theta} Y_{,\phi}\,, \tag{B.6}$$

$$\overline{Y}_\phi = -\sin\theta Y_{,\theta}\,. \tag{B.7}$$

The tensor basis functions are $\overline{Y}_{ab} \equiv 2\overline{Y}_{(a:b)} = [\hat{\epsilon}_a{}^c Y_{,c}]_{:b} + [\hat{\epsilon}_b{}^d Y_{,d}]_{:a}$. The components become

$$\overline{Y}_{\theta\theta} = \frac{1}{\sin^2\theta}\Big[\sin\theta Y_{,\theta\phi} - \cos\theta Y_{,\phi}\Big]\,, \tag{B.8}$$

$$\overline{Y}_{\theta\phi} = \frac{1}{2}\left[\frac{1}{\sin\theta} Y_{,\phi\phi} - \sin\theta Y_{,\theta\theta} + \cos\theta Y_{,\theta}\right]\,, \tag{B.9}$$

$$\overline{Y}_{\phi\phi} = -\Big[\sin\theta Y_{,\theta\phi} - \cos\theta Y_{,\phi}\Big]\,. \tag{B.10}$$

APPENDIX C

Two-point correlation function: generic formulation

Following [183], the full anisotropic two-point (auto-) correlation function of some quantity $X \equiv A + B + C + ...$, in redshift space is defined as

$$\begin{aligned}
\xi_{XX^*}(z_1, z_2, \delta\theta) &\equiv \left\langle X\Big(t(z_1), r(z_1)\hat{\boldsymbol{r}}_1\Big) X^*\Big(t(z_2), r(z_2)\hat{\boldsymbol{r}}_2\Big)\right\rangle , \qquad \text{(C.1)} \\
&= \langle X_1 X_2^*\rangle \\
&= \langle A_1 A_2^*\rangle + \langle B_1 B_2^*\rangle + \langle C_1 C_2^*\rangle \\
&\quad + \langle A_1 B_2^*\rangle + \langle A_1 C_2^*\rangle + \langle B_1 A_2^*\rangle \\
&\quad + \langle C_1 A_2^*\rangle + \langle B_1 C_2^*\rangle + \langle C_1 B_2^*\rangle + ... \\
&= \xi_{AA^*} + \xi_{BB^*} + \xi_{CC^*} + 2\xi_{(AB^*)} + 2\xi_{(AC^*)} + 2\xi_{(BC^*)} + ... , \qquad \text{(C.2)}
\end{aligned}$$

where $\hat{\boldsymbol{r}}_1 \cdot \hat{\boldsymbol{r}}_2 = \cos\delta\theta$, and the round brackets around the subscripts denote symmetrisation as usual. Expanding the quantities on the two-sphere, and relating them to the Newtonian potential Φ via some operator $\mathcal{L}$ (through, e.g. the Poisson equation) we have

$$A(t, \boldsymbol{r}) = \sum_{\ell m} \mathcal{L}_A\Big[\Phi^{\ell m}(t, r)\Big] Y_{\ell m}(\hat{\boldsymbol{r}}) , \qquad \text{(C.3)}$$

where $Y_{\ell m}$ the spherical harmonics. We can thus write generally that

$$\xi_{AB^*}(z_1, z_2, \theta) \;=\; \sum_{\ell m}\sum_{\ell' m'} \left\langle \mathcal{L}_A\left[\Phi_1^{\ell m}\right]\mathcal{L}_B\left[\Phi_2^{*\ell' m'}\right]\right\rangle Y_{\ell m}(\hat{\boldsymbol{r}}_1)Y_{\ell' m'}(\hat{\boldsymbol{r}}_2)\,. \tag{C.4}$$

Further assuming that we can straightforwardly factor out the initial condition of Φ from it's governing evolution equation (e.g. Bardeen equation), so that

$$\Phi^{\ell m}(t, r) = \phi(t, r)\Phi^{\ell m}_{\rm init}(r)\,, \quad \phi(t_{\rm init}, r) \equiv 1\,, \tag{C.5}$$

(C.4) then bcomes

$$\xi_{AB^*}(z_1, z_2, \theta) \;=\; \sum_{\ell\ell' mm'} \mathcal{L}_A\mathcal{L}_B\phi_1\phi_2 \left\langle \Phi^{\ell m}_{{\rm init}\,1}\Phi^{*}_{{\rm init}\,2}{}^{\ell' m'}\right\rangle Y_{\ell m}(\hat{\boldsymbol{r}}_1)Y_{\ell' m'}(\hat{\boldsymbol{r}}_2)\,. \tag{C.6}$$

Now, $\Phi^{\ell m}_{\rm init}(r)$ can be written as

$$\Phi^{\ell m}_{\rm init}(r) = \sqrt{\frac{2}{\pi}} i^\ell \int d^3k\, j_\ell(kr)\Phi_{\rm init}(\boldsymbol{k})Y_{\ell m}(\hat{k})\,, \tag{C.7}$$

which is related to the power spectrum via

$$\langle \Phi_{\rm init}(\boldsymbol{k}_1)\Phi^*_{\rm init}(\boldsymbol{k}_2)\rangle = \frac{2\pi^2}{k_1^3}\mathcal{P}_{\Phi_{\rm init}}(k_1)\delta^3(\boldsymbol{k}_1 - \boldsymbol{k}_2)\,. \tag{C.8}$$

The initial power spectrum of the Newtonian potential is given by

$$\mathcal{P}_{\Phi_{\rm init}}(k) = \frac{9}{25}\mathcal{P}_{\mathcal{R}}T^2(k)\,, \tag{C.9}$$

where $\mathcal{P}_{\mathcal{R}}(k_0)$ is the amplitude of the primordial curvature perturbation on some the pivot scale k_0, and $T(k)$ is the matter transfer function, with $T(k_0) \approx 1$. Note that since we fix the initial conditions with a flat FLRW power spectrum, we need to use the corresponding comoving coordinate r_F in (C.7), as opposed to the LTB coordinate r. Proper radial distance is independent of coordinates: $d_p(t_{\rm init}, r_F) = d_p(t_{\rm init}, r)$. Since $d_p(t_{\rm init}, r_F) = a(t_{\rm init})r_F$, we find that

$$r_F = (1 + z_{\rm init})\int_0^r dr\, \frac{a_\parallel(t_{\rm init}, r)}{\sqrt{1 - \kappa(r)r^2}} \equiv f(r)\,, \tag{C.10}$$

where $f(r) \approx (1+z_{\rm init})a_\perp(t_{\rm init},r)r$ since $\sqrt{1-\kappa(r)r^2} \approx 1$ for al r and $a_\parallel = \partial_r(a_\perp r)$. (5.9) then becomes

$$\Phi^{\ell m}_{\rm init}(r) = \frac{2}{\pi} i^\ell \int d^3k\, j_\ell(kf(r))\Phi_{\rm init}(\boldsymbol{k})Y_{\ell m}(\hat{k})\,, \tag{C.11}$$

Plugging (C.11) and (C.8) into (C.6) we get

$$\begin{aligned}
\xi_{AB^*}(z_1,z_2,\theta) &= 4\pi \sum_{\ell\ell' mm'} i^{\ell-\ell'} \int d^3k_2 \int d^3k_1\, k_1^{-3} \mathcal{L}_A\mathcal{L}_B\phi_1\phi_2 j_\ell(k_1 f_1) j_{\ell'}(k_2 f_2) \\
&\quad \times \delta^3(\boldsymbol{k}_1-\boldsymbol{k}_2)\mathcal{P}_{\Phi_{\rm init}}(k_1) Y_{\ell m}(\hat{k}_1) Y_{\ell' m'}(\hat{k}_2) Y_{\ell m}(\hat{\boldsymbol{r}}_1) Y_{\ell' m'}(\hat{\boldsymbol{r}}_2) \\
&= 4\pi \sum_{\ell\ell' mm'} i^{\ell-\ell'} \int d\ln k_1\, \mathcal{L}_A\mathcal{L}_B\phi_1\phi_2 j_\ell(k_1 f_1) j_{\ell'}(k_1 f_2) \\
&\quad \times \mathcal{P}_{\Phi_{\rm init}}(k_1) Y_{\ell m}(\hat{\boldsymbol{r}}_1) Y_{\ell' m'}(\hat{\boldsymbol{r}}_2) \int d\Omega_k\, Y_{\ell m}(\hat{k}_1) Y_{\ell' m'}(\hat{k}_1) \\
&= 4\pi \sum_{\ell m} \int d\ln k_1\, \mathcal{L}_A\mathcal{L}_B\phi_1\phi_2 j_\ell(k_1 f_1) j_\ell(k_1 f_2) \mathcal{P}_{\Phi_{\rm init}}(k_1) \\
&\quad \times Y_{\ell m}(\hat{\boldsymbol{r}}_1) Y_{\ell m}(\hat{\boldsymbol{r}}_2) \\
&= \sum_\ell (2\ell+1) \mathrm{P}_\ell(\cos(\theta)) C_\ell(z_1,z_2)\,,
\end{aligned} \tag{C.12}$$

where

$$C_\ell(z_1,z_2) = \int d\ln k\, \mathcal{L}_A\mathcal{L}_B\phi_1\phi_2 j_\ell(kf_1) j_\ell(kf_2) \mathcal{P}_{\Phi_{\rm init}}(k)\,. \tag{C.13}$$

Bibliography

[1] A. Einstein, "The Foundation of the General Theory of Relativity," *Annalen Phys.* **49** (1916) 769–822.

[2] E. Hubble, "A Relation between Distance and Radial Velocity among Extra-Galactic Nebulae," *Proceedings of the National Academy of Science* **15** (Mar., 1929) 168–173.

[3] A. Einstein, "Cosmological Considerations in the General Theory of Relativity," *Sitzungsber.Preuss.Akad.Wiss.Berlin (Math.Phys.)* **1917** (1917) 142–152. [LINK].

[4] W. L. Freedman, "Determination of cosmological parameters," *Phys.Scripta* **T85** (2000) 37–46, `arXiv:astro-ph/9905222 [astro-ph]`.

[5] A. A. Penzias and R. W. Wilson, "A Measurement of excess antenna temperature at 4080-Mc/s," *Astrophys.J.* **142** (1965) 419–421.

[6] G. Lemaître, "Expansion of the universe, A homogeneous universe of constant mass and increasing radius accounting for the radial velocity of extra-galactic nebulae," *"Mon.Not.Roy.Astron.Soc."* **91** (Mar., 1931) 483–490. [LINK].

[7] F. Iocco, G. Mangano, G. Miele, O. Pisanti, and P. D. Serpico, "Primordial Nucleosynthesis: from precision cosmology to fundamental physics," *Phys.Rept.* **472** (2009) 1–76, `arXiv:0809.0631 [astro-ph]`.

[8] A. H. Guth, "The Inflationary Universe: A Possible Solution to the Horizon and Flatness Problems," *Phys.Rev.* **D23** (1981) 347–356.

[9] S. Faber and J. Gallagher, "Masses and mass-to-light ratios of galaxies," *Ann.Rev.Astron.Astrophys.* **17** (1979) 135–183.

[10] G. R. Blumenthal, S. Faber, J. R. Primack, and M. J. Rees, "Formation of Galaxies and Large Scale Structure with Cold Dark Matter," *Nature* **311** (1984) 517–525.

[11] G. Efstathiou, W. J. Sutherland, and S. J. Maddox, "The cosmological constant and cold dark matter," *Nature* **348** (Dec., 1990) 705–707.

[12] B. Chaboyer, P. J. Kernan, L. M. Krauss, and P. Demarque, "A Lower limit on the age of the universe," *Science* **271** (1996) 957–961, arXiv:astro-ph/9509115 [astro-ph].

[13] **Supernova Search Team** Collaboration, A. G. Riess *et al.*, "Observational evidence from supernovae for an accelerating universe and a cosmological constant," *Astron.J.* **116** (1998) 1009–1038, arXiv:astro-ph/9805201 [astro-ph].

[14] **Supernova Cosmology Project** Collaboration, S. Perlmutter *et al.*, "Measurements of Omega and Lambda from 42 high redshift supernovae," *Astrophys.J.* **517** (1999) 565–586, arXiv:astro-ph/9812133 [astro-ph].

[15] J. A. Peacock, S. Cole, P. Norberg, C. M. Baugh, J. Bland-Hawthorn, *et al.*, "A Measurement of the cosmological mass density from clustering in the 2dF Galaxy Redshift Survey," *Nature* **410** (2001) 169–173, arXiv:astro-ph/0103143 [astro-ph].

[16] S. Allen, R. Schmidt, and A. Fabian, "Cosmological constraints from the x-ray gas mass fraction in relaxed lensing clusters observed with Chandra," *Mon.Not.Roy.Astron.Soc.* **334** (2002) L11, arXiv:astro-ph/0205007 [astro-ph].

[17] **WMAP Collaboration** Collaboration, D. Spergel *et al.*, "First year Wilkinson Microwave Anisotropy Probe (WMAP) observations: Determination of cosmological parameters," *Astrophys.J.Suppl.* **148** (2003) 175–194, arXiv:astro-ph/0302209 [astro-ph].

[18] S. Weinberg, "The Cosmological constant problems," arXiv:astro-ph/0005265 [astro-ph].

[19] E. V. Linder, "The Dynamics of Quintessence, The Quintessence of Dynamics," *Gen.Rel.Grav.* **40** (2008) 329–356, arXiv:0704.2064 [astro-ph].

[20] D. Bertacca, N. Bartolo, and S. Matarrese, "Unified Dark Matter Scalar Field Models," *Adv.Astron.* **2010** (2010) 904379, arXiv:1008.0614 [astro-ph.CO].

[21] S. Tsujikawa, "Modified gravity models of dark energy," *Lect.Notes Phys.* **800** (2010) 99–145, arXiv:1101.0191 [gr-qc].

[22] T. Buchert and S. Rasanen, "Backreaction in late-time cosmology," *Ann.Rev.Nucl.Part.Sci.* **62** (2012) 57–79, arXiv:1112.5335 [astro-ph.CO].

[23] K. Bolejko, M.-N. Celerier, and A. Krasinski, "Inhomogeneous cosmological models: Exact solutions and their applications," *Class.Quant.Grav.* **28** (2011) 164002, arXiv:1102.1449 [astro-ph.CO].

[24] J.-P. Uzan, "Dark energy, gravitation and the Copernican principle," arXiv:0912.5452 [gr-qc].

[25] R. Maartens, G. F. Ellis, and S. Stoeger, William R., "Limits on anisotropy and inhomogeneity from the cosmic background radiation," *Phys.Rev.* **D51** (1995) 1525–1535, arXiv:astro-ph/9501016 [astro-ph].

[26] R. C. Keenan, A. J. Barger, and L. L. Cowie, "Evidence for a 300 Megaparsec Scale Under-density in the Local Galaxy Distribution," *Astrophys.J.* **775** (2013) 62, arXiv:1304.2884 [astro-ph.CO].

[27] K. T. Inoue and J. Silk, "Local voids as the origin of large-angle cosmic microwave background anomalies I," *Astrophys.J.* **648** (2006) 23–30, arXiv:astro-ph/0602478 [astro-ph].

[28] I. Masina and A. Notari, "Detecting the Cold Spot as a Void with the Non-Diagonal Two-Point Function," *JCAP* **1009** (2010) 028, arXiv:1007.0204 [astro-ph.CO].

[29] M. Rubart, D. Bacon, and D. J. Schwarz, "Impact of local structure on the cosmic radio dipole," arXiv:1402.0376 [astro-ph.CO].

[30] I. Gott, J. Richard, M. Juric, D. Schlegel, F. Hoyle, M. Vogeley, *et al.*, "A map of the universe," *Astrophys.J.* **624** (2005) 463, arXiv:astro-ph/0310571 [astro-ph].

[31] K. Bolejko, "The effect of inhomogeneities on the distance to the last scattering surface and the accuracy of the CMB analysis," *JCAP* **1102** (2011) 025, arXiv:1101.3338 [astro-ph.CO].

[32] W. Valkenburg, "Perceiving the equation of state of Dark Energy while living in a Cold Spot," *JCAP* **1201** (2012) 047, arXiv:1106.6042 [astro-ph.CO].

[33] V. Marra, M. Paakkonen, and W. Valkenburg, "Uncertainty on w from large-scale structure," *Mon.Not.Roy.Astron.Soc.* **431** (2013) 1891–1902, arXiv:1203.2180 [astro-ph.CO].

[34] H. Alnes and M. Amarzguioui, "CMB anisotropies seen by an off-center observer in a spherically symmetric inhomogeneous Universe," *Phys.Rev.* **D74** (2006) 103520, arXiv:astro-ph/0607334 [astro-ph].

[35] M. Blomqvist and E. Mortsell, "Supernovae as seen by off-center observers in a local void," *JCAP* **1005** (2010) 006, arXiv:0909.4723 [astro-ph.CO].

[36] S. Foreman, A. Moss, J. P. Zibin, and D. Scott, "Spatial and temporal tuning in void models for acceleration," *Phys.Rev.* **D82** (2010) 103532, arXiv:1009.0273 [astro-ph.CO].

[37] B. Sinclair, T. M. Davis, and T. Haugbolle, "Residual Hubble-bubble effects on supernova cosmology," *Astrophys.J.* **718** (2010) 1445–1455, arXiv:1006.0911 [astro-ph.CO].

[38] J. Goodman, "Geocentrism reexamined," *Phys.Rev.* **D52** (1995) 1821–1827, arXiv:astro-ph/9506068 [astro-ph].

[39] J. Garcia-Bellido and T. Haugboelle, "Looking the void in the eyes - the kSZ effect in LTB models," *JCAP* **0809** (2008) 016, arXiv:0807.1326 [astro-ph].

[40] D. Garfinkle, "The Motion of galaxy clusters in inhomogeneous cosmologies," *Class.Quant.Grav.* **27** (2010) 065002, arXiv:0908.4102 [gr-qc].

[41] P. Bull, T. Clifton, and P. G. Ferreira, "The kSZ effect as a test of general radial inhomogeneity in LTB cosmology," *Phys.Rev.* **D85** (2012) 024002, arXiv:1108.2222 [astro-ph.CO].

[42] T. Clifton, C. Clarkson, and P. Bull, "The isotropic blackbody CMB as evidence for a homogeneous universe," *Phys.Rev.Lett.* **109** (2012) 051303, arXiv:1111.3794 [gr-qc].

[43] R. Caldwell and A. Stebbins, "A Test of the Copernican Principle," *Phys.Rev.Lett.* **100** (2008) 191302, arXiv:0711.3459 [astro-ph].

[44] P. Zhang and A. Stebbins, "Confirmation of the Copernican principle at Gpc radial scale and above from the kinetic Sunyaev Zel'dovich effect power spectrum," *Phys.Rev.Lett.* **107** (2011) 041301, arXiv:1009.3967 [astro-ph.CO].

[45] R. Caldwell and N. Maksimova, "Spectral Distortion in a Radially Inhomogeneous Cosmology," arXiv:1309.4454 [astro-ph.CO].

[46] C. Clarkson, B. Bassett, and T. H.-C. Lu, "A general test of the Copernican Principle," *Phys.Rev.Lett.* **101** (2008) 011301, arXiv:0712.3457 [astro-ph].

[47] C. Zunckel and C. Clarkson, "Consistency Tests for the Cosmological Constant," *Phys.Rev.Lett.* **101** (2008) 181301, arXiv:0807.4304 [astro-ph].

[48] S. February, J. Larena, M. Smith, and C. Clarkson, "Rendering Dark Energy Void," *Mon.Not.Roy.Astron.Soc.* **405** (2010) 2231, arXiv:0909.1479 [astro-ph.CO].

[49] R. Maartens, "Is the Universe homogeneous?," *Phil.Trans.Roy.Soc.Lond.* **A369** (2011) 5115–5137, arXiv:1104.1300 [astro-ph.CO].

[50] C. Clarkson, "Establishing homogeneity of the universe in the shadow of dark energy," *Comptes Rendus Physique* **13** (2012) 682–718, arXiv:1204.5505 [astro-ph.CO].

[51] J.-P. Uzan, C. Clarkson, and G. F. Ellis, "Time drift of cosmological redshifts as a test of the Copernican principle," *Phys.Rev.Lett.* **100** (2008) 191303, arXiv:0801.0068 [astro-ph].

[52] M. Quartin and L. Amendola, "Distinguishing Between Void Models and Dark Energy with Cosmic Parallax and Redshift Drift," *Phys.Rev.* **D81** (2010) 043522, arXiv:0909.4954 [astro-ph.CO].

[53] P. Mishra, M.-N. Célérier, and T. P. Singh, "Redshift drift in axially symmetric quasispherical Szekeres models," *Phys.Rev.D.* **86** no. 8, (Oct., 2012) 083520, arXiv:1206.6026 [astro-ph.CO].

[54] C.-M. Yoo, T. Kai, and K.-i. Nakao, "Redshift Drift in LTB Void Universes," *Phys.Rev.* **D83** (2011) 043527, arXiv:1010.0091 [astro-ph.CO].

[55] T. Clifton, P. G. Ferreira, and K. Land, "Living in a Void: Testing the Copernican Principle with Distant Supernovae," *Phys.Rev.Lett.* **101** (2008) 131302, arXiv:0807.1443 [astro-ph].

[56] K. Tomita and K. T. Inoue, "Probing violation of the Copernican principle via the integrated Sachs-Wolfe effect," *Phys.Rev.* **D79** (2009) 103505, arXiv:0903.1541 [astro-ph.CO].

[57] F. Wang and Z. Dai, "Testing the local-void alternative to dark energy using galaxy pairs," arXiv:1304.4399 [astro-ph.CO].

[58] B. Hoyle, R. Tojeiro, R. Jimenez, A. Heavens, C. Clarkson, *et al.*, "Testing Homogeneity with the Galaxy Fossil Record," *Astrophys.J.* **762** (2012) L9, arXiv:1209.6181 [astro-ph.CO].

[59] M. Seikel, S. Yahya, R. Maartens, and C. Clarkson, "Using H(z) data as a probe of the concordance model," *Phys.Rev.* **D86** (2012) 083001, arXiv:1205.3431 [astro-ph.CO].

[60] R. de Putter, L. Verde, and R. Jimenez, "Testing LTB Void Models Without the Cosmic Microwave Background or Large Scale Structure: New Constraints from Galaxy Ages," *JCAP* **1302** (2013) 047, arXiv:1208.4534 [astro-ph.CO].

[61] T.-J. Zhang, H. Wang, and C. Ma, "Testing the Copernican Principle with Hubble Parameter," arXiv:1210.1775 [astro-ph.CO].

[62] M. Zumalacarregui, J. Garcia-Bellido, and P. Ruiz-Lapuente, "Tension in the Void: Cosmic Rulers Strain Inhomogeneous Cosmologies," *JCAP* **1210** (2012) 009, arXiv:1201.2790 [astro-ph.CO].

[63] W. Valkenburg, V. Marra, and C. Clarkson, "Testing the Copernican principle by constraining spatial homogeneity," arXiv:1209.4078 [astro-ph.CO].

[64] P. S. Apostolopoulos, N. Brouzakis, N. Tetradis, and E. Tzavara, "Cosmological acceleration and gravitational collapse," *JCAP* **0606** (2006) 009, arXiv:astro-ph/0603234 [astro-ph].

[65] R. A. Sussman, "Back-reaction and effective acceleration in generic LTB dust models," *Class.Quant.Grav.* **28** (2011) 235002, arXiv:1102.2663 [gr-qc].

[66] P. Peter and J.-P. Uzan, *Primordial Cosmology.* Oxford University Press, 2009.

[67] V. F. Mukhanov, H. Feldman, and R. H. Brandenberger, "Theory of cosmological perturbations. Part 1. Classical perturbations. Part 2. Quantum theory of perturbations. Part 3. Extensions," *Phys.Rept.* **215** (1992) 203–333.

[68] G. Ellis and M. Bruni, "Covariant and Gauge Invariant Approach to Cosmological Density Fluctuations," *Phys.Rev.* **D40** (1989) 1804–1818.

[69] J. M. Bardeen, "Gauge Invariant Cosmological Perturbations," *Phys.Rev.* **D22** (1980) 1882–1905.

[70] J. Guy, M. Sullivan, A. Conley, N. Regnault, P. Astier, *et al.*, "The Supernova Legacy Survey 3-year sample: Type Ia Supernovae photometric distances and cosmological constraints," *Astron.Astrophys.* **523** (2010) A7, arXiv:1010.4743 [astro-ph.CO].

[71] H. Campbell, C. B. D'Andrea, R. C. Nichol, M. Sako, M. Smith, *et al.*, "Cosmology with Photometrically-Classified Type Ia Supernovae from the SDSS-II Supernova Survey," *Astrophys.J.* **763** (2013) 88, arXiv:1211.4480 [astro-ph.CO].

[72] **Dark Energy Survey Collaboration** Collaboration, T. Abbott *et al.*, "The dark energy survey," arXiv:astro-ph/0510346 [astro-ph].

[73] **LSST Science Collaborations, LSST Project** Collaboration, P. A. Abell *et al.*, "LSST Science Book, Version 2.0," arXiv:0912.0201 [astro-ph.IM].

[74] **Euclid Theory Working Group** Collaboration, L. Amendola *et al.*, "Cosmology and fundamental physics with the Euclid satellite," *Living Rev. Relativity* **16,** (2013) , 6, arXiv:1206.1225 [astro-ph.CO].

[75] P. L. Kelly, M. Hicken, D. L. Burke, K. S. Mandel, and R. P. Kirshner, "Hubble Residuals of Nearby Type Ia Supernovae Are Correlated with Host Galaxy Masses," *Astrophys.J.* **715** (2010) 743–756, arXiv:0912.0929 [astro-ph.CO].

[76] D. J. Schlegel, D. P. Finkbeiner, and M. Davis, "Maps of dust IR emission for use in estimation of reddening and CMBR foregrounds," *Astrophys.J.* **500** (1998) 525, arXiv:astro-ph/9710327 [astro-ph].

[77] J. C. Weingartner and B. Draine, "Dust grain size distributions and extinction in the Milky Way, LMC, and SMC," *Astrophys.J.* **548** (2001) 296, arXiv:astro-ph/0008146 [astro-ph].

[78] **SDSS Collaboration** Collaboration, M. Smith *et al.*, "The Effect of Weak Lensing on Distance Estimates from Supernovae," *Astrophys.J.* (2013) , arXiv:1307.2566 [astro-ph.CO].

[79] A. G. Riess, L. Macri, S. Casertano, H. Lampeitl, H. C. Ferguson, *et al.*, "A 3Telescope and Wide Field Camera 3," *Astrophys.J.* **730** (2011) 119, arXiv:1103.2976 [astro-ph.CO].

[80] W. L. Freedman, B. F. Madore, V. Scowcroft, C. Burns, A. Monson, *et al.*, "Carnegie Hubble Program: A Mid-Infrared Calibration of the Hubble Constant," *Astrophys.J.* **758** (2012) 24, arXiv:1208.3281 [astro-ph.CO].

[81] S. Suyu, T. Treu, R. Blandford, W. Freedman, S. Hilbert, *et al.*, "The Hubble constant and new discoveries in cosmology," arXiv:1202.4459 [astro-ph.CO].

[82] **Planck Collaboration** Collaboration, P. Ade *et al.*, "Planck 2013 results. XVI. Cosmological parameters," arXiv:1303.5076 [astro-ph.CO].

[83] L. Verde, P. Protopapas, and R. Jimenez, "Planck and the local Universe: quantifying the tension," arXiv:1306.6766 [astro-ph.CO].

[84] R. Jimenez and A. Loeb, "Constraining cosmological parameters based on relative galaxy ages," *Astrophys.J.* **573** (2002) 37–42, arXiv:astro-ph/0106145 [astro-ph].

[85] M. Moresco, L. Verde, L. Pozzetti, R. Jimenez, and A. Cimatti, "New constraints on cosmological parameters and neutrino properties using the expansion rate of the Universe to z 1.75," *JCAP* **1207** (2012) 053, arXiv:1201.6658 [astro-ph.CO].

[86] N. W. Boggess, J. C. Mather, R. Weiss, C. L. Bennett, E. S. Cheng, E. Dwek, S. Gulkis, M. G. Hauser, M. A. Janssen, T. Kelsall, S. S. Meyer, S. H. Moseley, T. L. Murdock, R. A. Shafer, R. F. Silverberg, G. F. Smoot, D. T. Wilkinson, and E. L. Wright, "The COBE mission - Its design and performance two years after launch," *Astrophys.J.* **397** (Oct., 1992) 420–429.

[87] **Planck Collaboration** Collaboration, P. Ade *et al.*, "Planck 2013 results. I. Overview of products and scientific results," arXiv:1303.5062 [astro-ph.CO].

[88] J. Carlstrom, P. Ade, K. Aird, B. Benson, L. Bleem, *et al.*, "The 10 Meter South Pole Telescope," *Publ.Astron.Soc.Pac.* **123** (2011) 568–581, arXiv:0907.4445 [astro-ph.IM].

[89] **SPTpol Collaboration** Collaboration, D. Hanson *et al.*, "Detection of B-mode Polarization in the Cosmic Microwave Background with Data from the South Pole Telescope," arXiv:1307.5830 [astro-ph.CO].

[90] **Planck Collaboration** Collaboration, P. Ade *et al.*, "Planck 2013 results. XXIII. Isotropy and Statistics of the CMB," arXiv:1303.5083 [astro-ph.CO].

[91] **SDSS Collaboration** Collaboration, D. J. Eisenstein *et al.*, "Detection of the baryon acoustic peak in the large-scale correlation function of SDSS luminous red galaxies," *Astrophys.J.* **633** (2005) 560–574, arXiv:astro-ph/0501171 [astro-ph].

[92] **SDSS Collaboration** Collaboration, W. J. Percival *et al.*, "Baryon Acoustic Oscillations in the Sloan Digital Sky Survey Data Release 7 Galaxy Sample," *Mon.Not.Roy.Astron.Soc.* **401** (2010) 2148–2168, arXiv:0907.1660 [astro-ph.CO].

[93] N. Padmanabhan, X. Xu, D. J. Eisenstein, R. Scalzo, A. J. Cuesta, *et al.*, "A 2 per cent distance to z=0.35 by reconstructing baryon acoustic oscillations - I. Methods and application to the Sloan Digital Sky Survey," *Mon.Not.Roy.Astron.Soc.* **427** no. 3, (2012) 2132–2145, arXiv:1202.0090 [astro-ph.CO].

[94] F. Beutler, C. Blake, M. Colless, D. H. Jones, L. Staveley-Smith, *et al.*, "The 6dF Galaxy Survey: Baryon Acoustic Oscillations and the Local Hubble Constant," *Mon.Not.Roy.Astron.Soc.* **416** (2011) 3017–3032, arXiv:1106.3366 [astro-ph.CO].

[95] C. Blake, E. Kazin, F. Beutler, T. Davis, D. Parkinson, *et al.*, "The WiggleZ Dark Energy Survey: mapping the distance-redshift relation with baryon acoustic oscillations," *Mon.Not.Roy.Astron.Soc.* **418** (2011) 1707–1724, arXiv:1108.2635 [astro-ph.CO].

[96] **BOSS Collaboration** Collaboration, K. S. Dawson *et al.*, "The Baryon Oscillation Spectroscopic Survey of SDSS-III," arXiv:1208.0022 [astro-ph.CO].

[97] T. Okumura, T. Matsubara, D. J. Eisenstein, I. Kayo, C. Hikage, *et al.*, "Large-Scale Anisotropic Correlation Function of SDSS Luminous Red Galaxies," *Astrophys.J.* **676** (2008) 889–898, arXiv:0711.3640 [astro-ph].

[98] E. Gaztanaga and A. Cabre, "The anisotropic redshift space galaxy correlation function: detection on the BAO Ring," arXiv:0812.2480 [astro-ph].

[99] X. Xu, A. J. Cuesta, N. Padmanabhan, D. J. Eisenstein, and C. K. McBride, "Measuring D_A and H at z=0.35 from the SDSS DR7 LRGs using baryon acoustic oscillations," arXiv:1206.6732 [astro-ph.CO].

[100] E. Sanchez, D. Alonso, F. Sanchez, J. Garcia-Bellido, and I. Sevilla, "Precise Measurement of the Radial Baryon Acoustic Oscillation Scales in Galaxy Redshift Surveys," *Monthly Notices of the Royal Astronomical Society,* **434** (2013) 2008, arXiv:1210.6446 [astro-ph.CO].

[101] L. Anderson, E. Aubourg, S. Bailey, F. Beutler, A. S. Bolton, *et al.*, "The clustering of galaxies in the SDSS-III Baryon Oscillation Spectroscopic Survey: Measuring D_A and H at z=0.57 from the Baryon Acoustic Peak in the Data Release 9 Spectroscopic Galaxy Sample," arXiv:1303.4666 [astro-ph.CO].

[102] D. Roig, L. Verde, J. Miralda-Escude, R. Jimenez, and C. Pena-Garay, "Photo-z optimization for measurements of the BAO radial direction," *JCAP* **0904** (2009) 008, arXiv:0812.3414 [astro-ph].

[103] E. Sanchez, A. Carnero, J. Garcia-Bellido, E. Gaztanaga, F. de Simoni, *et al.*, "Tracing The Sound Horizon Scale With Photometric Redshift Surveys," *Mon.Not.Roy.Astron.Soc.* **411** (2011) 277–288, arXiv:1006.3226 [astro-ph.CO].

[104] A. Gorecki, A. Abate, R. Ansari, A. Barrau, S. Baumont, *et al.*, "A new method to improve photometric redshift reconstruction. Applications to the Large Synoptic Survey Telescope," arXiv:1301.3010 [astro-ph.CO].

[105] N. Benitez, E. Gaztanaga, R. Miquel, F. Castander, M. Moles, *et al.*, "Measuring Baryon Acoustic Oscillations along the line of sight with photometric redshifs: the PAU survey," *Astrophys.J.* **691** (2009) 241–260, arXiv:0807.0535 [astro-ph].

[106] J. F. Navarro, C. S. Frenk, and S. D. White, "A Universal density profile from hierarchical clustering," *Astrophys.J.* **490** (1997) 493–508, arXiv:astro-ph/9611107 [astro-ph].

[107] S. W. Allen, A. E. Evrard, and A. B. Mantz, "Cosmological Parameters from Observations of Galaxy Clusters," *Ann.Rev.Astron.Astrophys.* **49** (2011) 409–470, arXiv:1103.4829 [astro-ph.CO].

[108] F.-X. Dupe, A. Rassat, J.-L. Starck, and M. Fadili, "Measuring the Integrated Sachs-Wolfe Effect," arXiv:1010.2192 [astro-ph.CO].

[109] H. Hoekstra and B. Jain, "Weak Gravitational Lensing and its Cosmological Applications," *Ann.Rev.Nucl.Part.Sci.* **58** (2008) 99–123, arXiv:0805.0139 [astro-ph].

[110] B. A. Bassett and R. Hlozek, "Baryon Acoustic Oscillations," arXiv:0910.5224 [astro-ph.CO].

[111] L. R. Abramo and T. S. Pereira, "Testing gaussianity, homogeneity and isotropy with the cosmic microwave background," *Adv.Astron.* **2010** (2010) 378203, arXiv:1002.3173 [astro-ph.CO].

[112] T. Biswas, A. Notari, and W. Valkenburg, "Testing the Void against Cosmological data: fitting CMB, BAO, SN and H0," *JCAP* **1011** (2010) 030, arXiv:1007.3065 [astro-ph.CO].

[113] S. D. Landy and A. S. Szalay, "Bias and variance of angular correlation functions," *Astrophys.J.* **412** (July, 1993) 64–71.

[114] P. C. Davies, "Multiverse cosmological models," *Mod.Phys.Lett.* **A19** (2004) 727–744, arXiv:astro-ph/0403047 [astro-ph].

[115] R. Watkins, H. A. Feldman, and M. J. Hudson, "Consistently Large Cosmic Flows on Scales of 100 Mpc/h: a Challenge for the Standard LCDM Cosmology," *Mon.Not.Roy.Astron.Soc.* **392** (2009) 743–756, arXiv:0809.4041 [astro-ph].

[116] U. Feindt, M. Kerschhaggl, M. Kowalski, G. Aldering, P. Antilogus, *et al.*, "Measuring cosmic bulk flows with Type Ia Supernovae from the Nearby Supernova Factory," *Astron.Astrophys.* (2013) , arXiv:1310.4184 [astro-ph.CO].

[117] Y.-Z. Ma and D. Scott, "Cosmic bulk flows on 50 h^{-1}Mpc scales: A Bayesian hyper-parameter method and multi-shells likelihood analysis," *Mon.Not.Roy.Astron.Soc.* **428** (2013) 2017, arXiv:1208.2028 [astro-ph.CO].

[118] T. Richardson, D. Spolyar, and M. Lehnert, "Plan beta: Core or Cusp?," arXiv:1311.1522 [astro-ph.GA].

[119] C. J. Copi, D. Huterer, D. J. Schwarz, and G. D. Starkman, "Large angle anomalies in the CMB," *Adv.Astron.* **2010** (2010) 847541, arXiv:1004.5602 [astro-ph.CO].

[120] O. Farooq, D. Mania, and B. Ratra, "Observational constraints on non-flat dynamical dark energy cosmological models," arXiv:1308.0834 [astro-ph.CO].

[121] J. Khoury and A. Weltman, "Chameleon cosmology," *Phys.Rev.* **D69** (2004) 044026, arXiv:astro-ph/0309411 [astro-ph].

[122] A. I. Vainshtein, "To the problem of nonvanishing gravitation mass," *Phys. Lett. B* **39** (1972) 393–394.

[123] G. Cognola, E. Elizalde, S. Nojiri, S. Odintsov, L. Sebastiani, *et al.*, "A Class of viable modified f(R) gravities describing inflation and the onset of accelerated expansion," *Phys.Rev.* **D77** (2008) 046009, arXiv:0712.4017 [hep-th].

[124] L. Lombriser, A. Slosar, U. Seljak, and W. Hu, "Constraints on f(R) gravity from probing the large-scale structure," *Phys.Rev.* **D85** (2012) 124038, arXiv:1003.3009 [astro-ph.CO].

[125] A. Abebe, A. de la Cruz-Dombriz, and P. K. S. Dunsby, "Large Scale Structure Constraints for a Class of f(R) Theories of Gravity," *Phys.Rev.* **D88** (2013) 044050, arXiv:1304.3462 [astro-ph.CO].

[126] G.-B. Zhao, "Modeling the nonlinear clustering in modified gravity models I: A fitting formula for matter power spectrum of f(R) gravity," arXiv:1312.1291 [astro-ph.CO].

[127] B. Jain, V. Vikram, and J. Sakstein, "Astrophysical Tests of Modified Gravity: Constraints from Distance Indicators in the Nearby Universe," *Astrophys.J.* **779** (Dec., 2013) 39, arXiv:1204.6044 [astro-ph.CO].

[128] G. F. R. Ellis, "Relativistic cosmology - Its nature, aims and problems," in *General Relativity and Gravitation Conference*, B. Bertotti, F. de Felice, and A. Pascolini, eds., pp. 215–288. 1984.

[129] G. F. R. Ellis and W. Stoeger, "The 'fitting problem' in cosmology," *Classical and Quantum Gravity* **4** (Nov., 1987) 1697–1729.

[130] T. Buchert, "Backreaction Issues in Relativistic Cosmology and the Dark Energy Debate," *AIP Conf.Proc.* **910** (2007) 361–380, arXiv:gr-qc/0612166 [gr-qc].

[131] C. Clarkson and O. Umeh, "Is backreaction really small within concordance cosmology?," *Class.Quant.Grav.* **28** (2011) 164010, arXiv:1105.1886 [astro-ph.CO].

[132] G. Lemaître, "L'Univers en expansion," *Annales de la Societe Scietifique de Bruxelles* **53** (1933) 51–+.

[133] R. C. Tolman, "Effect of Inhomogeneity on Cosmological Models," *Proceedings of the National Academy of Science* **20** (Mar., 1934) 169–176.

[134] H. Bondi, "Spherically symmetrical models in general relativity," *Monthly Notices of the Royal Astronomical Society* **107** (1947) 410.

[135] P. Szekeres, "A class of inhomogeneous cosmological models," *Communications in Mathematical Physics* **41** (Feb., 1975) 55–64.

[136] K. Bolejko, "Cosmological applications of the Szekeres model," arXiv:astro-ph/0607130 [astro-ph].

[137] H. Stephani, "Some perfect fluid solutions of Einstein's field equations without symmetries," *Classical and Quantum Gravity* **4** (Jan., 1987) 125–136.

[138] J. Plebanski and A. Krasinski, *An Introduction to General Relativity and Cosmology*. Cambridge University Press, 2006.

[139] J. Moffat and D. Tatarski, "The Age of the universe, the Hubble constant and QSOs in a locally inhomogeneous universe," arXiv:astro-ph/9404048 [astro-ph].

[140] K. Enqvist and T. Mattsson, "The effect of inhomogeneous expansion on the supernova observations," *JCAP* **0702** (2007) 019, arXiv:astro-ph/0609120 [astro-ph].

[141] K. Bolejko, "Supernovae ia observations in the lemaitre-tolman model," *PMC Phys.* **A2** (2008) 1, arXiv:astro-ph/0512103 [astro-ph].

[142] C.-M. Yoo, T. Kai, and K.-i. Nakao, "Solving Inverse Problem with Inhomogeneous Universe," *Prog.Theor.Phys.* **120** (2008) 937–960, arXiv:0807.0932 [astro-ph].

[143] N. Mustapha, C. Hellaby, and G. Ellis, "Large scale inhomogeneity versus source evolution: Can we distinguish them observationally?," *Mon.Not.Roy.Astron.Soc.* **292** (1997) 817–830, arXiv:gr-qc/9808079 [gr-qc].

[144] A. Iribarrem, P. Andreani, S. February, C. Gruppioni, A. Lopes, *et al.*, "Relativistic cosmology number densities in void-Lemaitre-Tolman-Bondi models," arXiv:1401.6572 [astro-ph.CO].

[145] H. Alnes, M. Amarzguioui, and O. Gron, "An inhomogeneous alternative to dark energy?," *Phys.Rev.* **D73** (2006) 083519, arXiv:astro-ph/0512006 [astro-ph].

[146] J. Zibin, A. Moss, and D. Scott, "Can we avoid dark energy?," *Phys.Rev.Lett.* **101** (2008) 251303, arXiv:0809.3761 [astro-ph].

[147] K. Bolejko and J. S. B. Wyithe, "Testing the Copernican Principle Via Cosmological Observations," *JCAP* **0902** (2009) 020, arXiv:0807.2891 [astro-ph].

[148] J. Garcia-Bellido and T. Haugboelle, "Confronting Lemaitre-Tolman-Bondi models with Observational Cosmology," *JCAP* **0804** (2008) 003, arXiv:0802.1523 [astro-ph].

[149] A. Moss, J. P. Zibin, and D. Scott, "Precision Cosmology Defeats Void Models for Acceleration," *Phys.Rev.* **D83** (2011) 103515, arXiv:1007.3725 [astro-ph.CO].

[150] J. P. Zibin, "Can decaying modes save void models for acceleration?," *Phys.Rev.* **D84** (2011) 123508, arXiv:1108.3068 [astro-ph.CO].

[151] M. Regis and C. Clarkson, "Do primordial Lithium abundances imply there's no Dark Energy?," *Gen.Rel.Grav.* **44** (2012) 567–579, arXiv:1003.1043 [astro-ph.CO].

[152] M.-N. Celerier, K. Bolejko, and A. Krasinski, "A (giant) void is not mandatory to explain away dark energy with a Lemaitre – Tolman model," *Astron.Astrophys.* **518** (2010) A21, arXiv:0906.0905 [astro-ph.CO].

[153] **WMAP Collaboration** Collaboration, G. Hinshaw *et al.*, "Five-Year Wilkinson Microwave Anisotropy Probe (WMAP) Observations: Data Processing, Sky Maps, and Basic Results," *Astrophys.J.Suppl.* **180** (2009) 225–245, arXiv:0803.0732 [astro-ph].

[154] C. Clarkson, T. Clifton, and S. February, "Perturbation Theory in Lemaitre-Tolman-Bondi Cosmology," *JCAP* **0906** (2009) 025, arXiv:0903.5040 [astro-ph.CO].

[155] K. Tomita, "Perturbations in a spherically symmetric inhomogeneous cosmological model with the selfsimilar region," *Phys.Rev.* **D56** (1997) 3341–3356.

[156] J. P. Zibin, "Scalar Perturbations on Lemaitre-Tolman-Bondi Spacetimes," *Phys.Rev.* **D78** (2008) 043504, arXiv:0804.1787 [astro-ph].

[157] P. Dunsby, N. Goheer, B. Osano, and J.-P. Uzan, "How close can an Inhomogeneous Universe mimic the Concordance Model?," *JCAP* **1006** (2010) 017, arXiv:1002.2397 [astro-ph.CO].

[158] U. Gerlach and U. Sengupta, "GAUGE INVARIANT PERTURBATIONS ON MOST GENERAL SPHERICALLY SYMMETRIC SPACE-TIMES," *Phys.Rev.* **D19** (1979) 2268–2272.

[159] C. Gundlach and J. M. Martin-Garcia, "Gauge invariant and coordinate independent perturbations of stellar collapse. 1. The Interior," *Phys.Rev.* **D61** (2000) 084024, arXiv:gr-qc/9906068 [gr-qc].

[160] C. Bonvin and R. Durrer, "What galaxy surveys really measure," *Phys.Rev.* **D84** (2011) 063505, arXiv:1105.5280 [astro-ph.CO].

[161] A. Challinor and A. Lewis, "The linear power spectrum of observed source number counts," *Phys.Rev.* **D84** (2011) 043516, arXiv:1105.5292 [astro-ph.CO].

[162] K. Tomita, "Gauge-invariant treatment of the integrated Sachs-Wolfe effect on general spherically symmetric spacetimes," *Phys.Rev.* **D81** (2010) 063509, arXiv:0912.4773 [astro-ph.CO].

[163] C. Clarkson, G. F. Ellis, A. Faltenbacher, R. Maartens, O. Umeh, *et al.*, "(Mis-)Interpreting supernovae observations in a lumpy universe," *Mon.Not.Roy.Astron.Soc.* **426** (2012) 1121–1136, arXiv:1109.2484 [astro-ph.CO].

[164] R. E. Smith, D. S. Reed, D. Potter, L. Marian, M. Crocce, *et al.*, "Precision cosmology in muddy waters: Cosmological constraints and N-body codes," arXiv:1211.6434 [astro-ph.CO].

[165] R. Maartens, G.-B. Zhao, D. Bacon, K. Koyama, and A. Raccanelli, "Relativistic corrections and non-Gaussianity in radio continuum surveys," *JCAP* **1302** (2013) 044, arXiv:1206.0732 [astro-ph.CO].

[166] C. Clarkson, G. Ellis, J. Larena, and O. Umeh, "Does the growth of structure affect our dynamical models of the universe? The averaging, backreaction and fitting problems in cosmology," *Rept.Prog.Phys.* **74** (2011) 112901, arXiv:1109.2314 [astro-ph.CO].

[167] M. Bruni, D. B. Thomas, and D. Wands, "Computing General Relativistic effects from Newtonian N-body simulations: Frame dragging in the post-Friedmann approach," arXiv:1306.1562 [astro-ph.CO].

[168] J. Adamek, D. Daverio, R. Durrer, and M. Kunz, "General Relativistic N-body simulations in the weak field limit," *Phys.Rev.* **D88** (2013) 103527, arXiv:1308.6524 [astro-ph.CO].

[169] S. February, C. Clarkson, and R. Maartens, "Galaxy correlations and the BAO in a void universe: structure formation as a test of the Copernican Principle," *JCAP* **1303** (2013) 023, arXiv:1206.1602 [astro-ph.CO].

[170] D. Alonso, J. Garcia-Bellido, T. Haugbolle, and J. Vicente, "Large scale structure simulations of inhomogeneous LTB void models," *Phys.Rev.* **D82** (2010) 123530, arXiv:1010.3453 [astro-ph.CO].

[171] R. A. Sussman, "Weighed scalar averaging in LTB dust models, part II: a formalism of exact perturbations," *Class.Quant.Grav.* **30** (2013) 065016, arXiv:1301.0959 [gr-qc].

[172] R. Nishikawa, C.-M. Yoo, and K.-i. Nakao, "Evolution of density perturbations in large void universe," *Phys.Rev.* **D85** (2012) 103511, arXiv:1202.1582 [astro-ph.CO].

[173] C. Cutler and D. E. Holz, "Ultra-high precision cosmology from gravitational waves," *Phys.Rev.* **D80** (2009) 104009, arXiv:0906.3752 [astro-ph.CO].

[174] C. Shapiro, D. Bacon, M. Hendry, and B. Hoyle, "Delensing Gravitational Wave Standard Sirens with Shear and Flexion Maps," *Mon.Not.Roy.Astron.Soc.* **404** (2010) 858–866, arXiv:0907.3635 [astro-ph.CO].

[175] R. LeVeque, *Numerical Methods for Conservation Laws*. Lectures in Mathematics ETH Zürich, Department of Mathematics Research Institute of Mathematics. Springer, 1992. [LINK].

[176] C. Clarkson and M. Regis, "The Cosmic Microwave Background in an Inhomogeneous Universe - why void models of dark energy are only weakly constrained by the CMB," *JCAP* **1102** (2011) 013, arXiv:1007.3443 [astro-ph.CO].

[177] J. Garcia-Bellido and T. Haugboelle, "The radial BAO scale and Cosmic Shear, a new observable for Inhomogeneous Cosmologies," *JCAP* **0909** (2009) 028, arXiv:0810.4939 [astro-ph].

[178] N. Padmanabhan and . White, Martin J., "Constraining Anisotropic Baryon Oscillations," *Phys.Rev.* **D77** (2008) 123540, arXiv:0804.0799 [astro-ph].

[179] A. Rassat and A. Refregier, "3D Spherical Analysis of Baryon Acoustic Oscillations," arXiv:1112.3100 [astro-ph.CO].

[180] D. Bertacca, R. Maartens, A. Raccanelli, and C. Clarkson, "Beyond the plane-parallel and Newtonian approach: Wide-angle redshift distortions and convergence in general relativity," *JCAP* **1210** (2012) 025, arXiv:1205.5221 [astro-ph.CO].

[181] F. Montanari and R. Durrer, "A new method for the Alcock-Paczynski test," *Phys.Rev.* **D86** (2012) 063503, arXiv:1206.3545 [astro-ph.CO].

[182] S. February, J. Larena, C. Clarkson, and D. Pollney, "Evolution of linear perturbations in spherically symmetric dust models," arXiv:1311.5241 [astro-ph.CO].

[183] T. Matsubara, "The Correlation function in redshift space: General formula with wide angle effects and cosmological distortions," *Astrophys.J.* (1999) , arXiv:astro-ph/9908056 [astro-ph].